

WISCONSIN SPACE GRANT CONSORTIUM

Proceedings of the 25th Annual  
Wisconsin Space Conference

August 14, 2015

EAA AirVenture Museum

Oshkosh, Wisconsin





NASA  
WISCONSIN  
SPACE GRANT  
CONSORTIUM

## Commercial Space

25<sup>th</sup> Annual Wisconsin Space Conference

August 14, 2015

Host: EAA AirVenture Museum, Oshkosh, WI



Copyright © 2015 Wisconsin Space Grant Consortium

Wisconsin Space Grant Consortium

Carthage College

2001 Alford Park Drive

Kenosha, WI 53140

January, 2016



NASA  
WISCONSIN  
SPACE GRANT  
CONSORTIUM

## Innovations in Flight

25<sup>th</sup> Annual Wisconsin Space Conference

August 14, 2015

Host: Experimental Aircraft Association, Oshkosh, WI

---

**Edited by:** Kevin M. Crosby, Director, Wisconsin Space Grant Consortium  
Christine Thompson, Program Manager, Wisconsin Space Grant Consortium

Kevin Anderson, Wisconsin Department of Public Instruction  
Eric Barnes, University of Wisconsin – La Crosse  
Karin Borgh, BioPharmaceutical Technology Center Institute  
Jeff Clark, Lawrence University  
Julie Dahlstrom, Carthage College  
Bill Dirienzo, University of Wisconsin – Sheboygan  
Duane Foust, University of Wisconsin – Platteville  
Rex Hanger, University of Wisconsin – Whitewater  
Coggin Heeringa, Crossroads at Big Creek  
Beth Johnson, University of Wisconsin – Fox Valley  
Robert Morrow, Orbital Technologies Corporation  
Bethany Reilly, University of Wisconsin – Fox Valley  
Danny Riley, Medical College of Wisconsin  
Leah Simon, Ripon College  
Glenn Spiczak, University of Wisconsin – River Falls  
Richard Stewart, University of Wisconsin – Superior  
Swapnil Tripathi, University of Wisconsin – Washington County  
Tate Wilson, Carroll University  
Sebastian Zamfir, University of Wisconsin – Stevens Point  
Todd Zimmerman, University of Wisconsin – Stout

**Cover Art:** Sonex SubSonex JSX-1. Courtesy: Experimental Aircraft Association

**Published by:** Wisconsin Space Grant Consortium  
Carthage College  
2001 Alford Park Drive  
Kenosha, WI 53140-1994

**Publication Data:** ISSN: 2374-8877 (print) / 2374-8885 (electronic)  
Frequency: annual publication; Year established: 1994.



Preface to the Proceedings of the 25<sup>th</sup> Annual Wisconsin Space Conference

### **Silver Space Grant!**

I recently had a chance to wander the ruins of the American Space Program. A few students and I toured the historic launch sites of the Mercury-Apollo era of build fast, learn from mistakes, rinse and repeat. Armed with Wikipedia, a flashlight, and GPS, we explored the reinforced blast shelters ("block houses"), escape tunnels, and flame deflectors left where they stood after the last launches in the late 1960s. There are more than a dozen of these concrete and steel relics disappearing into the trees and brush on the ocean south of KSC, each with a very unique place in history. The one pictured here has special significance because it is where the Apollo 1 disaster occurred. Only a small brass plaque, barely visible against a massive concrete and steel support leg, memorializes the place where Gus Grissom, Ed White, and Roger Chaffee died in the fire that swept through their Apollo spacecraft during a "plugs out" test days before the scheduled first launch of the Apollo program.



It struck me, as we hacked through the brush and overgrowth surrounding these monuments, that NASA is not very good at preserving our history. A space program looks forward. It does not look back. So while the Silver Anniversary of these *Proceedings* is a good time to reflect on the past, maybe it's an even better time to imagine the future. And that's what you'll find in these pages. From drones to dark matter, the sense of a present future can be found throughout the work selected for celebration at the 25<sup>th</sup> Annual Wisconsin Space Conference. *Innovations in Flight*, the theme for this year's event, works well as an umbrella for the future-facing scientific contributions of our students and faculty researchers. There is much to be excited about in the work selected for publication this year and it's gratifying to see Wisconsin making measurable contributions to our future in space and on earth.

I hope you read these pages with the same sense of optimism about aerospace-related STEM research in Wisconsin that I have.

*Kevin M. Crosby, Director, WSGC     January, 2016*



## *Wisconsin Space Grant Consortium Programs for 2015*

### **Student Programs**

• Undergraduate Scholarship • Undergraduate Research • Graduate Fellowship • Dr. Laurel Salton Clark Memorial Graduate Fellowship • University Sounding Rocket Team Competition • Student High-Altitude Balloon Launch • Student High-Altitude Balloon Payload • Industry Member Internships • NASA Academy Leadership Internships • NASA Centers/JPL Internships • NASA Reduced Gravity Team Programs • Student Travel Awards

### **Research Infrastructure**

The Research Infrastructure Program provides Research Seed Grant Awards to faculty and staff from WSGC Member and Affiliate Member colleges and universities to support individuals interested in starting or enhancing space- or aerospace-related research program(s).

### **Higher Education Incentives**

The Higher Education Incentives Program is a seed-grant program inviting proposals for innovative, value-added, higher education teaching/training projects related to space science, space engineering, and other space- or aerospace-related disciplines. The Student Satellite Program including Balloon and Rocket programs is also administered under this program.

### **Industry Program**

The WSGC Industry Program is designed to meet the needs of Wisconsin Industry member institutions in multiple ways including:

- 1) The Industry Member Internships (listed under students above),
- 2) the Industry/Academic Research Seed Program designed to provide funding and open an avenue for member academia and industry researchers to work together on a space-related project, and
- 3) the Industrial Education and Training Program designed to provide funding for industry staff members to keep up-to-date in NASA-relevant fields.

### **Aerospace Outreach Program**

The Aerospace Outreach Program provides grants to promote outreach programs and projects that disseminate aerospace and space-related information to the general public, and support the development and implementation of aerospace and space-related curricula in Wisconsin classrooms. In addition, this program supports NASA-trained educators in teacher training programs.

### **Special Initiatives**

The Special Initiatives Program is designed to provide planning grants and program supplement grants for ongoing or new programs which have space or aerospace content and are intended to encourage, attract, and retain under-represented groups, especially women, minorities and the developmentally challenged, in careers in space- or aerospace-related fields.

### **Wisconsin Space Conference**

The Wisconsin Space Conference is an annual conference featuring presentations of students, faculty, K-12 educators and others who have received grants from WSGC over the past year. The Conference allows all to share their work with others interested in Space. It also includes keynote addresses, and the announcement of award recipients for the next year.

### **Regional Consortia**

WSGC is a founding member of the Great Midwest Regional Space Grant Consortia. The Consortia consists of eight members, all Space Grants from Midwest and Great Lakes States.

### **Contact Us**

Wisconsin Space Grant Consortium  
Carthage College  
Kenosha, Wisconsin 53140-1994

Phone: (262) 551-6054  
E-mail: [spacegrant@carthage.edu](mailto:spacegrant@carthage.edu)  
Web: [spacegrant.carthage.edu](http://spacegrant.carthage.edu)

# 2015 Wisconsin Space Conference

## *Innovations in Flight*

### TABLE OF CONTENTS

<b>General Information</b> .....	i
<b>Issue Credits</b> .....	ii
<b>Director’s Welcome</b> .....	iii
<b>WSGC Programs</b> .....	iv

#### **Part One: Astronomy and Cosmology**

<i>A Search for a New Variable and Proper Motion Stars in the Galactic Disk</i> , Robert A Benjamin .....	1
<i>Observing Nebulosities: The Cygnus Superbubble</i> , Chris Christopherson, Nadia Kaltcheva .....	7
<i>Can Dark Matter Halos Change Shape? Examining the Adams Instability in Triaxial Systems</i> , Evan Dowling, Eric Barnes .....	12
<i>The Circulation of Ionized Gas in the Milky Way Galaxy</i> , Andrew Eagon .....	17
<i>Young Stellar Population of the Cygnus Star-forming Field</i> , Henri LeMieux, Nadia Kaltcheva .....	24
<i>Star Forming Rates and HI Gas Content in Galaxy Groups</i> , Sarah Martens .....	28
<i>Predicting Collisionless Equilibria in Dark Matter Simulations</i> , Robert J. Ragan .....	37

#### **Part Two: Physics and Engineering**

<i>Three Dimensional NURBS Modeling and Fabrication of Rotorcraft Design</i> , Geoffrey A. Ament .....	45
<i>Thunderstorm Electrification</i> , Stephanie Bradshaw .....	55
<i>Fire in Orbit: Equipping the Commercial Spaceflight Industry for Fighting Fire in Microgravity</i> , Trent Cybela .....	62
<i>Recent Progress in Lunar Helium-3 Extraction Research</i> , Aaron D.S. Olson .....	73

## Part Three: Biosciences and Geosciences

<i>Preliminary Assessment of Low-cost Unmanned Aerial Systems (UAS) for Creating Aerial Photographs for Natural Resource Research</i> , Eric Compas .....	81
<i>Riveting Hammer Vibration and Nerve Damage</i> , Jordan J. Zimmerman, Danny A. Riley, James L.W. Bain .....	91

## Part Four: Team Projects

<i>Monitoring Carbon Dioxide and Methane Levels above Retired Landfill and Forest Control Sites with a Tethered Aerostat to Determine Remediation Effectiveness</i> (WSGC Tethered Aerostat Program), Jesse Banick, Kathryn Lenz, Jonathan Sanders, Jeshanah Zolkowski .....	102
<i>Onset of Normal Field Instability in a Ferrofluid in Microgravity</i> , Amelia Gear, Tessa Rundle, Justin Barhite, Jordan Rice (COSG RockSat-C Program) .....	112
<i>Microwave Power Beaming using Ka-band Radar</i> (WSGC Tethered Aerostat Program), Travis Haugstad, Joel Nielsen .....	122
<i>Pioneer Rocketry 2015 WSGC Collegiate Rocket Competition</i> (Collegiate Rocket Launch), Jake Ellenberger, Adrian Guither, Trent Cybela .....	132
<i>Red Hawk Rocketry Boosted Dart</i> (Collegiate Rocket Launch), Akash Sen, Paul Ninneman, Katie VanderGalien, Jadee Kellogg, Robert Enright, Jimmy Izewski .....	140
<i>2015 WSGC Elijah High-Altitude Balloon Payload Project Final Report</i> , Ben Jensen, Nate Klassen, Woodrow Walker, Scott Frazier, Kai Swanson, Taylor Davitz .....	146
<i>Team Whoosh Generator 2015 WSGC Collegiate Rocket Competition</i> (Collegiate Rocket Launch), James Ihrcke, Eric Johnson, Leeta Russell, Stephan Skibinski, Braden Thiel .....	156
<i>2015 WSGC Elijah High-Altitude Balloon Launch Team Summer Report</i> , Jadee Kellogg, Daniel Ochoa, Jordan Petrie, Alana Tirimacco .....	166
<i>Badger Ballistics WSGC Collegiate Rocket Team 2015</i> (Collegiate Rocket Launch), Adrien Bossogo-Egoume, Lucas Jewell, Audrey Packer, Michael Warren .....	173
<i>Exploring the Capabilities of Drones for Undergraduate Research</i> , Erlan Wheeler .....	181

## Part Five: Conference Program

<b>2015 Wisconsin Space Conference Program</b> .....	185
--	-----

25<sup>th</sup> Annual Wisconsin  
Space Conference

PART ONE

Astronomy and Cosmology

# A Search for New Variable and Proper Motion Stars in the Galactic Disk

Robert A Benjamin<sup>1</sup>  
University of Wisconsin-Whitewater  
Whitewater, WI

## Abstract

Mid-infrared observations of sections of the Galactic Plane with the *NASA Spitzer Space Telescope* at two widely spaced epochs (2004-5) and (2012-13) have opened up the possibility of a large-scale search for variable stars, proper motion stars, and transients. This has required developing a new research infrastructure to merge and compare the two epochs of observations, and has led to the discovery of a surprising number of variable sources (over 100,000) and high proper motion sources (over 400). We quantify the probability that a star observed in the mid-infrared will show variability at a certain amplitude. Stars with apparent magnitude fainter than 10<sup>th</sup> magnitude (in the [3.6] micron bandpass) have a 0.6% probability of varying by more than 0.25 magnitudes. This probability increases to 14% for stars brighter than 6<sup>th</sup> magnitude. We also describe upcoming observations of the center of the Milky Way Galaxy.

## The Time Variable Milky Way Galaxy

One of the new frontiers of astrophysics is time-domain astronomy. Many stars flicker and occasionally flare, gamma ray and X-ray sources burst both within and outside the Galaxy, and supernovae explosions are now regularly recorded in distant galaxies across the universe. Even ordinary stars can change their brightness when eclipsed by companion stars or planets. Due to convection and sunspots, at the micro-magnitude level all stars are variable. The value of studying such sources has been demonstrated by NASA missions as varied as *Kepler*, which has statistically assessed the probability of stars having planets, to the *Wide-field Infrared Sky Survey (WISE)*, an all-sky survey that has the potential to yield tens of thousands of new variable stars (Klein et al. 2011). Ground-based projects such as the LSST (Large Synoptic Survey Telescope), the top priority ground-based project in the 2010 astronomy decadal report, will survey the sky repeatedly. This mission will produce as much data every night as can be found in the entire Library of Congress, and will unveil the time-variable sky, with the only limitation being the significant dust-extinction in the Galactic plane.

Thanks to our work with the on-going GLIMPSE survey, a mid-infrared survey of the Galactic plane using NASA's *Spitzer Space Telescope*, we have amassed a database of over 239 million sources (Benjamin et al 2003; Churchwell et al 2009). The chief advantage of infrared wavelengths is that the effects of dust extinction are minimal on the observations. Stars that are completely invisible in the optical can often be very bright in the infrared. In the last few years,

---

<sup>1</sup> This work was supported by a 2014 Research Infrastructure Grant from the Wisconsin Space Grant Consortium. The author would like to acknowledge the invaluable help of *Dr. Juliana Constantinescu* (University of Wisconsin-Whitewater) for her help in creating class activities to allow her students to confirm our variable stars and proper motion candidates, *Brian Babler* (University of Wisconsin-Madison) for his work in providing the matched source lists and blinking images, and UW-Whitewater students *Brandon Behnke*, *Kwun Ming Chan*, and *Fenglin Xi* for their help in researching the proper motion stars and doing the optical follow-up work at WIYN 0.9m for variable star candidates.

we were fortunate enough to be able to re-survey parts of the Galactic disk first surveyed in 2004-2005. This resulted in over 150 square degrees overlap with over 27.7 million sources in common. A comparison between the catalogs for these two surveys led to the identification of over 140,000 variable star candidates. This was a completely new undertaking for us, and required the development of a new research infrastructure.

### **Finding and Confirming Variable Stars in the Galaxy**

The goal of the original GLIMPSE program (Benjamin et al. 2003) was three-fold: (1) a complete census of the (luminous) stellar content of the Galaxy, (2) mid-infrared coverage of the stellar, proto-stellar, and diffuse emission of a huge number of star forming regions in the Galactic plane, and (3) discovery of new classes of objects that had previously been hidden by the large columns of interstellar dust. On all three counts, this program was successful (Churchwell et al 2009). It confirmed the previously disregarded “Long Bar” of the Galaxy (Benjamin et al 2005), rekindled interest in spiral structure of the Galaxy (Benjamin 2008), allowed for estimates of the current star formation of the Galaxy based on young stellar objects (YSOs; Robitaille & Whitney 2010), and has yielded large catalogs of new classes of objects including infrared dark clouds (Peretto & Fuller 2009), stellar outflows from high mass protostars (Cyganowski et al 2008), and high mass YSOs and asymptotic giant branch (AGB) stars (Robitaille et al 2008). These catalogs provide uniform samples to study the large-scale star formation of the Milky Way in a statistical meaningful way.

*Deep GLIMPSE* re-surveyed the inner part of the Milky Way galaxy from March 2012 to March 2013, following the changing latitude of the warp on the far-side of the Galactic disk. The original GLIMPSE survey, which covered galactic longitudes  $|l| < 65^\circ$  and latitudes  $|b| < 1^\circ$  did not cover the warp extending up to  $|b| < 3^\circ$ . *Deep GLIMPSE* partially overlapped with this original survey; the overlap regions had 27.7 million sources in common.

More than 100,000 sources, 0.36% of the total, are variable at the 2-sigma level for all measured bands (with a minimum of two bands). Figure 1 shows the probability that a source of a given magnitude will show variability at a given amplitude. Determining what type of sources these are has become one of our principal projects. Only 56% had 2MASS K band (2.2 micron) measurements, and only 3% of these variables were matched to known objects within 10 arcseconds using the astronomical database SIMBAD. In the matched sample, our variable sources include 618 AGB stars, 182 sources in the vicinity of star-forming dark clouds, 128 YSOs, and 117 previously known variable stars. Over the summer of 2015, we selected a continuous  $1.5 \times 0.5$  region of the Galactic plane for nightly optical monitoring with the WIYN 0.9m telescope to confirm the variability and obtain further constraints on a subset of these variable stars. The analysis of these data are ongoing.

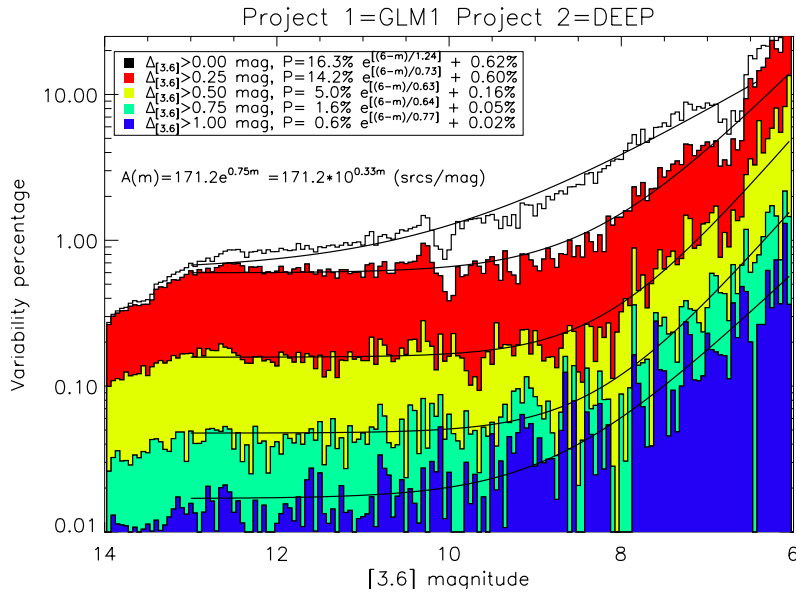


Figure 1. The probability of a star of a given observed [3.6] magnitude ( $m$ ) being variable as a function of observed magnitude for different variability amplitudes. For stars fainter than  $m=10$ , the variability probability asymptotes to a fixed value that ranges from 0.02% (for variability amplitudes greater than 1.0 mag) to 0.6% (for variability amplitudes greater than 0.25 mag). For sources brighter than  $m=10$ , the probability of a source being variable increases by a factor of 30 by the time one reaches  $m=6$ . Presumably a large fraction of these brighter sources are asymptotic red giant branch stars.

## A Surprising Number of Proper Motion Stars

While confirming our variable stars via visual inspection, we began to notice many proper motions source, i.e. sources that moved noticeably with respect to background stars over a decade's time. Such sources are generally assumed to be nearby, and given the fact that many of them are bright in the infrared but not seen in the optical wavelengths, they are probably low-mass stars or substellar "brown dwarfs" (or else very distant, high- or hyper-velocity stars). There are many reasons these objects are of potential scientific importance so we redirected our program to focus on these objects. Figure 2 shows the motion of one newly discovered source on the sky and how well our measurements of proper motions compare to previous works.

We found 395 high proper motion stars  $> 100$  milli-arcseconds/year down to a limiting infrared magnitude of  $m_{[3.6]} = 13$  of which nearly three-quarters are new discoveries. Spectral follow-up of three of these sources (so far) have uncovered three mid-to-late M dwarfs, one of which (GLIMPSE 1713-3952) is known to have X-ray flares and is likely to be only 20 pc from the Sun. Of our new detections, all but five could be associated with a source in the 2MASS catalog that confirmed the proper motion at a third epoch in time. All of these objects are in areas of the sky that had been optically surveyed for proper motion in the past without detecting these sources, indicating that mid-infrared observations are sensitive to sources that escape detection in other wavelengths.

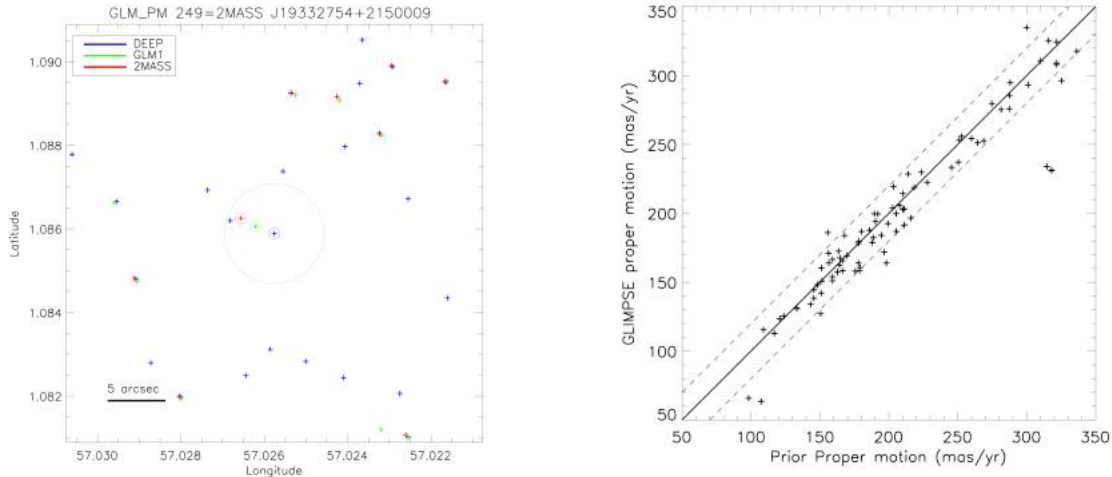


Figure 2 [Left]. The proper motion of GLIMPSE 1933+2150, a new late M/early L companion to the G2V star HD 184385 located 25 pc from the Sun. [Right] A comparison of GLIMPSE proper motions to published proper motions for recovered sources. The diagonal band shows that most sources agree to within 20 mas/year.

## One Final GLIMPSE

The discovery of so many high proper motion objects made us aware of the scientific value of obtaining a second epoch of observations to the Galactic center direction with the Spitzer Space Telescope. Thanks to the research program described in this work we were able to successfully propose for 97 additional hours on Spitzer to re-image the most extinguished, most crowded section of the Milky Way (Figure 3, 4), where no other telescopes have done systematic proper motion studies. This project has several scientific goals:

(1) *Measure the stellar velocity dispersion both parallel and perpendicular to the Galactic plane as a function of (1) direction and (2) depth.* By defining samples of red clump giants or red giant branch stars of different magnitudes, we will probe different depths through the Galactic bulge (Nidever et al 2012).

(2) *Search for streaming motions in the mean proper motion of sources as a function of Galactic latitude and longitude.* The central bar of the Milky Way is complex, consisting of central "triaxial bulge", an "X-shaped" vertical structure, and a thin in-plane "Long Bar" (confirmed with GLIMPSE data in Benjamin et al. 2005). The dynamical models that produce these structures predict different proper motions for front-side and back-side sections. These have been potentially observed (again, well off the plane) by Sumi et al (2013) and Poleski et al (2013).

(3) *Search for brown dwarfs in crowded fields.* Brown dwarfs, being nearby, have high proper motions and relatively isotropic distribution on the sky. Because of stellar crowding, the Galactic plane is the hardest place in the sky to look for such objects. As a result, there may still be interesting objects there that can not be detected with WISE because of the severe confusion WISE would face in the inner Galaxy. Our experience with detecting proper motion sources further out in the disk suggest we will find about 150 to 250 of these objects in the proposed survey. We have developed a collaboration with Dr. Davy Kirkpatrick to obtain spectroscopic follow-up of interesting sources.

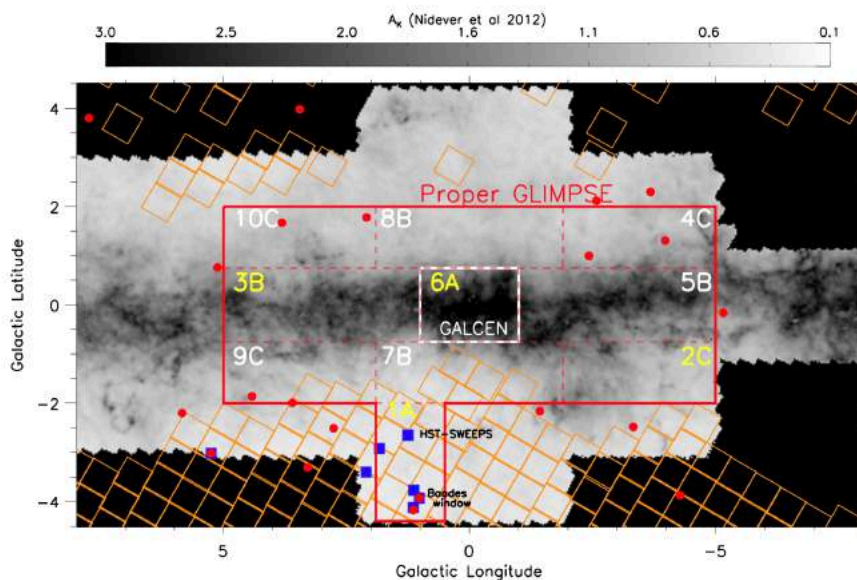


Figure 3. A view of our approved proper motion survey area superimposed on a two-dimensional dust extinction map generated using GLIMPSE data (Nidever et al 2012). Small optical windows observed in previous proper motion studies are shown with blue squares. Large-area coverage by the optical survey OGLE III (Udalsky et al 2008) is shown with orange tiles, and the location of globular clusters are noted with red circles. At mid-infrared wavelengths, the vast majority of this area has less than one magnitude of extinction. The central (GALCEN) region and Baade's window (Priority A) require 18.0 of observing time. The fields adjacent to GALCEN require 45 hours. The diagonal corners of our survey area will require 34.5 hours.

(4) *Search for future microlensing events.* One of the holy grails of brown dwarf science is obtaining empirical mass measurements against which to compare to theory. It has often been stated that such mass measurements are possible only in binary systems whose orbital parameters are well constrained. However, the discovery of brown dwarfs against the Galactic Plane makes it possible, in special cases, to measure the masses of single brown dwarfs. For brown dwarfs whose astrometric paths can be measured with milliarcsecond accuracy, candidate lensing events of background stars by the brown dwarf can be predicted in advance (e.g., Lepine & DiStefano 2012).

(5) *Search for hyper-velocity stars.* An ever-growing sample of "hyper-velocity" stars have been found in the Galactic halo (Brown et al 2012). These stars have speeds up to 800 km/s and are generally assumed to be ejected when a binary system near the supermassive black hole of the Milky Way is disrupted (Rossi et al 2014). There is some support for this idea given the presence of large number of young stars near Galactic center (Fritz et al 2014). Since we will be carrying out a uniform and symmetric proper motion survey of the bulge which is practically unaffected by extinction, we expect to be able to put meaningful limits on these models. The most exciting possibility is that we will catch one of these stars close enough to the Galactic Center to place constraints on this ejection scenario.

Decades-long proper motion surveys are rarely planned in advance, but the longevity of the Spitzer Space Telescope, the IRAC camera, and the GLIMPSE pipeline allow for the possibility of making nearly identical observations and data products a decade later, a rarity in Galactic

astronomy. This was not an avenue we anticipated, but the WSGC Research Infrastructure program has allowed us to go down an interesting new road in Galactic astronomy.

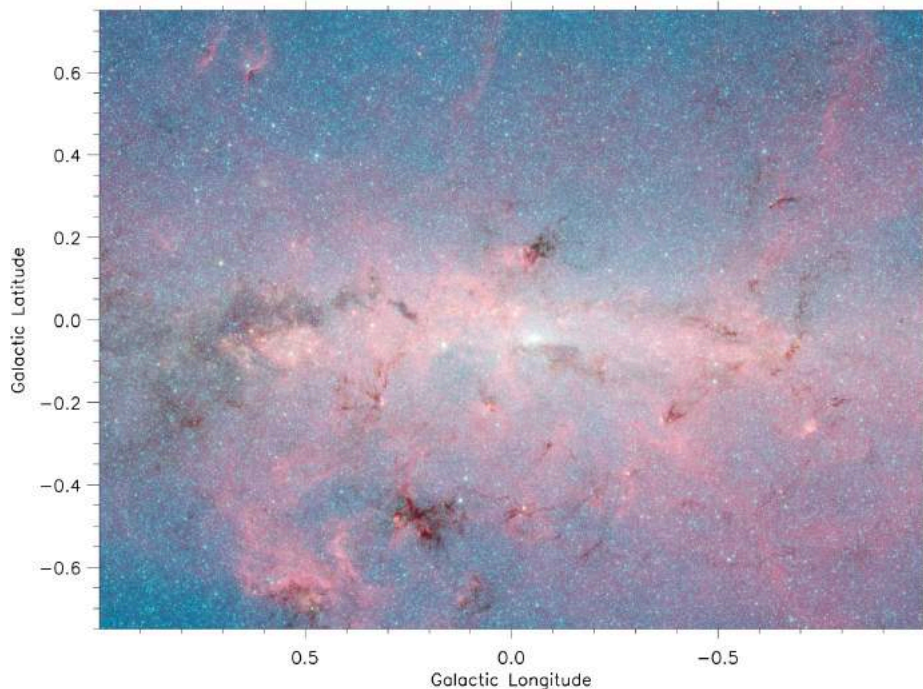


Figure 4. Mid-infrared image of the GALCEN area ( $|l| < 1^\circ$  and  $|b| < 0.^\circ 75$ ) (PI: S. Stolovy). This area will be observed with same procedure as in 2005: five-dither, two-second frame time observations. The observing plans we have provided are comparable to the original GALCEN observations. Since this area was never re-observed by *Spitzer*, we will also be providing new constraints on mid-infrared stellar variability in this region.

## References

- Benjamin, R.A. et al 2003, Publications of the Astronomical Society of the Pacific 115, 953.  
Benjamin, R.A. et al 2005, Astrophysical Journal Letters, 630, 149.  
Benjamin, R.A. 2008, in Astrophysical Society of the Pacific Conference Volume 387, 375.  
Brown, W.R. et al 2012, Astrophysical Journal Letters, 754, 2.  
Churchwell, E.B. et al 2009, Publications of the Astronomical Society of the Pacific, 121, 213.  
Cyganowski, C. J. et al 2008, Astronomical Journal, 136, 2391.  
Fritz, T.K. et al 2014, arXiv.org/1406.7568.  
Klein, C. R., Richards, J. W. Butler, N. R., Bloom, J. S. 2011, Astrophysical Journal 738, 185.  
Lepine, S. & Di Stefano, R. 2012, Astrophysical Journal, 749, 6.  
Nidever, D. et al 2012, Astrophysical Journal Supplement, 201, 35.  
Peretto, N. & Fuller, G.A. 2009, Astronomy & Astrophysics, 505, 405.  
Poleski, R. et al 2012, Astrophysical Journal, 776, 76.  
Robitaille, T.P. et al 2008, Astronomical Journal, 136, 2413.  
Robitaille, T.P. & Whitney, B.A. 2010, Astrophysical Journal Letters, 710, L11.  
Rossi, E.M. et al 2014, Astrophysical Journal, 795, 125.  
Sumi, T. et al 2013, Monthly Notices of the Royal Astronomical Society, 432, 124.

## Observing Nebulosities: The Cygnus Superbubble

Chris Christopherson<sup>1</sup>, Nadia Kaltcheva  
Department of Physics and Astronomy  
University of Wisconsin Oshkosh  
Oshkosh, WI 54901

### Abstract

The Galactic star-forming complexes are best delineated by the distribution of the ionized interstellar matter which is always associated with active star-formation. Observations of these regions at specific emission lines are helpful in determining the overall distribution of the interstellar gas and dust, and also tracing supernova shock fronts and regions of strong stellar winds. Amateur astrophotography equipment is often useful in obtaining homogeneous coverage of large-scale star-forming fields that in some cases does not yet exist as part of professional all-sky surveys. For this project we observe the Cygnus star-forming complex in the Hydrogen- $\alpha$ , Hydrogen- $\beta$  and Oxygen-III (500.7 nm) emission lines. We use a computer-guided modified Digital Single Lens Reflex (DSLR) camera combined with a wide-angle lens to image a  $22^\circ \times 17^\circ$  field, including in this way all prominent star-formation sites in Cygnus.

### Introduction

The Cygnus star-forming complex is one of the largest isolated features of interstellar gas and dust recognized in the Milky Way. In the sky, it is associated with the Northern Cross asterism, the bright supergiant star Deneb and the picturesque North America and Pelican emission nebulae (Fig. 1). Observations in the X-ray, radio and optical part of the spectrum reveal a giant ring of hot gas of about 400 pc in diameter, known as the Cygnus superbubble. Filled with regions of star formation, it is surrounded by a shell of gaseous filaments and obscuring dust clouds known as the Great Cygnus Rift. The structure and the energetics of this extended region of expanding interstellar matter are still not well understood. Since, within the Milky Way, Cygnus is located along the local Orion spur, star-forming structures at different distances are possibly located along the line of sight. Indeed, recent X-ray emission findings (Uyaniker et al. 2001) suggest that the dominant nebulosity in the Cygnus field, Sh 2-109 (Sharpless, 1959), consists of overlapping, not physically related, features.

According to current theories, stars form in clouds of interstellar gas and dust. Only a small fraction of the newly born stars are significantly greater in mass than the Sun, but they emit vast amounts of high-energy radiation into the surrounding space. Their radiation pressure, in turn, triggers the formation of more stars. Studying the interplay between stars and interstellar matter allow us to reveal key aspects of the star-formation process.

---

<sup>1</sup>Research done with the support of the Wisconsin Space Grant Consortium, NASA Space Grant College and Fellowship Program, NASA Training Grant #NNX14AP22H

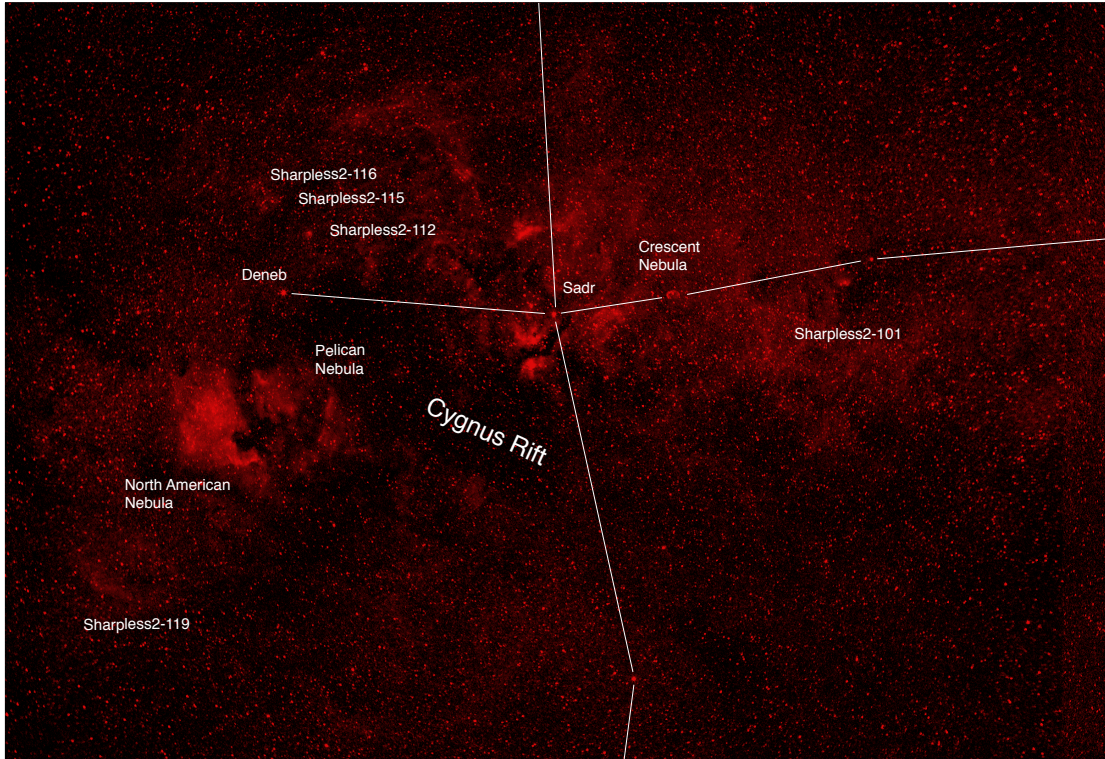


Figure 1. Unprocessed image of the Cygnus region in Hydrogen- $\alpha$ . Some of the more notable objects in the region are labeled and the constellation Cygnus is outlined.

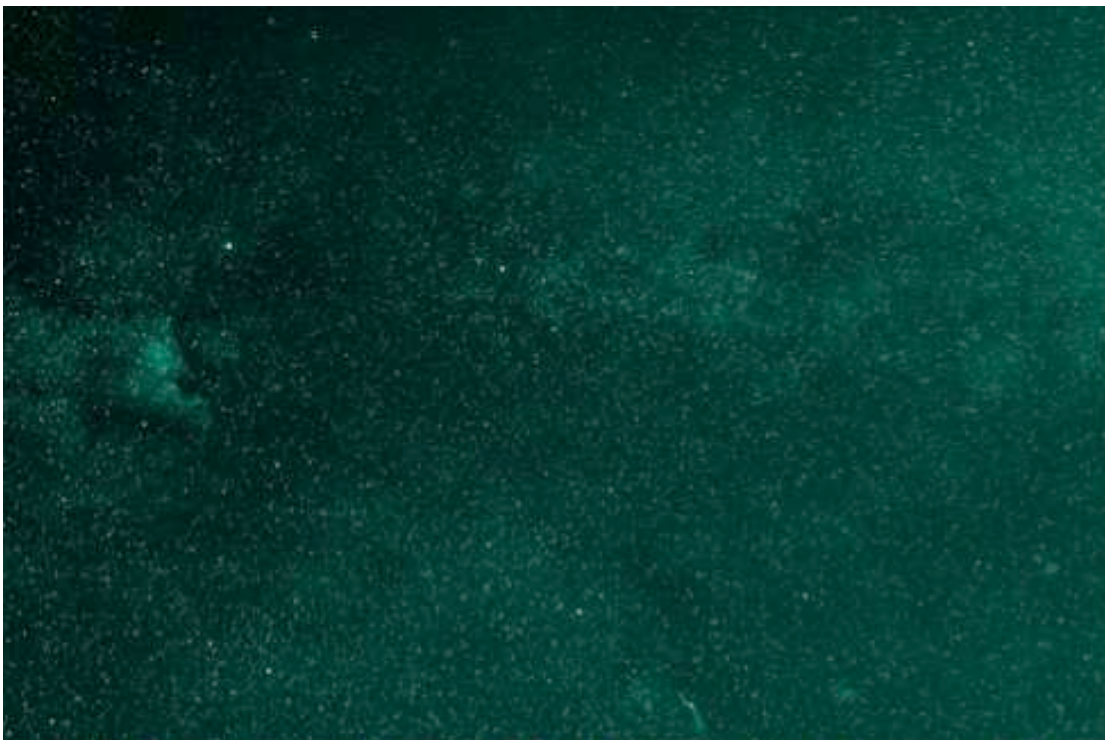


Figure 2. Oxygen III image of the Cygnus Superbubble. A part of the well-known supernova remnant, the Veil nebula, is shown at the bottom of this image.

The conditions of the interstellar matter found in active star-formation sites can be analyzed based on the intensity of specific emission lines. For example, photometry in the Balmer emission lines, similar to the work done for some galactic and extragalactic nebulosities by Caplan and Deharveng (1985) and Cox, Deharveng and Caplan (1987), can be used to study the dust associated with the star-forming regions. Similarly, the morphology of a star-forming field at Hydrogen- $\alpha$  ( $H\alpha$  hereafter) and doubly ionized oxygen [O III] helps to better understand the physical condition and evolutionary stage of the nebulae around very energetic stars (see for example Gruendl et al., 2000).

## Results

We utilize wide-field astrophotography equipment to image the Cygnus superbubble in  $H\alpha$  (656 nm), [OIII] (500.7 nm) and  $H\beta$  (486 nm) emission lines using 12-nm FWHM (Full Width at Half Maximum) filters. The equipment used was a computer-controlled guided telescope mount in combination with a modified DSLR camera and 50 mm F1.4 camera lens (Fig. 3). This allowed for most of the Cygnus star-forming field to be captured. DSLR's are designed to only capture visible light even though the sensors are sensitive into ultraviolet and infrared wavelengths. The cameras are built with an internal ultraviolet and infrared (UV/IR) cut filter to accomplish this. To allow for the capturing of images outside of the visual band, the UV/IR cut filter was removed and replaced with a filter from Baader Planetarium, which allows 400 nm to 700 nm light through. The Baader filter allowed for 99% of  $H\alpha$  light to pass through versus 25% with the original filter. The observations were performed during summer and fall of 2014 from various sites in Wisconsin. Nearly 40 images and 100 calibration frames were obtained to produce the combined science images.

Fig. 4 shows the ratio of  $H\alpha$  to  $H\beta$  emission, which traces the overall distribution of the interstellar dust. Both  $H\alpha$  and  $H\beta$  are recombination lines providing the overall distribution of



Figure 3. Research telescope. The guide-scope and camera on the left ensure accurate tracking while imaging. On the right is the modified DSLR camera used to collect the data.

ionized material. The interstellar extinction selectively changes the intensities of the observed spectral lines and can be calculated comparing the observed Balmer decrement to the theoretical one. Fig. 4 is constructed in a way that regions of high extinction appear dark. One can trace the high-extinction filaments across the field. This comparison between the  $H\alpha$  and  $H\beta$  emission indicates that the largest extinction in the field is found in the North America Nebula and around the young cluster NGC 6910.

The [OIII] line at 500.7 nm is driven by collisional excitation and its intensity increases with the temperature of the interstellar gas. An [OIII] image of the Cygnus field is shown in Fig. 2, where part of a well-known supernova remnant, the Veil Nebula, is seen at the bottom. A comparison between the  $H\alpha$  and [OIII]

emission would trace regions where the physical conditions change rapidly due to supernova shock fronts and strong stellar radiation. The preliminary processing of these images suggests no measurable offset between the  $H\alpha$  and  $[OIII]$  emission peaks, which probably implies shock fronts propagating into dense medium. The most intense  $[OIII]$  emission we detected was in the North America Nebula, which possibly indicates a presence of low-density high-temperature gas surrounded by a denser, cooler gas.

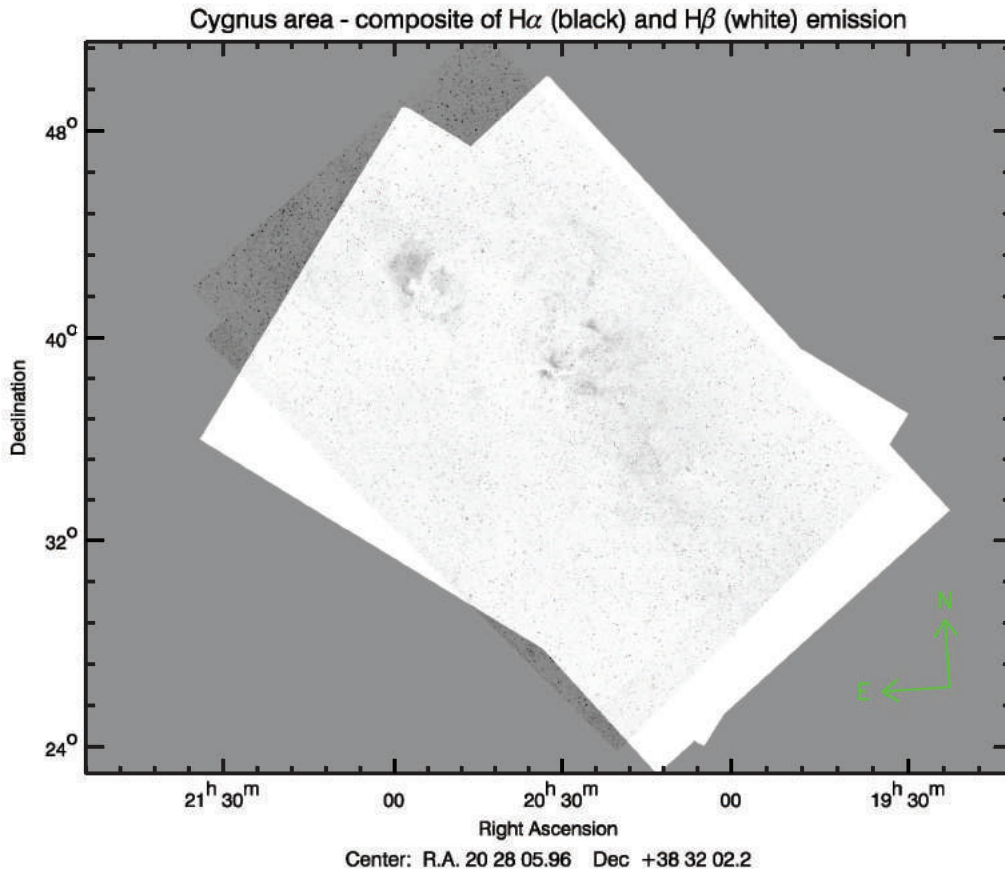


Figure 4. Ratio of the intensity of the  $H\alpha$  emission to the  $H\beta$  emission. Darker regions are where more extinction is present.

### Future work

Depending on ambient conditions, a cool-down time of between five and ten minutes is needed to keep the image sensor at a consistent temperature and simplify noise removal. Work is currently being done to improve the image quality and increase the speed with which they can be taken. A thermoelectric cooler is being designed and built to keep the image sensor at a consistent temperature and reduce the cool-down time between images. With the improved equipment, the data collection will continue including more star-forming fields.

Acknowledgements: We are thankful to Dr. V. Golev for his help with data reduction that was instrumental for this project. UW Oshkosh small student-faculty collaborative grant is also acknowledged.

## References

- Caplan, J., Deharveng, L., 1985. "Absolute H-alpha and H-beta photometry of LMC HII regions." *Astronomy & Astrophysics Supplement Series*, 62, 63.  
<http://adsabs.harvard.edu/abs/1985A&AS...62...63C>
- Cox, P., Deharveng, L., Caplan, J. 1987. "Extinction and reddening towards compact Galactic HII regions." *Astronomy & Astrophysics*, 171, 277.  
<http://adsabs.harvard.edu/abs/1987A&A...171..277C>
- Gruendl, R. A., Chu, Y. H., Dunne, B. C., & Points, S. D. 2000. "A morphological diagnostic for dynamical evolution of Wolf-Rayet bubbles." *The Astronomical Journal*, 120(5), 2670.  
<http://dx.doi.org/10.1086/316830>
- Sharpless, S. 1959. "A Catalogue of H II Regions." *Astrophysical Journal Supplement*, 4, 257.  
<http://dx.doi.org/10.1086/190049>
- Uyaniker, B., Fürst, E., Reich, W., Aschenbach, B., Wielebinski, R., 2001, "The Cygnus superbubble revisited." *Astronomy & Astrophysics*, 371, 675.  
<http://dx.doi.org/10.1051/0004-6361:20010387>

# Can Dark Matter Halos Change Shape? Examining the Adams Instability in Triaxial Systems

Evan Dowling, Dr. Eric Barnes

Department of Physics  
University of Wisconsin-La Crosse

**Abstract:** A recently discovered instability causes non-spherical orbits within dark matter halos to exponentially diverge into more spherical orbits. The instability was studied in limited regimes within the Adams et al. (2007) work. This project has replicated and extended the ideas to a static potential system that is accurate to all distances away from the potential's center as well as found an easy visualization for the arising instability. A better understanding of dark matter's behavior will help explain dark matter's halo structure and mass distribution that surrounds galaxies.

## Introduction

Over the last forty years, substantial evidence has been found that suggests the majority of the mass within the universe is not stored within planets, stars, and intergalactic dust, but rather is hidden in the form of mysterious dark matter. This material is appropriately named, due to its peculiar property of not interacting with light. In fact, in the simplest current picture of dark matter behavior, gravity is the only force dark matter feels. Galaxies, like the one we inhabit, are hypothesized to be enveloped in dark matter halos whose mass can outnumber the residing stars 10 to 100 times (e.g., Salpeter 1978; Rubin 1979; Sancisi & Allen 1979). So, why did astrophysicists and astronomers come to the conclusion that there needs to be so much “dark” mass?

It turns out the answer doesn't lie in just one area, but several. Once astronomers looked up to the night sky and painstakingly measured the velocities of the constituent stars within observable galaxies, they noticed speeds larger than expected. The amount of visible mass could not account for the gravitational force needed to keep the galaxies bound together (e.g., Rubin & Ford 1970). Similarly, large amounts of mass beyond that accounted for by visible matter is needed to account for a phenomenon called gravitational lensing. Due to mass's ability to curve space-time, light follows curved paths near massive objects. This “bending” is analogous to the impact of an optical lens on a beam of light. To match astronomers' lensing observations, more matter than can be directly seen is needed (Schechter & Wambsganss 2004; Ferreras et al. 2005). Finally, analyses of recent observations of the cosmic background radiation coincide with predictions made if the total mass in the universe far exceeds the mass attributed to protons, neutrons, and electrons (Spergel et al. 2007).

In an effort to better understand a substance that seems to prefer being hidden, astrophysicists have relied on computer simulations. Tracking orbits of particles that represent dark matter through collisionless systems is intended to cut through the fog and discover the true behavior of dark matter and the galaxies it underlies. Extensive research has been done laying the foundation for computational methods to analyze orbital systems (e.g. deZeeuw & Merritt 1983; Statler 1987; Holley-Bockelmann et al. 2001, 2002; Poon & Merritt 2002; Terzic & Sprague 2007).

Even the earliest studies of orbits found hints of instabilities (Henon 1973). One of the most widely studied of these instabilities has become known as the radial orbit instability (Merritt & Aguilar 1985; Barnes et al. 1986; Palmer & Papaloizou et al. 1987). A short summary of this type of instability starts with a spherical system, hosting particles on radial orbits (ones that would pass through the center of the sphere). The instability grows as neighboring orbits tend to become aligned along a direction that has slightly more particles than others. In the end, a spherical system can be transformed into an ellipsoidal system.

The instability we are interested in studying is essentially the inverse of the radial orbit instability. Instead of facilitating the change from spherical to ellipsoidal, the Adams instability acts to remove orbits that support non-spherical shapes. This instability was first identified using static (unchanging) gravitational fields produced by simple, analytically-describable mass density distributions. We use the term “simple” in the sense that the mathematical descriptions were abridged from an assumption of nearness to the potential’s center. Particles that are perturbed slightly from certain orbits exponentially diverge from paths taken by non-perturbed particles. With orbits undergoing the instability being deflected in random directions, one would expect the host system to become more spherical or, at least, have a limited range of non-sphericity.

During the award period, we explored and expanded on the results on orbital instabilities expressed in Adams et al. (2007). The first step in this research project was to duplicate the results by converting relevant mathematical representations into computer code and comparing simulations given appropriate initial conditions. After this initial step was completed, we wanted to extend the accuracy of the instability to the entire range of the potential. Since the analytic forces depended on the assumption of nearness to the center it caused the equations to become increasingly inaccurate as the position grew away from the center. In our work we investigated different methods in order to accurately account for the forces and potential at all distances away from the center.

## **Simulation and Results**

This work was completed within the University of Wisconsin-La Crosse physics computer lab and was entirely based on computational methods and analyses. Our computational investigation can be broken into two main parts.

Part one involved using computer simulations to replicate the work that first identified the orbital instability in non-spherical systems. This was done by transcribing the mathematical expressions for gravitational forces and potential into computer code; in our investigation the programming language was chosen to be FORTRAN. In order to best conserve energy for orbital integration an adaptive-timestep, fifth-order Runge-Kutta scheme was used. This numerical method allowed us to conserve orbit energy to a specified tolerance ( $\Delta E/E < 10^{-5}$ ). With this complete we built analysis code in a second language, IDL, to read the output and display the data in graphs of position vs. time or surface of sections. Surface of section graphs are plots of position vs. velocity with various sets of orbits that share a common energy. This is done by adjusting a particles initial velocity (kinetic energy) in relation to its distance from the

potentials center (potential energy) to guarantee that all particles start with identical total energies. To signal the onset of instabilities, the graphs show how unstable orbits lead to exponentially increasing position vs. time curves (Figs. 2 & 5) and appear as swarms of unconnected points (Fig. 6) within surface of section plots.

Replication of the results from Adams et al. 2007 and confirmation of the instability shortly followed.

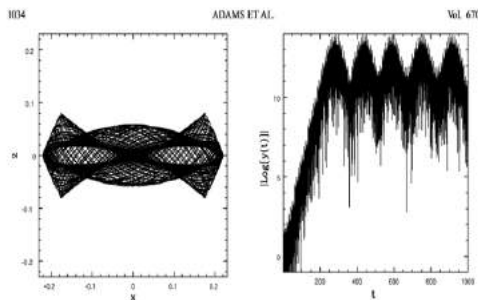


Figure 1. Graphs from Adams et al. Left: Orbit in principal x, z plane. Right: Development of instability with initial  $y = 10^{-8}$  (scaled distance).

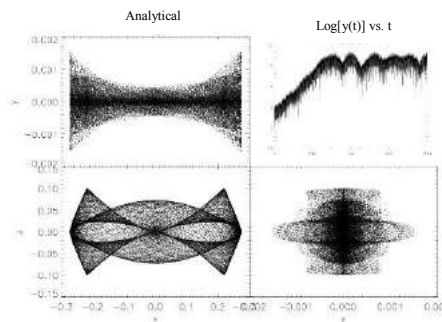


Figure 2. Orbit with nearly identical initial conditions as Fig 1. Panels show orbit shape in various axis planes. Top right: log plot showing exponential growth.

Looking at the left portion of Fig. 1 from Adams et al. and the bottom left graph of Fig. 2 the overall orbital shape within the x, z plane is nearly identical. More importantly the logarithmic plots in both graphs show exponential growth in the y-position values meaning an instability, caused from the initial state, was present.

In order to better understand the instability, we sought for an easy visualization that might give grounds for its existence. When considering the limiting case of a particle traveling along one axis towards the center, we noticed that there was a discontinuous force behavior as it crosses the origin, like what is shown in Fig. 3. Once a particle crosses the origin it experiences a rapid, instantaneous force change. This “jerk” appears to assist in the instability of non-spherical orbits.

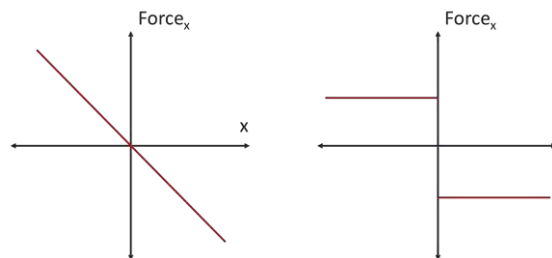


Figure 3. Left: x-force behavior with non-zero y and z position. Right: x-force behavior with y and z approximately zero with respect to x.

Part two involved looking at a new system that allowed us to study the full potential accurately. This meant creating a new method to determine the forces and potential in contrast to the analytical descriptions used in part one. We went with numerically integrating the true expressions for potential and forces on a 3D grid. During an orbit, spline interpolation, another numerical method, was used to determine force values between grid points based on the perceived behavior of the grid. Using the same orbital integration Runge-Kutta method allowed for an acceptable energy conservation ( $\Delta E/E < 10^{-4}$ ). Energy conservation was calculated by

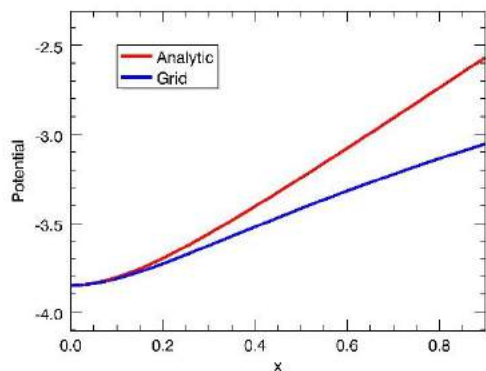


Figure 4. Differences between the analytical- and grid-based potentials.

determining the spread in the energy values and dividing by the average energy magnitude. A low  $\Delta E/E$  number signifies nearly constant energy values and energy conservation. The new grid-based description of the potential eliminated the error in values of force and potential since it doesn't rely on the approximation of nearness to the center. This is important since the grid-based potential deviates significantly from the analytical potential (correct only near the center) for larger radial distances, seen in figure 4.

Further examination of this new grid-based potential has produced unstable orbits similar to those in Fig. 2 (Fig. 5) as well as evidence of the instability within a broader study of orbits seen in the inner fuzzy regions of the surfaces of section plot (Fig. 6).

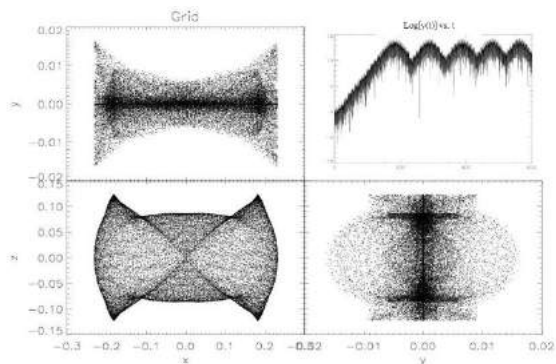


Figure 5. Top right: log plot showing exponential growth. Other plots show orbit shape in various axis planes.

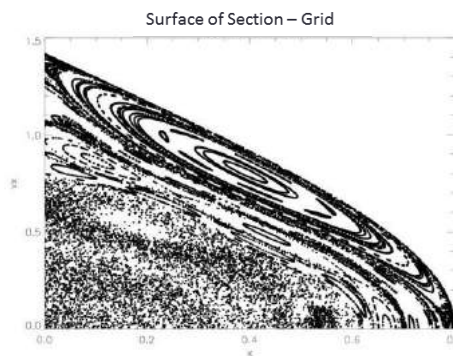


Figure 6. Surfaces of section of orbits with small initial y-position values.

For the sets of orbits within Fig. 6 the instability exists for x-position values as high as 0.6. The value 0.6 is a normalized distance of galactic dimension used to make the position variables dimensionless. When looking at Fig. 4 this instability exists even when the grid-based potential vastly differs from the analytical potential used in part one.

## Conclusion

Through our investigation on the Adams instability we have verified past investigations as well as examined the instability in new ways. From reworking the initial investigation on the Adams instability, we developed the necessary analysis techniques to tackle new approaches on where the old investigation may be lacking. Also, by validating the instability with the analytical expressions we gained insight into an easy visualization on the source of the instability. From reforming the potential and forces into a 3D grid based on their true values we have overcome the inaccuracies that effected the initial investigation. This new approach also confirmed that instabilities exists throughout the entire potential and not just the inner regions where the previously studied analytical approximations were valid.

## Future Work

Our eventual goal is to search for evidence of the instability in  $N$ -body simulations, where there is no analytic description of the gravitational potential. With either positive or negative evidence, this investigation should merit publication in a peer-reviewed journal. These simulations involve many ( $N$ ) point particles evolving through time under their mutual gravitational attractions. Such a system has a “bumpy” potential due to discreteness effects – particles are not smoothly distributed about every location in space. Adjusting for cosmological conditions, such as an expanding universe, we have begun creating simulations that will provide a very different testbed for comparison to the static potentials.

## References

- Adams, F., Bloch, A., Butler, S., 2007, ApJ, 670, 1027-1042.
- Barnes, J., Hut, P., & Goodman, J. 1986, ApJ, 300, 112.
- de Zeeuw, T., & Merritt, D. 1983, ApJ, 267, 571.
- Ferreras, I., Saha, P., Williams, L. L. R. 2005, ApJ. Lett., 623, 5-8.
- Henon, M. 1973, A&A, 24, 229
- Holley-Bockelmann, K., Mihos, J. C., Sigurdsson, S., & Hernquist, L. 2001, ApJ, 549, 862.
- Merritt, D., & Aguilar, L. A. 1985, MNRAS, 217, 787.
- Palmer, P. L., & Papaloizou, J. C. P. 1987, MNRAS, 224, 1043.
- Poon, M. Y., & Merritt, D. 2001, ApJ, 549, 192 (PM01). 2002, ApJ, 568, L89.
- Rubin V. C., Kent Ford W., 1970, ApJ, 159, 379
- Rubin, V. C. 1979, Comments Astrophys., 8, 79-88.
- Salpeter, E. E. 1978, in IAU Symp. 77, Structure and Properties of Nearby Galaxies, ed. E. M. Berkhuijsen & R. Wielebinski (Dordrecht:Reidel), 23-26.
- Sancisi, R., Allen, R. J. 1979, Astron. & Astrophys., 74, 73-84.
- Schechter, P. L., Wambsganss, J. 2004, in IAU Symp. 220, Dark Matter in Galaxies, ed. S. D. Ryder, D. J. Pisano, M. A. Walker, and K. C. Freeman, 103.
- Spiegel, D. N., Bean, R., Dore, O., Nolta, M.R., Bennett, C.L., Dunkley, J., Hinshaw, G., Jarosik, N., Komatsu, E., Page, L., Peiris, H.B., Verde, L., Halpern, M., Hill, R.S., Kogut, A., Limon, M., Meyer, S.S., Odegard, N., Tucker, G.S., Weiland, J.L., Wollack, E., Wright, E.L. 2007, ApJ. Supp., 170, 377-408.
- Statler, T. S. 1987, ApJ, 321, 113.
- Terzic, B., & Sprague, B. J. 2007, MNRAS, 377, 855.

# **The Circulation of Ionized Gas in the Milky Way Galaxy**

Andrew Eagon

University of Wisconsin-Whitewater

September 15, 2015

## **Abstract**

We use the Wisconsin H-alpha Mapper (WHAM) all sky survey to observe kinematic properties of ionized interstellar gas in the Galaxy. WHAM's survey is a velocity resolved map of the H-alpha emission from the Milky Way with a one-degree spatial resolution and 12.8 km s<sup>-1</sup> velocity resolution. Using this data the first and second moments are calculated and mapped to provide insight on the kinematic properties of the Galaxy. This research was funded by the Wisconsin Space Grant Consortium and supported by the NSF REU site grant to the University of Wisconsin-Madison

## Background

Gas makes up 99% of the Milky Way Galaxy and plays a major role in our understanding of the structure of the Galaxy. This gas is in constant motion around the center of the Milky Way. Understanding the velocity structure of the ionized regions of this gas in the Milky Way provides valuable insight about the Galaxy. Velocity structure provides input on the ionized gas' distance not only from the Sun, but from the center of the Milky Way. This insight opens up the study of galactic structure through the use of a longitude-velocity (L-V) diagram or through the use of a rotation curve map. An L-V diagram is used to identify spiral arms or other prominent features in the Galaxy however this is not the main focus of this study. Wisconsin H-alpha Mapper (WHAM) spectra's mean velocities can be compared to a galactic rotation map (figure 3) to place a distance to given objects or dense clouds of ionized gas. As mentioned earlier using data from WHAM it is possible to characterize the structure of the ionized regions.

The WHAM survey contains 49607 spectra each representing the spatially integrated emission of a one-degree patch in the sky. The data was taken in two sky surveys to complete the all-sky survey. Two-thirds of the sky was completed at Kitt Peak Observatory for the WHAM Northern Sky Survey, the mapper was then moved to Chile to complete the WHAM All-Sky Survey. One of the benefits to this data is it provides insight on velocity information of each WHAM pointing. This survey was used to create a variety of all-sky maps based on this velocity information.

In the past many ionized regions have been discovered most of which have no velocity information to go with them. The WHAM survey provides velocity information in an all-sky map. This means that a lot of the discovered regions will have velocities placed to them for the first time. I worked this summer to create a system to analyze the WHAM survey to characterize the velocity information of each pointing. A visualization of WHAM pointing size can be seen in a comparison of figure 1 to figure 2.

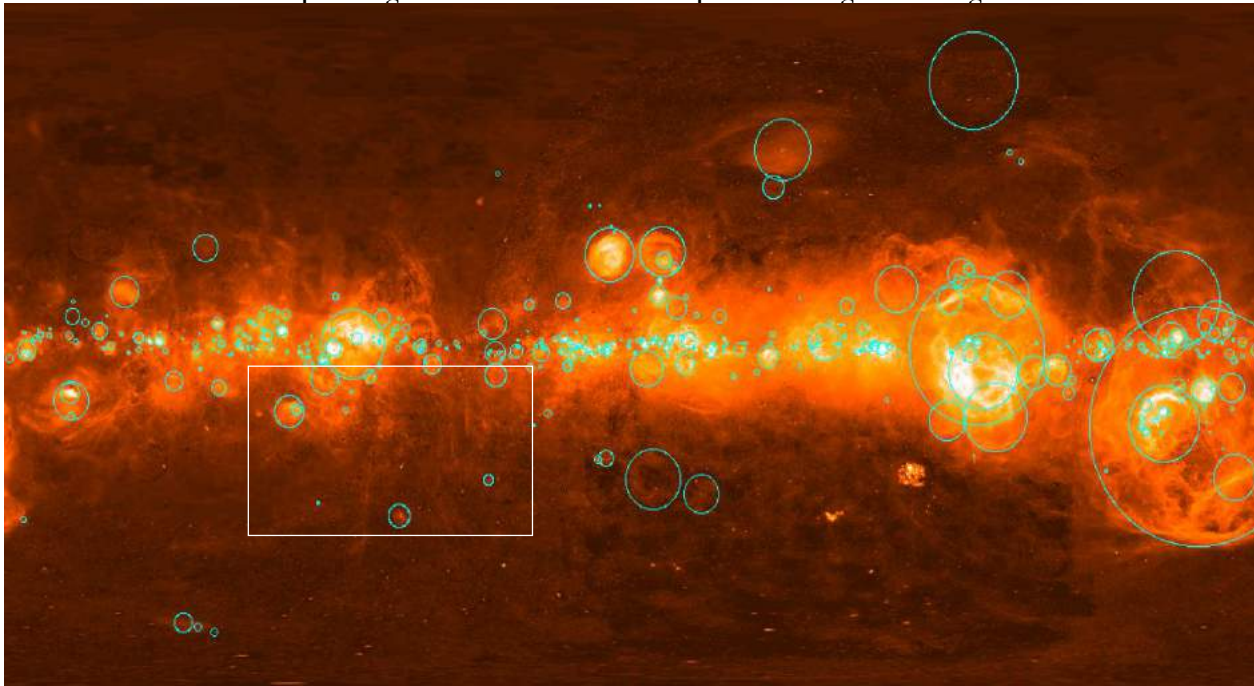


**Figure 1:** Finkbeiner all sky map of H-alpha emission showing newly discovered regions from the efforts of the REU program at University of Wisconsin-Madison, 2015. The white box can be seen below zoomed in.

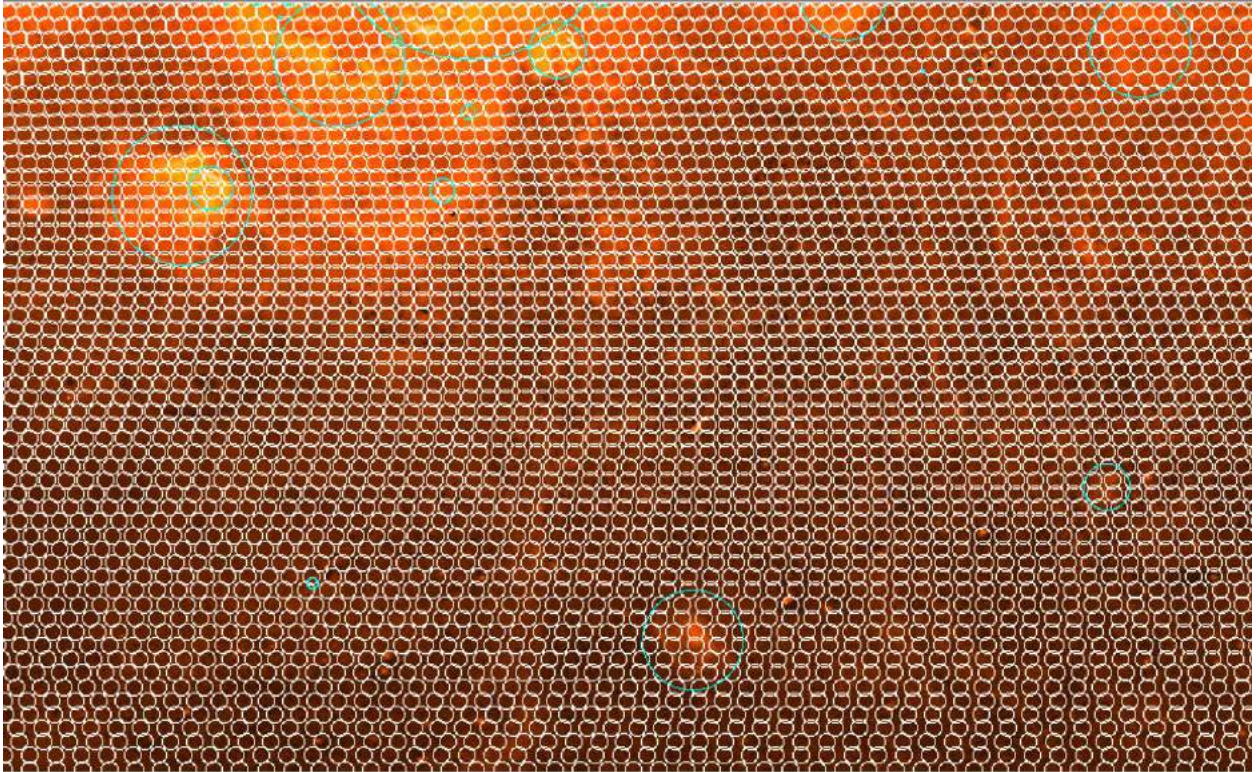


**Figure 2:** This image gives an example of the size of each WHAM pointing's size.

Each spectra's overall intensity, mean velocity, standard deviation, skew and kurtosis were calculated. These values characterize the spectra of the WHAM data making it easier to interpret. With these values new sky maps were created to help identify patterns in the data.

### Procedure

The extensive data collected by the WHAM was simplified and characterized by the use of moment calculations. The moment calculations take a probability, like a spectral power distribution, and put a value to characteristics like size (zeroth moment), position (first moment) and width (second moment). Other values like the skew and kurtosis were mentioned but are not the main focus of this study. An example WHAM spectra can be seen in Figure 3, their Gaussian like properties allow us to apply the moments to them.

The zeroth moments were calculated algebraically by "adding" up the total intensity (area under the spectra). The first and second moment calculation can be seen below. These calculations were also done algebraically using a computer program based on equation 1 and equation 2.

$$\bar{v} = \frac{\int vI(v)dv}{\int I(v)dv}$$

**Eqn. 1**

$$SD = \sqrt{\frac{\int (v-\bar{v})^2 I(v)dv}{\int I(v)dv}}$$

**Eqn. 2**

The first moment, in this situation, gives the intensity weighted velocity average of a spectrum which means we can place a velocity center to each spectrum. This is useful in placing a distance to the objects in the WHAM pointing corresponding to that spectrum. This is made possible by comparing the average velocity of the pointing to a galactic rotation map.

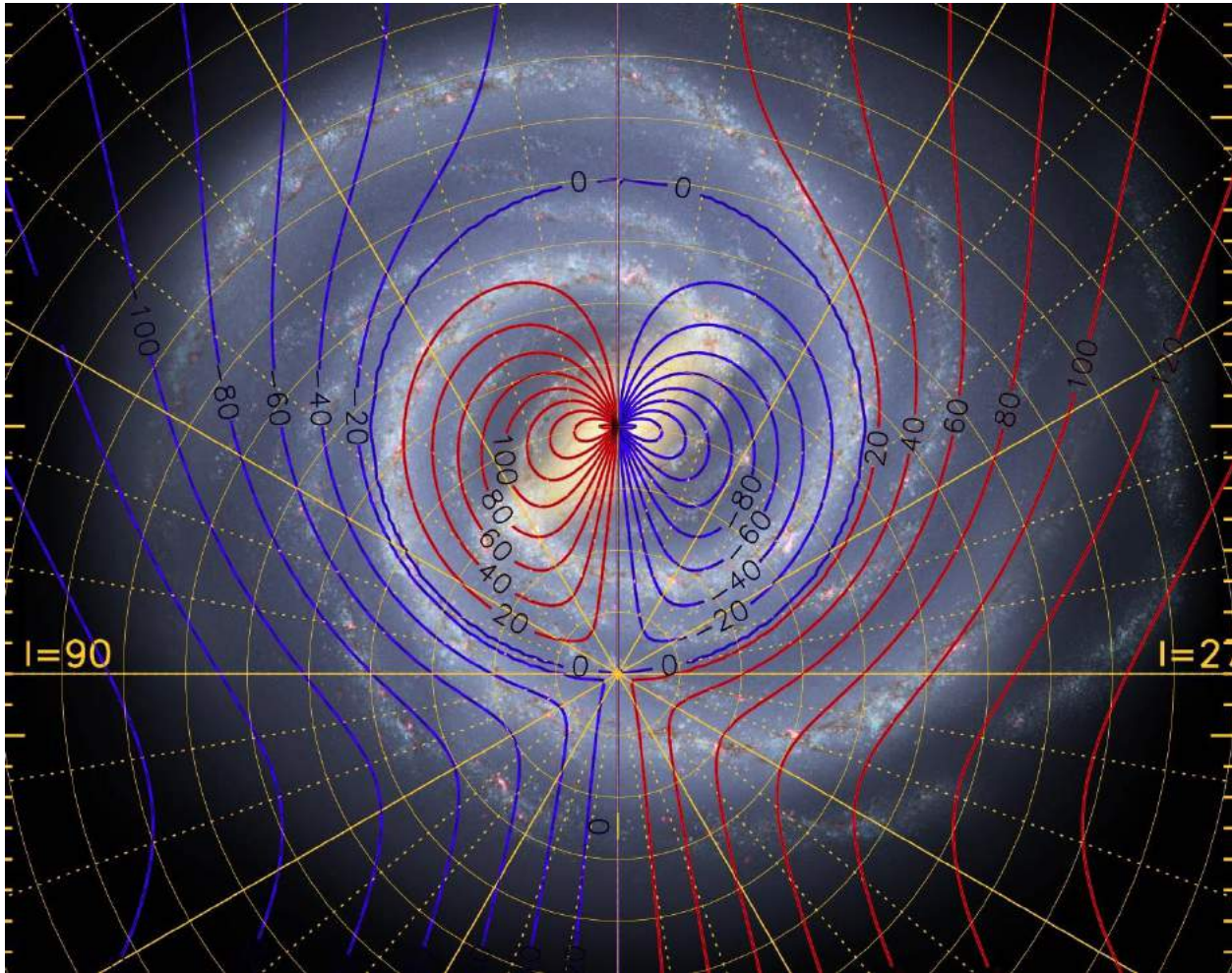


**Figure 3:** Hurt-McClure rotation map. This "artist's conception" image of the Milky Way Galaxy by Robert Hurt (Spitzer Science Center/IPAC/JPL) shows most of the claimed structures in the Galaxy, where the Sun, located at the center of the polar grid, is assumed to be  $R_0=8$  kpc from Galactic center. Superimposed is the line-of-sight velocity that would be measured from gas at a given position, assuming the rotation curve obtained by McClure-Griffiths and Dickey (2007, ApJ 671, 427). The Galaxy is divided into four quadrants. Galactic longitude  $l=0$  to  $90$  deg (where longitude runs counter-clockwise) is the 1st quadrant,  $l=90$ - $180$  deg is the 2nd quadrant, etc. (Description Courtesy of University of Wisconsin-Madison)

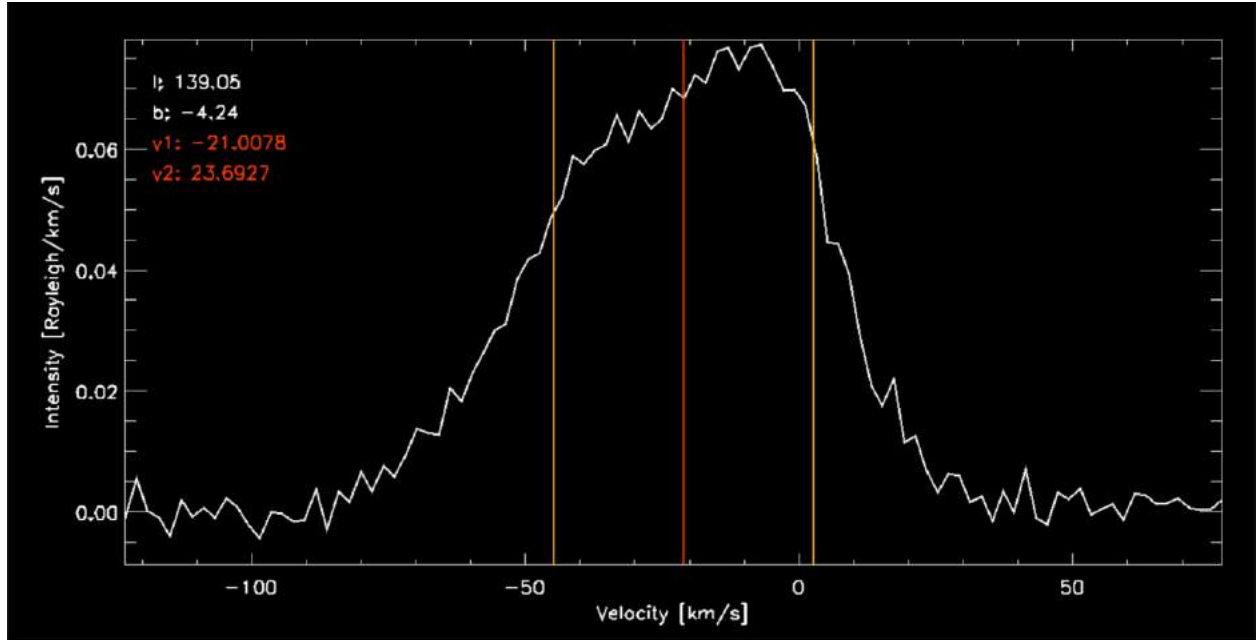


**Figure 4:** This shows an example WHAM spectra with velocity on the x-axis in km/s and intensity on the y-axis in Rayleigh per km/s with first ( $v_1$ ) and second ( $v_2$ ) moment calculations displayed on the plot. The second moment, in yellow, shows the standard deviation or variance from the mean velocity.

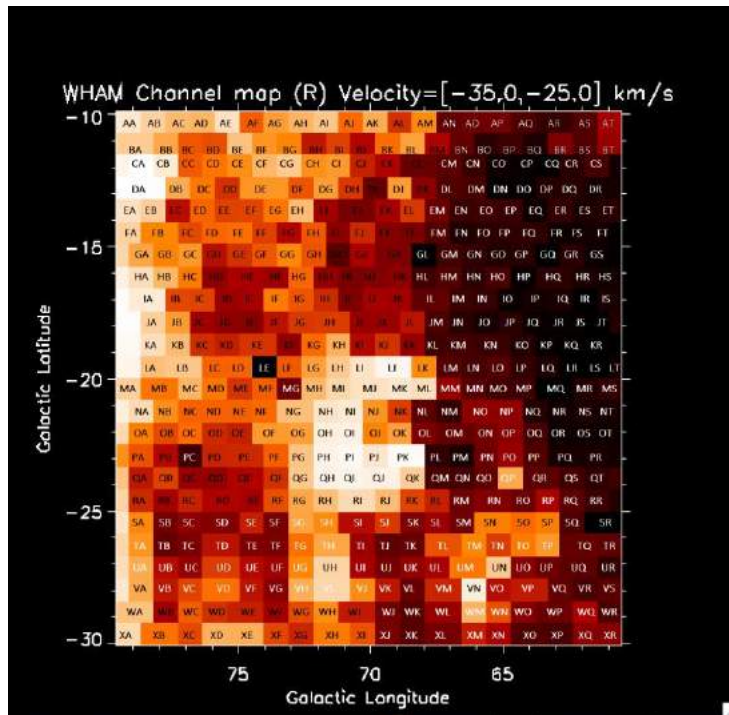


**Figure 5: Pixel per Spectra map.** Once the moments were calculated, each WHAM pointing was then converted to a pixel on a longitude vs. latitude all sky map that could then be observed to look for patterns in the survey. Above is an example of a section of the zeroth moment map. Each pixel is labeled and has a corresponding spectra.

## Results

The results of this project are two new all sky maps from the WHAM data which allow for a better understanding of the kinematic properties of structures in the Milky Way Galaxy.

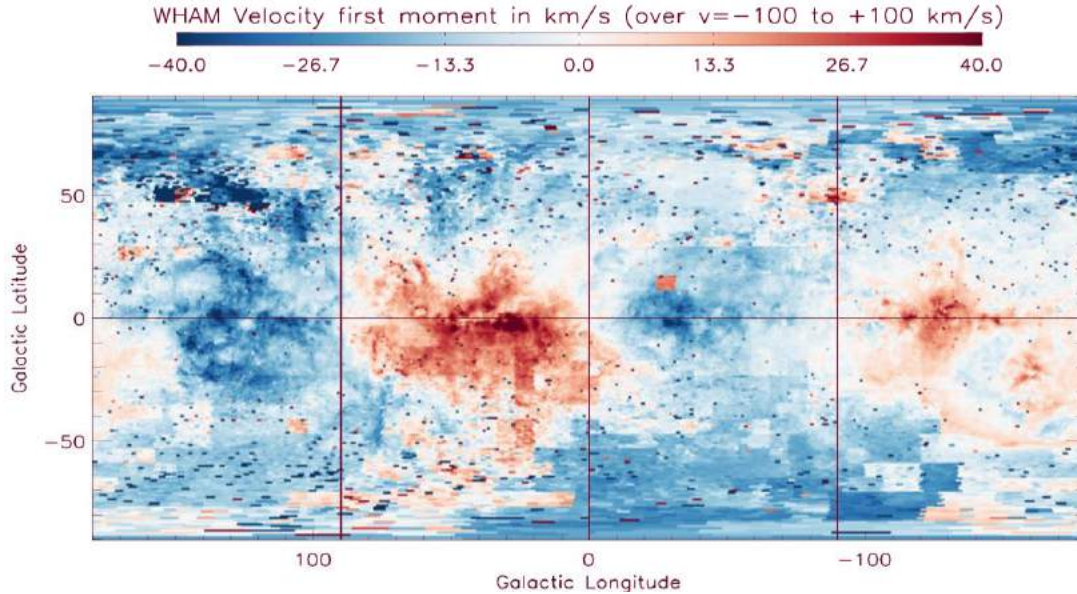


**Figure 6: (Above)** This map shows the all-sky survey with the calculated intensity weighted velocities for each pointing. The intensity weighted velocities of the ionized gas in the Milky Way shows alternating direction for each quadrant due to galactic rotation.

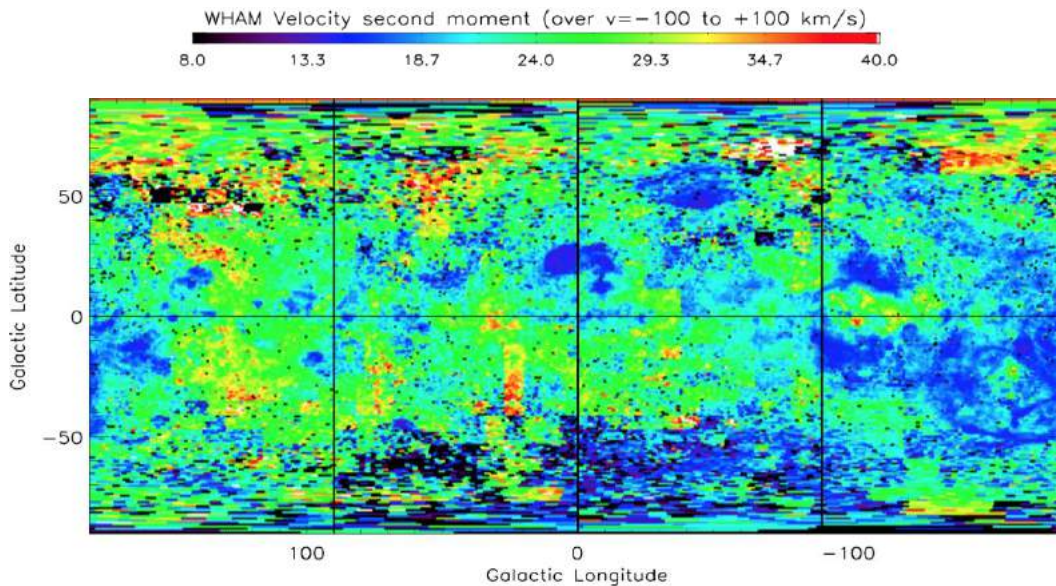


**Figure 7:** This map shows the all-sky survey with the calculated standard deviation of the intensity weighted velocity for each pointing. The standard deviation (or “width”) of the spectra is low in the direction of bright ionized nebulae due to the fact that gas at one single velocity dominates the spectrum. Areas of large second moment indicate either intrinsically wide lines or multiple components, widely separated in velocity. These latter regions have been targeted for future study.

## Conclusion

The first moment map highlights the effects of galactic rotation which we expect to see based on the Hurt-McClure rotation map in figure 3. Another interesting finding in the first moment is the lack of galactic rotation at higher latitudes. It can be seen that above the plane galactic rotation peters off at about  $25^\circ$  and below the plane galactic rotation peters out at about  $-38^\circ$  at which point the direction of the gas seems to be mostly blue shifted. This overall blue shift, at higher latitudes, tells us that the majority of ionized gas above and below the disk of the Galaxy is coming in towards the plane of the Galaxy.

The second moment map highlights properties of bubbles (regions of gas being ionized by a source such as an O star or by a supernovae remnant). It can be seen that, on the second moment map, familiar regions such as the Orion-Eridanus and the Spica H-II region have a low second moment. This is a characteristic that comes out due to intensity weighted calculations; bright regions with single peaks will tend to lower the width of a given spectra. However, towards the centers of some bubbles such as the gum nebula, a wider second moment is observed. This tendency for bubbles to have a wider second moment in their centers is due to the intensity weighting as well; widely separated (in velocity) equally bright peaks will produce a wider second moment. The equally bright peaks are indicative of the front and back side of the bubbles as they expand, this interesting characteristics of bubbles can be used to help find bubbles in the WHAM data in the future.

## Acknowledgements

To the Wisconsin Space Grant Consortium at Carthege College for providing the financial support to make my research possible. Also, to the team at University of Wisconsin-Madison for providing access to the preliminary reduction for the WHAM data, Matt Haffner and Brian Babler for their efforts calibrating the data and Alexander Orchard for help in providing the tools and insights used for this analysis.

## References

- L.M. Haffner, R.J. Reynolds, S.L. Tufte, G.J. Madsen, K.P. Jaehnig, & J.W. Percival D. 2003, The Wisconsin H-alpha Mapper Northern Sky Survey
- R.R. Linder, C. Vera-Ciro, C.E. Murray, S. Stanimirovic, B. Babler, C. Heiles, P. Hennebelle, W.M. Goss, & J. Dickey, D. Autonomous Gaussian Decomposition
- Lagache, G., Haffner, L.M., Reynolds, R.J., and Tufte, S.L. 2000, A&A, 354, 247
- Spitzer, L.J., & Fitzpatrick, E.L. 1993, ApJ, 409, 299

# Young Stellar Population of the Cygnus Star-Forming Field

Henri LeMieux, Nadia Kaltcheva

Department of Physics and Astronomy  
University of Wisconsin Oshkosh  
Oshkosh, WI 54901

## Abstract

We provide homogeneous estimates of the color excess and distance to several open clusters located toward the prominent nebulosity Sh 2-109 (Sharpless, 1959) in Cygnus. Based on the revised distances, we found these clusters to form two layers at 2700 and 5200 light-years (ly) from the Sun, suggesting star-forming regions overlapping along the line of sight in this direction.

## Introduction

The Cygnus star-forming region harbors many young open clusters and several OB associations containing numerous massive young stars. The field is dominated by the prominent nebulosity Sh 2-109, which might be a complex of several overlapping regions of ionized hydrogen (H II regions). Since the line of sight towards Cygnus is along the local Orion spiral arm, the identification of individual stellar and interstellar structures is problematic. The field is also quite obscured by interstellar dust and analyzing its morphology and stellar content is a difficult experiment (Straizys et al. 2014). This study is focused on the massive stellar content of Sh 2-109, primarily on its population of young open clusters, with the purpose of providing new insights on its structure.

## Methodology and Data

The approach that distinguishes this study from previous investigations is the choice of the photometric system to utilize. We use data in the intermediate-band  $uvby\beta$  photometric system (Strömgren 1966, Crawford & Mander 1966). The system consists of ultraviolet  $u$ , violet  $v$ , blue  $b$ , yellow  $y$  filters and two filters with a different width centered at the  $H\beta$  line in the hydrogen spectrum. The  $uvby\beta$  photometry allows the derivation of stellar physical parameters, such as true brightness and temperature, with high precision. These parameters are then used to calculate homogeneous distances (and age estimates in some cases) of the young stellar groups in the region. The photometric  $uvby\beta$ -distances have been tested via the *Hipparcos* astrometric data and extensive studies of star-forming fields (see for example Kaltcheva & Golev 2011) and have been shown to be reliable.

The data was extracted from the photometric  $uvby\beta$  catalog by Hauck and Mermilliod (1998). Our sample contains data on more than ten open clusters, as included in Table 1. The cluster name and its galactic coordinates (longitude  $l$  and latitude  $b$ , measured in degrees) are listed in the first three columns. The color excess  $E(b-y)$  and the distance modulus (DM), derived here, follow. The color excess  $E(b-y)$  is a measure of the extinction of stellar light due to the interstellar matter between us and the stars. The distance modulus is a parameter used to calculate stellar distance as  $d=10^{((DM+5)/5)}$  measured in parsecs.

## Results

Figure 1 presents an example of the procedure we follow to calculate  $E(b-y)$  and DM for each cluster. The plots reflect the data for the young open cluster NGC 6910. Since we have restricted our sample only to stars younger than B9 spectral type, we use the calibration by Crawford (1978) to find  $E(b-y)$  and correct all photometry for the interstellar extinction. Then we utilize the calibration of Balona & Shobbrook (1984) to find the absolute stellar magnitude and calculate the distance modulus. We apply this procedure to every star in a given cluster. Then we evaluate the  $E(b-y)$  vs. DM diagram along with a histogram of individual stellar distances to estimate an average  $E(b-y)$  and DM as listed in Table 1. In some cases, when the literature data on a cluster's metallicity is available, we can estimate the age of the cluster via theoretical isochrones and the DM we obtained. As an example, the PARSEC isochrones, overplotted on the  $V_0$  vs.  $(b-y)_0$  diagram for NGC 6910, are shown on the top-right panel of Fig. 1. The PARSEC isochrones are sets of stellar tracks and isochrones in several photometric systems computed with the PAdova and TRieste Stellar Evolution Code (Bressan et al. 2012). Here the  $V_0$  is the apparent stellar magnitude corrected for interstellar extinction and  $(b-y)_0$  is a color index which is corrected for extinction. A comparison of the location of the stars to the theoretical isochrones provides an age estimate of  $2 \times 10^6$  years for NGC 6910.

**Table 1.** Open clusters with available  $uvby\beta$  photometry in the Cygnus star-forming field.

Cluster	$l^\circ$	$b^\circ$	$E(b-y)$	DM
TR 37	099.295	03.735	0.35	9.46
NGC 6871	072.645	02.054	0.33	11.7
IC 4996	075.353	01.306	0.45	11.19
NGC 6913	076.916	00.605	0.65	9.73
NGC 6910	078.673	02.022	0.75	10.73
NGC 7063	083.06	-09.89	0.07	9.06
NGC 7039	087.879	-01.705	0.1	9.43
NGC 7062	089.967	-02.740	Doubtful cluster	
NGC 7092	092.403	-02.242	0.02	6.54
IC 5146	094.383	-05.495	0.36	9.73
NGC 7209	095.496	-07.339	0.16	9.94
NGC 7243	098.857	-05.524	0.17	9.36

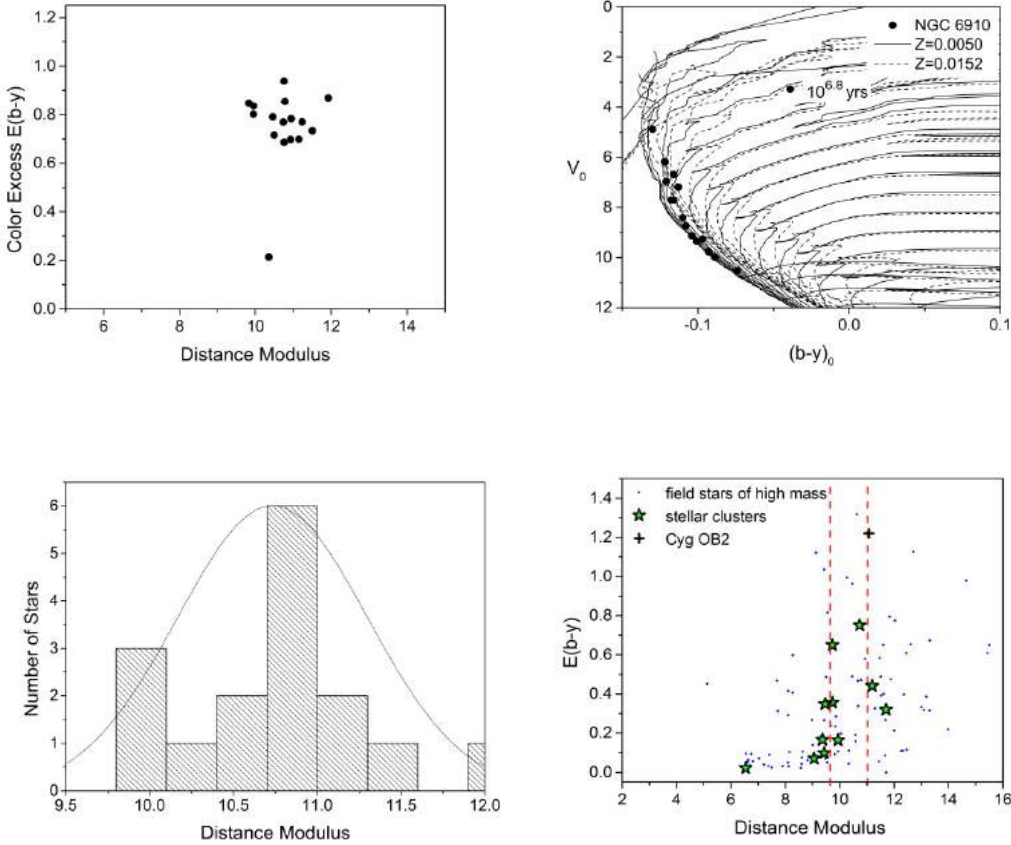


**Figure 1.** Left: The  $E(b-y)$  vs. DM plot and the histogram of stellar distances for NGC 6910. Right top:  $V_0$  vs.  $(b-y)_0$  diagram for NGC 6910 together with selected isochrones overplotted. Right bottom: the  $E(b-y)$  vs. DM plot for all clusters in Table 1.

## Conclusions

The homogeneous distances for the sample of young open clusters that we derived in this study yield new information on the overall structure of the Cygnus field. It appears that these clusters form two layers, at distance moduli of 9.6 and 11 mag (Fig. 1 right bottom). This corresponds to 830 pc (2700 ly) and 1580 pc (5200 ly), respectively. This may be an indication that two star-forming regions at different distances are overlapping in this direction. Our result supports recent X-ray emission findings (Uyaniker et al. 2001) suggesting that the dominant nebulosity Sh 2-109 consists of overlapping, and potentially not physically related, features. Thus, this analysis, based on revised cluster distances, supports previous arguments against an explanation of Sh 2-109 as a single object.

We plan to extend our study of the stellar content of Sh 2-109 by including the catalog of optically visible open clusters and candidates by Dias et al. (2014). This catalog contains more than 250 open clusters with available distance and age determinations located toward the Cygnus star-forming field. Analyzing this data will further contribute to the study of the properties of the open-cluster population within the boundaries of Sh 2-109, including its morphology and energetics.

### **Acknowledgements**

This study made use of the NASA Astrophysics Data System, SIMBAD database and WEBDA open cluster database operated at the Institute for Astronomy of the University of Vienna.

### **References:**

- Bressan, A., Marigo, P., Girardi, L. Et al., 2012, MNRAS, 427, 127  
Crawford D. L. & Mander J., 1966, AJ, 71, 114  
Dias, W. S., Alessi, B. S., Moitinho, A., Lepine, J. R. D., 2002, A&A, 389, 871D  
Kaltcheva, N. & Golev, V., 2011, Stellar Clusters & Associations: A RIA Workshop on Gaia. Proceedings, p. 299  
Sharpless, S. 1959, ApJ Suppl., 4, 257  
Straizys V., Milasius K., Boyle P., et al., 2014, AJ, 455, 850  
Strömberg B., 1966, ARA&A, 4, 433  
Uyaniker, B., Fürst, E., Reich, W., Aschenbach, B., Wielebinski, R., 2001, A&A, 371, 675

# Star Forming Rates and HI Gas Content in Galaxy Groups

Sarah Martens

Department of Astronomy, University of Wisconsin- Madison

We compare the star formation rates with the respective HI properties of 4854 galaxies in 743 different groups. Using data from the SDSS and the GALEX all sky survey (AIS) we measure the star formation rates and NUV-r colors as a function of the total group mass, position within the group, and HI content as derived from the Arecibo Legacy Fast ALFA (ALFALFA) survey. The NUV-r colors are consistent with star forming field galaxies. We show how the quenching of the star formation is correlated with galaxy HI content and how both are affected by a group environment. <sup>i</sup>

## 1. Introduction

Galaxies residing in group environments have been shown to experience different evolutionary patterns than galaxies that are not in such tidally strong environments (Hess&Wilcots, 2013). Features such as NUV r color and HI mass can be analyzed to create an image of stellar population in galaxies with respect to their HI mass, two values known to be inversely proportional (as gas is the fuel to produce stars), at least in isolated environments. Studying how these values change in each galaxy with respect to their distance from the center of the group, we show how group environments affect galaxy star formation rates and gas content, leading to a possible loss of HI gas causing halt in star formation, or quenching. In Hess&Wilcots 2013 it was found that HI detections in galaxies decrease as the number of members in a group increases. Others found that galaxies, when organized in NUV-r color vs. r magnitude plots, tend to gather in a blue cloud of galaxies with a younger-forming stellar populations and a red sequence containing galaxies that have been recently quenched and therefore have an older stellar population than the former (Schawinski et al., 2014). There has been speculation of there being a third grouping, the green valley, of galaxies independent of both the red sequence and blue cloud, however this has been found to be only a transitional period between youthful energetic galaxies and older quenched galaxies with larger stellar populations (Schawinski et al., 2014).

We utilize three sources of astronomical data to perform our study. Sloan Digital Sky Survey (SDSS) provides the original sample used in Hess&Wilcots of 4854 different galaxies and the respective data in the optical. We then used the GALEX catalog to obtain the UV data of the galaxies from our original sample that could be detected. With this new sample we incorporate the galaxies HI data from the Arecibo Fast Legacy ALFA Survey (ALFALFA Survey). In this

---

<sup>i</sup> Thank you to the Undergraduate ALFALFA TEAM with NSF grant AST-1211005, Wisconsin Space Grant Consortium, and The National Space Grant College and Fellowship Program NASA Training Grant #NNX14AP22H

paper we present an analysis of HI mass detections from Hess&Wilcots and star formation rates as a function of relative distance of a galaxy from the group center. This paper is organized as follows. In Section 2 we discuss our three data sources: the optical data from the SDSS Data Release 7, the NUV and FUV magnitudes and luminosities derived from GALEX data, and the HI from the ALFALFA Survey. We also discuss the limiting of our sample by galaxies that are non UV-detected and the sky coverage of this sample. In Section 3 we analyze the significance of our results in the scope of the evolution of galaxies in group environments and in Section 4 we draw conclusions from these implications.

## 2. Data

Our original data is based upon the group sample that is described thoroughly in Hess&Wilcots(2013). Sloan Digital Sky Survey provided data ranging from 114.199844 to 247.473602 in right ascension and from 3.808206 to 29.015427 in declination. The size of this original sample in the optical was decreased when we began to incorporate GALEX data. Many of the galaxies from our original weren't detected in the UV. With this new sample we then compared their HI masses using the ALFALFA survey data from Hess&Wilcots 2013.

**2a. SDSS:** We obtained the original sample of galaxies involved in our investigation from Sloan Digital Sky Survey DR 7 which defined group galaxies by the friends of friends algorithm as described in Hess&Wilcots 2013, which can be referenced for a more detailed description of the original sample. We began our investigation with 4854 galaxies in 743 different groups ranging from 3 to 525 members in a group. This data contained information on right ascension and declination along with redshift. We used the redshift SDSS values to calculate the distances of these original galaxies using Hubble's Law, and we were later able to find the relative distances of each of the galaxies to the center of their respective group in Mpc. Using the HI data from ALFALFA, this allowed us to study the relationship of HI mass and star formation as a function of distance from group center, using distance from the center as a proxy for the time in which a galaxy would remain a member of a group.

**2b. GALEX:** The orbiting space telescope, GALEX, provided the ultraviolet data to contribute to our study. Our sample was limited slightly because of a portion of the galaxies detected by SDSS went undetected by GALEX. In order to determine which galaxies from SDSS were UV detected we had to search for matches around each of the original SDSS measurements. We chose 0.0001 as the range the differences between the right ascension and declination of both sources could be in order to be considered a match. The matched data was divided amongst the multiple surveys in the GALEX catalog the Medium Imaging (MIS), All-Sky Imaging (AIS), and Nearby Galaxy (NGS) of which we chose the most complete, the AIS, to be our modified sample of UV detected galaxies. The All Sky Imaging Survey (AIS) was done to by necessity to maintain the largest and most consistent and cohesive sample possible. The galaxies from our original SDSS data that were detected by GALEX experienced more star formation in there recent history, as the highly energetic light produced by young stellar populations are what allow the galaxies to be UV detected. From data provided by the AIS we were able to calculate the absolute magnitudes and luminosities of the galaxies, the equations used can be viewed in the Section 3. These new values enabled us to analyze the difference of the NUV-r color of galaxies with respect to their r-magnitudes and their distance from the center of their respective group.

This relationship allows us to observe how star formation rates, respond to the intensity of a group environment based on proximity.

**2c. ALFALFA:** The ALFALFA survey is an HI profiling survey from Arecibo Observatory which has the ability to detect low mass and volume HI content to  $10^6$  solar masses and has a positional accuracy of approximately 20 arc seconds) in the local universe (Haynes, Martha). HI data from the 2011 ALFALFA sample, which covered 40 percent of the complete survey area, contributes essentially to our analysis of star formation and quenching of galaxies in group environments as it represents the potential a galaxy has to producing more stars. The data we received from the ALFALFA survey allows for further analysis of galaxies evolution contributing to the existing optical (SDSS) and UV (GALEX) data to develop a deeper understanding of the effects of group and clustered environments on the stellar formation and gas content. For a more detailed description of the survey see Haynes et al. 2011.

**2d. Sky Coverage and HI Detections:** We used the Hess&Wilcots 2013 sample of 4500 galaxies in 754 different groups from SDSS ranging in the right ascension and declination measurements stated earlier. Of this original sample groups of less than 3 members had been deemed ineffective to study because forces due to the group dynamic may not be as distinguishable from a non-group environment or as consistent as with the larger more stable groups. Sky coverage was in part limited by the All-Sky Imaging Survey (AIS) from GALEX which we chose as the most complete survey provided by GALEX (as discussed in Section 2b). In Hess&Wilcots 2013 the original right ascension and declination measurements from SDSS where matched with those given in the ALFALFA Survey containing the HI data in order to determine which galaxies had detected gas mass. For more information on the sky coverage of the sample reference Hess&Wilcots 2013.

### 3. Results

Beginning with a sample of galaxies, the respective groups they resided in, along with their positional and optical data from SDSS we used CasJobs query to retrieve the respective far and near UV data for all of the galaxies. After organizing the UV and optical data we then converted our apparent NUV and FUV magnitudes in to absolute magnitudes. We then used them to calculate the near and far UV luminosities using a Python code. The following equations were used where FUV is the apparent far UV magnitude,  $c$  is the speed of light,  $z$  is the redshift, and MFUV is the absolute far UV magnitude.

$$MFUV = (FUV - 5)(\log\left(\frac{c * z}{7}\right))$$

$$Luminosity FUV = (3.846 * 10^{26})(e^{\frac{MFUV-4.47}{-2.5}})$$

The same equations above were used to find the absolute magnitude and luminosity of the near UV data. With this more complete and informative data, we made plots using TOPCAT (Tool for Operations on Catalogs and Tables) software of the absolute NUV magnitude as a function of the r-band magnitude from SDSS. These plots allow us to discuss the number of stars in a galaxy and their ages, looking at blue cloud vs. red sequence galaxies. Figure 1 is our complete sample plotted in this manner. Very few galaxies that have a very low r magnitude (high luminosities) are detected. The high luminosity galaxies that are detected have a lower UV output. This conclusion can be drawn intuitively because galaxies that aren't detected in the optical ranges, which have lower energy, will surely then not be detected in a higher energy wavelength.

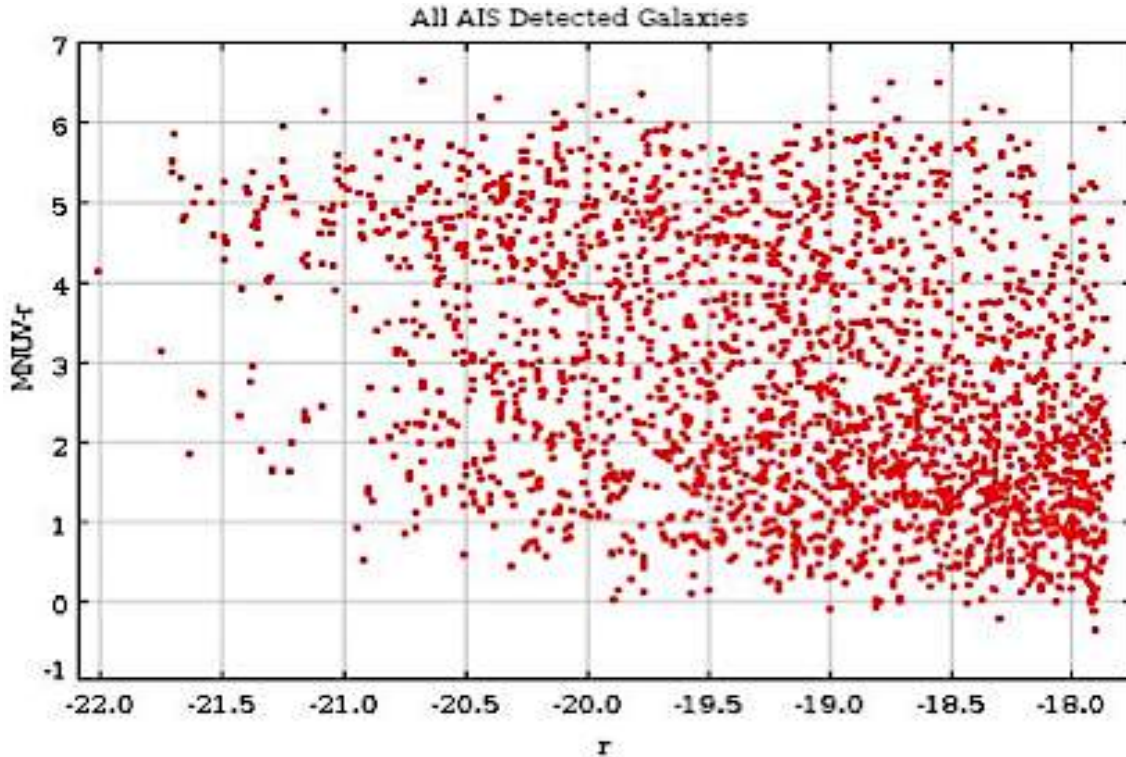


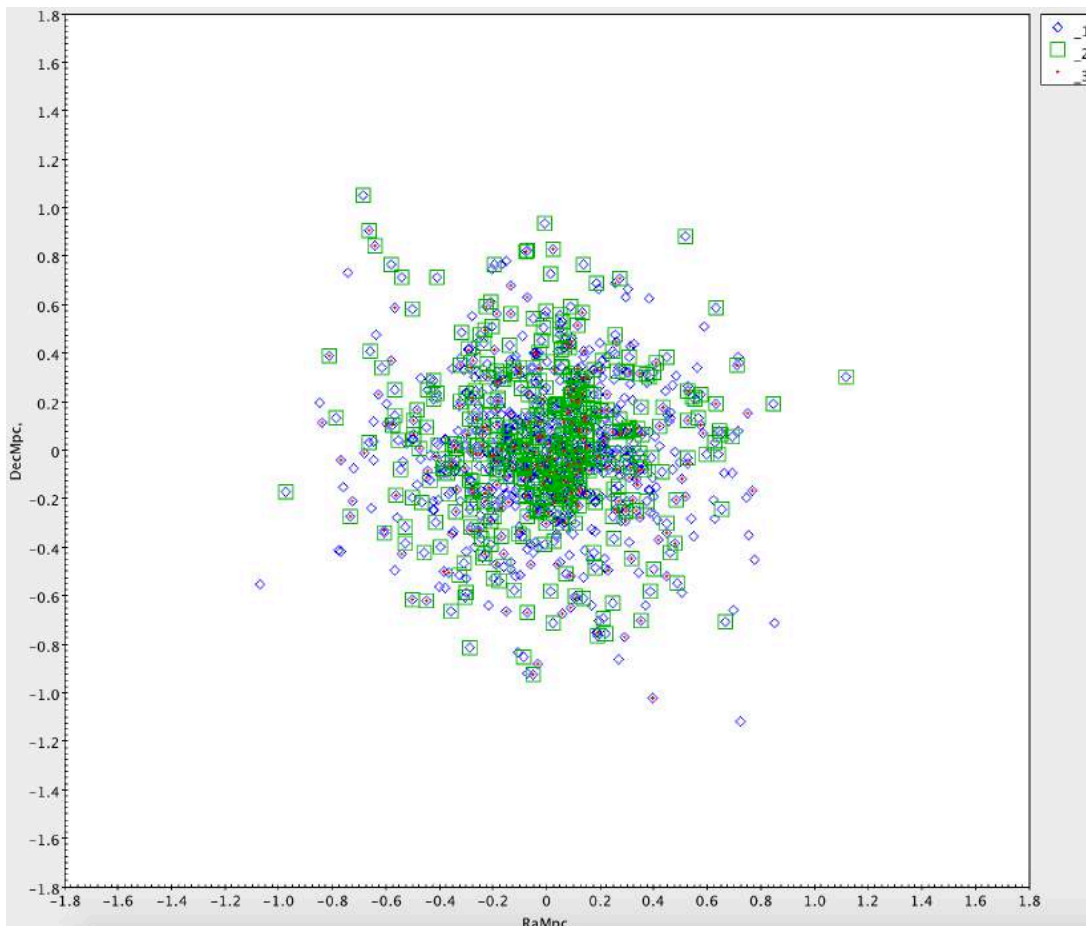
Figure 1: The difference of near UV and rband magnitudes plotted against rband magnitudes for all UV detected galaxies in the sample.

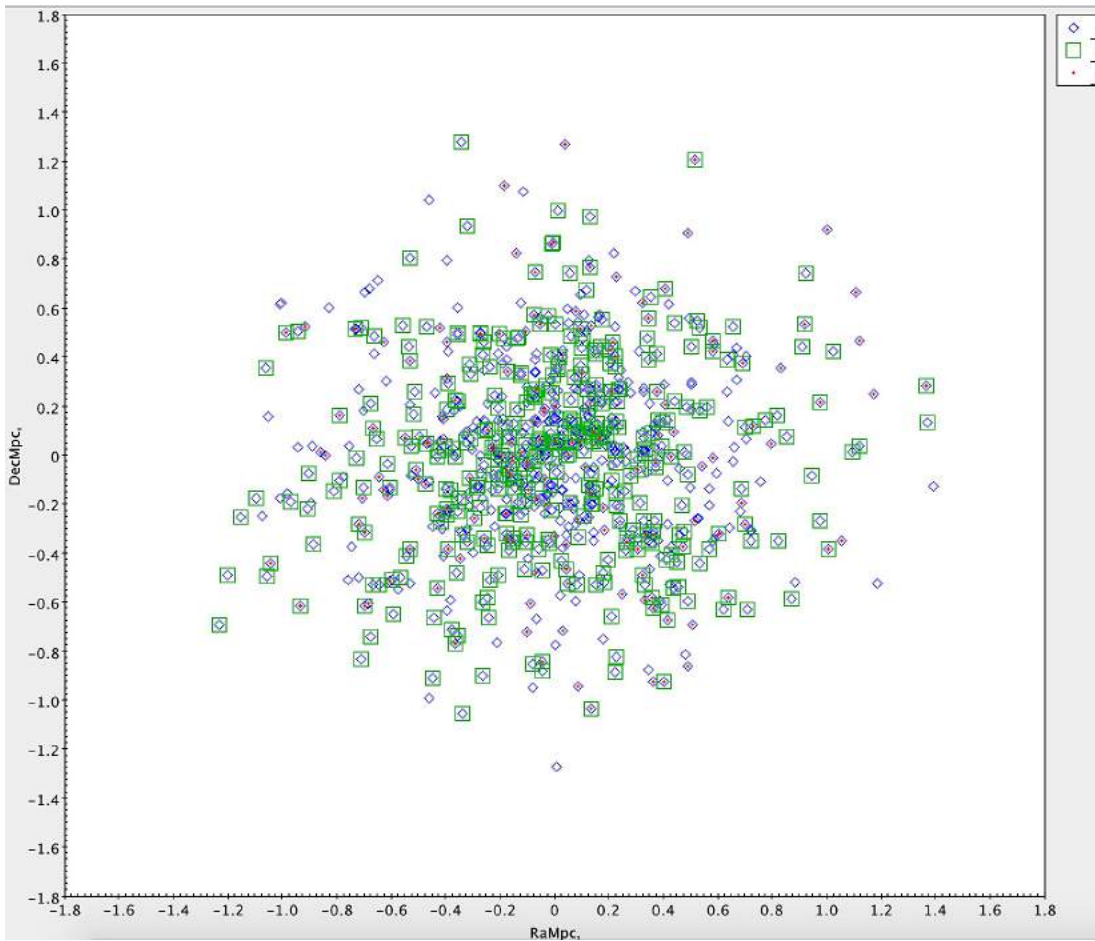
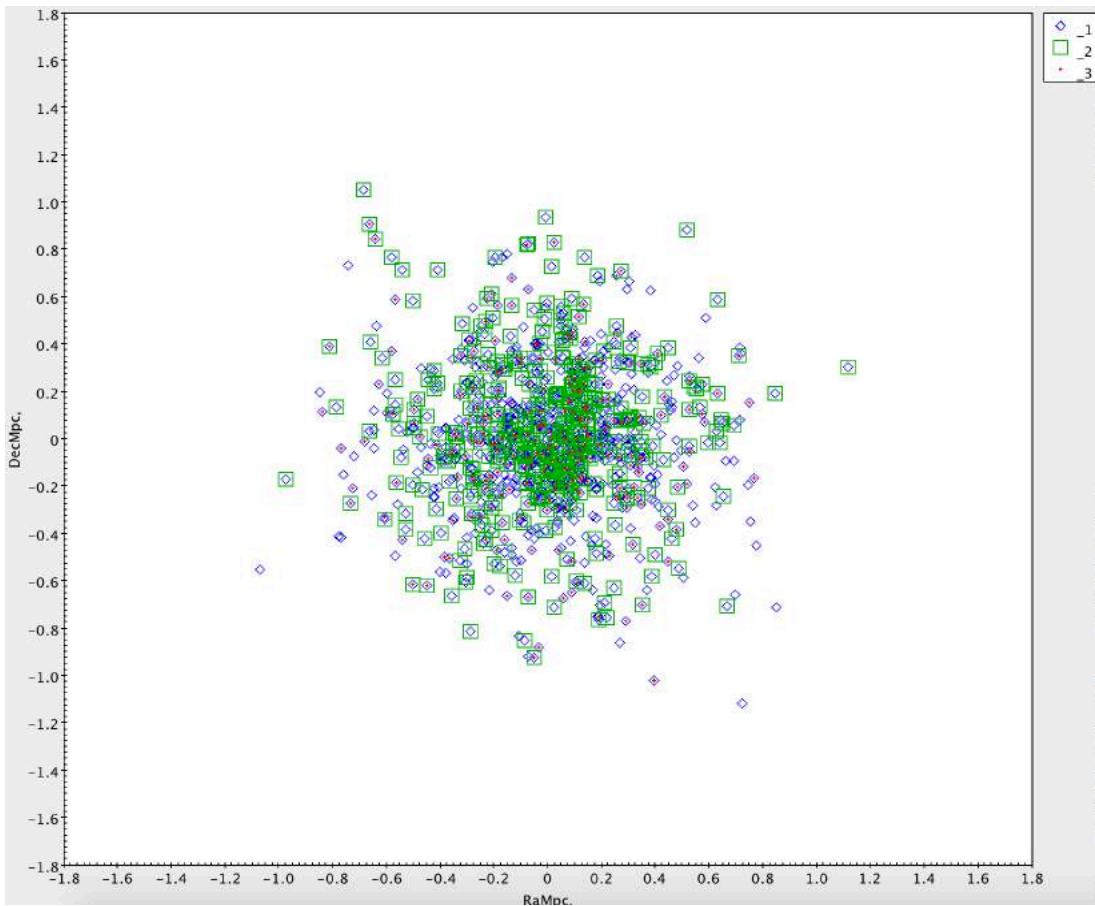
However, moving toward the higher r magnitudes (lower luminosities) there is a higher UV output. Also there is somewhat of a gradient of galaxy concentration with the lowest concentration in the area of smaller r magnitude and higher NUV (corresponding to the red sequence galaxies) and the more densely populated region being of high magnitude and low NUV (corresponding the blue cloud). This lends itself to the idea that galaxies within group environments undergo rapid star formation due possibly to strong tidal forces collapsing gas reserves. The many blue cloud galaxies, and the sparseness of red sequence supports this idea of ongoing quenching within group environments as blue cloud galaxies become quenched.

In order to analyze the spatial distribution of UV detected and HI mass galaxies with respect to the center of their groups we had to convert our original RA and DEC measurements to Mpc using the following equation:

$$RaMpc = \frac{(Ra - GroupRa) \left(\frac{c * z}{70}\right)}{(206265 * 3600)}$$

The same equation was used with respect to finding the declination in Mpc from the center of the group. After plotting the SDSS spatial distributions of the galaxy groups we then plotted the spatial distributions of the UV and HI detected galaxies on top in order to discuss a possible relationship between distance from the group center and UV and HI magnitude Figure 2. The HI data provided the known relationship between the stellar mass and gas content (in general in an isolated system will show an inverse relationship as stellar formation requires gas content) and allowed us to analyze further the possibility of quenching in galaxy groups. The more galaxies in each group that are UV detected, especially near the center will increase evidence for galaxy quenching at large, as seen in Figures 2. Meaning that galaxies residing in groups initially will experience a high star formation rates and gas depletion, leaving them energetic with a large stellar population but with no future potential of high levels of star formation, leaving them to become red sequence galaxies. In reference to red diamonds in the figures, we see an extreme depletion of galaxies having HI as group membership increases (similarly to Hess&Wilcots), especially nearer to the center of the group. The results of these plots coincide well with the interpretation of the UV distributions because the heavy UV detections nearly the center are rich in new stars but have no more HI reserves. This also heavily supports the theory of the quenching of gas in galaxies in groups due to tidal and gravitational forces increasing with higher membership.





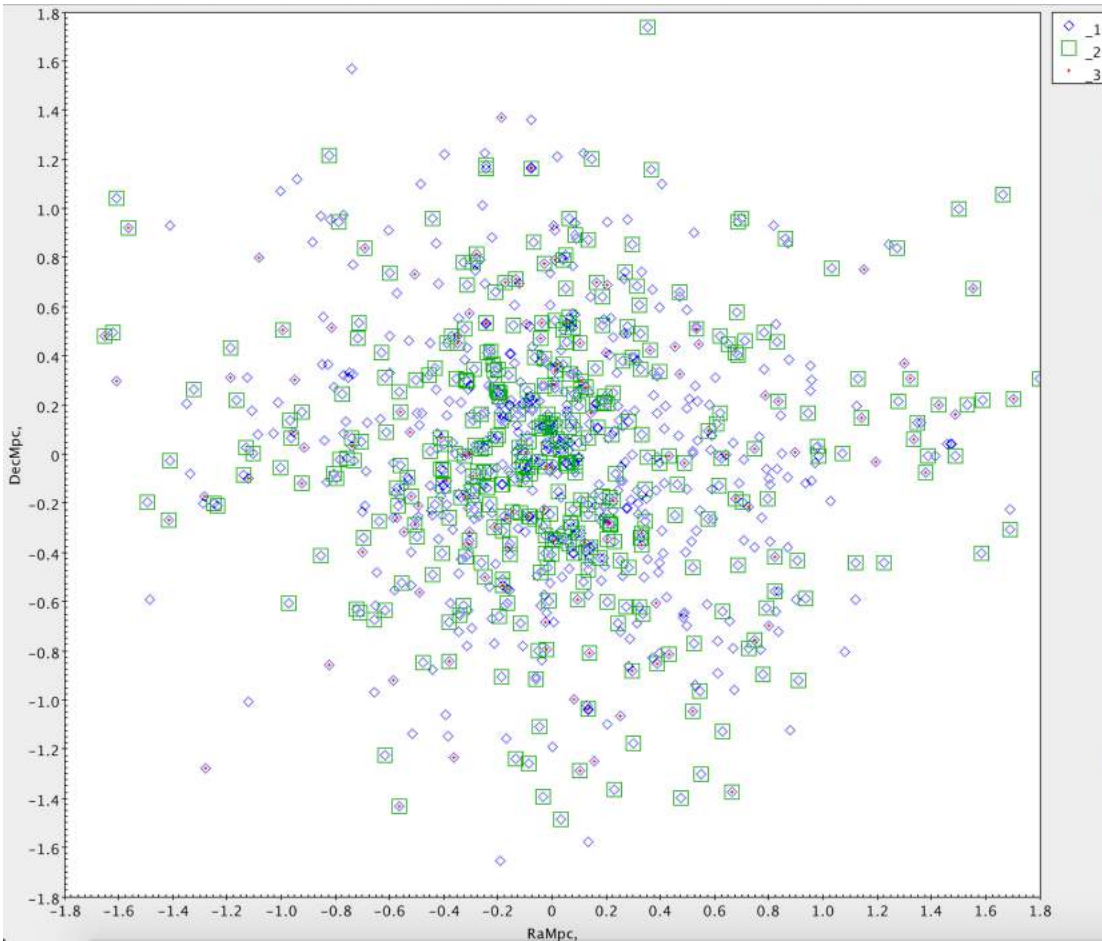


Figure 2: Y-axis: Declination in Mpc [-1.8, 1.8]. X-axis: Right Ascension in Mpc [-1.8, 1.8]. From top: all groups with 4-5 members, all groups with 6-9 members, all groups with 10-19 members, all groups with 20-50 members. The blue diamonds represent SDSS detections, the red crosses HI detections, and the green squares UV detections around the center of each galaxy group at the origin. The smallest groups remain tight around the group center, we presume the cause of this to be even smaller membership: with less there is much less gravitational pull allowing for galaxies to be at larger radii. While remaining fairly evenly concentrated throughout in the optical the UV detections throughout all bins (see Figure 3), HI detection concentration goes up in smaller membership groups and down with larger membership groups. With fewer galaxies there can be less gravitational power that would cause depletion of HI reserves via stripping and galactic interactions that occur with more galaxies.

**3a. UV Analysis from GALEX:** Plots that represent the NUV-r color as a function of r magnitude show that many galaxies of higher r magnitude do not have high detections in the NUV-r color. Galaxies which have a large population of stars will have higher UV magnitudes, which based on the plotted data means that galaxies with a higher stellar population tend to have lower magnitude in the visible spectrum, represented by r magnitude. Our plot (Figure1) shows a heavy concentration of galaxies with higher rband magnitudes and low NUV-r band magnitudes (the blue cloud). This leads us to conclude it plausible that group environments for galaxies cause a rapid surge in star formation before stripping member galaxies of HI and ending star formation.

**3b. Spatial Analysis:** Using the same UV data from GALEX we pursued to identify any pattern between the distance in Mpc from the center of the group and the galaxies that were

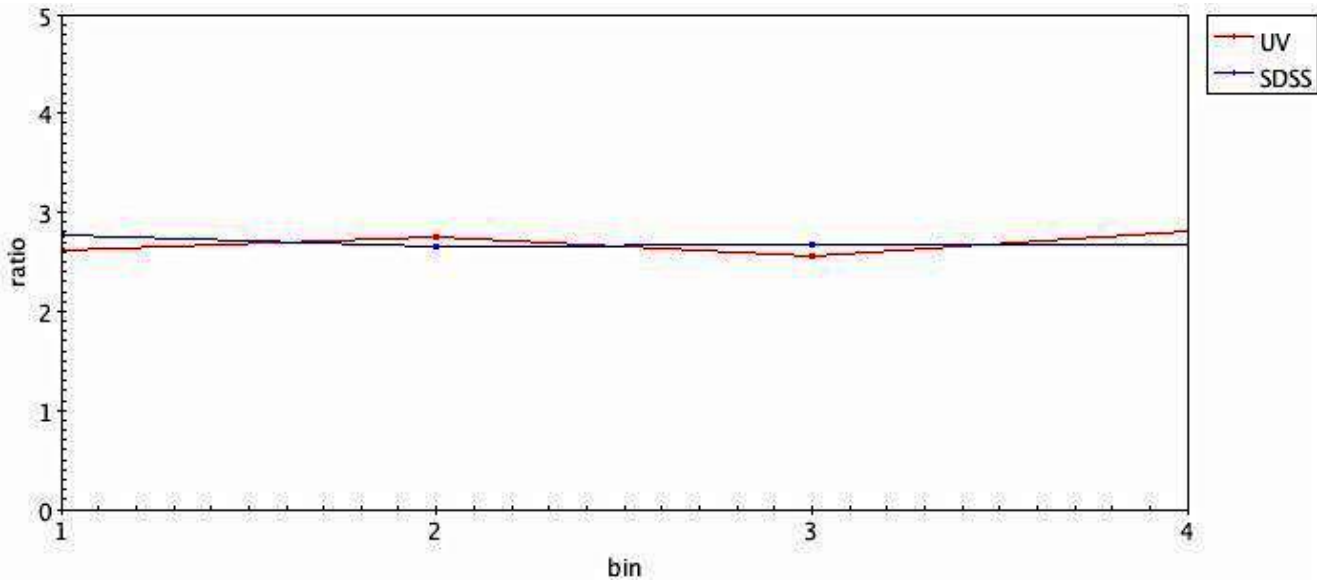


Figure 3: The four bins based on membership are indicated on the x-axis as integers 1-4. The concentration of UV detections is indicated as the red line while SDSS detection concentration is indicated in blue. The concentration was found by dividing two crucial radii: the radius 'x' from the group center at which 75% of galaxies detected are within said distance from center, and the radius at which 25% of galaxies detected are within said distance from center 'x'. Then for each bin, I divided the 75% x-radii by the 25% radii for both UV and SDSS detections to find the concentrations. Both UV and SDSS concentrations remain pretty evenly distributed throughout all bins while the concentration of HI detections has an inverse relationship with number of galaxies in a group, as found in Hess&Wilcots 2013.

detected in the UV. We see in Figures 2 that galaxies toward the higher density areas of the group are more likely to be UV detected, and have a higher stellar population. This shows the tidal forces, which are stronger in higher density environments, indeed have an effect on galaxies causing jarring of gas reserves leading to star formation. However, we found no correlation between group membership and the concentration of UV detections near the center. We then looked at the HI data from ALFALFA as a function of spatial distribution, similar to in Hess&Wilcots 2013. This resulted in finding that the concentration of HI detections of galaxies near the center has an inverse relationship with the number of members in a group, and also that as a group grows in members the spatial distributions of HI detections increases (Hess&Wilcots 2013). There exists less HI detected galaxies near the center due to the increased tidal and gravitational strengths from the increased membership. For a more in depth analysis of the HI detection patterns please see Hess&Wilcots 2013.

#### 4. Conclusion

A large picture of galaxy evolution can be formed from the HI data analysis described in Hess&Wilcots 2013 combined with the UV detection analysis made in this paper. Based on the results described earlier and displayed in the plots the following are supported: galaxies in groups begin with a rapid star formation rate (blue cloud) due to tidal forces of the group as seen by the UV analysis both in the spatial distribution and the NUV-r color and r magnitude. Near this time galaxies also begin being stripped of HI mass as seen in the spatial distributions and discussed in Hess&Wilcots 2013 (both effects intensified the closer a galaxy is to the center of the group as gravitational and tidal forces increase with the density of galaxies in a area) as they move

towards becoming more characteristic of red sequence older and quenched galaxies. These statements validate the theory of quenching by means of HI depletion through the forces of a galactic group along with the idea that star formation rate has inverse proportionality with distance in Mpc to the center of a group.

## References

[Hess and Wilcots,2013] Evolution in the HI Gas Content of Galaxy Groups: Pre- Processing and Mass Assembly in the Current Epoch The Astronomical Journal  
<http://arxiv.org/abs/1308.4646>

[Schawinski and Urry et al.] The green valley is a red herring: Galaxy Zoo reveals two evolutionary pathways toward quenching of star formation in early and late type galaxies. Advance Access publication <http://arxiv.org/abs/1402.4814>

[Haynes et al..] The Arecibo Legacy Fast ALFA Survey: The  $\alpha$ .40 HI Source Catalog, its Characteristics and their Impact on the Derivation of the HI Mass Function. The Astronomical Journal <http://arxiv.org/abs/1109.0027>

Haynes, Martha. "The Arecibo Legacy Fast ALFA Survey." *The Arecibo Legacy Fast ALFA Survey*. 1 Apr. 2013. Web. 1 June 2014. <http://egg.astro.cornell.edu/index.php/>

# Predicting Collisionless Equilibria in Dark Matter Simulations

Robert J. Ragan

Department of Physics, University of Wisconsin – La Crosse<sup>1</sup>

By using a transformation from phase-space variables to a set of orthogonal Hermite-Legendre polynomials, the dynamics of one-dimensional self-gravitating systems has been reduced to a linear set of equations. This transformation changes the long-range forces into local interactions in the new problem. This makes it possible to determine the steady-state solutions by projecting the initial conditions into the time-independent solutions.

## 1. Introduction

Astrophysicists have made significant progress in forming a consistent picture of how large-scale structures (namely galaxies and galaxy clusters) form through the use of  $N$ -body computer simulations. In fact simulations are the main tool for determining the role dark matter halos play in structure and evolution of galaxies. These models vary in their level of detail – some include only gravitational interactions, while others include additional gas dynamics and stellar evolution. Although these simulations reproduce observed self-gravitating objects, their behavior is not fully characterized and the driving mechanisms in their evolution are not fully understood. Some questions that still need to be answered are: What determines the equilibrium state of such a system? How does the final state depend on the initial conditions? What features are universal? What role does entropy play in the relaxation process?

Although realistic models do enable us to reproduce observed structures, their complexity makes analysis very difficult and mostly empirical in nature. For this reason, my UW-L colleague Eric Barnes, and I have been studying one-dimensional collisionless systems. These systems relax to quasi-stationary equilibria via self-gravity in a very similar fashion to 3-d systems, but are much easier to analyze. In particular, their phase-space distributions can be linearized and expanded in terms of orthogonal polynomials. The equations of motion of the expansion coefficients can be written as a sparse linear system. Diagonalization of the equations of motion yields the spectrum and modes of the dynamics as well as the time-independent solutions.

This approach allows us to predict the final equilibrium state from the initial conditions. But more than that, it gives a very illuminating picture of the phase-space motion of the system in terms of the evolution of the expansion coefficients whose equations of motion are local in that couplings are only between nearest-neighboring coefficients. This gives a compelling picture of conserved quantities like energy and fine-grained entropy that evolve via continuity-type equations in coefficient space. Furthermore, higher-order expansions should yield information

---

<sup>1</sup> This work was supported a WSGC Research Infrastructure Program grant.

about correlations between different modes, such as how they develop and how they relate to the energy and entropy of the system. Taken together with  $N$ -body simulations this investigation should yield a deeper understanding of the role of dark matter halos in galaxy formation.

## 2. Background

There is a broad consensus among astrophysicists and cosmologists that visible matter makes up only 5% of the mass-energy of the universe. Another 25% is thought to be weakly-interacting dark matter (Spergel et al., 2003), and the remaining 70% is hypothesized to be dark energy. The picture has been inferred from the velocity curves of star orbits within galaxies (Rubin & Ford,

1970), the motion of galaxies within clusters (Zwicky, 1937), gravitational lensing (Clowe et al., 2006), and rate of expansion of the universe.

In particular studies of individual galaxies indicate that the observed velocity curves are due to halos of dark matter that surrounds galaxies.  $N$ -body simulations of galaxies can involve billions of point masses interacting via gravity, sometimes with additional gas physics and stellar evolution. These studies have been successful in reproducing typically observed galactic structures (density profiles, velocity curves, etc.) from “cosmological” initial conditions, i.e. nearly uniform, expanding mass distributions (Navarro et al., 1997, 2004).

Dark matter interacts via gravity but its motion is assumed to be *collisionless*. A natural question that arises is: how does a dark matter halo relax? Computer simulations indicate that relaxation is generally incomplete, that different initial conditions lead to different equilibria. In fact, for 3-d systems there is no self-gravitating thermal equilibrium with a uniform temperature (Lynden-Bell 1967), and in general systems partially relax to an equilibrium state belonging to continuum of quasi-stationary states (Hohl & Felix, 1967).

Numerous attempts have been made to understand the details of collisionless relaxation processes (Taylor & Navarro, 2001; Hansen & Moore, 2006; Lithwick & Dalal, 2011). Although they have added new insights, none of them have provided a comprehensive physical picture. Progress in this direction is the motivation of this project.

Instead of tackling the full 3-d problem head-on, we have chosen to study 1-d self-gravitating systems. These systems are a lot easier to analyze and simulate yet they possess many of the essential features of interest, like long-range forces, self-gravitation, and collisionless relaxation. On the other hand the 1-d problem lacks 3-d properties like angular momentum and tidal forces.

The collisionless phase-space ( $x, v$ ) evolution of 1-d systems is described by the one-dimensional Vlasov equation (Alard and Colombi, 2005 and references therein)

$$\frac{\partial f}{\partial t} + v \frac{\partial f}{\partial x} + a(x) \frac{\partial f}{\partial v} = 0 \quad \text{Eq.1}$$

where  $f(x, y)$  is the phase space distribution function and  $a(x)$  is the acceleration due to self-gravitation. For 1-d systems the gravitational force is range-independent so the acceleration is given simply by  $a(x) = -g(M_{>} - M_{<})$ , where  $M_{>(<)}$  is the total mass to the right (left) of  $x$ , and  $g$  is the 1-d gravitational constant.

Studies of the 1-d model have a long history (Camm, 1950). These studies focus usually focus on either cosmological problems (instabilities of uniform density) (e.g. Miller et al., 2007), or isolated self-gravitating systems (e.g. Schulz, 2013). Most of the analyses of isolated systems has been performed using action-angle variables  $(E, t)$  from which a general solution can be obtained, at least of the linearized Vlasov equation (e.g. Barre et al., 2011). But the calculations are rather cumbersome and opaque, and physical quantities are not easily analyzed in this approach.

We have found another way to analyze the linearized Vlasov equation, by considering perturbations of thermal equilibrium, i.e.  $f = f_0 + \delta f$ . In contrast to the 3-d case, the 1-d case possesses a bound state of thermal equilibrium that maximizes entropy

$$f_0(x, v) = A e^{-v^2/2\sigma^2} \operatorname{sech}^2(gMx/2\sigma^2) \quad \text{Eq.2}$$

where  $\sigma$  is the velocity dispersion and  $A$  is a normalization constant. After linearizing the Vlasov equation about  $f_0$ , one can expand the perturbations in terms of Hermite (in velocity) and Legendre polynomials (in position) in the form

$$\delta f(x, v, t) = f_0(x, v) \sum_{m,n} c_{mn}(t) G_{mn}(x, v) \quad \text{Eq.3}$$

where the polynomials the  $G_{mn}$  are a complete set of orthogonal normalized polynomials,

$$G_{mn}(x, v) = \sqrt{\frac{2n+1}{2^m m!}} H_m(v) P_n(\tanh(x)) \quad \text{Eq.4}$$

( $x$  and  $v$  have been rescaled), and the  $c_{mn}(t)$  are time-dependent expansion coefficients. The equations of motion of the coefficients are then given by the linear system

$$\frac{d}{dt} c_{mn} = \sum_{ij} L_{mn}^{ij} c_{ij} \quad \text{Eq.5}$$

where the couplings  $L_{mn}^{ij}$ , determined from Eq.1 are only between *neighboring* coefficients (i.e.  $i, j = m \pm 1, n \pm 1$ ), and are time-independent. Thus, the original phase space  $(x, v)$  evolution is transformed into an evolution of coefficients on the positive  $(m, n)$  quarter plane (Fig. 1). The

initial value is solved by projecting the initial perturbation onto the orthonormal polynomials and evolving the system according to Eq.5. These equations define a very rich model whose physical properties are easy to investigate. We have been able to derive 1<sup>st</sup>- and 2<sup>nd</sup> -order expressions for kinetic and potential energy as well as fine- and coarse-grained entropy.

Alternatively, the system can also be analyzed as an eigenvalue problem

$$i\omega_k C_k = LC_k \tag{Eq.6}$$

with a spectrum of real frequencies  $\{\omega_k\}$  and complete set of eigenvectors  $C_k$ . This approach reveals a  $\omega = 0$  subspace of eigenvectors corresponding to the time-independent solutions of Eq.5, (and hence of Eq.1). These time-independent solutions form the basis of equilibria states that result from relaxation. In this picture, relaxation is viewed as a de-phasing of all the  $\omega \neq 0$  components in the initial conditions.

Unfortunately, truncation of the series to some  $(m_{\max}, n_{\max})=(M, N)$  domain is a non-trivial problem, because reflections occur at the truncation boundaries. We have tried several approaches, including fixed boundaries, absorbing boundaries, and or small amounts of damping, but none are completely satisfactory and their impact on the time-dependent solutions is still not fully understood. Fortunately, the truncation problem can be side-stepped by considering the time-independent solutions.

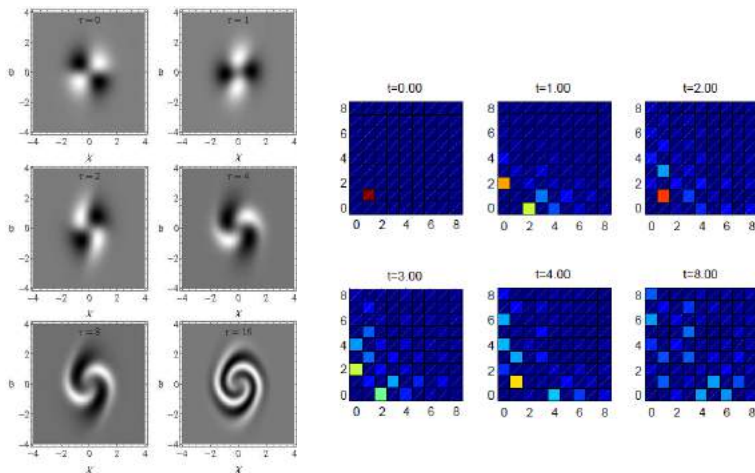


**Figure 1** Comparison of evolution in phase space (x,p) and coefficient space (m,n).

### 3. Time-independent solutions

The focus of this work was the subspace of time-independent solutions, which allows us to predict the final state from the initial state, but also allows us to study the redistribution of energy and entropy resulting from relaxation in a very precise way.

The time-independent solutions can be obtained in a variety of ways. One can simply diagonalize Eq.6 numerically to obtain approximate solutions, but this approach suffers from the truncation effects at the  $m=M$  and  $n=N$  boundaries. Alternatively one can solve Eq.5 with  $\frac{d}{dt}c_{mn} = 0$  directly, and this results in recursion relations for the time-independent solutions. Since there are an infinite number of degenerate solutions spanning the subspace, they have to be orthogonalized via a Gram-Schmidt procedure (Fig. 2). The solutions naturally truncate at some  $m_{max}$  which serves as an index. There is an additional complication in that  $L$  is not Hermitian, but this has been overcome with the use of left- and right-sided eigenvectors.

One can also obtain *exact* solutions by expanding the velocity in a Hermite series and solving the resulting (coupled) differential equations for  $\delta f$  directly. This approach is cumbersome but provides a benchmark for comparison with approximate solutions.

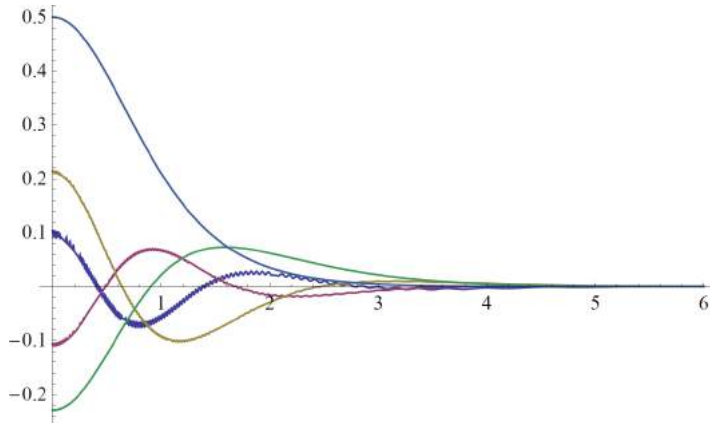


**Figure 2.** Density profiles of orthogonalized time-independent solutions.

Once a suitable set of orthonormal time-independent solutions has been obtained, the final states will be compared with 1-d N-body solutions for a variety of initial conditions (Fig. 3). This process should allow us to identify different classes of initial conditions according to what final states they project into. In particular, it will be interesting to see how these final states relate to the family of distribution functions obtained by maximizing coarse-grained entropy using Lynden-Bell statistics (Lynden-Bell, 1967), thus yielding a very stringent test of their applicability.

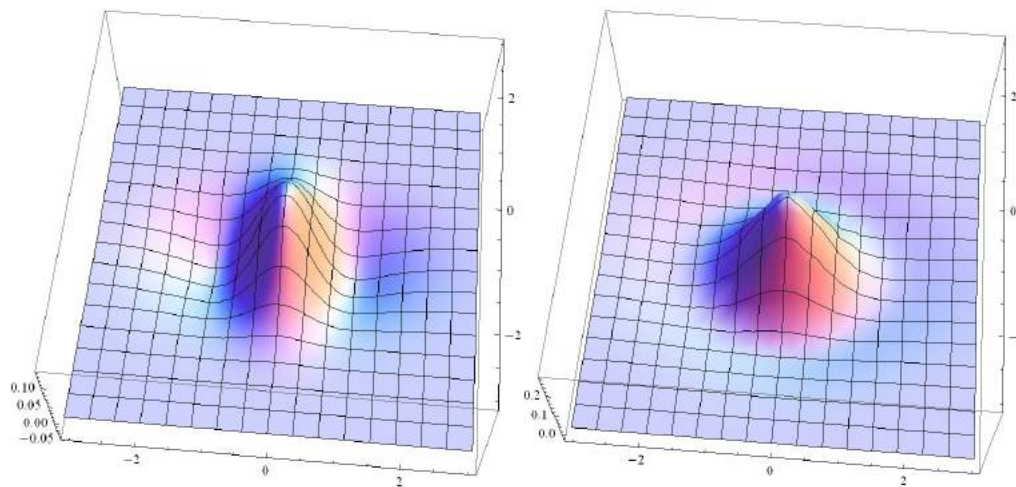


**Figure 3.** Example of initial conditions (left) and corresponding steady- state solution (right).

#### 4. Summary

To summarize, the goals of this work were: to perform a complete analysis of the time-independent subspace of solutions of isolated 1-d self-gravitating systems that have been slightly perturbed from the state of maximum entropy,  $f_0$ . This involved: (1) obtaining these solutions in various representations (as eigenvectors, recursive solutions, and exact solutions of coupled differential equations), (2) using these solutions to predict the equilibrium state for different initial conditions, (3) analyzing and interpreting the redistribution of energy and fine-grained entropy in the evolution of these systems from their initial conditions, (4) extending the calculations to 2<sup>nd</sup>-order to study the behavior of correlations, and (5) performing  $N$ -body simulations to verify our predictions and to determine their range of validity.

#### REFERENCES recommend journal abbreviations be more than single letter words

Alard C., Colombi S., 2005, MNRAS, 359, 123

Barnes, E. I., Ragan, R. J. 2014, MNRAS, 437, 2340 This reference is not cited in text.

Barr'e J., Olivetti A., Yamaguchi Y.Y., 2011, J. Phys. A, 44, 405502

Camm G.L., 1950, MNRAS, 110, 305

Clowe D., Bradac M., Gonzalez A.H., Markevitch M., Randall S.W., Jones C., Zaritsky D., 2006, ApJ, 648, L109

Hansen S.H., Moore B., 2006, New Ast., 11, 333

Hohl & Felix, 1967 this reference is cited but not in references

Lithwick Y., Dalal N, 2011, ApJ, 734, 100

Lynden-Bell, D. 1967, MNRAS, 136, 101

Miller B.N., Rouet J., Le Guirriec E., 2007, Phys. Rev. E, 76, 6705

Navarro J.F., Frenk C.S., White S.D.M., 1997, ApJ, 490, 493

Navarro J.F. et al., 2004, MNRAS, 349, 1039

Ragan, R. J., Mullin, W. J., Wiita, E. B. 2005, J. Low Temp. Phys., 138, 693 this reference not cited in text

Rubin V.C, Ford W.K., 1970, ApJ, 159, 379

Schulz A.E., Dehnen W., Jungman G., Tremaine S., 2013, MNRAS, 431, 49

Spergel D.N. et al., 2003, ApJS, 148, 175

Taylor J., Navarro J., 2001, ApJ, 563, 483

Zwicky F., 1937, ApJ, 86, 217

# 25<sup>th</sup> Annual Wisconsin Space Conference

## PART TWO

### Physics and Engineering

# Three Dimensional NURBS Modeling and Fabrication of Rotorcraft Design

Geoffrey A. Ament<sup>1</sup>

NASA Ames Research Center, Mountain View CA, 94035  
University of Wisconsin Platteville, Platteville WI, 54115

## Abstract

Before an aircraft is put into production, it must undergo a variety of tests inside a wind tunnel. Rather than performing these tests on a full-scale plane, scaled models are often utilized. Scaled models allow an aircraft to be tested in smaller facilities, can be built quickly, and can save money, as long as the physics being studied scale correctly. Another use for aircraft models is to demonstrate *how* a model aircraft is built and tested in a wind tunnel, showing aircraft interior and how the exterior mechanics operate. The objective of this project was to show the steps involved in building a model aircraft and what these models can be used for. The model aircrafts worked on and mentioned in this paper include the Large Civil Tilt Rotor (LCTR2) and XV-15 Tilt Rotor Research Aircraft. Models are either computer modeled from blueprints or provided by our mentor, Eduardo Solis. The models are constructed using the program Rhino, prototyped in a MakerBot 3D printer, and finally 3D printed using the Dimension Elite printer and a laser cutter. The models do not have real working engines; they are only for display and educational purposes; the models only show only how the model airframes are built using the stated 3D printers and laser cutters. Four engineering interns worked on this project. As Project Leader, I distributed the workload for the three major projects - the LCTR2 model, the XV-15 RotCFD model, and the 1/6-scale model of the 7-Foot by 10-Foot Wind Tunnel.

## Nomenclature

NURBS	=	Non-Uniform Rational Basis Spline
LCTR(2)	=	Large Civil Tilt Rotor (2)
VTOL	=	Vertical Take Off and Landing
XV-15	=	XV-15 Tilt Rotor Aircraft
Rhino	=	Rhinoceros 5 3D NURBS Modeling Software
RotCFD	=	Computational Fluid Dynamics Software

## Introduction

To help adapt to a crowded airspace, the LCTR2 and XV-15 were designed to allow for vertical takeoff. This design allows for efficient use of aircraft runways, allowing more aircraft to land in airports. Before these aircraft designs can be put into production, they must undergo a series of tests. Instead of running these tests on a full scale aircrafts, models are created to quickly and inexpensively test an aircraft in a wind or water tunnel. Another use of aircraft models is to demonstrate how the tested or full scale models operate. This paper will illustrate the design procedure that goes into building model LCTR2 and XV-15 rotorcrafts for demonstration and testing purposes.

---

<sup>1</sup>Thanks to Wisconsin Space Grant Consortium for making this research opportunity possible. Special thanks to my mentors William Warmbrodt and Eduardo Solis for their support throughout the project.

## Project Background

**LCTR2 Background.** The NASA Heavy Lift Rotorcraft Systems Investigation evaluated various aircraft designs to determine which rotorcraft system could be flown safely for the civil mission. With that said, because of the expected 100,000 lb aircraft weight traveling at 350 knots, designing such an aircraft could prove difficult. After investigation, the Large Civil Tilt Rotor (LCTR) proved to be the most promising aircraft for performance, stability and safety (1). The goal of these aircraft is to compete with current jet aircraft and help a crowded airspace. The aircraft is to carry 120 passengers with baggage, travel 1200 nm, and travel mach 0.6 at 30,000 feet (3). A picture of the LCTR aircraft can be seen in Figure 1.

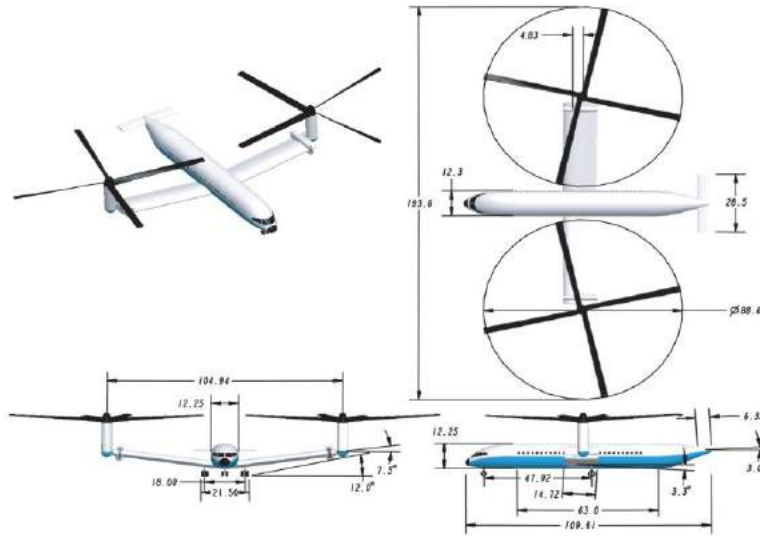


Figure 1. Shows the LCTR concept model. All dimensions shown are in ft and degrees (2).

In April 2012, the LCTR was first tested in the NASA Ames 7-Foot by 10-Foot Wind Tunnel. The model was tested in airplane mode as well as helicopter mode; in helicopter mode, the nacelles were rotated between 60 and 95 degrees and tested up to 80 knots. A much smaller model was tested in both modes in the NASA Ames Fluid Mechanics Laboratory Water Tunnel. Picture of the models tested in air and in water in these tunnels can be seen in Figures 2.

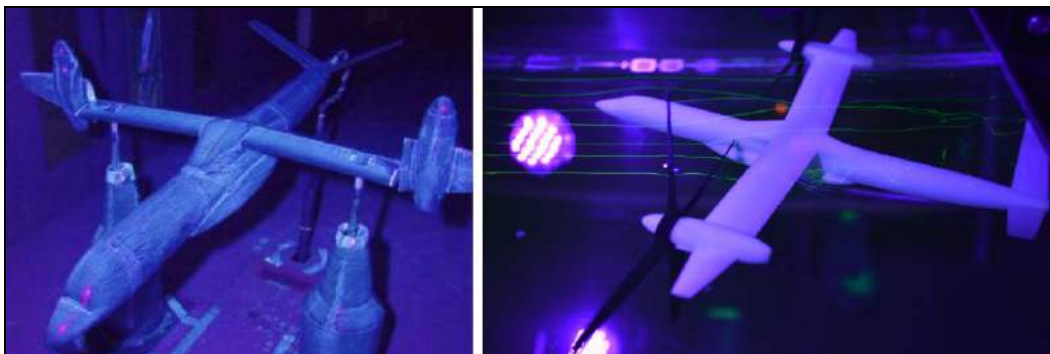


Figure 2. Left, LCTR2 model tested in 7x10 ft wind tunnel. Right, LCTR2 model tested in water tunnel.

**XV-15 History.** The XV-15 vertical takeoff and landing aircraft would be ideal for short haul, civilian transport air travel. A picture of this aircraft can be seen in Figure 3 (1). In 1997, an full-scale aero acoustic test was performed on the XV-15 rotor at the NASA Ames Research Center to analyze tilt rotor noise with the goal of reducing it; the test was conducted in the 80- by 120-Foot Wind Tunnel test section. To help reduce noise, the number of rotors blades were increased from three to four.



Figure 3. Shows a picture of the XV-15.

## Design Process

**Rhino Program and Machine Tools.** Before starting physical construction of the model aircraft, the models had to be digitalized using the 3D modeling program Rhino. Rhino has the ability to render models to provide a visual of how the physical model will look. Once a digital version of the aircrafts was input into Rhino, the parts had to be 3D printed and / or laser cut. In preparation for fabrication, we were trained on these machines and other Space Shop equipment. With the combined knowledge of Rhino and other Space Shop equipment, the models were ready for 3D printing and assembly.

**LCTR2 Model Design.** The LCTR2 model built this summer was a scaled replica of the model tested in the 7 by 10 ft wind tunnel. After a 1 to 1 scale model was digitalized in Rhino, the model was scaled down to be 1/44 of the original blueprint. Further, the model needed to showcase how the wind tunnel test model was built, demonstrating both interior and exterior construction. To accomplish this, the model needed to be 3D printed in sections; this allows the user to pull pieces off the LCTR2 model to view how the wind tunnel test model was built internally and externally. For demonstration purposes, only half of the aircraft can be pulled

apart; the second half of the aircraft is completely intact. A overview of the LCTR2 model, assembled and pulled apart can be seen in Figure 4.

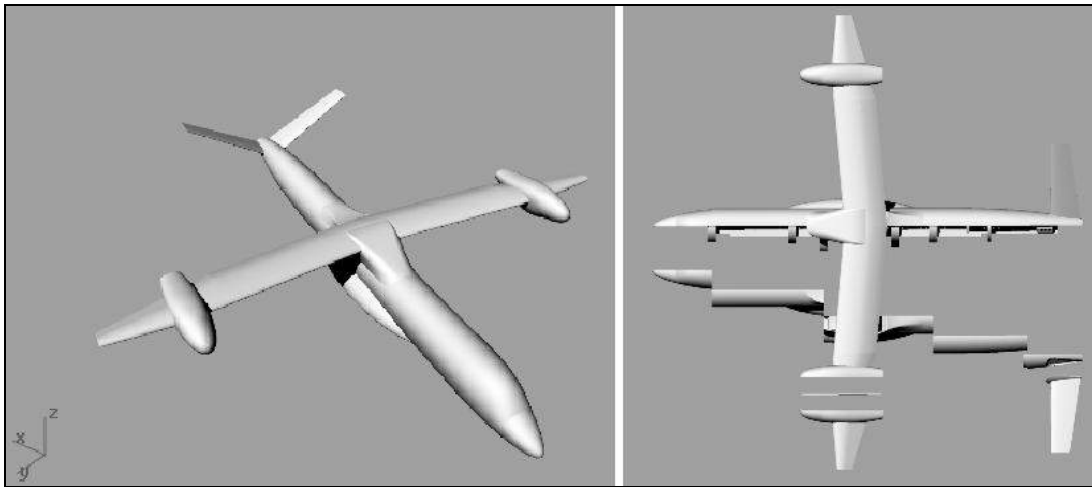


Figure 4. Left, shows a rendered view of the 1/44 scale LCTR2 in Rhino. Right, shows how the rendered model can be pulled apart.

Before the model could be printed, the pull apart pieces needed to be designed such that they could easily be detached from the model (Figure 4). To accomplish this, pin inserts were implemented on each detachable piece; a 3D model showing these pin hole attachments can be seen on the central body piece of the LCTR2 model in Figure 5.

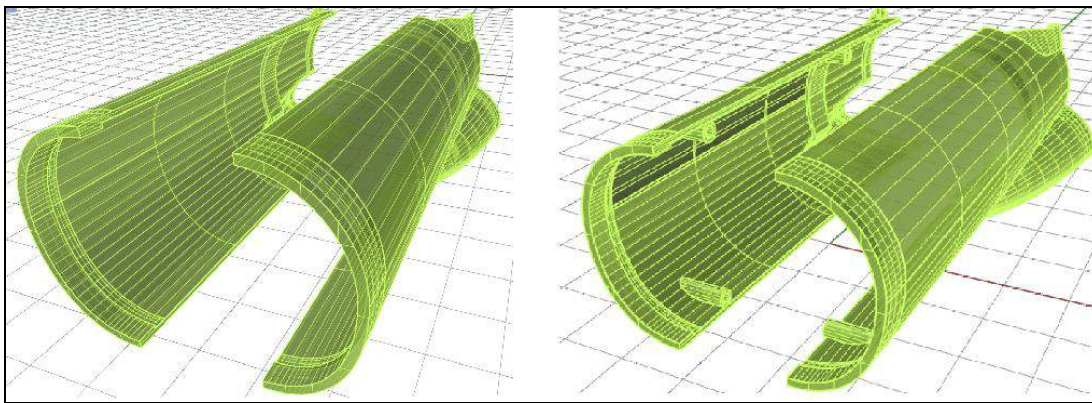


Figure 5. On left, notice the original model had no way of fastening one side of the model body to the other. On right, the left design was upgraded to include pin hole inserts to attach or remove the model side panels.

Overall, the aircraft contains 50 plastic 3D printed pieces modeled in Rhino, 10 of which are detachable. The aircraft is held together by a 1.5 inch by 1.5 inch aluminum core. Once all 50 pieces were separated in the Rhino software, they were 3D printed using a high resolution 3D printer, the Dimension Elite. With that said, before printing on the Dimension Elite, some parts were prototyped on a MakerBot 3D printer; Figure 6 shows the LCTR2 3D printed parts.



Figure 6. LCTR2 model 3D printed parts along with the aluminum core to hold parts together.

After each part was 3D printed, each piece was test fitted before fabrication. Once all pieces fit properly, each piece was sanded until smooth to touch; if a surface has imperfections, the piece required bondo and re-sanding of the area. Once all pieces were sanded, primer was applied to help fill any remaining imperfections in the model surfaces. Once dry, the pieces were then wet sanded. This process was repeated until the model was free of imperfections. Lastly, a black coat was added to give the LCTR2 model a matte finish. This fabrication process can be seen in Figures 7 and 8.



Figure 7. Left to right, shows initial sanding, application of primer and black paint to the 3D printed pieces.



Figure 8. Shows an assembled model of the LCTR2 without attached blades.

**LCTR2 Rotational Base Design and LCTR2 Base Attachment.** After the LCTR2 model was complete, the model was attached to a rotational base which allowed for 360 degree rotation as well as pitch angle of  $\pm 15$  degrees via shepherds crook. To do this, the model needed to sit on two elevated columns which inserted into the rotational base. In addition, the shepherds crook needed to insert into the base, allowing for the shepherds crook rod to slide in and out of the base. A rendered view of the LCTR2 model mounted on the rotational base can be seen in Figure 9.



Figure 9. Rendered view of the 1/44 scale LCTR2 model on a 360 degree rotational base.

The base was created using layers of acrylic with a few ABS plastic parts. Base dimensions can be seen in Figure 10; base parts cut by laser or 3D printed parts can be seen Figure 11.

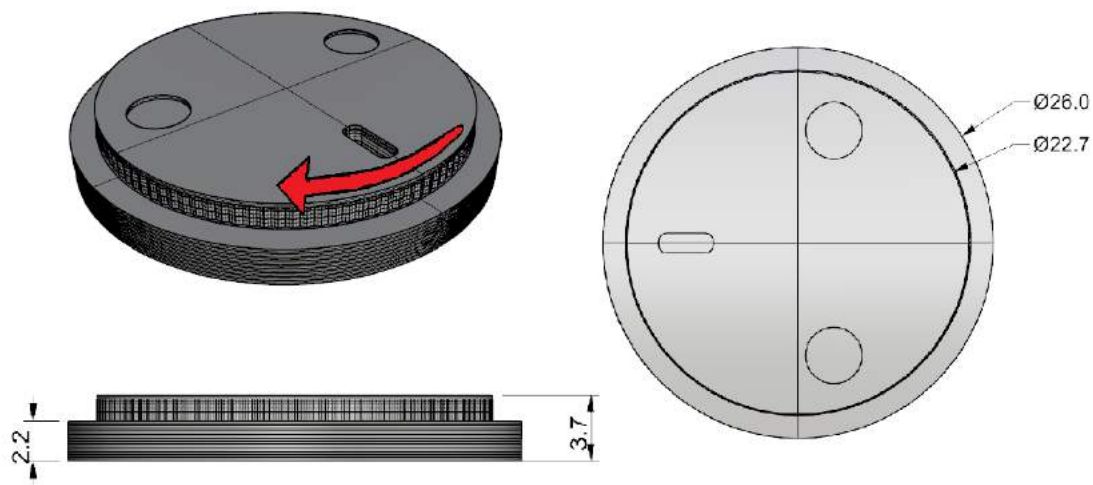


Figure 10. 360-degree LCTR rotational base, all dimensions shown are in inches.

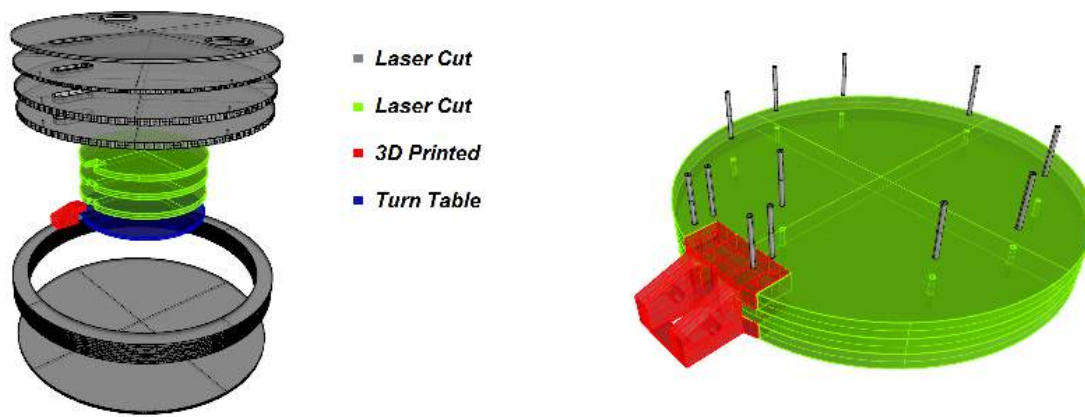


Figure 11. Left, shows exploded view of the laser cut and 3D printed parts. The blue round disk represents the turntable which rotates the model. Color coding is for illustration purposes only and does not represent the final product. Right, shows how the 3D printed parts and acrylic sheets were physically assembled together via 5/32 inch pins.

Once the laser cut and 3D printed parts were ready, the parts were then sent through the same fabrication process as the LCTR2 model: sanding, wet sanding, application of bondo, and painting. Pictures of this process can be seen in Figures 12 through 14.



Figure 12. Left, shows the base being laser cut. Right, shows the assembly process of the laser cut pieces.



Figure 13. Shows the fabrication process: dry wet sanding, application of bondo, priming and painting the acrylic pieces.



Figure 14. Shows the final assembly of fabricated base.

To allow the shepherds crook to pitch the model, two mechanical connection were implemented to connect the base with shepherds crook. The first connection (seen in red) uses a 1/4 in diameter by 2 in pin to pivot the shepherds crook; it is mounted to the base (seen in green) which can be seen in Figure 15.



Figure 15. Mechanical connection (red) between shepherds crook (gray) and base (green).

The second mechanical connection allows the shepherds crook to easily change inclination angle. By pushing down or pulling up on the mechanism, the rod will be fixed / not fixed into position. This design allowed the user to intuitively and quickly change the model angle. Figure 16 shows the design process of 3D modeling, 3D printing and assembly.



Figure 16. Left to right, shows the design process from 3D modeling, 3D printing to physical assembly. This mechanism allows the LCTR2 to be locked at a certain pitch angle.

**XV-15 Design Process for RotCFD Analysis.** Similar to the LCTR2, the XV-15 was digitalized from blueprints into Rhino. With the LCTR2, the model had been previously digitalized by Eduardo Solis; what was left was to modify the existing files, print and fabricate the pieces. For this model, the XV-15 was started from scratch. However, the digitalized XV-15 would not be physically built, it would be used for RotCFD simulations; because the model was used for simulation rather than display, a XV-15 model could be quickly digitalized. To do this, images of the original blueprints needed to be inserted into the Rhino software; once the images were set, the blueprint images needed to be scaled to the actual size of the XV-15. After scaling is complete, A wireframe of the aircraft can be generated by tracing the curves according to the blueprint images. This general shape will allow a network surface to connect the wireframe edges to create the curved surfaces of the aircraft; this can be seen in Figure 17.

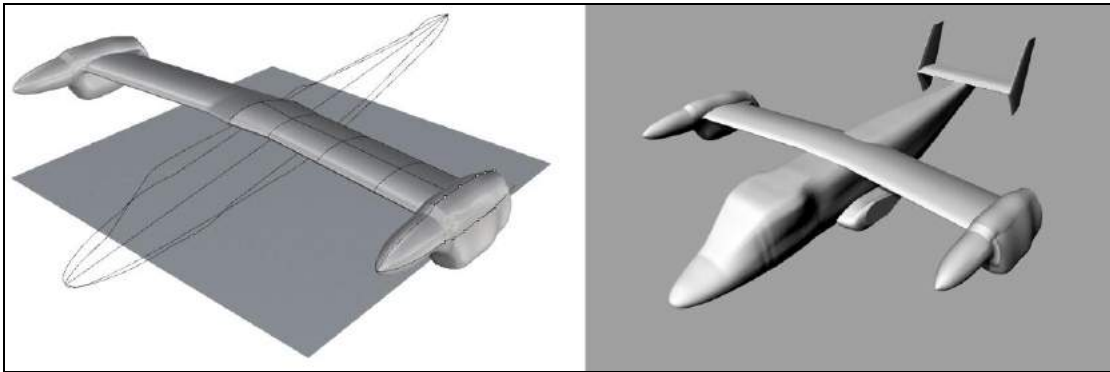


Figure17. Shows how the XV-15 aircraft was digitalized using the Rhino software.

Once the model was complete, the file was converted into an *.stl file* to be analyzed in RotCFD. RotCFD is a program built to simulate rotorcraft / turbines and analyze performance. This program can run with low computational budget, that is, no need for a supercomputer. Figure 18 shows the XV-15 running in the RotCFD simulation software.

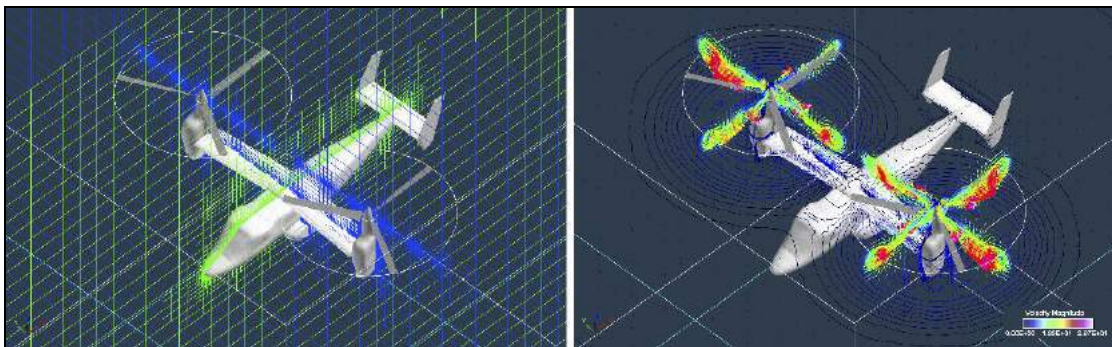


Figure 18. XV-15 model in RotCFD.

### Complications For all Projects

The first complication was getting use to the software Rhino to build the models. Eduardo Solis was very helpful in providing tutorials and additional help when using Rhino. After a few weeks of work, I became familiar with Rhino and was ready for 3D printing the Rhino created parts.

Because printing parts can be very time consuming, we had to manage our 3D print time and stay on it to print all parts before fabrication could take place. Thirdly, because there were multiple people working on the same model, we had to make sure everyone's computer model had the same scaled parts, or else our 3D printed pieces would not fit together. Lastly, because we were given multiple projects to complete, I organized a gantt chart so that group members could have a visual in how much time they have to finish their projects by end date.

## **Conclusions**

A scale model of the LCTR2 aircraft (which rests on a rotational base), RotCFD model of the XV-15, and a 1/6<sup>th</sup> scale 7-Foot by 10-Foot Wind Tunnel model with a second LCTR2 model built to scale down to the 1/6<sup>th</sup> scale wind tunnel were worked on throughout the internship program. These projects will provide the general public with a better understanding of how LCTR2 model was built for testing in the 7-Foot by 10-Foot Wind Tunnel, give a better understanding of how wind tunnels work and benefit aircraft development and improvement. The LCTR2 aircraft was completely modeled, fabricated and assembled showing how this model was built and used in the 7-Foot by 10-Foot Wind Tunnel test section. Second, a RotCFD model of the XV-15 was produced and is currently being used for aerodynamic analysis. Lastly, the 1/6<sup>th</sup> scale wind tunnel has been designed and fabricated, but has yet to be assembled; long term, electronics will be incorporated into the Wind Tunnel model to show how the test section operates when running a test.

## **Acknowledgments**

I would like to thank the Wisconsin Space Grant for funding this project, without them this would not have been possible. Special thanks to my mentors William Warmbrodt and Eduardo Solis for helping me along the way to complete my projects, thanks to Larry Young for helping me as I worked with the MakerBot. Special thanks to the workers at the Space Shop, Alex Mazhari, Randall Ticknor and Bryan Hackett for printing our parts throughout the summer. Lastly, thanks to Kristen Kallstrom for providing me the opportunity to work at NASA Ames Research Center for the summer.

## **References**

- <sup>1</sup> Ref. 1 - pdf, Solis, E., "General Information on 2105 Summer Internship Models", Mountain View, CA.
- <sup>2</sup> Acree, C., "Impact of Technology on Heavy Lift Tiltrotors," Proceedings of the American Helicopter Society 62nd Annual Forum, Phoenix, AZ, May 9-11, 2006.
- <sup>3</sup> Acree, W.C., "Integration of Rotor Aerodynamic Optimization with Conceptual Design of a Large Civil Tilt Rotor", Presented at the American Helicopter Society Specialists' Conference on Aeromechanics, January 20-22, 2010
- <sup>4</sup> History.nasa.gov, 'Chapter 7 On the Eve of Shuttle (1973-1980),' Available: <http://history.nasa.gov/SP-4406/chap7.html>

# Thunderstorm Electrification

Stephanie Bradshaw<sup>1</sup>

Department of Physics and Astronomy  
Carthage College  
Kenosha, WI

## Abstract

Understanding how thunderstorms work is important as it can help assess risks associated with electrical activity in thunderstorms and other phenomena of a somewhat similar nature such as volcanic eruptions, heavy snowstorms, and large hurricanes. We started with a review of the scientific literature in order to grasp the current knowledge and understanding of electrification processes in thunderstorms. We then investigated what types of observations could be made using CAERENet (Carthage Atmospheric Electricity Research and Education Network) electric field mills. We also built mathematical models of electric charge, current, and electric field using Python. A comparison between computer model/simulations and electric field mill observed data would be used to better understand electrification processes in naturally occurring thunderstorms.

## Background

Thunderstorms have been studied in the past in various approaches including balloon experiments. Balloons have been deployed into thunderstorms with an attached payload, which often included tools used to measure various parameters such as electric field. Electric field data suggested the existence of distinct charge regions inside of a thunderstorm due to the positive and negative electric field trends (Stolzenburg 2008). These regions are typically tripole structures. A normal polarity tripole structure has a lower region of positive charge, a middle negative charge region, and an upper positive charge region. Inverted polarity storms have charge regions opposite those in normal polarity storms (Rust 2005). They contain a lower negative charge region, a middle positive charge region, and an upper negative charge region, and the conditions in which inverted polarity storms form are not well-understood.

Both normal and inverted polarity structures are further complicated by screening charges and by variability of meteorological conditions within a thunderstorm. Screening charges typically form around the borders of the thunderstorm as a natural consequence of the conductivity of the atmosphere. Inside of a thunderstorm updraft and non-updraft regions can exist. Updraft regions experience vertical velocities exceeding one meter per second. Non-updraft regions experience downward vertical motion or heavy precipitation. The updraft and non-updraft regions inside of a thunderstorm tend to produce varied charge structures. Figure 1 shows the difference between the charge regions in an updraft versus a non-updraft region as adapted from Stolzenburg (2008). The updraft regions tend to have a normal tripole structure while the non-updraft regions tend to form a more complicated structure with extra charge regions.

<sup>1</sup>Funding provided by the Undergraduate Research Award through the Wisconsin Space Grant Consortium  
Advisor: Dr. Brant Carlson

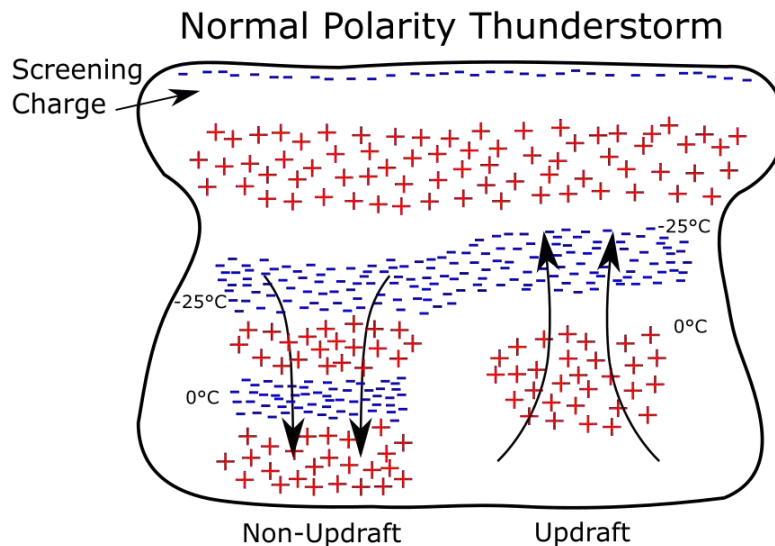


Figure 1: A representation of the positive (red) and negative (blue) charge regions of a thunderstorm with respect to an updraft and non-updraft structure. This model is adapted from Stolzenburg and Marshall's data (2008).

Throughout scientific history, there have been many theories explaining how thunderstorms electrify or how the charges are separated into the observed charge regions. Investigating literature sources revealed the dominance of one theory called the Relative Diffusional Growth Rate Theory (Saunders 2008). The theory involves the collision and separation of ice and graupel particles to form charge regions inside of a thunderstorm. Graupel is considered a soft hail and is formed when super-cooled water droplets rime a snowflake (NOAA 2010). Graupel is also a larger particle than an ice particle.

The Relative Diffusional Growth Rate Theory indicates charge is transferred between particles when they collide (Saunders 2008). The charge transferred depends on the growth rate of the ice and graupel particles. Whichever particle is growing fastest by vapour diffusion at collision will charge positively upon separation. This happens because the particle growing fastest at collision loses mass, while the particle growing slowest gains mass (Saunders 2008). The mass lost and gained is associated with negative charge because of the way ions diffuse in the particle (Dash 2001). Therefore, a neutrally charged particle that loses mass during a collision will become positively charged because there are less negative charges than positive charges. After charging, the particles move (by gravity and convection) to form regions of charge. Since graupel is a larger particle, it is more likely to fall down with gravity while the ice particle is more likely to move upwards with convection in a thunderstorm. Figure 2 shows a collision between a graupel and an ice particle and the resulting charge. Figure 3 shows how the Relative Diffusional Growth Rate Theory could work within a normal polarity tripole structure thunderstorm.

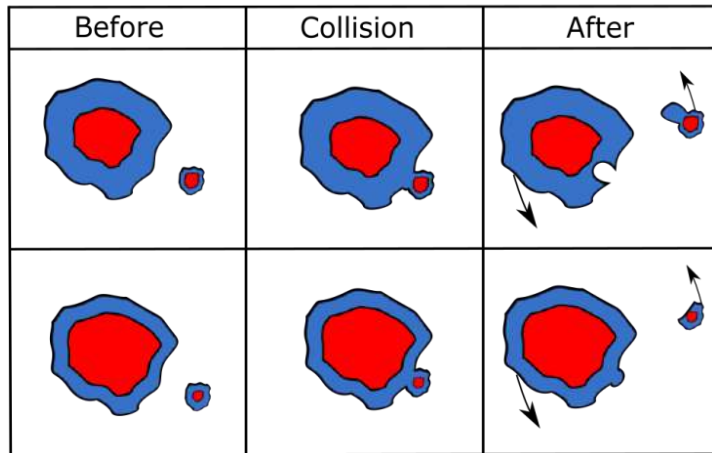


Figure 2: A depiction of the Relative Diffusional Growth Rate Theory as a graupel particle (large particle) collides with an ice particle (small particle). The particles have an inner positive charge region (red) and outer negative charge region (blue) due to the way ions within particles (Dash 2001). The amount of color in each particle is not drawn to scale. Each particle starts out neutrally charged in the before section. The top row represents the graupel particle as growing faster than the ice particle. The bottom row represents the ice particle growing faster than the graupel particle. The up and down arrows indicate the direction of particle motion with gravity and convection.

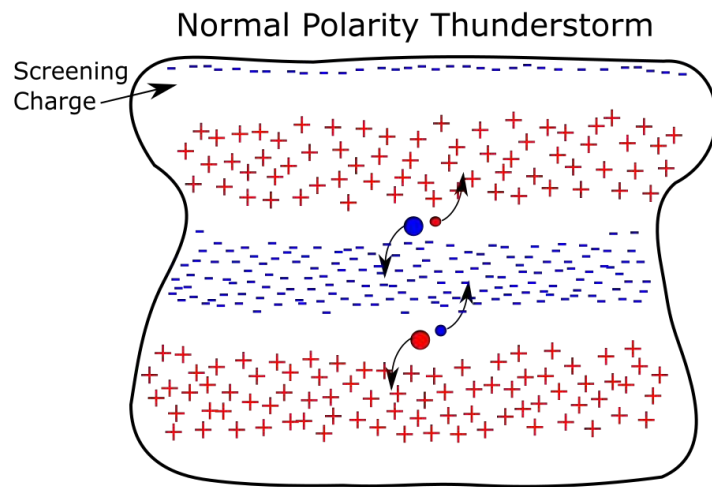


Figure 3: A representation of the Relative Diffusional Growth Rate Theory in a normal polarity thunderstorm. Red represents positive and blue represents negative charge values. Graupel particles are the larger circles while the smaller circles represent ice particles. The particles move upwards and downwards with gravity and convection.

The Relative Diffusional Growth Rate Theory has primarily been studied in laboratory settings such as in a cloud chamber (Saunders 2008). Cloud chambers have allowed scientists to study thunderstorms in a controlled, easily accessible environment. The problem with cloud chamber experiments is the conditions inside a thunderstorm tend to be difficult to attain in a cloud chamber, so extrapolating from cloud chamber results to thunderstorm conditions is difficult.

## Methods

Knowing what was found about thunderstorms from the literature, it is clear there are areas within thunderstorm electrification that are not well understood or observed. The Relative Growth Rate Theory has evidence supporting it within cloud chambers but few observations have been performed in a natural thunderstorm environment. We hope to use CAERENet electric field mills (an instrument which measures the electric field from the ground) to study the electrification processes in a natural environment by determining charge geometry and dynamics. In order to understand what kind of insight an electric field mill could lend to studying electrification processes, one needs to understand how to interpret electric field mill data to infer the charge geometry and dynamics of thunderstorms. Models were created using Python for the purpose of understanding how to interpret the electric field mill data.

The models utilized various mathematical methods including the Method of Images, the Poisson Equation, and the Steady State Charge Conservation Equations. The Poisson equation is  $\nabla^2 \varphi + \frac{\rho}{\epsilon_0} = 0$  where  $\varphi$  is the electric potential and  $\rho$  is the charge density. The Steady State Charge Conservation Equations are  $\nabla \cdot \mathbf{j} + \frac{\partial \rho}{\partial t} = 0$  and  $\nabla \cdot (\sigma \mathbf{E} + \mathbf{j}_{src}) = 0$  where  $\mathbf{j}$  is the current,  $\rho$  is the charge density,  $\mathbf{j}_{src}$  is the current at the source,  $\mathbf{E}$  is the electric field, and  $\sigma$  is the conductivity. The Steady State Charge Conservation Equations can also be represented by the equation  $\nabla \sigma \cdot \nabla \varphi + \sigma \nabla^2 \varphi - \nabla \mathbf{j}_{src} = 0$  with the variables being the same as in the first two Steady State Charge Conservation Equations. The equation for the Method of Images is  $E_y = \frac{-2Qh}{4\pi\epsilon_0(a^2+h^2)^{\frac{3}{2}}}$  where  $E_y$  is the electric field,  $Q$  is the charge,  $h$  is the height above the ground, and  $a$  is the distance from the center of the storm to the electric field mill.

To model a thunderstorm, current regions (arrays of current values) and conductivity values were used as input values. Using these current and conductivity values, we used the Steady State Conservation Equation ( $\nabla \sigma \cdot \nabla \varphi + \sigma \nabla^2 \varphi - \nabla \mathbf{j}_{src} = 0$ ) to determine the electric potentials with boundary conditions given by the Method of Images. The electric potentials give the electric fields necessary to reach the steady state and thus gives us an estimate of the charge density and electric fields of a slowly developing storm. The model result of special importance to CAERENet is the electric field at ground level because CAERENet's electric field mills measure the electric field at the ground. Comparisons can be made between the models and the electric field mill data, which aids the interpretation of the latter. Figures 4.1-4.4 show the charge distribution, electric potential, electric field, and electric field at the ground output values when two long regions of current were used as the input.

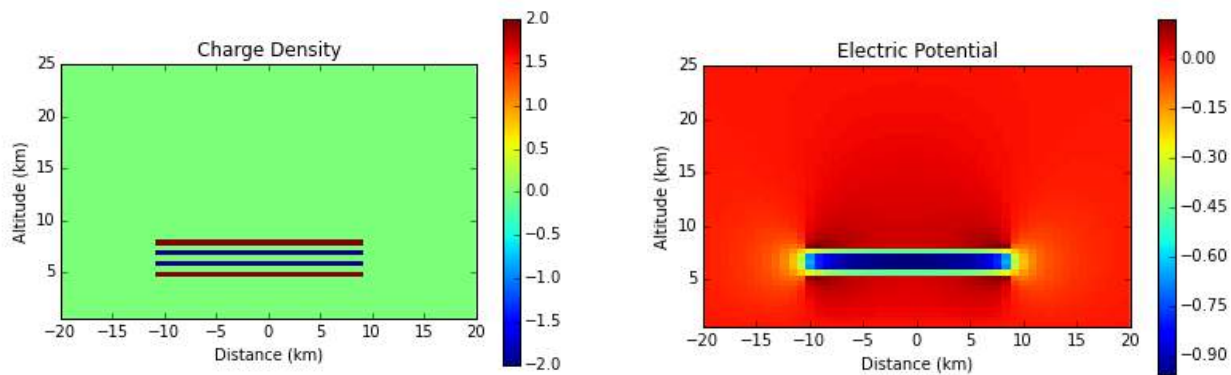


Figure 4.1-4.2: These figures show the charge distribution and the electric potential obtained as an output from the thunderstorm model when two long regions of current were used as inputs. This created a normal polarity tripole thunderstorm structure (positive bottom, overall negative middle, and positive top). The bars on the right of each panel indicate the positive and negative values for the colors in the figures. The actual values listed in the color bar are subject to rescaling.

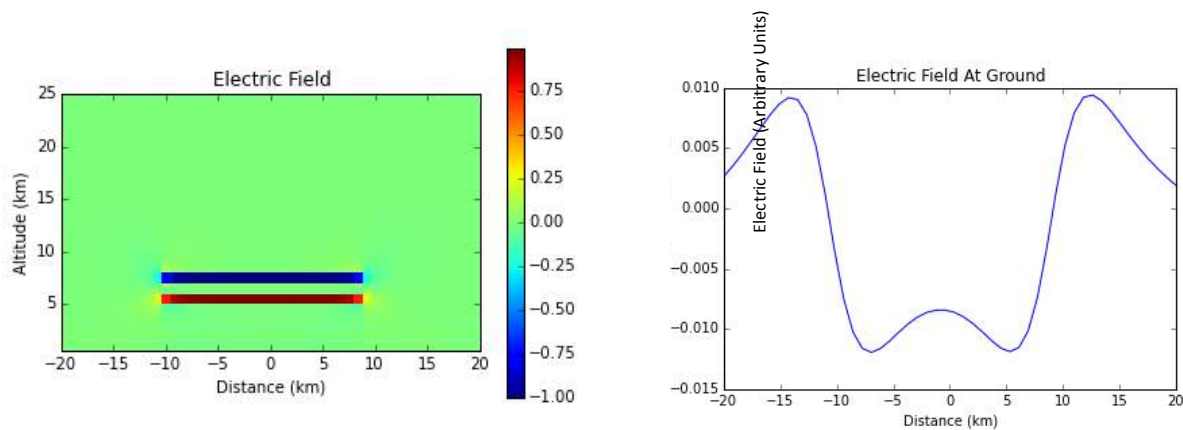


Figure 4.3-4.4: These figures show the electric field and the electric field at the ground obtained as an output from the thunderstorm model when two long regions of current were used as inputs. Figure 4.3 (left) indicates the electric field values throughout the entire model. The colors on the bar indicate the values for electric field, and are subject to rescaling similar to Figures 4.1 and 4.2. The blue values in the figure tend to be negative while the red values tend to be positive. Figure 4.4 (right) represents the electric field data in Figure 4.3 at the ground level. The values for electric field are in arbitrary units because some constant values were simplified in the model to allow the model to run at a reasonable speed.

## Results

The goal of using the thunderstorm models was to be able to better understand the data from CAERENet’s electric field mills. The models were analyzed for trends in the hopes that they would prove insightful when analyzing the electric field mill data. Some trends of interest were the reversal distance, or where the electric field mill data changed from positive to negative (the zero value), and the absolute minimum and maximum magnitude values. The parameters were changed inside of the model to see how these focus areas changed. One way the parameters were changed was by bringing a normal polarity tripole structure closer to the ground (the altitudes of the inputted current regions were changed), and the trends found are shown in Figures 5.1 and 5.2. As the storm structure moved closer to the ground, the reversal distance moved closer to the storm, and the absolute minimum and maximum magnitudes increased

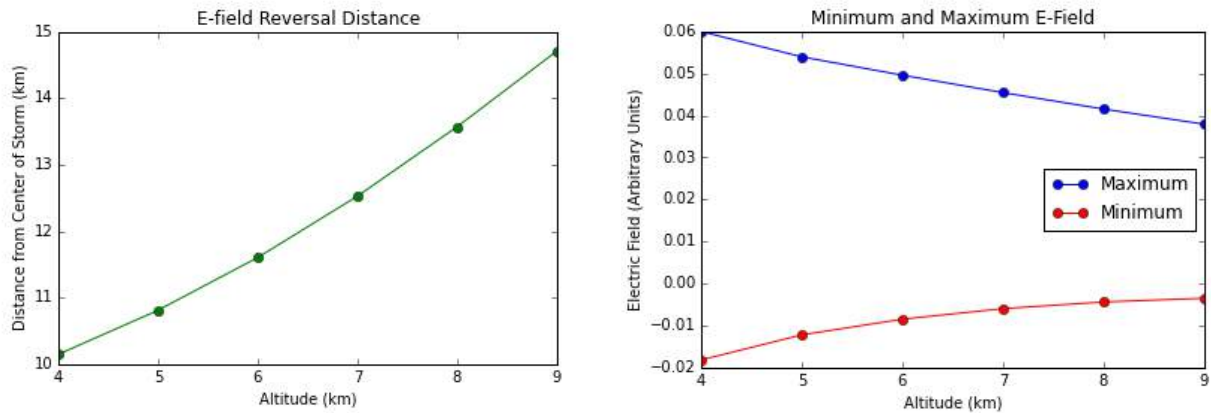


Figure 5-5.1 and 5.2: The trends found when a normal polarity tripole structure was moved closer to the ground are indicated here. The altitudes of the inputted current regions were changed for six simulations, and each simulation's reversal distance is indicated with a data point on each graph. Figure 5.1 (left) shows data for the reversal distance and Figure 5.2 (right) shows the data for the absolute minimum (red) and maximum (blue) magnitude values.

Besides moving a storm structure closer to the ground, the parameters were changed by varying the conductivity in the atmosphere and varying the number of current regions used to give extra regions of charge. The trends found using these parameters were more complicated and are yet to be fully understood. Therefore, they have not been included here. The CAERENet team hopes to collect experimental data with the electric field mills in the near future. The trends found with the Python models will continue to be evaluated in the future and be compared to electric field mill data, when the data is available, to better understand the data and the electrification processes at work inside of a thunderstorm.

### Concluding Remarks

It is evident from this research project, as well as the literature available on the topic of thunderstorms, the electrification processes in thunderstorms are complicated and not yet well understood. Though studied in cloud chambers, there remains little evidence of the Relative Diffusional Growth Rate Theory in nature. In the future, the CAERENet team hopes to continue to evaluate trends from the Python models to understand the electric field mill data, which will hopefully shed light on the geometry and dynamics of charges within thunderstorms and thus help understand the electrification processes. This will hopefully indicate whether or not the Relative Diffusional Growth Rate Theory is playing a role in the electrification processes in naturally occurring thunderstorms.

### References

- Dash J, Mason B, Wettlaufer J, et. al. (2001). *Theory of charge and mass transfer in ice-ice collisions*. Journal of Geophysical Research 106, 20395-20402.
- NOAA (2010). *Glossary:G's*. National Weather Service. Retrieved from [http://www.srh.noaa.gov/jetstream/append/glossary\\_g.htm](http://www.srh.noaa.gov/jetstream/append/glossary_g.htm)
- Rust W., MacGorman D., Bruning E., et. al. (2005). *Inverted-polarity electrical structures in thunderstorms in the Severe Thunderstorm Electrification and Precipitation Study (STEPS)*. Atmospheric Research, 76, 247-271.

Saunders, C. (2008). *Charge Separation Mechanisms in Clouds*. Space Sci Rev 137, 335-353.

Stolzenburg M., Marshall T. (2008). *Charge Structure and Dynamics in Thunderstorms*. Space Sci Rev 137, 355-372.

**Fire in Orbit:  
Equipping the Commercial Spaceflight Industry for Fighting Fire in Micro-Gravity**  
(Revised and amended September, 2015)

Trent Cybela<sup>1</sup>

Orbital Technologies Corporation, Madison WI  
University of Wisconsin – Platteville, Platteville WI

**List of Terms**

CCiCap	Commercial Crew Integrated Capability
ECLSS	Environmental Control and Life Support System
EVA	Extra-Vehicular Activity
FWM	Fine Water Mist
ISS	International Space Station
LEO	Low Earth Orbit
PFE	Portable Fire Extinguisher
UHPFE	Ultra High Pressure Fire Extinguisher
USOS	United States Orbital Segment

**Abstract**

For several years, Orbital Technologies (ORBITEC) has had keen interest in the development of a portable fire suppression system intended for use in commercial spaceflight applications. With the aid of recent developments in fine water mist (FWM) atomization technologies, and partnerships with the University of Wisconsin – Platteville, a portable fire extinguisher (PFE) prototype has been developed and constructed. The commercial extinguisher is capable of operation in both gravity and microgravity environments regardless of orientation, and eliminates the use of toxic carbon dioxide as a fluid suppressant. Preliminary testing of the PFE prototype has demonstrated promising discharge ranges and rates at various pressures. Testing has also confirmed the prototype's ability to extinguish stored energy fires, in the form of lithium ion batteries.

**Introduction**

In the design of new space habitats and vehicles, considerations for the prevention and suppression of fires must be made. As far back as the Mercury and Gemini missions, astronauts had at their disposal various methods by which to extinguish fires (Friedman, 1999). PFE technology used today onboard the ISS is outdated, expensive, and not conducive for investment by the commercial spaceflight industry. Advances in fire suppression technology can be applied to new PFE systems which are effective at eliminating many common microgravity fire threats while being cost effective, lightweight, and portable. ORBITEC stands at a position currently to leverage industry experience towards creating a new PFE system for microgravity environments. In order to move forward, a strong foundation must be established in the history, causes, and current methods used to extinguish fires in space. A first-level prototype was completed in December of 2014.

---

<sup>1</sup> Special thanks to the Wisconsin Space Grant Consortium (WSGC) who provided the necessary funding for student involvement in this project.

## Fire Science Overview

There are three elements required for a combustion reaction to take place: a fuel source, oxidizer, and heat energy. Removal of just one of these three elements will cause a fire to collapse. Most portable fire suppression systems focus on the removal of the oxidizer or heat energy from the combustion system. This is done because removing the fuel source after the advent of a fire is typically not practical. The three components required for combustion are the same both on earth and in space. The behavior of fire in microgravity however, is different compared to earth.

The “teardrop” shape of a candle flame does not occur in orbit. On Earth, the flame’s shape is defined by the effects of gravity: the buoyancy of hot gases and movement of convection currents. Without gravity fire takes a much more spherical shape, as shown in Figure 1. There is no natural convection in microgravity. In the absence of an upward direction for a fire to burn, it burns in all directions. Typically microgravity fires burn slower as well; mainly because flames tend to be weaker without the aid of convection currents. New oxygen is not “swept” into the fire but needs to diffuse into the combustion area, which takes more time to accomplish (Friedman, 1999). Fires in space:

1. Burn at slower rates
2. Burn at lower temperatures, requiring less heat energy
3. Burn at lower oxygen levels, using 2-3% less oxygen compared to earth.



Figure 1: N-Heptane burning in micro-gravity, Credit: NASA.

These factors mentioned, fire in space can be both harder to detect and more persistent. Although we had previously mentioned the absence of natural convection in microgravity, there are other methods of airflow which occur in these environments. Human spaceflight requires ventilation systems to circulate and filter the enclosed atmosphere. These systems can be very effective at moving large volumes of gas and vapors over short periods of time. The ISS — having a pressurized internal volume of 388 cubic meters — could easily circulate smoke and harmful gases through the entire station in less than a half hour period (McKinnie, 1997). Additionally, airflow from the ventilation system has the ability to stoke potential fires, or give direction and speed to fires that already have started to burn.

## Historical Overview

Over the course of 30 years from 1967 to 1997 there have been a least seven recorded incidents of fire onboard spacecraft and space stations (Barr, 2010; Sanchez, 2000). Figure 2 gives a

timeline of incidents along with the specific craft involved (red crosses denote loss of life or life threatening situation). Aside from the Apollo 1 fire in 1967 all incidents occurred during actual flight. The frequency of these incidents together with other risk assessment analysis led NASA to predict that over the lifespan of the ISS a minimum of two fires would occur on the station (McKinnie, 1997). With the operating life of the station now expected to extend past 2024, it is likely the probability of fire will increase as the station ages.

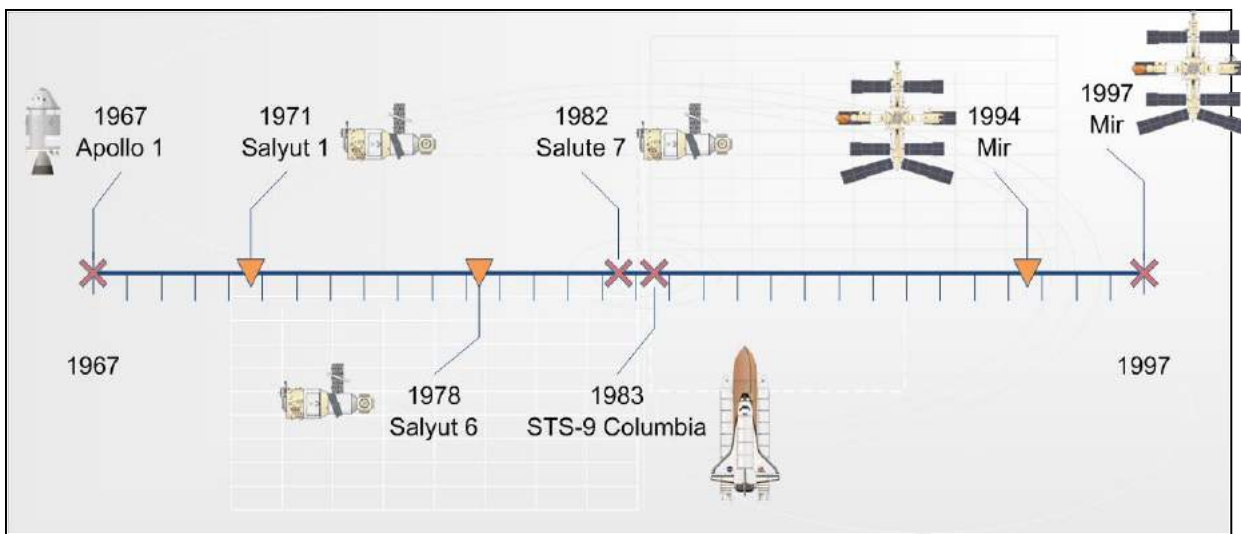


Figure 2: Timeline of fire occurrences. Red crosses denote life threatening situations.

The most serious of the orbital fires occurred on space station Mir. The station caught fire twice both in 1994 and 1997. The '97 event was the most serious, where a failure in one of two oxygen generation systems onboard caused a fire which burned for 15 minutes before finally self-extinguishing (Figure 3). The crew was not able to suppress the reaction because the foaming-agents used in the station's PFEs were designed to blanket and suffocate fire. Because the system which had caught fire was designed to generate oxygen, blanketing the fire to eliminate oxygen was ineffective. The system created oxygen by burning what is commonly called "oxygen candles". Similar candles to those onboard the station are commonly used throughout the commercial airline industry to generate emergency oxygen for passengers.



Figure 3: Fire-damaged panel onboard Mir, Credit: NASA.

### **Fire Modes in Microgravity**

Fire is taken very seriously onboard the ISS. The USOS alone houses thirteen fire extinguishers, and many studies have been done to determine the most likely causes of fire. Besides oxygen candles, various spaceflight applications (including astronaut EVAs) require elevated oxygen as part of the ambient atmosphere, which heightens the risk of fire. There is also growing concern regarding the amount of lithium-ion (Li-ion) batteries currently being used on the ISS in laptops and other electronics. Looking forward it is likely that commercial spaceflight will continue to rely heavily on these batteries. Precedence can be set by the 2013 Boeing 777 electrical fires, which were caused in part from newly integrated lithium-ion batteries. These batteries can also burn in the absence of atmospheric oxygen as well. This property eliminates one possible mode of defense against spacecraft fires, which would include depressurizing the cabin to remove the oxygen.

Liquid chemical fires are possible as well, although less likely to occur in habitable segments of a spacecraft. Hydrazine is a common fuel source for both power and propulsion in the space industry. A hydrazine leak from several of space shuttle Columbia's auxiliary power units caused a fire which could have crippled the craft's hydraulic systems needed for re-entry (Barr, 2010).

Historically through to the present, electrical fires have always been a great concern when regarding human spaceflight. Due to the size and volume constraints placed on Earth-launched vehicles, electrical wiring is typically packed as tight as possible inside a spacecraft. These wires are many times hidden away behind panels where it would be very difficult to visually identify the source of any smoldering or combustion taking place in the wire bundles. It is important to note that reaching the necessary heats for combustion is much easier in microgravity. Overheated motors, bearings, wires and other components will remain hot longer due to a lack of convective heat transfer in microgravity (Friedman, 1999).

## Current Systems

The US orbital segment's PFE represents the most modern system currently available for space (Wieland, 1999). It is a compressed CO<sub>2</sub> extinguisher, designed to be discharged completely in the event of a fire over a 60 second period. A diagram of the PFE can be seen in Figure 4. It carries 6 lbs (2.7 kg) of CO<sub>2</sub> with a net weight of 12 lbs (5.35 kg). The discharge pressure is around 850 psi (8.56 MPa). The design intent behind this device was the elimination of fires which cannot be directly observed, occurring behind electrical panels or inside experiment racks onboard the ISS. In many ways it is a brute force tool, meant to indiscriminately fill a large volume quickly and remove breathable air from the combustion reaction. For this reason it is also required for astronauts to use portable breathing equipment while operating the PFE, else they may be injured by the large concentrations of CO<sub>2</sub>. During operation, rapid expansion of the enclosed gas will cause the tank surface temperature to drop as low as -37 degrees C. Once the fire is extinguished the additional carbon dioxide is scrubbed by environmental controls, and excess pressure is vented from the cabin to space.

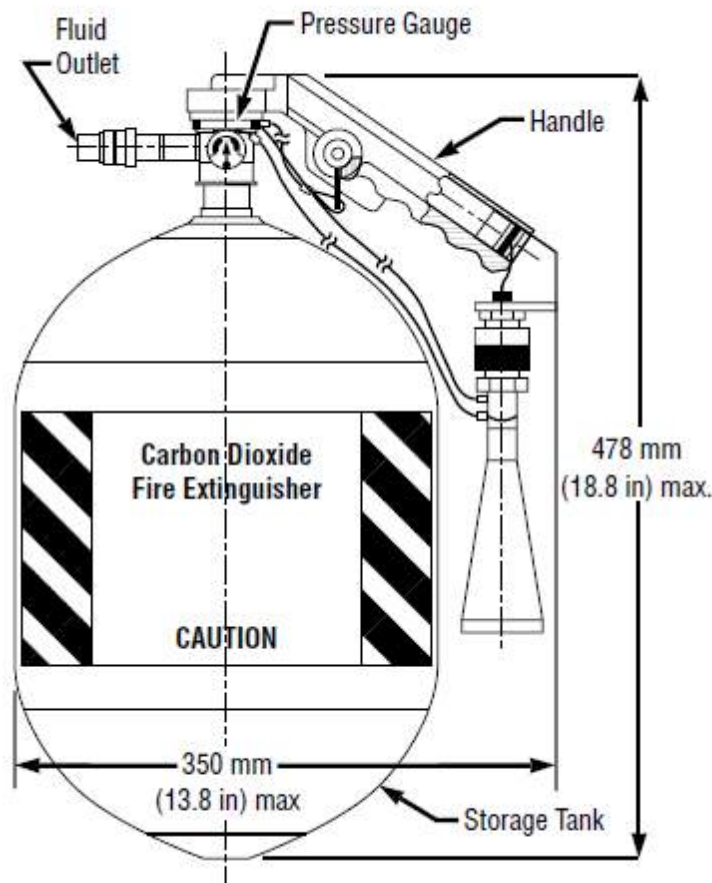


Figure 4: USOS PFE Diagram, Credit: NASA.

Analyses of the present options for space-application fire extinguishers lead us to conclude they are not acceptable for commercial spaceflight. For instance, they are far too expensive. The sales price for just one USOS unit is approximately one million dollars. They are also heavy, cannot be easily operated single-handed, and take up a large volume of usable storage space. A PFE

suitable for commercial spaceflight needs to be highly mobile, effective at removing most if not all of the fire hazards previously discussed, and cost effective. This is why ORBITEC will develop a more acceptable alternative for spaceflight applications. Doing so will require several important decisions to be made regarding the function of the device. Mainly, the type of fluid used as a fire suppressant will need to be determined.

The use of gas as a suppressing fluid is a good choice for microgravity environments because of its ability to fill three-dimensional space. Liquid suppressants travelling through free space tend to “ball up” due to surface tension effects and “wander around” instead of canvassing the combustion event (Butz, Carriere, Abbud-Madrid, & Easton, 2011) (Butz, Carriere, Abbud-Madrid, & Easton, 2011). Liquids however do have other properties which could apply very well to microgravity applications, provided the delivery mode is effective at concentrating the fluid to where the fire actually occurs.

### New Technologies

Over the past decade studies have been conducted on the effectiveness of water-based fire suppression systems for microgravity. Studies led by researchers at the Colorado School of Mines used atomized water droplets to fight microgravity fires (Angel & McKinnon, 2003). The findings from these studies have been subsequently applied to the development of delivery methods for these highly atomized droplets referred to as FWM (fine water mist) systems (Butz & Abbud-Madrid, 2010). FWM allows liquid to behave in open areas like gases, operating three-dimensionally and creating a dense fog rather than a continuous stream of fluid. This gas-like behavior is enhanced by the microgravity environment of a spacecraft.

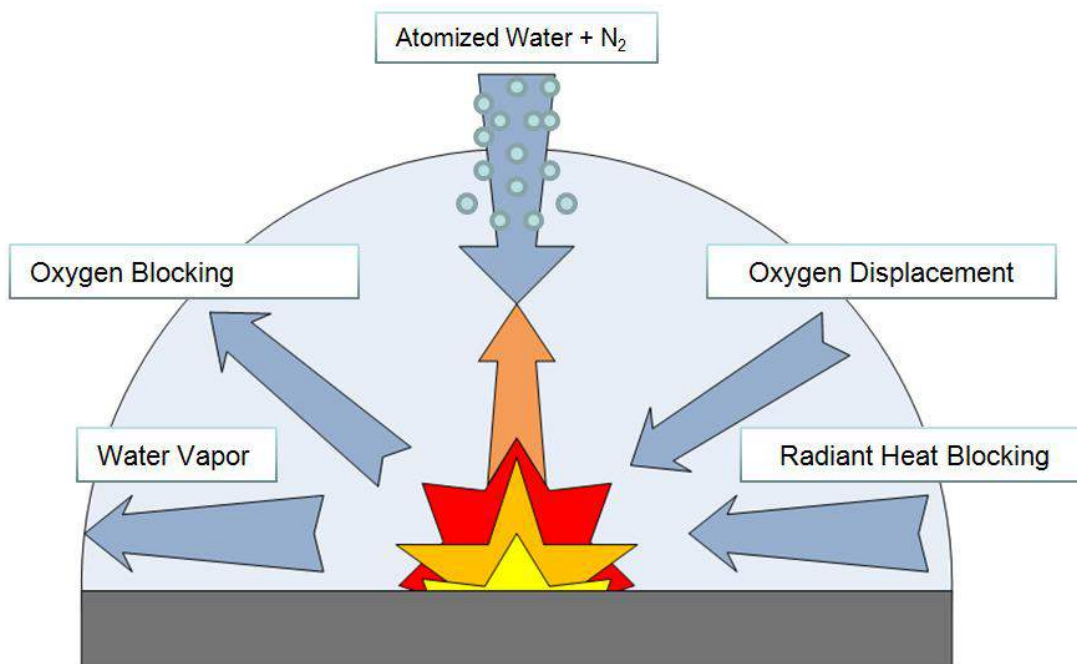


Figure 5: Diagram of PFE spray/combustion interaction.

Water has a very large latent heat capacity; meaning its ability to absorb heat energy is substantial. By delivering water to the fire as micron-sized droplets the liquid can readily absorb

conducted and radiated heat, rapidly decreasing the thermal energy in the system below what is necessary for sustained combustion. As the water droplets begin to vaporize, the resulting steam displaces ambient oxygen to quicken the extinguishing process (Figure 5). The FWM valve assembly works to atomize the water droplets by mixing a continuous water stream with nitrogen (an inert gas) prior to expulsion from the nozzle (Figure 6). Under ultra-high pressure (UHP), the nitrogen and water mix effervescently and travel in tandem towards the fire. By using compressed nitrogen as part of the PFE system, the mean diameter of the water droplets is reduced to sizes otherwise unobtainable using only mechanical fluid separation (Butz & Abbud-Madrid, 2010). The use of nitrogen also works to further reduce the amount of available oxygen in the combustion area. Research done onboard space shuttle Columbia in 2003 showed that water droplets between 20 and 50 microns in diameter were most effective at absorbing the heat energy of fire (when produced by hydrocarbon droplets). This level of atomization is possible with the FWM system.

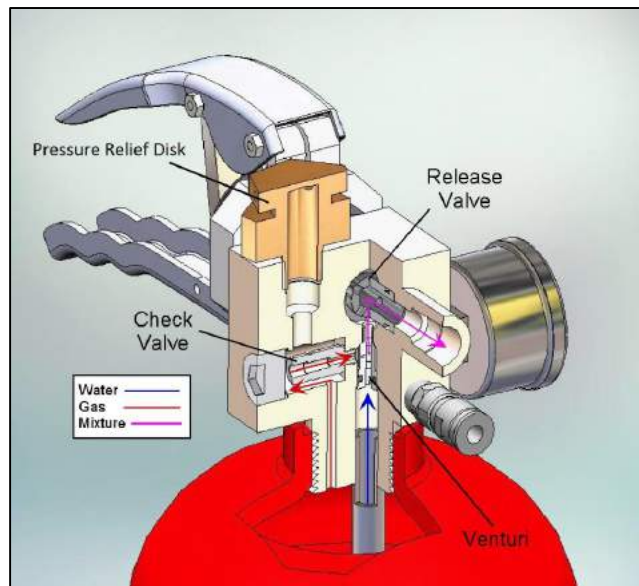


Figure 6: FWM PFE fluid flow path, Credit: ADA Technologies.

Because operation of the PFE will require the storage and pressurization of both nitrogen and water, a novel two-phase fluid management system was developed for use with the FWM nozzle assembly. Leading design alternatives involved the use of an elastic bladder housed in the PFE's tank. The water-filled bladder would be kept under pressure by compressed nitrogen which fills the remainder of the tank's volume. The tank and bladder assembly needs to withstand pressures in excess of 1000 psi for nominal atomization to take place.

Other fluid storage methods were also explored. Another design would include taking advantage of the unique physics of micro-gravity and capillary-actions to deliver the fluids into the FWM assembly. This method would work without needing to physically separate the gas and liquid phases inside the tank, but would also make operation of the PFE under normal gravity much more difficult. For reasons including cost, the simpler bladder design was chosen for early prototype development.

## Prototype Testing

The first PFE prototype was completed in early December, 2014; standing 18in tall with a tank diameter of 5.25in. Fully loaded with water and nitrogen, the system has a weight of approximately 12lb (5.3kg). The finished prototype along with a graphical cross section of the interior can be seen in Figure 7.

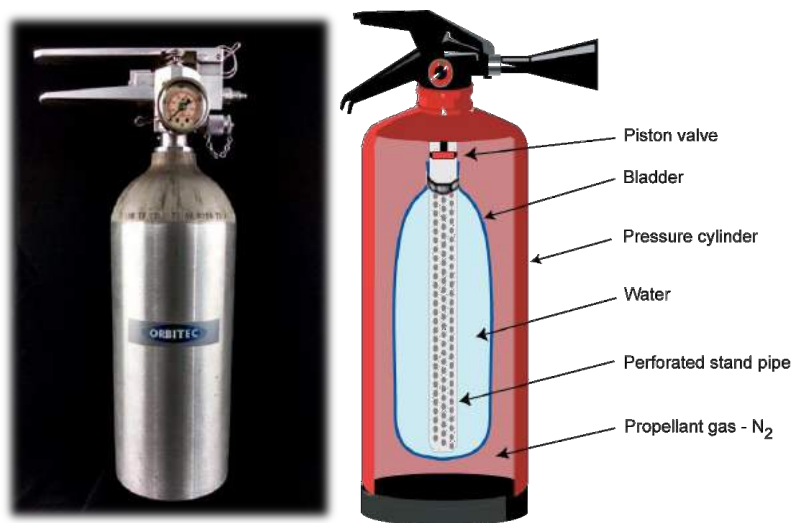


Figure 7:UHPFE Prototype with Cross Section Graphic

Time constraints limited preliminary testing to several simple criteria. Namely the effects of starting pressure and PFE orientation on discharge duration, and the effectiveness of the system against a lithium ion battery fire. All testing was video recorded for future review and evaluation.

The PFE can be held consistently at any orientation using the developed test stand shown in Figure 8. Although simulating microgravity conditions was not possible for this early stage testing, the ability to discharge the PFE in multiple orientations (vertically, inverted, etc.) allowed for the elimination of result bias based on the direction of gravity. Testing showed consistent discharge times regardless of orientation, lasting approximately 10 seconds at maximum pressure. At maximum pressure, the PFE also showed consistent throw distances in excess of 25 feet. With decreasing initial pressure, discharge durations increase as shown in Figure 9. Higher pressures are required for more effective atomization of the suppressing fluids however, and the critical point at which droplet size becomes ineffective has yet to be established.



Figure 8: Discharging UHPFE on test stand

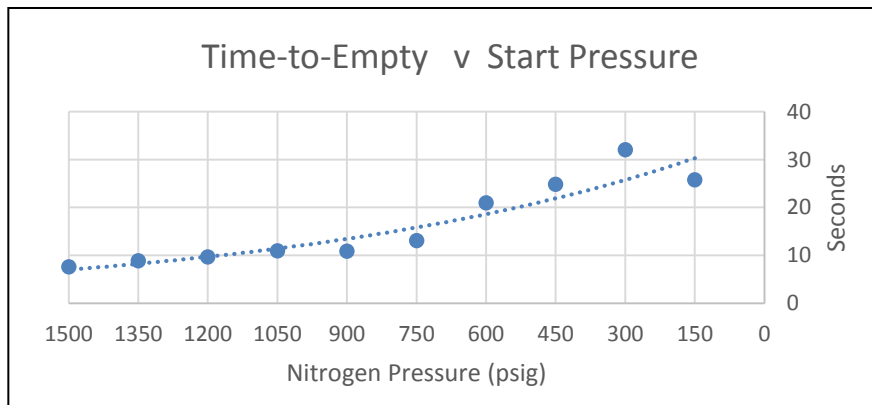


Figure 9: Graph showing relationship between discharge duration and tank pressure

The Canon BP-930 lithium ion battery was chosen for testing the effectiveness of the PFE prototype. This battery was selected because it is known to be currently used onboard the ISS in critical applications, including portable oxygen monitors used in EVA preparation. The batteries were enclosed in a protective cage, and combusted using a hotplate. The applied heat causes degradation of the anode-cathode barriers within the battery, and creates electrical shorts which sustains the production of heat energy. This process is also known as “thermal runaway”. The batteries were allowed to burn with a sustained flame for several seconds prior to PFE discharge, as shown in Figure 10.



Figure 10: Battery fire (left) and UHPFE discharge (right)

In two separate tests, the PFE was able to extinguish the battery fires. In the second battery fire test, a re-ignition of the battery occurred; after which the remaining fluid in the PFE was discharged to successfully extinguish the fire a second time.

### **Conclusion**

The results produced over the course of this design and testing period show great promise for the future applications of the ORBITEC UHPFE. Simple and cost effective, the system is shown in preliminary testing to function appropriately regardless of orientation. More exciting was the prototype's performance against live lithium ion battery fires; against which the PFE functioned as hoped and extinguished both fire events.

Over the coming months, ORBITEC will continue to work with both university partners and the Wisconsin Space Grant Consortium (WSGC) to build, test, and validate ultra-high pressure portable fire extinguishers suitable for commercial spaceflight applications. By building this PFE we will be closer to the creation of a great commercial product, which in turn will help protect the lives of astronauts.

## References

- Angel, A.-M., & McKinnon, J. T. (2003). *Suppression of Premixed Flames by Water Mist in Microgravity: Findings from the MIST Experiment on STS-107*. Golden: Colorado School of Mines.
- Barr, S. (2010). *Evaluating Failures and Near Misses in Human Spaceflight History for Lessons for Future Human Spaceflight*. Houston: The Aerospace Corporation.
- Butz, J. R., Tuchi, C. S., Kimball, A., McKinnon, T., & Riedel, E. P. (2014). *Patent No. 8746357 B2*. United States of America.
- Butz, J., Carriere, T., Abbud-Madrid, A., & Easton, J. (2011). Zero Gravity Aircraft Testing of a Prototype Portable Fire Extinguisher for use in Spacecraft. *International Association for the Advancement of Space Safety*.
- Friedman, R. (1999). *Fire Safety in the Low-Gravity Spacecraft Environment*. Cleveland: NASA Glenn Research Center.
- Hickman, J. M., Dietrich, D. L., Hicks, M. C., Nayagam, V., & Stocker, D. (2012). FLEX: A Decisive Step Forward in NASA's Combustion Research Program. *1st Annual International Space Station Research and Development* (p. 21). Denver: American Astronautical Society.
- Martin, C. E., & Dalee, R. C. (1993). *Spacecraft Fire Detection and Suppression (FDS) Systems: An Overview and Recommendations for Future Flights*. Warrendale, PA: SAE.
- McKinnie, J. M. (1997). *Fire Response Aboard the International Space Station*. Warrendale, PA: SAE.
- Rodriguez, B., & Young, G. (2013). Development of the International Space Station Fine Water Mist Portable Fire Extinguisher. *American Institute of Aeronautics and Astronautics*, 1-8.
- Sanchez, M. J. (2000). *A Human Factors Evaluations of a Methodology for Pressurized Crew Module Acceptability for Zero-Gravity Ingress of Spacecraft*. Houston: NASA Johnson Space Center.
- Smith, R. L., & Kashiwagi, T. (1989). *Expert Systems Applied to Spacecraft Fire Safety*. Gaithersburg: National Institute of Standards and Technology.
- UCSD Jacobs. (2012, January 31). *How Do You Fight Fire in Space? Experiments Provide Some Answers*. Retrieved June 30, 2014, from UCSD Jacobs School of Engineering: [http://www.jacobsschool.ucsd.edu/news/news\\_releases/release.sfe?id=1156](http://www.jacobsschool.ucsd.edu/news/news_releases/release.sfe?id=1156)
- Wieland, P. O. (1999). *Living Together in Space: The Design and Operation of the Life Support Systems on the International Space Station*. Huntsville: NASA Marshall Space Flight Center.
- Youngblood, W. W., & Vedha-Nayagam, M. (1989). *Advanced Spacecraft Fire Safety: Proposed Projects and Program Plan*. Huntsville: Wyle Laboratories.

# Recent Progress in Lunar Helium-3 Extraction Research

Aaron D.S. Olson

Engineering Physics Dept., University of Wisconsin-Madison<sup>1</sup>

## Abstract

Research is ongoing to develop a prototype lunar volatiles extraction system that will demonstrate a process for acquiring helium-3 for future fusion power plants that would produce little to no radioactive waste, and other volatile gases that can be used for life support in space. The prototype system is called the Helium Extraction and Acquisition Test bed (HEAT). Testing of HEAT will focus on obtaining information on the rate of <sup>3</sup>He extraction possible and to what extent thermal energy recovery can be employed in this kind of volatile extraction system. Before demonstrating the evolution of <sup>3</sup>He out of regolith simulant, simulant that is embedded to a known concentration must be available in order to gauge the performance of HEAT. An implantation device is being developed to implant helium into batches of JSC-1A regolith simulant for HEAT. The implantation device under development is referred to as the Solar Wind Implanter (SWIM).

## Introduction and Background

In 1986, researchers at the University of Wisconsin-Madison (UW-Madison) made the connection that helium-3 (a light isotope of helium) embedded in the lunar soil from the solar wind could be used to fuel nuclear fusion reactors that produce power without any radioactive waste (Wittenberg et al. 1986). Since then, research on the physics of producing power from two different helium-3 (<sup>3</sup>He) fusion reactions has taken place along with research on the technology required to extract and collect <sup>3</sup>He from the loosely bound lunar top soil (or regolith) at the UW-Madison Fusion Technology Institute (FTI). The FTI Inertial Electrostatic Confinement (IEC) fusion devices have been used to study the physics of <sup>3</sup>He fusion since the 1990's. Three designs of lunar <sup>3</sup>He miners have also been developed since 1988 at the FTI (Gajda 2006; Sviatoslavsky and Jacobs 1988; Sviatoslavsky 1993). Recently, a research effort on demonstrating the lunar <sup>3</sup>He extraction process outlined in the past miner designs, in a laboratory setting, has commenced (Olson 2013; Olson et al. 2015). The current progress of this effort will be further discussed in the following sections of this paper.

## Research Objectives

The goal of this research is the development and testing of a prototype volatiles extraction system that will demonstrate a process for acquiring embedded <sup>3</sup>He from lunar regolith. This prototype system is referred to as the Helium Extraction and Acquisition Test bed (HEAT) and it is based on the past FTI Mark series miner designs. HEAT is currently being developed to process 157 g/s of JSC-1A lunar regolith simulant, 1/1000<sup>th</sup> of the mass flow rate of the Mark series designs. A conceptual model of the HEAT system is shown in Figure 1. The simulant to be processed will have a 20 ppb concentration of implanted <sup>3</sup>He. HEAT's thermal energy recovery efficiency and its rate of <sup>3</sup>He gas release will be evaluated relative to the Mark designs. Before demonstrating the evolution of helium out of regolith simulant, simulant that is embedded to a known concentration must be available in order to gauge the performance of the extraction system. Beyond the Apollo and Lunakhod lunar soil samples, there is no regolith or regolith

---

<sup>1</sup> The work presented in this paper would not have been possible without the support of the Wisconsin Space Grant Consortium Graduate Fellowship Award and the NASA Space Technology Research Fellowship Program

simulant that has already been implanted with solar wind volatiles that is available for experimental studies. An implantation device is being developed to implant helium into batches of JSC-1A simulant.  $^4\text{He}$  will be used at first and  $^3\text{He}$  may be used after the device's operational performance is completely tested in order to keep costs down. The implantation device is referred to as the Solar Wind Implanter (SWIM).

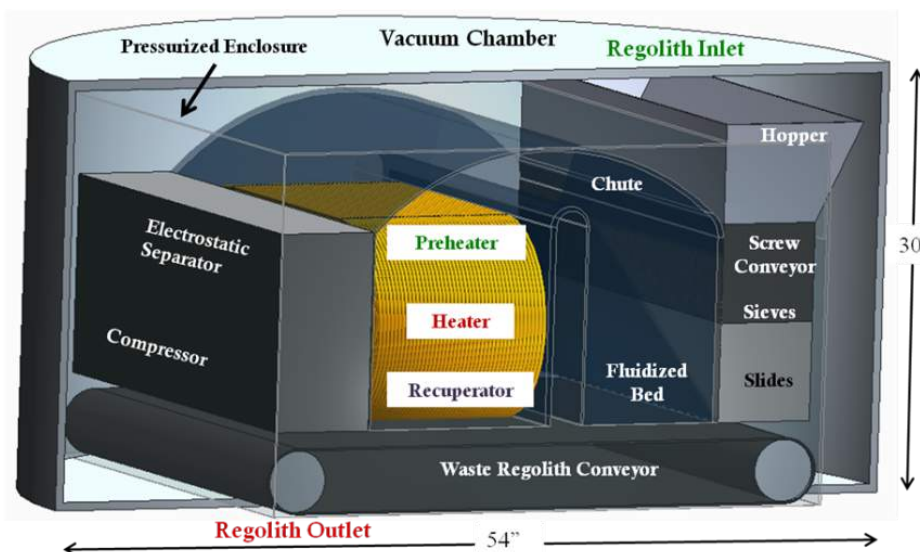
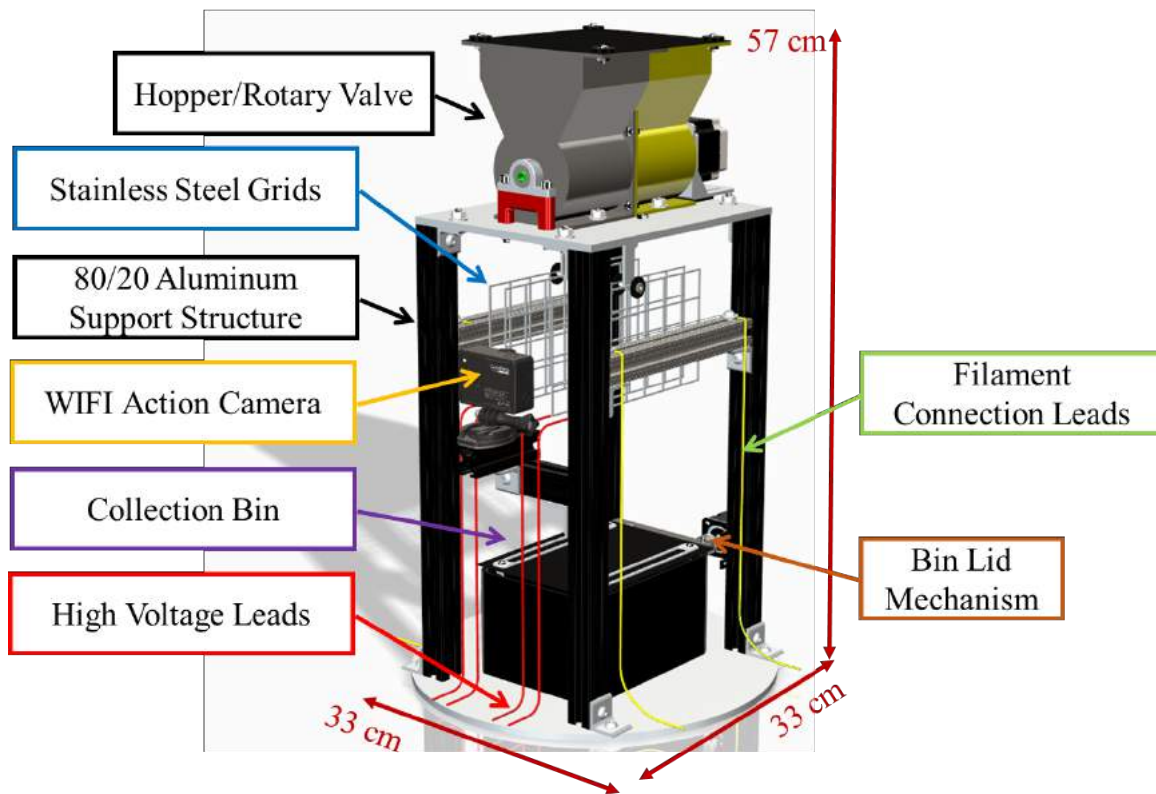


Figure 1. Concept of the HEAT system with a heat pipe heat exchanger shown in gold color

### Solar Wind Implanter Progress

In the past, lunar analog materials such as the minerals Ilmenite and Olivine, have been implanted with helium using Plasma Source Ion Implantation (PSII) at UW-Madison (Kuhlman and Kulcinski 2012). The PSII method worked well enough for small samples of a few grams, but isn't practical for batches of hundreds of grams to a few kilograms of implanted simulant. The SWIM device is being developed to implant helium into batches of 5-100 micron JSC-1A regolith simulant. The concept for SWIM consists of having a controllable downward flow of simulant (coming out of a hopper/feeder device) that passes between planar electrode grids that produce a lateral (perpendicular to the falling simulant) flux of electrostatically accelerated helium ions inside of a vacuum chamber held below  $\sim 100$  mTorr of helium. The voltage potential between the electrodes determines the energy that the helium ions pick up before impacting the falling simulant particles. The solar wind that impacts the lunar surface is traveling between 300 – 900 km/s. To mimic that amount of energy ( $\sim 1-2$  keV/amu), an electrostatic potential of around 4-8 kV is required between a set of parallel electrodes. There are essentially four parts to SWIM: a hopper/feeder system, the system's support structure, the electrodes and tungsten filaments needed to drive helium ions into the simulant and a collection bin for the implanted simulant. These components can be seen in Figure 2. The process of implanting the JSC-1A simulant occurs in four steps. The first step is to fill the hopper/feeder with up to 2 kg of simulant before closing the vacuum chamber. Once a vacuum ( $< 10$  mTorr) is pulled on the vacuum chamber, the system can be backfilled with helium to  $\sim 100$  mTorr. The third step is to turn on the high voltage power supply that provides the 8 kV potential between the anode and cathode grids and to turn on the filament power supply that negatively biases and heats the tungsten filaments. The low pressure helium gas in the SWIM vacuum chamber is

ionized via electron impact ionization, i.e., thermally released electrons from the tungsten filaments kick off electrons from helium atoms to produce helium ions. With the grid and filament power supplies on, a flux of helium ions will be accelerated through the cathode grids. It is currently estimated that with a 16 V potential across each filament will result in a current density through the grids that provides the 20 ppb implantation desired. The fourth step is the controlled release of simulant from the hopper/feeder. A mass flow rate of  $\sim 6$  g/s out of the feeder in a tenuous and thin stream allows for a sufficient dose into the simulant particles. Figure 3 illustrates the operation of the SWIM device and the placement of the grids relative to the stream of falling simulant.



**Figure 2. Components of the SWIM system**

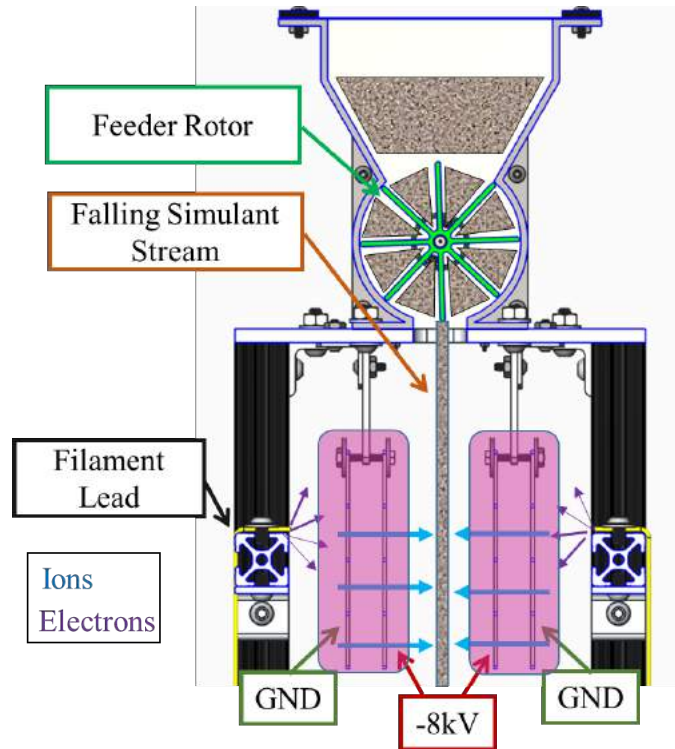


**Figure 3. Operation of the SWIM device. The anode and cathode grids are ~1.6 cm apart. Each grid is ~18 cm by 10 cm by 0.3 cm thick. Each grid is approximately 90% open with 2.5 cm width gap openings.**

As of August of 2015, the first preliminary tests of the SWIM device have been completed. Figure 4 illustrates the operation of the SWIM device from multiple angles and during various operational steps. Simulant was dropped through a helium plasma discharge (where the ions flow), but the plasma current density and electrostatic potential were not adequate for the desired level of implantation in the initial tests. Design alterations/upgrades to the grid geometry are being worked on for future system operation. Furthermore, upgrades to the instrumentation system to measure the plasma current and a more reliable means to capture images and video of the simulant flow through the the plasma are also being developed.

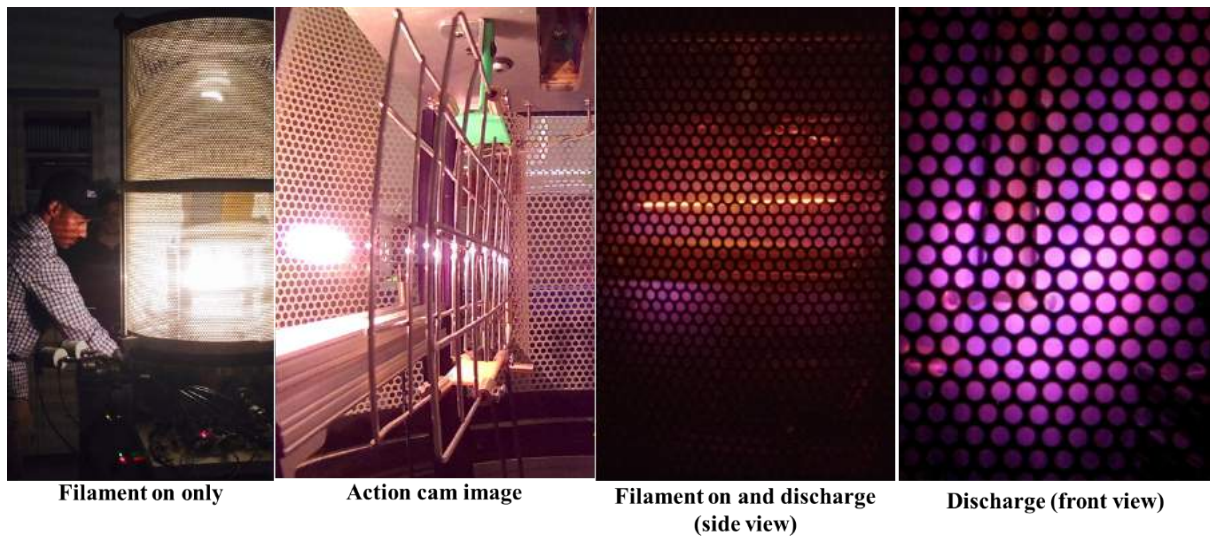


**Figure 4. Constructed SWIM system in various operation modes**

## Helium Extraction and Acquisition Test Bed Progress

HEAT, when fully constructed, will heat simulant up to 700 °C in a moving bed heat pipe heat exchanger (HPHX). At this temperature ~85% of the embedded helium will have diffused out of the simulant. At ~1000 °C, ~100% of the embedded helium should be released, but the risk arises for the release of system damaging sulfur containing gases (Pepin et al. 1970). The use of heat pipes in the heat exchanger allows for the recuperation of thermal energy in the system, i.e., simulant that has already given up its implanted helium will pre-heat incoming volatile rich simulant. In the FTI lunar miner designs, a thermal energy recovery efficiency of 85% was selected. The heat pipes in HEAT are being designed to achieve this level of energy recovery. The previous lunar <sup>3</sup>He miner designs utilize concentrated solar thermal energy to heat the regolith. The HEAT system will use electrical resistance heating in place of solar thermal power. The heat transfer between the heat pipes and resistance heating elements and the regolith simulant within the HEAT device is dependent on the gravity driven velocity field of the simulant flowing through the device. Niegsch developed a model for granular flow through tube banks that takes into account the stagnation and void spaces that are characteristic of granular flow around obstacles. The model estimates a velocity field as well as the heat transfer coefficient between the tubes and the granular material (Niegsch et al. 1994). This model is being used to design the heat pipe arrangement for the HEAT system. Before constructing HEAT, testing of the simulant flow through a representative heat pipe arrangement of copper and stainless steel tubes is being done to validate the Niegsch model results with experimental data. This testing is occurring within a device referred to as the Granular Flow Experiment (GFX). The design of the GFX is illustrated in Figure 5 and a closer view of the pipe matrix is shown in Figure 6 along with the actual hardware. The GFX will be used to find the minimum inter-pipe spacing possible along with obtaining flow field and heat transfer experimental data. Particle image velocimetry (PIV) measurements from the GFX will be compared to the flow results of the Niegsch model and potentially granular CFD simulations as well.

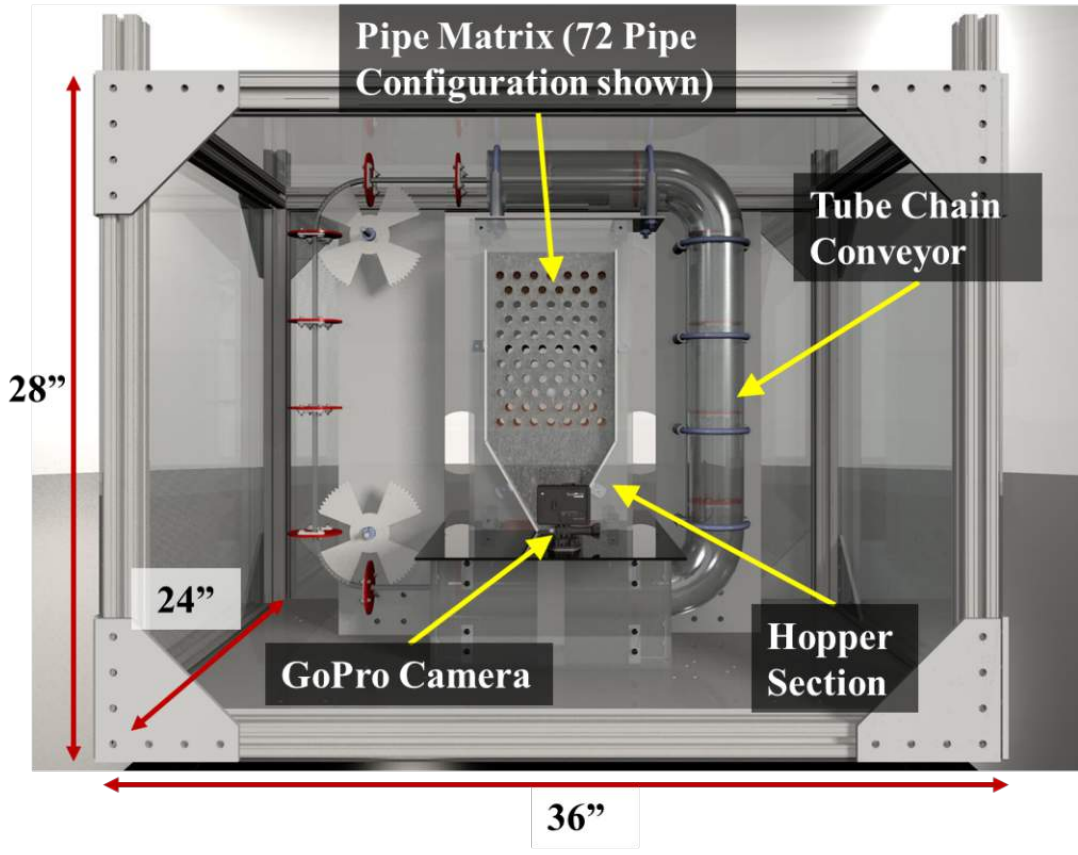


Figure 5. Updated GFX design illustrating the new pipe matrix/hopper design and tube chain conveyor.

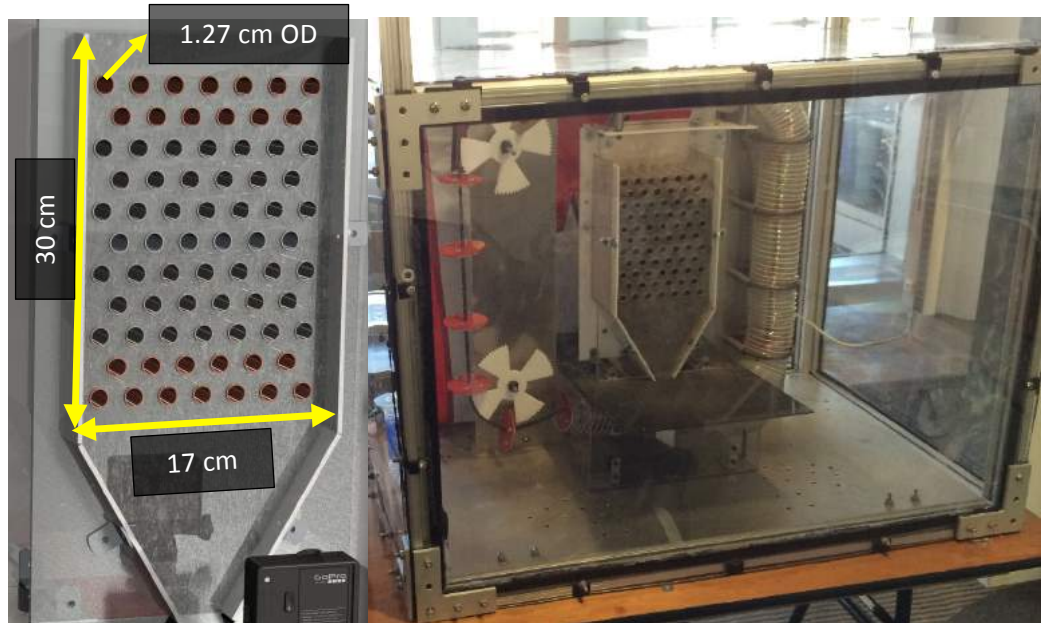


Figure 6. Pipe matrix cross section (left) and partially constructed GFX iteration 2 (right) at the 2015 Engineering Expo

## Conclusion

At the end of this research endeavor, a fully functional HEAT system will be constructed and tested for its continuous release rate of  $^3\text{He}$  and its thermal energy recovery efficiency. The instrumentation system for HEAT will record temperature measurements and trace gas measurements. These measurements will be used to determine the thermal energy efficiency of the HEAT system. If the regolith reaches 700 °C in the center of the HEAT heating system and exits the heating system at 130 °C, then the system will have an 85% thermal energy recovery efficiency. Trace gas concentration will be measured with an RGA. RGA measurements of the atmosphere inside of the HEAT system will give the concentration of helium as a function of time. The release rate of helium will be determined from these measurements. Based on the results of the functioning system, design improvements or alterations that will allow the system to achieve a higher release rate or a higher thermal energy recovery efficiency will be recommended. This will be key for future design work for a pilot scale lunar  $^3\text{He}$  miner. A summary of the HEAT system's goals and the measurement criteria for these goals is shown in Table 1.

**Table 1. Summary of HEAT Goals**

Goal	Evaluation Criteria
$^3\text{He}$ release rate of 17 mg/hr (1/1000 <sup>th</sup> of Mark series designs)	RGA measurements of atmosphere inside of the HEAT system
Achieve 85% thermal energy recovery efficiency	Change in temperature of the regolith simulant throughout the HEAT system as measured by thermocouples
Recommendations to improve the system for a future lunar pilot scale miner	Design alterations to increase the $^3\text{He}$ release rate and the energy recovery efficiency

## References

- Gajda, M. (2006). "A Lunar Volatiles Miner." University of Wisconsin-Madison, M.S. Thesis.
- Kuhlman, K., and Kulcinski, G. L. (2012). "Helium Isotopes in the Lunar Regolith - Measuring Helium Isotope Diffusivity in Lunar Analogs." *Moon: Prospective Energy and Material Resources*, Springer Praxis, 22–56.
- Niegsch, J., Koneke, D., and Weinspach, P. M. (1994). "Heat transfer and flow of bulk solids in a moving bed." *Chemical Engineering and Processing*, 33, 73–89.
- Olson, A. D. S. (2013). "The Mark IV: A Scalable Lunar Miner Prototype." *International Astronautical Congress 2013, Beijing, China, IAC-13.A3.2B.7*.
- Olson, A. D. S., Santarius, J. F., and Kulcinski, G. L. (2015). "Design of a Lunar Solar Wind Volatiles Extraction System." *Proceedings of the Wisconsin Space Conference*, 1(1).
- Pepin, R. O., Nyquist, L. E., Phinney, D., and Black, D. C. (1970). "Rare Gases in Apollo 11 Lunar Material." *Proceedings of the Apollo 11 Lunar Science Conference*, 1435 – 1454.
- Sviatoslavsky, I. N. (1993). "The Challenge of Mining He-3 on the Lunar Surface: How All the Parts Fit Together." *Space 94, The 4th International Conference and Exposition on Engineering, Construction and Operations in Space, and The Conference and Exposition/Demonstration on Robotics for Challenging Environments, February 26 - March 3, 1994, Albuquerque NM Also: WCS*.
- Sviatoslavsky, I. N., and Jacobs, M. K. (1988). "Mobile Helium-3 Mining and Extraction System and Its Benefits Toward Lunar Base Self-Sufficiency." *Wisconsin Center for Space Automation and Robotics Technical Report (WCSAR-TR) AR3-8808-1*.
- Wittenberg, L. J., Santarius, J. F., and Kulcinski, G. L. (1986). "Lunar Source of He-3 for Commercial Fusion Power." *Fusion Technology*, 10, 167.

# 25<sup>th</sup> Annual Wisconsin Space Conference

## PART THREE

### Biosciences and Geosciences

## **Preliminary Assessment of Low-cost Unmanned Aerial Systems (UAS) for Creating Aerial Photographs for Natural Resource Research**

Eric Compas<sup>1</sup>

Department of Geography, Geology, and Environmental Science  
University of Wisconsin-Whitewater  
Whitewater, WI

### **Abstract**

The recent significant reduction in the cost of unmanned aerial systems (UAS) has expanded access to this technology to researchers in a variety of fields. For aerial mapping, UAS holds the promise to substantially increase the resolution of imagery and provide better control over when imagery is produced. In the natural resources, UAS could greatly expand the type of research questions that can be asked at a relatively low cost. This research assessed the utility and characteristics of low-cost UAS aerial photography for natural resource applications. Four craft, commercial fixed-wing and multirotor and handbuilt fixed-wing and multirotor, were tested in this study. Our findings conclude that UAS aerial photography is approximately 10x more detailed than traditional aerial photography, but issues with spatial accuracy and available flight weather may limit its use for some applications.

### **Introduction**

Significant technological improvements in microcontrollers and batteries and lower overall costs have increased the access to unmanned aerial systems (UAS), also known as “drones,” to civilian and research communities (Samant and Datta 2014). Increased energy densities of batteries, particularly lithium-ion based formulas, and the reduced size and broader access to inertial measurement units (IMU) and high-accuracy global positioning system (GPS) units has allowed both commercial and open source communities to produce UAS at much lower cost with increased capabilities. For example, the on-paper capabilities of a \$25,000-40,000 system just a few years ago are currently available for around \$3,000. This reduction in costs substantially increases the general availability of UAS to researchers in a broad set of fields. Furthermore, given the ready availability of UAS components, researchers have the option of constructing their own UAS for as little as \$500.

Potential advantages of UAS-derived aerial photography including producing imagery at a time desired by the research, e.g. release of a tracked animal, to repeat imagery fairly frequently, e.g. track the senescence of vegetation in the fall, and produce high resolution and detailed imagery.

---

<sup>1</sup> The author would like to acknowledge the support of the Wisconsin Space Grant Consortium (WSGC) Research Infrastructure program in conducting this research.

With commercial UAS and consumer-grade cameras, imagery with 1 cm resolution is possible over small areas. In addition, the UAS can be deployed on short notice to capture events such as natural disasters or other unexpected phenomenon. These advantages are significant compared to conventional aerial photography which requires substantial planning and cost and is often captured, at most, once a year in most places.

Given the rapid evolution of available UAS technology, general assessments and limitations of UAS imagery from just a few years ago (e.g. Zongjian 2008) are no longer relevant. Accordingly, the purpose of this research is to ascertain the characteristics and limitation of UAS-derived aerial photography using contemporary, generally available systems. This assessment includes determining the limits of spatial accuracy, image resolution, and aerial coverage along with anecdotal observations on field use of the equipment. We investigated these characteristics for four craft, commercial fixed-wing and multirotor UASes and handbuilt fixed-wing and multirotor UASes, and post-processed our imagery with both commercial and opensource software. For this study, we did not investigate the spectral characteristics of the consumer-grade cameras typically used on low-cost UAS since we were largely interested in true-color, traditional aerial photography for visual analysis (see Hunt et al. 2010 and Rabatel et al. 2012).

## **Background**

UAS technology has seen widespread testing for natural applications, with research in areas such as wildlife research (Jones IV et al. 2006), rangeland monitoring (Laliberte et al. 201), and natural hazard mapping (Hirokawa et al. 2007). In general, these studies have shown that UAS imagery is relatively inexpensive, flexible in its acquisition time, and often of better quality than traditional image sources. Additionally, the technology potentially allows for the posing of novel research questions in many of these areas.

A UAS for aerial mapping comprises multiple, synchronized components to successfully complete a mission. Field components include the airframe with motors and control surfaces, flight controller, a GPS, a redundant radio system, and a camera, along with a ground control station with a computer and RC-style transmitter (for manual flight). The ground control software allows for the generation of pre-planned flight path the craft will follow with significant allowance for both end-to-end and side-to-side overlap of photos. Once launched, the craft is switched into an autonomous mode and flies the preplanned route. Imagery is taken throughout the flight path either at a predetermined interval, e.g. once every three seconds, or a set distance. Fixed-wing aircraft require manual landing while multirotor craft can both launch and land autonomously. The result of the mission is between tens to hundreds of images to be processed.

Post-processing and merging imagery is required in order to generate a usable mosaic of the area of interest. A technique from computer vision, called structure-from-motion (SfM), is used as an

effective tool to simultaneously merge large sets of imagery and create an elevation model of the surface (Westoby et al. 2012). The result of the SfM processes is a single orthorectified image for use in geographic information systems (GIS) and/or remote sensing software packages for further analysis.

Within the USA, Federal Aviation Administration (FAA) rules regarding drones, while permissive, do present some limitations for the use of UAS for research (Rango and Laliberte 2010). Craft are required to fly below 400' above ground level, within visual line of sight, and cannot be used over populated areas and within certain controlled airspaces, e.g. large airports. In addition, some states have imposed additional regulations, largely to protect privacy. For most natural resource applications, these current regulations do not pose significant limitations. The FAA currently has draft regulations for UAS that are likely to change this legal framework substantially in 2016.

## **Methods**

Our methods included the acquisition of both fixed-wing and multirotor commercial UAS, purchasing parts and building two UAS from scratch, conducting field trials of all four units, post-processing imagery from successful flights, and characterizing the image characteristics from each.

We purchased two commercial units: an E384 fixed-wing system from Event38 ([www.event38.com](http://www.event38.com)) for \$2,500 which included two consumer-grade Canon S100 cameras and a SOLO quadcopter from 3D Robotics ([3drobotics.com](http://3drobotics.com)) for \$2,100 which included a GoPro HERO4 Silver for a camera and a stabilizing gimbal. Both units use versions of an open source autopilot project, ArduPilot or APM, as flight controllers. Additionally, the components for APM-based fixed-wing and quadcopter platforms were purchased from a variety of vendors costing \$450 and \$550, respectively, not including camera costs. A separate, mirrorless, higher resolution camera, a Sony a5100 with a fixed 16mm lens, was purchased (\$700) to test on all platforms. Being APM-based, both commercial and hand-built units were compatible with a ground station control software called Mission Planner used in all testing. Autonomous missions, including aerial photography survey grids, were planned and carried out with these UAS combinations. We received formal training on our first purchase, the E384 fixed-wing craft, from Event38 which included the somewhat difficult task of manually landing the plane.

For processing our imagery, we used two different workflows, both utilizing structure-from-motion (SfM) photo stitching software. One path utilized a combination of open source tools including VisualSfM (Wu 2014) and CMPMVS (Jancosek 2012) to create an orthorectified and stitched aerial photograph. The second used a commercial package, Pix4D (\$1,990 for an educational license), to carry out the same workflow.

Three test sites were identified that had sufficient landing space for the fixed-wing craft (an approximately 100m by 30m obstruction-free strip), grassland and forest vegetation, and human structures. At these sites, a series of flights were flown varying the following: with and without differential GPS ground control, with each of the available camera platforms, and at various altitudes (20, 40, 60, and 80m above ground level). After each flight, the resulting imagery (ranging from 150 to 700 separate photographs) was processed with both open source (VisualSFM/CMPMVS) and commercial (Pix4D) packages and the results were compared. At all altitudes we used a ground target to ascertain the practical image resolution of the pre- and post-processed aerial photographs (see Figure 1).

We quantified image quality both qualitatively through visual inspection and quantitatively through the final image cell resolution and through observing a standardize ground target to determine the *ground resolved distance* (Cambell 2002, 275), a standard measure of image spatial resolution. The ground target contains squares from 1 to 7 cm in size rotated at 0°, 22.5°, 45°, and 67.5° (see Figure 1). For quality testing, we used the 3DR Solo and the Sony a5100 camera allowing us to minimize horizontal speed of the camera and maximizing resolution.

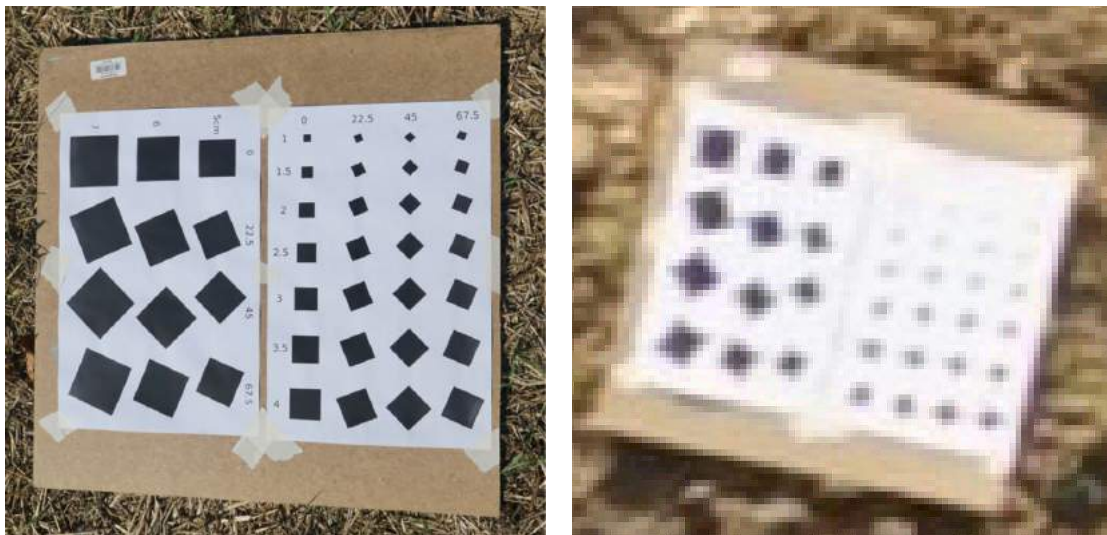


Figure 1. Ground resolved distance target seen from ground (left) and 40 m altitude (right).

The theoretical image cell resolution was calculated using simple trigonometry from the camera sensor size and resolution while the average cell resolution was reported by the Pix4D software (cell resolution varies due to changing elevations and camera angles across the study area). The ground resolved distance was measured by visual inspection of the ground target in unprocessed JPEG images and the final orthorectified image mosaic at each flight altitude. A size was determined to be “resolved” if all squares in a given row were visible. So, for the 40 m altitude image in Figure 1, the ground resolution distance was 2.0 cm.

The spatial accuracy, the correct placement of the image on earth's surface, was calculated through the use of differential GPS. Prior to flying, a set of markers (bright orange soccer cones) were spread within and around the area as ground control points to be imaged and locations determined using a Trimble GeoXH GPS unit. Using ESRI's ArcGIS software, these locations were compared with the visible markers in the Pix4D orthorectified image (which uses the GPS locations at which images are taken) and the distance between these locations measured. In addition, both the Pix4D and VisualSFM images were georeferenced using these ground control points in ArcGIS using an affine, or first order polynomial, transformation. The georeferencing tool provides a measure of how well the resulting image fits the provided ground control points.

Given that our goal was to create aerial photographs for visual interpretation, we did not measure or explore the spectral resolution of the resulting imagery or assess our imagery for traditional remote sensing techniques such as image classification or measurements of vegetation health. Others (e.g. Hunt et al. 201) have noted the poor spectral resolution and overlap between neighboring bands in consumer grade cameras that limit utility for direct physical measurements.

Finally, we collected anecdotal information on the field experiences of our flights and compiled a list of advantages and disadvantages of the platforms we used and the overall process of UAS image acquisition.

## **Results**

We successfully flew and carried out autonomous missions with all four UAS platforms. However, only with the two commercial platforms were we able to consistently carry out aerial mapping missions. With the commercial platforms, we were able to carry out all of our test flights to assess image quality and accuracy with details provided below.

With all our platforms we experienced uncontrolled and anomalous flights which resulted in "crashes" with all platforms. While the commercial units needed minor repairs, e.g. replacing a broken propeller, the handbuilt units required major repairs including replacement components, e.g. complete quadcopter frame. In addition, the uncontrolled flights of the handbuilt platforms raised safety concerns. In one instance, the quadcopter experienced a "fly away" and flew approximately 2,000 m off course, passed a preset "geofence," across a state highway, and crashed after the pilot switched to manual control and turned off the throttle. Given these safety concerns and the potential to damage expensive cameras, we did not complete mapping missions with the handbuilt units within our research timeframe.



Figure 1. Example imagery of same location with 1.6 cm resolution UAS imagery on left and 46 cm resolution 2012 Wisconsin Regional Orthophotography Consortium (WROC) imagery on right (source [WisconsinView](#)).

We were successful in completing missions both with the fixed-wing and multirotor craft. Being fully autonomous, the multirotor proved much simpler to deploy and could be launched from any site requiring only a 1x1 meter space to launch and land. The disadvantage was the mapping area that could be covered. At 80 m altitude, approximately 16 hectares (40 acres) could be mapped per battery. Since the fixed-wing required manual landing, a large landing strip (approx. 30 x 100m) aligned with the current wind direction and with the opportunities for “go arounds” was necessary. At two out of our three sites, the landowner mowed special landing strips for us to us. The advantage of the fixed-wing was a substantial increase the mapping area with up to 120 hectares (300 acres) per flight.

For a subset of our imagery, we post-processed using both the open source VisualSFM and the commercial Pix4D. While both were successful in generating usable image mosaics, there was substantial differences in the processing procedure and the resulting image quality of each. The open source tools were much more likely to crash, could not handle more than 500 images within a set, and even with substantial match points between overlapping images, often left unprocessed holes in the middle of our study areas. Additionally, the open source tools resampled the source imagery resulting in a resolution one-quarter that of Pix4D, e.g. from 1cm to 4cm. Accordingly, we utilized Pix4D for most of our postprocessing work.

Table 1 shows the result of our image resolution measurements using the commercial Pix4D

package. In general, our average cell resolution as reported by Pix4D was close to the theoretical cell resolution across all altitudes. As for ground resolution distances, a general rule of thumb is that objects of twice the cell size are generally visible – a theoretical ground resolution distance. We found that for lower altitudes, this relationship held for unprocessed images. However, this distance increased within the processed (orthorectified and mosaiced) imagery and with higher altitudes. While the process of merging multiple overlapping images is likely to reduce overall resolution, it is unclear why the increase in altitude led to a loss in resolution.

Table 1. Theoretical and observed image resolution and ground resolution distance.

<b>Flight altitude</b>	<b>Theoretical cell resolution (cm)</b>	<b>Pix4D average cell resolution (cm)</b>	<b>Theoretical ground resolution distance (cm)</b>	<b>Observed unprocessed ground resolution distance (cm)</b>	<b>Observed Pix4D orthorectified ground resolution distance (cm)</b>
20m	0.49	0.54	0.98	1.5	1.5
40m	0.98	0.99	1.96	2.0	3.0
60m	1.47	1.53	2.94	3.0	6.0
80m	1.96	2.03	3.92	5.0	6.0

Anecdotally, the resolution provided by the imagery from all altitudes provides substantially more information and detail than is visible (approximately by one order of magnitude, 10x) in traditionally available 1 or 2 m resolution imagery available through programs such as the National Agriculture Imagery Program (NAIP). Individual plants and trees are visible, allowing for detailed distribution and extent metrics to be calculated and compared through time. The 20 m and 40 m imagery provide nearly two orders of magnitude (100x) the resolution of traditional aerial photography.

For spatial accuracy, an image with a significant number of ground control points ( $n=13$ ) was used to demonstrate the spatial accuracy of UAS imagery. The image was taken with the fixed wing aircraft using the Canon s100 camera with built-in GPS at an 80 m altitude. The measured root-mean-squared (RMS) error between the ground control points in the image and differential GPS was 2.25 m ( $n = 13$ ). After an affine transformation was applied using all 13 points, this RMS error was reduced to 0.46 m. Note that the direction of the ground control errors were not consistent. This means the spatial inaccuracy is not systematic and, therefore, errors are the result of shifts in different directions throughout the image. Any attempt to increase accuracy beyond the 0.46 m would require a higher-order transformation, i.e. “rubber sheeting,” with substantially more ground control points. These inaccuracies, particularly in the image without the affined transformation applied, raise concerns about the use of UAS repeat photography to compare patterns and distributions through time. The 2.25 m error is 110 times larger than the average cell resolution for this altitude. Any fine-scale mapping and change detection of vegetation extents or patterns would have to account for such spatial inaccuracies.

Other anecdotal observations from our UAS mapping include suggested field procedures and safety, the vagaries of weather, the limited mapping area, and the challenges of building a UAS from scratch. First of all, safety did not emerge as a significant issue with our UAS field experiences. In general, we followed the Academy of Model Aeronautics' Aircraft Safety Code (AMA 2014) and guidelines for autopilot system (AMA 2013). We also established standard procedures for pre-flight preparations, e.g. charging batteries, and pre-flight checklists, e.g. control surface tests. One site was within 5 miles of a local airfield, and we contacted both commercial operators at the airport well before conducting flights. Additionally, we did have two occasions when a small aircraft entered the area in which we were mapping. On both occasions, while there was a substantial difference in the altitude of our craft and the occupied aircraft, we still quickly shifted to manual override and lowered the plane to nearly ground level. The most significant safety concern we encountered was the safe charging and storage of the lithium phosphate batteries used in small UAS. They can self ignite if damaged in a crash, are overcharged, or are undercharged. Most UAS batteries do not contain the over- and under-charge protection circuitry common on other consumer grade electronics. While encountering no fires, we damaged and retired three batteries during the year-long course of this grant.

Second, while theoretically one could sample a study area at a fixed interval for change detection, e.g. once per week, the weather does not always cooperate. Ideally, all images in a sequence would be taken at a fixed interval, at the same time of day (or same sun angle), and with little to no cloud cover or haze. In addition, the wind during this time frame needs to be 15 mph or less. In reviewing this last summer's weather, we found that only 7 days from May 1 to August 31 that met this criteria.<sup>2</sup>

Third, we found that the area we wanted to map was constrained both by the area that can be mapped on a given set of flight batteries and within the FAA requirement of keeping the aircraft in sight at all times. With the fixed-wing craft, we were able to consistently map around 120 hectares (300 acres) per flight, while with the quadcopter, we could only map 16 hectares (40 acres) per flight. Of our three study sites, none could be mapped in a single flight. All required multiple flights, which dramatically increased time in field and often resulted in setup errors or changing weather conditions. Additionally, some portion of each study area required moving to a new location to enable observation of the craft in that portion of the site and, in one study location, one portion of the site was unreachable due to insufficient observation points.

Finally, we found that building a UAS from scratch meant spending a considerable amount of time on the technology itself, rather than using it for mapping. To build an effective UAS, one needs to understand flight dynamics, propeller and motor options, connection various microcontroller devices and the electronic limitations and requirements of each, and the ability to

---

<sup>2</sup> Based on Madison, WI raw METAR data within this time period.

troubleshoot when the inevitable issue emerges. The cost-effectiveness of scratch building a UAS is mitigated once one has purchased additional parts for fixing mishaps and in calculating the value in one's time in learning the technology and building a unit. Unless a research project required customized UAS functionality, e.g. RFID readers or collision avoidance systems, the off-the-shelf commercial units were much more cost-effective for collecting usable imagery.

## **Conclusions**

Given the goal of producing high resolution and spatially accurate aerial photography from low-cost UAS "drones," this research project was successful in creating photography and measuring its general characteristics. This background research in UAS technology will better allow other researchers to design studies based on UAS technology and assess the utility of UAS technology to address their specific research questions. In general, aerial mapping with UAS allows for at least an order of magnitude (and nearly two) increase in the resolution of aerial photography available for natural resource applications. Given the additional researcher control over when and where imagery is taken, UAS mapping represents a new, potent, low-cost tool for assessing natural resource patterns and changes. Given our experience with both commercial and built-from-scratch UAS, we recommend commercial units for most mapping applications.

The technology, though, has important caveats for adoption by a potential researcher. The technology requires a substantial time commitment to become properly trained and gain an understanding of effective mapping and safety procedures. Additionally, depending on the study region, weather may prove a confounding factor and limit repeat photography for change detection. Finally, the spatial accuracy of imagery is relatively low if not combined with expensive differential GPS equipment.

## **Acknowledgements**

In addition to WSGC, I would like to thank all of the Advanced GIS students, Aaron King and Tyler Tomaszewski in particular, who helped with the building and testing of our UAS program.

## **References**

- Academy of Model Aeronautics (AMA). 2013. *Radio Controlled Model Aircraft Operation Utilizing Failsafe, Stabilization and Autopilot Systems (AMA Document #560)*. Available at <http://www.modelaircraft.org/files/560.pdf> (accessed May 15, 2014).
- Academy of Model Aeronautics (AMA). 2014. *AMA National Model Aircraft Safety Code*. Available at <https://www.modelaircraft.org/files/105.pdf> (accessed May 15, 2014).
- Campbell, J. 2002. *Introduction to Remote Sensing*. 3rd ed. New York, NY: CRC Press. pp. 654.
- Hirokawa, R., Kubo, D., Suzuki, S., Meguro, J., and Suzuki, T. 2007. "A Small UAV for

- Immediate Hazard Map Generation.” In *AIAA Infotech@Aerospace 2007 Conference and Exhibit. American Institute of Aeronautics and Astronautics*. Accessed August 7, 2015. <http://arc.aiaa.org/doi/abs/10.2514/6.2007-2725>.
- Hunt, E.R., Hively, W.D., Fujikawa, S.J., Linden, D.S., Daughtry, C. and McCarty, G.W. 2010. “Acquisition of NIR-Green-Blue Digital Photographs from Unmanned Aircraft for Crop Monitoring.” *Remote Sensing* 2 (1): 290–305.
- Jancosek, M. and Pajdla, T. 2012. Multi-View Reconstruction Preserving Weakly-Supported Surfaces. *IEEE Conference on Computer Vision and Pattern Recognition 2011*. <http://cmp.felk.cvut.cz/~jancom1/JancosekCVPR11.pdf>. Accessed June 5, 2014.
- Jones IV, G.P., Pearlstine, L.G. and Percival, H.F. 2006. “An Assessment of Small Unmanned Aerial Vehicles for Wildlife Research.” *Wildlife Society Bulletin* 34 (3): 750–58.
- Laliberte, A.S., Herrick, J.E., Rango, A. and Winters, C. 2010. “Acquisition, Orthorectification, and Object-Based Classification of Unmanned Aerial Vehicle (UAV) Imagery for Rangeland Monitoring.” *Photogrammetric Engineering & Remote Sensing* 76 (6): 661–72.
- Rabatel, G., Gorretta, N. and Labbe, S. 2012. “Getting Simultaneous Red and near Infrared Bands from a Single Digital Camera for Plant Monitoring Applications.” In . Valencia, Spain. [http://cigr.ageng2012.org/images/fotosg/tabla\\_137\\_C1122.pdf](http://cigr.ageng2012.org/images/fotosg/tabla_137_C1122.pdf).
- Rango, Albert, and Andrea S. Laliberte. 2010. “Impact of Flight Regulations on Effective Use of Unmanned Aircraft Systems for Natural Resources Applications.” *Journal of Applied Remote Sensing* 4 (1): 043539–043539.
- Samant, H., and Datta, A. 2014. “Domesticating the Drones.” *Geospatial World*. 5 (5):34-40.
- Westoby, M. J., J. Brasington, N. F. Glasser, M. J. Hambrey, and J. M. Reynolds. 2012. “‘Structure-from-Motion’ Photogrammetry: A Low-Cost, Effective Tool for Geoscience Applications.” *Geomorphology* 179: 300–314.
- Wu, C. 2014. VisualSFM: A Visual Structure from Motion System. <http://ccwu.me/vsfm> Accessed June 5, 2014.
- Zongjian, L. 2008. “UAV for Mapping—low Altitude Photogrammetric Survey.” *International Archives of Photogrammetry and Remote Sensing*, Beijing, China. [http://www.isprs.org/proceedings/XXXVII/congress/1\\_pdf/202.pdf](http://www.isprs.org/proceedings/XXXVII/congress/1_pdf/202.pdf).

# Riveting Hammer Vibration and Nerve Damage

Jordan J. Zimmerman<sup>1</sup>, Danny A. Riley, James L. W. Bain

Department of Cell Biology & Neuroanatomy; Medical College of Wisconsin, Milwaukee, WI  
Department of Biomedical Engineering; Marquette University, Milwaukee WI

## Abstract

Hand Arm Vibration Syndrome (HAVS) is an occupational disease affecting 50% of riveting hammer operators after 10 years of work.<sup>1</sup> Current international standards (ISO 5349) seeking to protect workers from occupational vibration are not effectively predicting HAVS onset.<sup>1-3</sup> Scarce research has been done which investigates the long term effects of riveting hammer vibration exposure and nerve regeneration. The present study examines the effects of typical occupational vibrational exposure on cutaneous mechanosensory peripheral nerve populations (lanceolates) and as well as nerve bodies (dorsal root ganglion) that are responsible for nerve regeneration. A piezoelectric sensor-based data acquisition system is used rather than the traditional laser vibrometer. Although data analysis is not complete, current results show that the piezoelectric system is a viable means of vibrational analysis for both laboratory and workplace research. It records dominant kilohertz frequencies in the riveting hammer vibration signal which are currently overlooked by ISO 5349.

## 1. Introduction

Hand-Arm Vibration Syndrome (HAVS) is a neurodegenerative and vasospastic disease observed in workers who regularly use handheld percussive power tools. In the United States alone, 1.5 million workers are exposed to hand-transmitted vibration.<sup>4</sup> HAVS symptoms include numbness, blanching, and tingling of the fingers as well as loss of fine motor control.<sup>5</sup> Symptoms may be severe enough to warrant a change in occupation.<sup>6</sup>

Past research has shown that the occurrence of HAVS is directly related to the duration and repetitiveness of vibration exposure.<sup>2</sup> Namely, 50% of workers who use pneumatic riveting hammers develop HAVS after 10 years of work.<sup>1</sup> The International Organization for Standardization (ISO) standard 5349 attempts to estimate the risk associated with the operation of handheld power tools. It employs a frequency weighting calculation that claims frequencies <16 Hz are most harmful, while frequencies >160 Hz can essentially be ignored. In contrast, the riveting hammer (among a multitude of handheld power tools) exhibits dominant vibrational energy in the kHz range.<sup>3</sup> In both theory and reality, ISO 5349 severely underestimates the risk of HAVS onset.<sup>1-3</sup>

The final stages of HAVS are well documented but their onset is not well understood. The permanence of HAVS also increases with vibration exposure duration, but the precise threshold between permanent and reversible damage is unknown.<sup>4</sup> A rat tail model has been developed and produces similar peripheral nerve

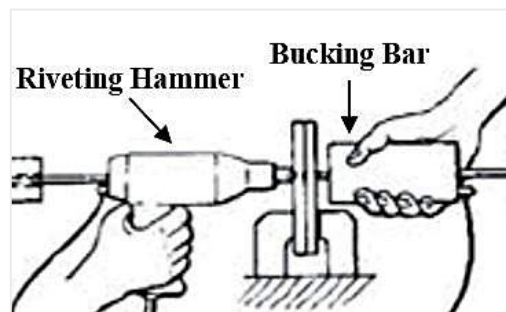


Figure 1: Demonstration of how the riveting hammer and bucking bar are used in unison to set a rivet. (Dandanell and Engstrom, 1986) [1]

<sup>1</sup> The findings described in this paper were financially supported by the Wisconsin Space Grant Consortium (WSGC). The mentorship of Dr. Danny Riley and Mr. James Bain has served as a pivotal foundation for all research described in this article. Additional thanks are given to Dr. John LaDisa of Marquette University for approving this research to serve as the author's undergraduate thesis.

damage in rats to what is observed in workers with HAVS.<sup>4,7</sup> The rat tail model simulates vibration exposure as seen by workers who operate the bucking bar. The bucking bar is a steel bar used with the riveting hammer to set a rivet. Interestingly enough, bucking bar operators experience more high frequency (kHz) vibration and more commonly exhibit HAVS than workers who operate the riveting hammer.<sup>1,7</sup>

Exposure to a single, 12 minute bout of riveting hammer vibration results in mechanosensory nerve destruction when observed 4 days after the delivery of vibration.<sup>2</sup> While acute exposure to riveting hammer vibration has been studied, a long term model replicating occupational exposure has received little to no attention. Nearly all long term HAVS studies used vibrational shakers to deliver vibration, rather than the riveting hammer. Vibrational shakers are capable of delivering single frequencies at limited accelerations, while the riveting hammer vibration signal consists of a wide range of frequencies with varying accelerations. Since workers received regular exposure to riveting hammer vibration, it is necessary to include both of these aspects.

The present study examines the effects of typical occupational vibrational exposure on cutaneous mechanosensory peripheral nerve populations and as well as nerve cell bodies that are responsible for nerve regeneration. The previously developed rat tail model was combined with a novel piezoelectric-based data acquisition method. The recorded vibrational signal was analyzed and interpreted in terms of transmissibility. The nerve damage quantification portion of this study is still underway.

## 2. Methods

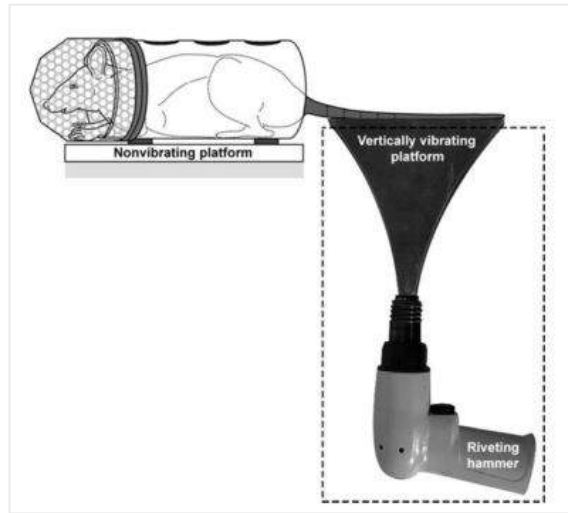
**A) Animals.** Thirty six female, 5 week old, Sprague Dawley rats were used for this study. All animal handling, testing, and surgery was approved by the Medical College of Wisconsin's Institutional Animal Care and Use Committee (IACUC). The animals were randomly assign to one of the four following groups (n=9):

- (1) 5 week control – animals are placed in control restraint for 12 min/day, 5 days/week (Mon-Fri) for 5 weeks, and euthanized on the sixth Monday.
- (2) 5 week vibration – animals are placed in vibration restraint for 12 min/day, 5 days/week (Mon-Fri) for 5 weeks, and euthanized on the sixth Monday.
- (3) 5 week control with recovery – animals are placed in control restraint for 12 min/day, 5 days/week (Mon-Fri) for 5 weeks. The animals remain in standard vivarium housing for weeks 6-10 and are then euthanized on the eleventh Monday.
- (4) 5 week vibration with recovery – animals are placed in vibration restraint for 12 min/day, 5 days/week (Mon-Fri) for 5 weeks. The animals remain in standard vivarium housing for weeks 6-10, and are then euthanized on the eleventh Monday.

The rats were acclimated to the restraint used for 12 minute intervals for 5 days prior to testing. Once rats were loaded into the tubular restraints, both the restraint and the rat's tail were taped securely to the tabletop to fully mimic experimental restraint conditions. Rats were housed overnight in a temperature-controlled vivarium room, and transported daily to the laboratory for testing. Food and water were available ad libitum, except during the 5 minute commute from the housing room to the laboratory

**B) Piezoelectric Rat Tail Model.** The present, piezoelectric rat tail model is largely derived from the laser vibrometer-based rat tail model used and described in previous studies.<sup>2,3,8</sup>

A rat is gently coerced into a PVC tube restraint which is then secured to the nonvibrating platform. The loaded restraint is positioned so that the relaxed, fur-skin interface of the tail aligns with the proximal end of the riveting platform. Masking tape is placed laterally to secure the tail to the riveting platform. This setup is duplicated to form a control restraint and a vibration restraint. Animals belonging to the control group are placed in the control restraint, in which the riveting platform is stationary. Animals belonging to the vibration groups are placed in the vibration



restraint, in which the riveting platform is mounted on a vertically-fixed riveting hammer. The vibration restraint is enclosed by a noise attenuation box in order to prevent audial discomfort. The vibration restraint uses two piezoelectric sensors (1 ventral and 1 dorsal) to record the vibrational output of the riveting hammer. An electric timer set to 12 minutes is wired to a voltage dependent airline valve. When a voltage is applied, the airline value opens and allows the pneumatic riveting hammer to operate.

Figure 2: Vibration restraint setup. The dashed line represents the noise attenuation box that encases the riveting hammer portion of the vibration restraint (Raju et al 2011) [2].



Figure 3: Step-by-step placement of the piezoelectric sensors on the vibration restraint. (A) The rat tail sits relaxed on the riveting platform. Circled in red is the fur-skin interface of the rat tail which is used to align the tail with the riveting platform. Outlined in blue is the ventral piezoelectric sensor. (B) Four tapes are placed laterally before the dorsal piezoelectric sensor is placed. (C) The dorsal piezoelectric sensor is then secured.

**C) Piezoelectric Sensors.** Two Smart Material Corp. Macro Fiber Composite M8503-P2 (MFCs, or piezoelectric sensors) were used to record the vibrational signal produced by

the riveting hammer. Piezoelectric sensors consist of a manmade piezo ceramic sealed between electrodes a polyimide film. When experiencing a load, the stressed piezo ceramic's dipole alignment changes, creating a voltage. The voltage can be measured at the metal contacts due to the internal arrangement of the electrode and conductor layers. The M8503-P2 piezoelectric sensors are able to detect frequencies up to 3MHz, making them ideal for the investigation of the kHz vibrations within the riveting hammer signal. Traditionally, MFC piezoelectric devices have been used to sense and respond to vibrations on satellites and aircraft. To our current knowledge, this is the first study which repurposes the MFCs to record power tool vibration in an animal.

Before placement on the tail, two strands of flexible headphone wire were soldered to each piezoelectric sensor, one strand to each of the two metal contacts. After the newly formed junction was cooled to room temperature, cyanoacrylic glue was used to shield the exposed solder joint and adhere the first 4mm of wire to the piezoelectric sensor in order to alleviate the sensitive solder joint from vibrational stress. Once assembled, the free ends of the piezoelectric sensor wires were clamped into the terminals on the National Instruments (NI) 9222 Analog Voltage Module. The NI 9222 module connects to the NI cDAQ-917 chassis, which then connects to a laptop via USB. A baseline recording is made with both sensors lying flat on the riveting platform.

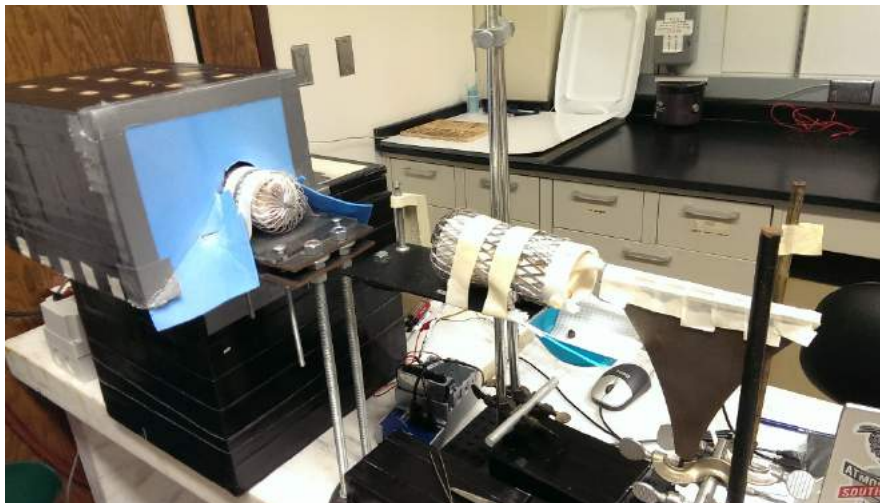


Figure 4: Loaded vibration restraint (left) and loaded control restraint (right). The NI hardware sits beneath the suspended restraints.

Once the sensors are placed on the tail, data collection is initiated when the riveting hammer begins reciprocating for at least 10 seconds. Three or four collections were made per day, resulting in every animal in either vibration group to be recorded once a week. Previous research has shown the riveting hammer vibration signal to contain a maximum frequency of roughly 16 kHz.<sup>3</sup> To sufficiently abide by the Nyquist sampling rate, a sampling rate of 75 kHz was chosen. A custom made Virtual Instrument (VI) was used in NI LabVIEW to record the raw voltage and calculate the power spectrum of the vibrating piezoelectric sensors.

**D) Non-survival surgery.** A ketamine-based anesthetic cocktail was administered intramuscularly to the rat's left quadriceps. The injection site was massaged occasionally

to encourage the circulation of anesthetic. Surgery began when the animal was no longer responsive to a foot-pinch. Laying dorsal side up, an axial incision was made and held exposed by hemostats. A pneumothorax was performed. The perfusion needle was maneuvered to puncture and rests inside the left ventricle. The right auricle was cut, and the perfusion machine began to pump saline. When clear saline flowed out of the right auricle, fixative was pumped through the animal. Once fixed, the tail and lower spine were excised. The tail segments (C5, C6, C11, C12) and tail tip were excised, chemically fixed, and stored. The lower spine was placed directly into fixative to preserve sensory neuron ganglia.

**E) Tissue processing.** Tail segment C12 was cut into 16 serial, 60 micron sections using a cryostat microtome. Sections underwent immunostaining and were examined under a fluorescence microscope. Lanceolate nerve complexes are mechanoreceptors that surround the hair follicles in the skin of rat tails. Digital images were taken of lanceolates and are currently being quantified as to number and integrity. Degradation of lanceolate complexes would attribute to the symptomatic numbness observed in HAVS.

Dorsal root ganglia (DRG) contain neuronal cell bodies which are vital for the regeneration of sensory nerve fibers. They were dissected from spinal segments S4-6, but are yet to be examined histologically. A reduction in DRG cell count (i.e, cell death) would explain the inability to regenerate nerve fibers. This would then serve as physiological evidence for the permanence of HAVS.

### 3. Results

The VI recorded the riveting hammer's vibrational signal in both the time and frequency domains. To test the efficacy of the new piezoelectric-based rat tail model, the time domain

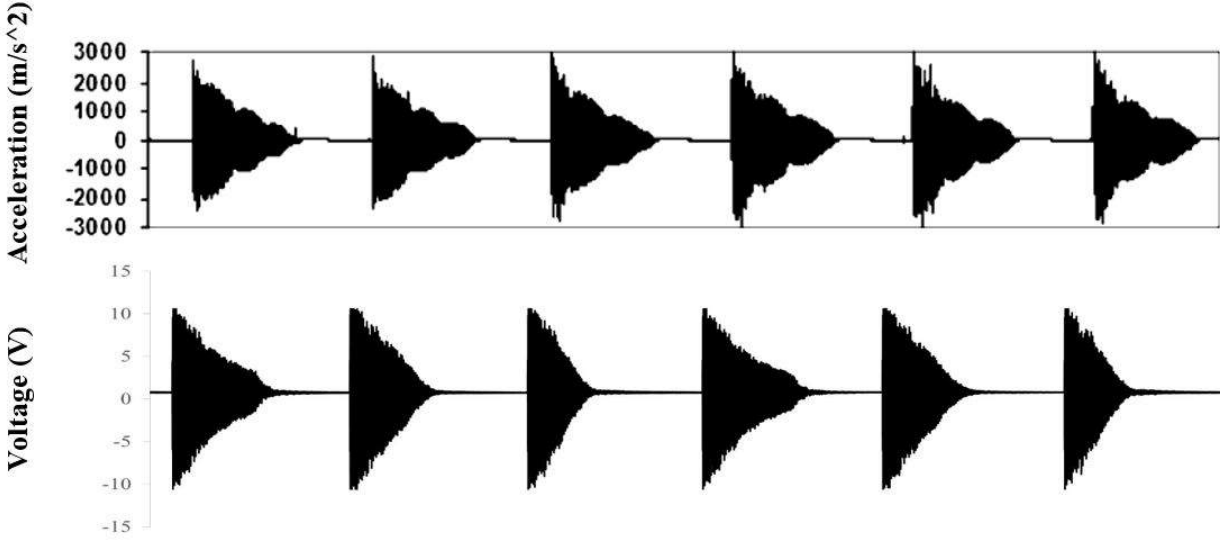


Figure 5: (Top) Riveting hammer vibrational signal as recorded by the laser vibrometer in [6] (Bottom) Riveting hammer vibrational signal as recorded by the piezoelectric/LabVIEW system. Although not shown, both plots share a similar time axis. Each triangular pulse represents a single oscillation of the riveting hammer.

voltage signal can be compared with the acceleration recorded by the laser vibrometer (Fig. 5). As calculated by LabVIEW, the power spectrum describes the energy contribution associated with each frequency in the vibrational signal (Fig 6). ISO 5349 employs a frequency weighting

$$\text{Mag}_w = \text{Mag}_{uw} \times \left(\frac{16 \text{ Hz}}{f}\right) \tag{1}$$

formula (Eq. 1) in which the unweighted magnitude is multiplied by the quotient of 16 Hz and the signal’s frequency (Fig. 7).

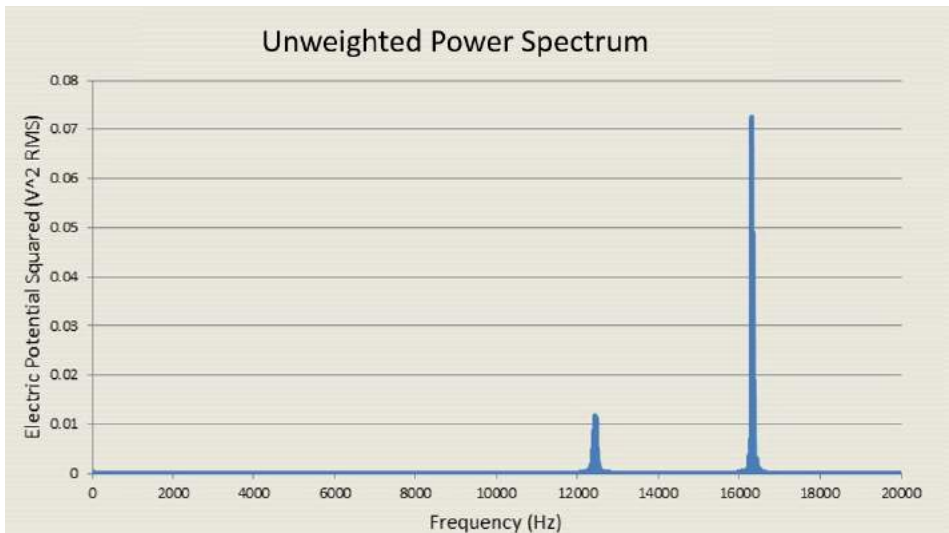


Figure 6: Although 10 frequencies were examined, the two highest at 12.4 and 16.3 kHz contain nearly all of the signal’s energy. When the ISO weighting formula is applied the 16.3 kHz signal, its magnitude as well as associated risk is decreased by more than three orders of magnitude.

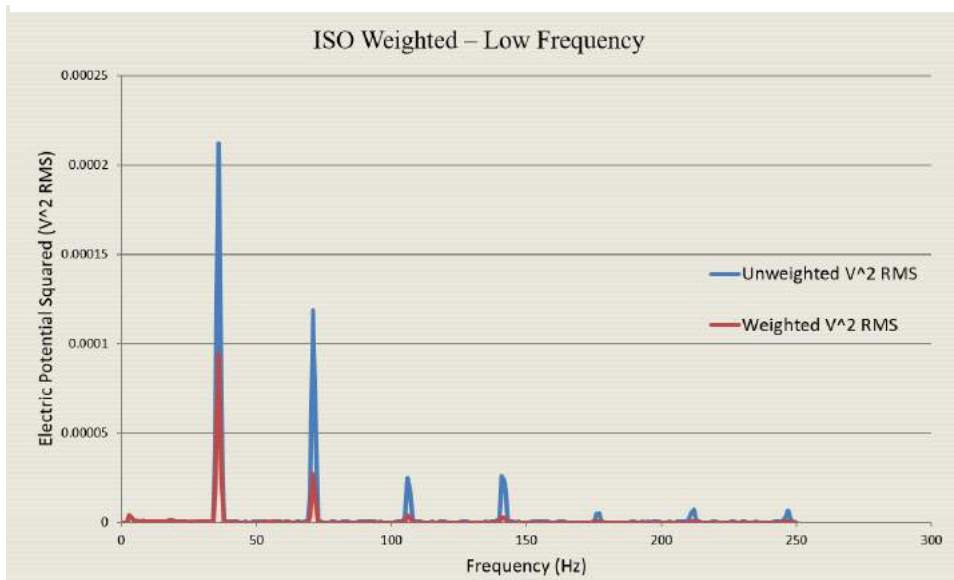


Figure 7: A magnified view detailing the lower frequencies represented in the riveting hammer signal. The y-axis scale in this plot is 320 times smaller than that of Fig. 6.

Several programs were written in the C language to analyze the approximately 135 million collected data points. Ten distinct frequencies were found to contribute nearly all of the signal’s

vibrational energy (36, 72, 105, 138, 174, 210, 3.9k, 8.4k, 12.4k, and 16.3k Hz). The power spectrum peaks belonging to each of these frequencies were averaged together for each sensor. This resulted in 10 values for each sensor. The quotient of the average dorsal and ventral sensor outputs is called the transmissibility (Eq. 2). Since a substantial difference in output voltage

$$\text{Transmissibility} = \frac{\text{Dorsal Sensor Output}}{\text{Ventral Sensor Output}} \quad (2)$$

(sensitivity) was observed in each sensor, the transmissibility is calculated in reference to the dorsal sensor’s baseline reading recorded each day before animal testing began. A transmissibility equal to 1 describes a frequency which is neither attenuated nor amplified after interacting with the rat tail. A frequency with a transmissibility greater than 1 suggests that the rat tail is resonating. Frequencies with a calculated transmissibility less than 1 are believed to represent an absorption of vibrational energy by the rat tail. Absorbed vibrational energy is thought to damage a plethora of biological structures, both macroscopic and microscopic, consequently contributing to the neurodegeneration observed in HAVS.

Table 1: Average power spectrum peaks for the 10 dominant frequencies recorded in the riveting

Frequency (Hz)	Avg. Trans.
36	7.76
72	1.34
105	1.81
138	3.10
174	4.16
210	18.47
3900	0.57
8400	2.25
12400	0.24
16300	0.19

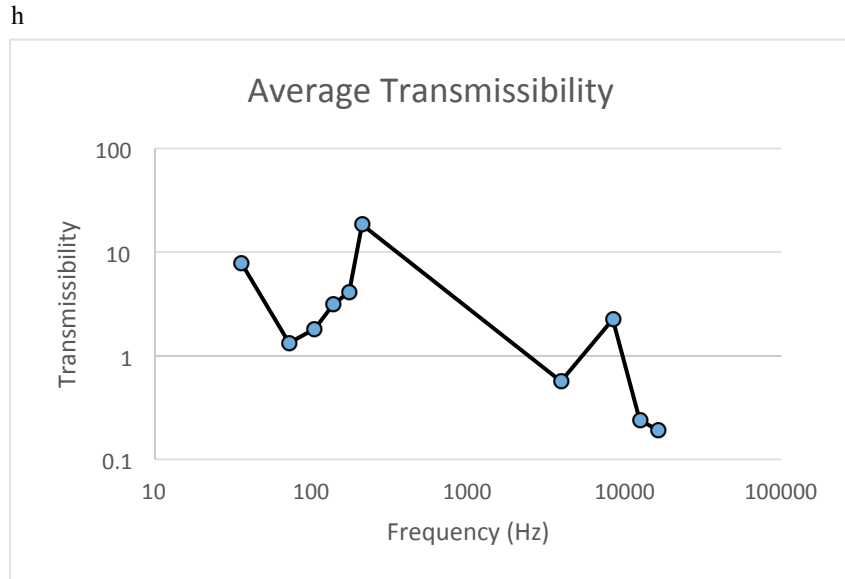


Figure 8: Transmissibility is heavily dependent on the energy associated with each frequency. There is still uncertainty in the field regarding if a large transmissibility and/or a low is to blame for the adverse effects of hand-arm vibration.

hammer vibrational signal.

#### 4. Discussion

The visual similarities between the laser vibrometer and piezoelectric system suggest that piezoelectric sensors are a viable alternative for vibrational analysis in the field of hand-arm vibration (Fig. 5). The piezoelectric system's cost is 1/100 that of the laser vibrometer. Its small size and varying composition (both flexible ceramic and rubber) further encourage the much needed investigation of HAVS both in the workplace and laboratory to readdress ISO 5349.

Findings show that the riveting hammer vibration signal is dominated by two different kHz frequencies, both of which exhibit a transmissibility value less than 0.25 (Fig. 6 and Table 1). It is easy to believe that these large changes in energy are responsible for whatever changes may be observed in nerve populations, but that may not be the case. The frequency response of the piezoelectric sensors has not been characterized. This may attribute to the slight differences noted between power spectrums collected by the laser vibrometer and piezoelectric system.<sup>3</sup>

While the initial scope was to examine the effects of recovery over a period of 5 weeks, weekend recovery from Friday to Monday can be analyzed in terms of the vibrational signal. The biodynamic response of the rat tail changes throughout the extended exposure to vibration. Transmissibility describes this response, and recordings from Friday and a following Monday may be compared to show the biological efforts of short term recovery. Perhaps the short recovery promoted by the typical work week causes the cellular repair mechanisms to be susceptible to vibration damage when the work week resumes.

Although initial findings seem promising, no relationships or observations can be made regarding the various nerve populations at this juncture of quantification.

#### 5. References

1. Dandanell R, Engstrom K. Vibration from riveting tools in the frequency range 6 Hz-10 MHz and Raynaud's phenomenon. *Scand J Work Environ Heal.* 1986;12(4):338-342.
2. Raju SG, Rogness O, Persson M, Bain J, Riley D A. Vibration from a riveting hammer causes severe nerve damage in the rat tail model. *Muscle and Nerve.* 2011;44(November):795-804.
3. Xu XS, Riley D A., Persson M, et al. Evaluation of anti-vibration effectiveness of glove materials using an animal model. *Biomed Mater Eng.* 2011;21:193-211.
4. Loffredo M a., Yan JG, Kao D, Lin LZ, Matloub HS, Riley D A. Persistent reduction of conduction velocity and myelinated axon damage in vibrated rat tail nerves. *Muscle and Nerve.* 2009;39(6):770-775.

5. Fridén J. Vibration Damage to the Hand: Clinical Presentation, Prognosis and Length and Severity of Vibration Required. *J Hand Surg (British Eur Vol .* 2001;26 (5 ):471-474.
6. Goldsmith PC, Molina F A, Bunker CB, et al. Cutaneous nerve fibre depletion in vibration white finger. *J R Soc Med.* 1994;87(July):377-381.
7. McKenna KM, McGrann S, Blann A D, Allen J A. An investigation into the acute vascular effects of riveting. *Br J Ind Med.* 1993;50(2):160-166.
8. Welcome DE, Krajnak K, Kashon ML, Dong RG. An investigation on the biodynamic foundation of a rat tail vibration model. *Proc Inst Mech Eng H.* 2008;222:1127-1141.

# 25<sup>th</sup> Annual Wisconsin Space Conference

## PART FOUR

### Team Projects

# Monitoring Carbon Dioxide and Methane Levels above Retired Landfill and Forest Control Sites with a Tethered Aerostat to Determine Remediation Effectiveness

Jesse Banick, Kathryn Lenz, Jonathan Sanders, Jeshanah Zolkowski<sup>1</sup>

University of Wisconsin-Fox Valley, Menasha

**Abstract:** The chemical composition of the ambient air not only affects the health of human beings, but also the health of the planet. This study examined how the decay of waste matter influenced the concentration of carbon dioxide and methane in ambient air. By measuring the level of these two gases above a forest control site and a retired landfill site, the researchers analyzed the effectiveness of the remediation methods utilized on the retired landfill in reducing carbon dioxide and methane emissions. Two carbon dioxide sensors, affixed to a payload, hung beneath a tethered aerostat. The collected data seemed to show that the concentration of carbon dioxide on the retired landfill was equal to the concentration at the control site. However, as the data may have been influenced by sensor limitations, more analysis needs to be done to make conclusions about the remediation effectiveness.

## Introduction and Literature Review

**Landfills, carbon dioxide, and methane.** Each load of refuse added to a landfill provides a meal for microorganisms living inside. As these organisms perform their metabolic processes, they release a variety of gases, comprised mainly of carbon dioxide and methane (EPA, 2000). These emissions continue even after the landfill has been covered and seeded. Waste management companies have utilized multiple capping methods to reduce these gaseous emanations. For example, if the method involves a vegetative layer, the aeration of the soil is increased greatly. This allows oxygen to diffuse more readily into the soil (Abichou, Kormi, Yuan, Johnson, & Francisco, 2015). If toxins such as methane are oxygenated, they are not as detrimental to the environment.

While including vegetation in landfill capping proves to be important in itself, the type of vegetation also matters. Depending on the climate, soil constituents, and overall ecology of the area, different plant species will prosper and multiply. Healthier plants tend to photosynthesize more, having more leaves and chloroplasts. This increased rate of photosynthesis allows the plant to capture carbon dioxide and build sugars faster. Although the impact of plant species on atmospheric carbon dioxide is cited more often in literature, their impact on methane concentration is not as well known. Methanotrophs, small organisms that intake methane as an energy source, thrive in the soil of landfills with dense foliage. According to Stralis-Pavese and her colleagues (2004), the abundance of these bacteria depends on the plant species present. Finding the optimal environment for methane consumption by methanotrophs will help curb the amount of methane in the ambient air. Understanding the role of landfill capping and seeding in gas emissions has been a small chapter in the history of atmospheric research.

<sup>1</sup>This research was made possible by Wisconsin Space Grant Consortium, Dr. Beth A. Johnson, Dave's Sport and Marine in Kaukauna, City of Kaukauna, High Cliff State Park, Weld Specialty in Kaukauna, Dan Hawk, other UW Fox Valley Faculty (Dr. Brian Rukamp, Joy Perry, Dr. Martin Rudd), and our Affiliate Student Interns (Leigh Hayes, Katie Stadler, William Talbot, Zach Dorn, Erika Petersen, Cassondra Parsons).

**History of carbon dioxide and methane monitoring.** Interest in the concentration of greenhouse gases has prompted scientific research for over 50 years. Consistent monitoring of carbon dioxide levels began in the mid-1900s with Charles David Keeling. Keeling used infrared sensor techniques to read the carbon dioxide concentration at Mauna Loa Observatory in Hawaii, discovering pertinent trends. The concentration of carbon dioxide across the globe rose steadily (Roston, 2008). Teachers, authors, and businesses have dedicated classes, books, and products to the prevention of this trend. They focus on the role of human beings in the rise of carbon dioxide. Burning fossil fuels to power vehicles, furnaces, and industrial machines emit these gases into the atmosphere.

Monitoring of another small molecule, methane, has a more recent history. Scientists started to track its atmospheric concentration about 20 years after carbon dioxide. Although it traps more heat in the Earth's atmosphere than carbon dioxide, its concentration is minute in comparison (Roston, 2008). Along with the aforementioned landfill-related production of methane, oil companies also unearth the gas while drilling (Climate Central, 2012). Although carbon dioxide and methane are microscopic, they can cause problems that are macroscopic.

**Greenhouse gases and climate change.** The most cited and far-reaching consequence of higher levels of carbon dioxide and methane in the atmosphere is the greenhouse effect, which causes climate change. The emissions of carbon dioxide that originate from landfills are low at only 0.1% of total carbon dioxide emissions (Carbon Dioxide Emissions by Sector, 2015). However, landfill emissions of methane contribute 18% of its total emissions (U.S. Methane Emissions by Source, 2013). With the Environmental Protection Agency (EPA) reporting about 3,500 landfills in the United States as of 2012, improving bioremediation at landfills could help curb the concentration of these gases in Earth's atmosphere (U.S. Environmental Protection Agency, 2012). The concentration of these two gases in the atmosphere causes climate change by blocking portions of the sun's radiation from exiting the Earth's atmosphere, causing the radiation to reflect back to the ground and warm the overall temperature of Earth (Climate Central, 2012). The rise of greenhouse gases is expected to contribute to various effects that could be detrimental to the Earth's health. The increased temperatures caused by climate change may lead to an escalation of heat stroke and other heat related illnesses. Climate change will also impact Earth's ecology by causing more forest fires. Forest fires are especially dangerous since they will result in a lack of trees to remove carbon dioxide from the atmosphere, compounding the initial problem (Greenhouse Gases, 2015). Another hypothesis is that climate change will not increase temperatures evenly across Earth, but only in certain parts. This would alter normal precipitation and evaporation patterns, causing natural plant communities to shift along with precipitation trends (Climate Change Causes, 2015). Another impact of climate change is glacial formations melting.

This would cause a rise in the ocean's water level, displacing communities that live under sea level, as well as saltwater getting into the water table (Greenhouse Gases, 2015).

## Methods

**Ascent of the tethered aerostat.** The tethered aerostat, a Lighter Than Air Systems (LTAS) Kingfisher Aerostat K7.5U, held 230 cf of helium. The 7-lb lift capacity dictated the amount of equipment allowed on the payload. The planned concept of operations, locking the winch for five minutes at 50m, 70m, and 90m above ground level, was followed as closely as possible. The five minute lapses were meant to give the sensors time to adjust to the new elevation and gain an accurate reading of the gas concentration at that altitude. However, the wind caused unexpected altitude variations during the lapse periods. These fluctuations did not allow the sensors to remain suspended at the planned elevations.



Figure 1. The aerostat is shown below; the payload was suspended by ropes below the balloon. Photo by Beth Johnson

**Measurement of gas concentrations, GPS, and altitude data.** Three sensors took readings while attached to the ascending payload. The MG-811 carbon dioxide sensor worked as a galvanic cell to produce output voltages corresponding to the concentration of carbon dioxide in the air around it ("MG811 CO<sub>2</sub> Sensor," n.d.). The range at which this device senses is 350-10,000ppm. The other carbon dioxide sensor, the K-30 sensor, gained readings with non-dispersive infrared waveguide methods (Datasheet: K-30 Sensor," 2015). Having a range of 0-2000ppm, this sensor proved to be more fine-tuned since its range spanned the expected results evenly and completely. Although the sensitivity of 1% ( $\pm 20$ ppm) and accuracy of 3% ( $\pm 30$ ppm) is large in this application, the uncertainty would be lessened greatly by calculating an uncertainty in the mean concentration at each site, provided with a large collection of sensor readings. The last sensor, the MQ-4 methane sensor, was present on the payload but did not produce

reliable data and was not included in this report (Hanwei Electronics, n.d.). The voltage output from the output pins on each sensor travelled through a wire and resistor pack to the positive input pins on the GPS Aim XTRA (GAX). The GAX sent this voltage data, along with altitude and GPS data, to the AIM Base receiver attached to a ground computer. This data saved on the computer through the GAX software.

**Power supply and payload board.** An 11.4V 2200mAh LiPo battery powered the GPS Aim XTRA, while the sensors ran off of a 7.4V, 2200mAh battery. A teardrop-shaped piece of birch, artist-grade plywood provided support for research equipment. This plywood hung from the aerostat by three ropes attached to a swivel tethered to the aerostat. A metal tail steadied the payload in the wind.

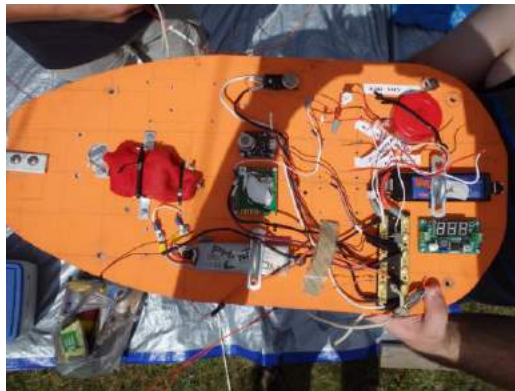


Figure 2. Batteries, sensors, a camera, the GPS Aim XTRA, and other equipment were mounted on the board. Photo by Beth Johnson

**Location of retired landfill and control site.** The retired landfill this study analyzed was the former Lehrer Landfill located in Kaukauna, Wisconsin. The aerostat ascended at latitude 44.261777°N longitude 88.267557°W. After collecting data at this location, the aerostat was transported to High Cliff State Park. The launch site in the park was near Indian Mound Trail, latitude 44.155251°N longitude 88.296176°W.

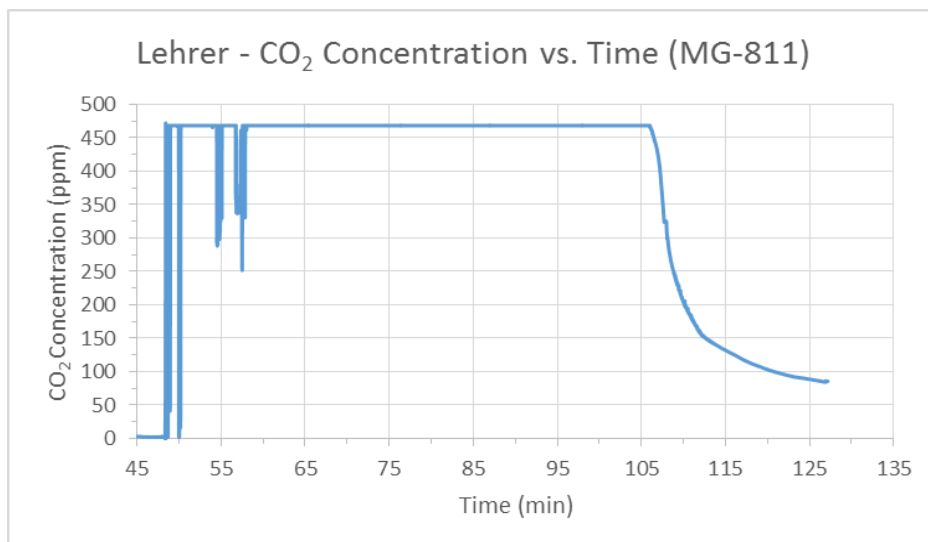


Figure 3. Map of the approximate locations of Lehrer Landfill (red circle) and High Cliff State Park (blue triangle) in Northeast Wisconsin.

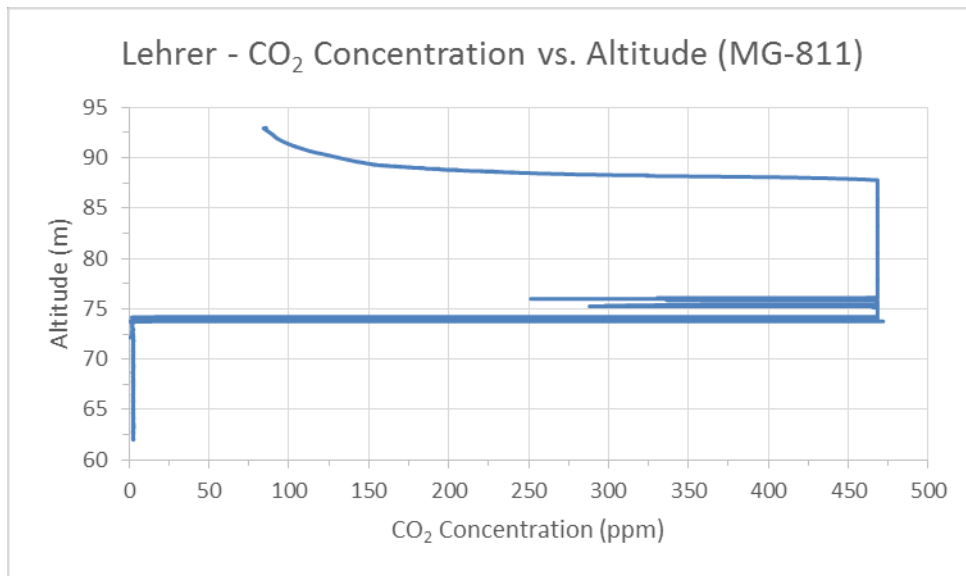
Source: Wisconsin Department of Natural Resources

## Data and Observations

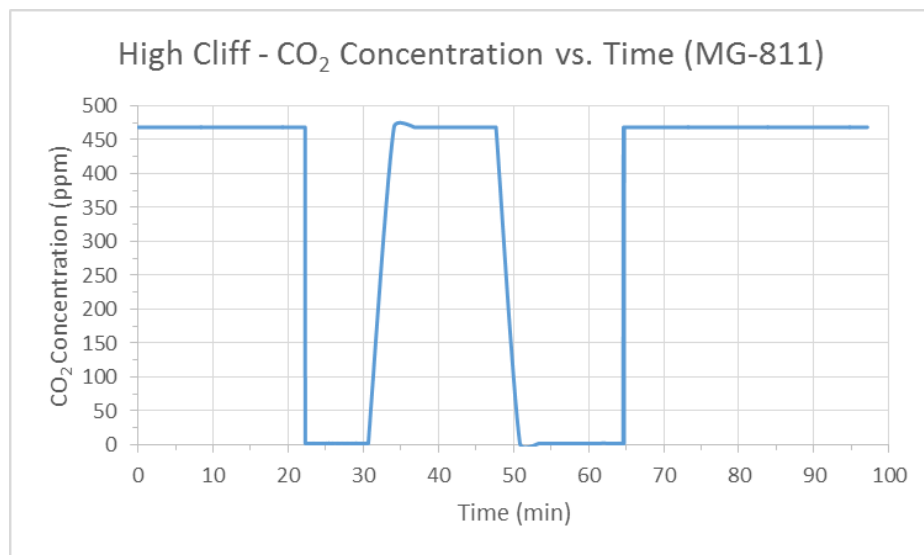
The first sets of data presented are Graphs 1a and 1b, representations of the data collected from Lehrer Landfill with the MG-811 carbon dioxide sensor. Graph 1a plots carbon dioxide concentration versus the amount of time the sensor was functioning. In Graph 1b, the concentration of carbon dioxide is plotted versus the altitude the aerostat achieved during the launch. Graphs 2a and 2b follow, which are representations of the data collected from High Cliff State Park with the MG-811 carbon dioxide sensor. Graphs 3a and 3b also represent data from High Cliff State Park, but from the K-30 carbon dioxide sensor. Graphs 2a, 2b, 3a, and 3b are of the same format as graphs 1a and 1b. Power supply issues were experienced at both sites, and are responsible for many of the otherwise inexplicable fluctuations seen in the graphs. Since the voltage-concentration conversion was unknown, the concentration in parts per million (ppm) were calculated by assuming High Cliff State Park (the control) had approximately 400 ppm (the average CO<sub>2</sub> concentration of clean air). The data was collected as an analog voltage from both sensors, which was averaged. That average was then assumed to be approximately 400 ppm, which allowed the creation of a conversion factor for ppm per volt. In addition, the altitude values from the GPS Aim XTRA did not match observed heights. Battery troubles may have caused this discrepancy. This problem became apparent at High Cliff State Park; as a result, the altitude values on these graphs were approximated. While the payload rose, the gas concentration data seemed unrelated to altitude deviations. Therefore, the altitude correction does not have a large bearing on the research results.



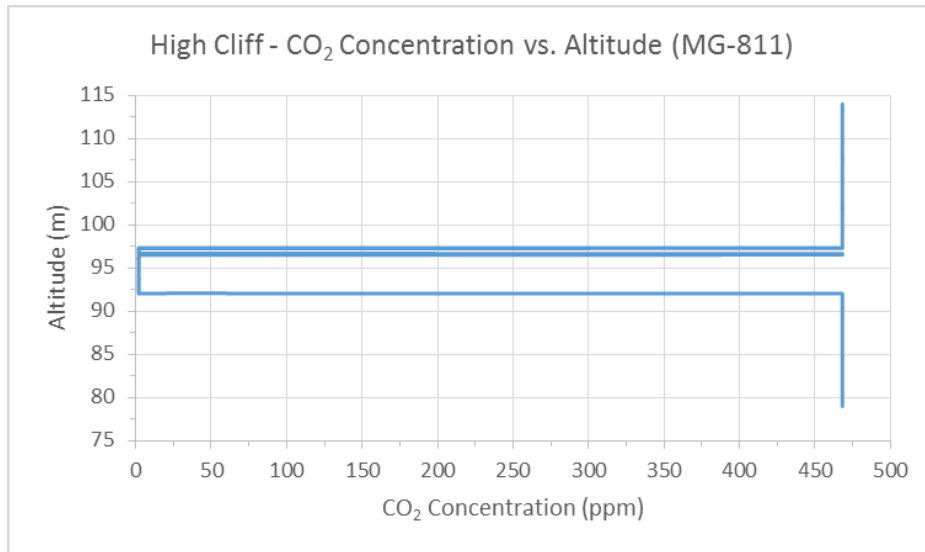
Graph 1a: A graph of CO<sub>2</sub> concentration versus time of the MG-811 at Lehrer Landfill. Time is on the x-axis from 45-135 min. CO<sub>2</sub> Concentration from the MG-811 carbon dioxide sensor is on the y-axis from 0-500 ppm. The time before 45 minutes was omitted due to a connection or battery failure that resulted in a reading of zero. When the graph decreases rapidly at the end, this is due to the battery failing and supplying less power to the sensor.



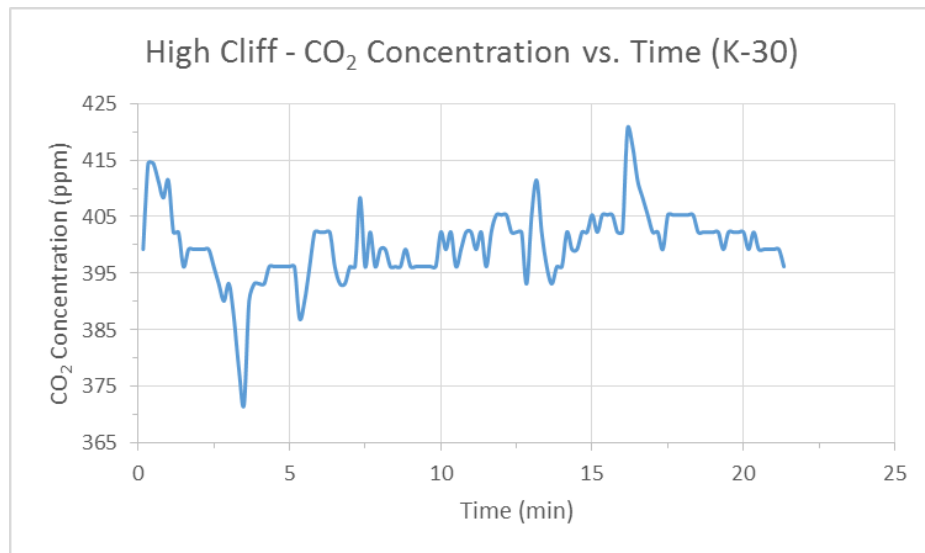
Graph 1b: A graph of CO<sub>2</sub> concentration versus altitude of the MG-811 at Lehrer Landfill. Altitude is on the y-axis from 60-95 m. CO<sub>2</sub> concentration from the MG-811 carbon dioxide sensor is on the x-axis from 0-500 ppm. The altitude before 60 m was omitted because there were no data points. The altitude is above sea level, and we launched from over 50m above sea level. Unexpected drops in CO<sub>2</sub> concentration are believed to be due to battery failure.



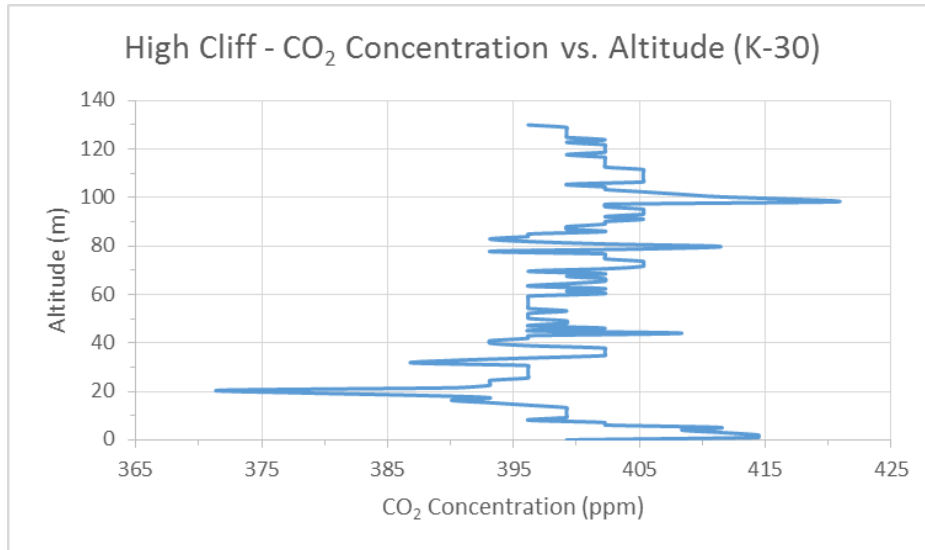
Graph 2a: A graph of CO<sub>2</sub> concentration versus time of the MG-811 at High Cliff State Park. Time is on the x-axis from 0-100 min. CO<sub>2</sub> concentration of the MG-811 carbon dioxide sensor is on the y-axis from 0-500 ppm. The times where the CO<sub>2</sub> concentration reaches zero is believed to be due to battery failure, which resulted in the sensor being unable to read the concentration of carbon dioxide.



Graph 2b: A graph of CO<sub>2</sub> concentration versus altitude of the MG-811 at High Cliff State Park. Altitude is on the y-axis from 75-115 m. CO<sub>2</sub> concentration of the MG-811 carbon dioxide sensor is on the x-axis is from 0-500 ppm. The altitude before 75 m was omitted because there were no data points. The altitude is above sea level, and the platform was launched from over 50m above sea level. The CO<sub>2</sub> concentration reaching 0 ppm is believed to be due to battery failure.



Graph 3a: A graph of CO<sub>2</sub> concentration versus time of the K-30 carbon dioxide sensor at High Cliff State Park. The sensor was within its error margin, and the fluctuations show that the sensor was not simply reading a preset “maximum” or “minimum” voltage. The peaks may be a result of changing wind velocities. Therefore, the sensor responds to its environment.



Graph 3b: A graph of CO<sub>2</sub> concentration versus altitude of the K-30 at High Cliff State Park. Please refer to the explanation of Graph 3a for an analysis of data peaks and depressions.

### Discussion

Although the data appears to illustrate equal concentrations of carbon dioxide at the retired landfill and control site, more testing is required in order to deem this information reliable. The voltage corresponding to the highest concentration on the MG-811 is about 3.3V, which may have simply been the maximum voltage on the sensor. Therefore, the unchanging graph concentrations may not be accurate. As can be seen on the graph from the MG-811 sensor, there are two drastic drop offs where the voltage falls to 0V. This is a result of a loose connection between the sensor and either the power supply or the GAX, and not a result of a drop in ppm detected.

The drops that are seen on graph 1b are not the only complications that arose from the power supply. The GAX coordinates that came from the control site are also skewed due to a lack of power. Being that the real time data was viewed on the ground computer unit while the aerostat was afloat, it became apparent that the GAX was providing false elevation coordinates. Once the aerostat had landed, a simple voltage test revealed that the battery supplying energy to the GAX was no longer charged. This has no detrimental effect on the data, because both of the sensors remain consistent at all elevations throughout the second launch at the control site.

## Conclusion

After launching at Lehrer Landfill and High Cliff, permission to launch at Outagamie County Landfill in Little Chute, WI was granted. Outagamie County Landfill is an active landfill and will enable the completion of the bioremediation analysis. Once the active landfill's data is obtained, a comparison between the data from the control and retired sites will be made. This will show how effective the remediation methods were in returning the concentrations of carbon dioxide to the ambient air's original concentration at the control.

Another part of research will be testing for heavy metal ions in the groundwater that surrounds the test sites. The purpose of this test is to see if there are any other heavy metals prevalent at landfill versus control. This will also tell whether the plants at the retired landfill are having any effect on the other heavy metals present.

To further ascertain the relationship between the landfill and its vegetation, analysis of pictures taken from above the launch site by the ADC Micro will be done in the coming months. With this camera, pictures can be filtered such that the percentage of healthy plants in a given area will be apparent. This will be correlated with how effective the bioremediation is. The plan is to identify the species of plants on these sites to see if any plants in particular are helpful in removing carbon dioxide and methane.

A major flaw in this launch was a lack of correspondence with the MG-81 sensor. The MG-811 sensor does not have a clear voltage associated with a certain concentration of carbon dioxide. An experiment containing bromothymol blue along with CO<sub>2</sub> will be conducted in a controlled environment to make sure that the MG-811 sensor is reading at an increasing rate in accordance with the bromothymol blue. More research will be done to reveal a voltage to ppm correspondence for this particular sensor.

The ultimate goal of this research is to determine if planting vegetation on inactive landfills helps counter the emission of carbon dioxide and methane. This research also examines the effects of vegetation on the presence of heavy metal ions. In order to determine this, it is necessary to analyze the concentrations of carbon dioxide and methane in the atmosphere, as well as analyzing heavy metal ions in groundwater nearby. In addition, landfills with various types of vegetation will be compared to discover the optimal planting method for improving environmental sustainability at landfill sites.

## References

- Abichou, T., Kormi, T., Yuan, L., Johnson, T., & Francisco, E. (2015). Modeling the effects of vegetation on methane oxidation and emissions through soil landfill final covers across different climates. *Waste Management*, 36230-240. doi:10.1016/j.wasman.2014.11.002
- Carbon Dioxide. (2013, August 7). Retrieved September 15, 2015, from Wisconsin Department of Health Services website: <https://www.dhs.wisconsin.gov/chemical/carbondioxide.htm>
- Carbon Dioxide Emissions by Sector, 2013 (Excluding LULUCF)* [Image]. (2015, July 2). Retrieved from [https://www.gov.uk/government/uploads/system/uploads/attachment\\_data/file/441367/Carbon\\_Dioxide\\_2013\\_Issue1.1.pdf](https://www.gov.uk/government/uploads/system/uploads/attachment_data/file/441367/Carbon_Dioxide_2013_Issue1.1.pdf)
- Climate Change Causes: A Blanket around the Earth. (n.d.). Retrieved September 15, 2015, from Climate Change: Vital Signs of the Planet website: <http://climate.nasa.gov/causes/>
- Climate Central. (2012). *Global Weirdness: Severe Storms, Deadly Heat Waves, Relentless Drought, Rising Seas, and the Weather of the Future*. New York, NY: Pantheon Books.
- Datasheet: K-30 Sensor* [Fact sheet]. (2015, May). Retrieved September 7, 2015, from <http://co2meters.com/Documentation/Datasheets/DS30-01%20-%20K30.pdf>
- Greenhouse Gases Pose Threat to Public Health. (n.d.). Retrieved September 15, 2015, from News website: <http://www.hsph.harvard.edu/news/features/bernstein-greenhouse-gases-health-threat/>
- Hanwei Electronics. (n.d.). *Technical Data MQ-4 Gas Sensor* [Fact sheet]. Retrieved September 7, 2015, from <http://www.sainsmart.com/zen/documents/20-011-957/MQ-4.pdf>
- Methane: Health Effects and Incident Management. (n.d.). Retrieved September 15, 2015, from: <https://www.gov.uk/government/publications/methane-properties-uses-and-incident-management>
- MG811 CO2 Sensor* [Fact sheet]. (n.d.). Retrieved September 7, 2015, from <http://www.dfrobot.com/image/data/SEN0159/CO2b%20MG811%20datasheet.pdf>
- Roston, E. (2008). *The Carbon Age: How Life's Core Element Has Become Civilization's Greatest Threat*. New York, NY: Walker.
- Stralis-Pavese, N., Sessitsch, A., Wellharter, A., Reichenauer, T., Riesing, J., Csontos, J., & ... Bodrossy, L. (2004). Optimization of diagnostic microarray for application in analysing landfill methanotroph communities under different plant covers. *Environmental Microbiology*, 6(4), 347-363. doi:10.1111/j.1462-2920.2004.00582.x
- U.S. Environmental Protection Agency List of Municipal Solid Waste Landfills* [Image]. (2012, April 2). Retrieved from <http://www3.epa.gov/epawaste/nonhaz/municipal/landfill/section3.pdf>
- U.S. Methane Emissions, By Source* [Image]. (2013, May 9). Retrieved from <http://www3.epa.gov/climatechange/ghgemissions/gases/ch4.html>
- Wolfe, L. (n.d.). *Winnebago Lake* [Map]. Wisconsin Department of Natural Resources. Retrieved from <http://dnr.wi.gov/lakes/maps/DNR/0139900a.pdf>

# Onset of Normal Field Instability in a Ferrofluid in Microgravity

Amelia Gear, Tessa Rundle, Justin Barhite, and Jordan Rice\*

Department of Physics, Carthage College, Kenosha Wisconsin

## Abstract

In the presence of a uniform, perpendicular magnetic field, a phenomenon known as normal field instability (NFI) occurs in a ferrofluid. The theory describing the NFI identifies a critical magnetic field below which no magnetically driven surface deformations occur. This critical field depends on the gravitational acceleration and, according to the theory, should disappear as local gravitational acceleration approaches zero. Previous studies have been inconclusive on the existence of a critical magnetic field in reduced gravity. For our work, we designed a payload for a suborbital rocket mission which launched through the RockSat-C program. Our experiment incorporated a ferrofluid sample and a uniform magnetic field which could be varied across a discrete range of value. During the microgravity portion of the rocket's flight, we obtained video of the ferrofluid's behavior to compare it to data taken in Earth's gravity.

## Introduction to Ferrofluids

A ferrofluid is a magnetic liquid composed of nanoscale ferrous particles suspended in a low-viscosity carrier fluid. When subjected to a magnetic field, surface deformation of the ferrofluid occurs along the magnetic field lines. Normal Field Instability (NFI) is the onset of this deformation, and occurs only when the applied magnetic field exceeds a critical value [Rosensweig, 1985]. A ferrofluid experiencing NFI can be seen in Figure 1. A typical ferrofluid will be approximately 85% carrier fluid by volume [Rosensweig, 1985]. Most ferrofluids are water or oil based. The carrier fluid must be low-viscosity so that it remains flowable, even in the presence of an applied magnetic field. A ferrofluid must also have a high magnetic susceptibility, causing a large response in reaction to an applied magnetic field [Rosensweig, 1982].

The suspended magnetic particles generally have a particle density of  $10^{23}$  particles per meter, and are 3-5 nm in size [Rosensweig, 1985]. The particles remain suspended in the carrier fluid due to thermal agitation, which prevents them from settling out of the fluid even in the presence of an applied magnetic field. Each particle is coated in a dispersant, which prevents the particles from sticking together, becoming large enough that they would settle out of the fluid due to magnetic and gravitational forces [Rosensweig, 1985]. The dispersant is formed out of long chain molecules, with the polar head of each molecule absorbed into the surface of the ferrous particle [Rosensweig, 1985]. The tails of the molecules, which are 10 to 20 Angstroms then surround the particle and act as an elastic cushion [Rosensweig, 1982]. These

---

\*This project was funded by the Wisconsin Space Grant Consortium and Carthage College, and made possible through the RockSat-C program provided by the Colorado Space Grant Consortium.

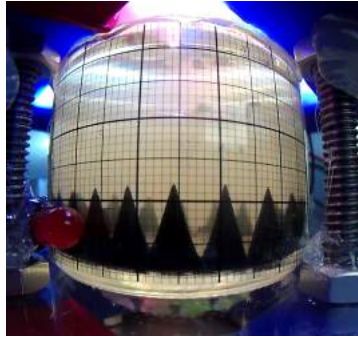


Figure 1: A ferrofluid is subjected to an external magnetic field, deforming into distinct peak and valley pattern. Due to the internal shape of the container, the fluid pools around the edges of the container.

tails are in constant motion, wiggling as the particle moves through the fluid. This motion causes the coated particles to repel one another should they come in contact [Rosensweig, 1985].

As the magnetic field increases, the magnetic dipole moments of the particles will tend to become aligned. In the presence of a strong applied magnetic field all the magnetic particles in a ferrofluid will align with the magnetic field, similar to a compass needle in an magnetic field [Rosensweig, 1982]. The magnetic field at which the particles are completely aligned and are no longer knocked out of alignment due to thermal agitation is dubbed the saturation magnetization, and this value varies with the composition of the ferrofluid [Rosensweig, 1985]. A ferrofluid will remain flowable even under saturazation magnetization [Rosensweig, 1985]. Each ferrous particle in a ferrofluid is inherently magnetized to saturation magnetization, and it is the fluid's net magnetization that is of import [Rosensweig, 1982].

**Normal field instability.** A ferrofluid will deform into a series of regular peaks and valleys under a uniform magnetic field applied perpendicularly to the surface of the fluid. This behavior is referred to as normal field instability (NFI). The distinct peak-and-valley pattern can be seen in Figure 1, in which the high points are the peaks and the low points, between the peaks, are the valleys. This behavior is determined by the minimization of total energy, and only occurs when the magnetic field exceeds a critical value.

**Minimization of energy.** The ferrofluid's patterns of deformation are governed by the minimization of energy. Under an applied magnetic field, the dominating terms in a ferrofluid's energy are the magnetic energy, gravitational energy, and surface energy. The magnetic energy drives deformation, while the surface and gravitational energy oppose it, acting as stabilizing forces to keep the surface of the ferrofluid flat [Abou, Bérengère Wesfreid, José-Eduardo Rouz, 2000]. When the magnetic field is of sufficient strength to partially overcome the surface and gravitational energies surface perturbations occur.

An individual particle will be attracted to a high magnetic field, so that particles would tend to move together to regions of strong magnetic fields. This is prevented by thermal motion, causing the particles to remain spread throughout the fluid. The necessity of having a high ratio of thermal to magnetic energy dictates maximum particle size in



Figure 2: A ferrofluid exposed to an increasing magnetic field. As the magnetic field increases, the peak height of the ferrofluid increases.

a ferrofluid. The small particle size prevents the particles from experiencing sufficient gravitational force to cause separation from the fluid, and each particle will experience a much stronger magnetic than gravitational force [Rosensweig, 1985].

**Critical magnetic field.** Deformation in a ferrofluid will only occur in the presence of a magnetic field of sufficient strength to partially overcome the stabilizing forces of gravity and surface tension. The magnetic field at which deformation occurs is referred to as the critical magnetic field. The equation for the critical magnetic field is shown in Equation 1 [Chong et al., 2012].

$$H_{crit} = \sqrt{\frac{(1 + \chi)(2 + \chi)\sqrt{g\rho\sigma}}{\chi^2\mu_0}} \quad (1)$$

In Equation 1,  $\sigma$  denotes surface tension,  $\rho$  fluid density, and  $\chi$  the susceptibility of the ferrofluid. The term  $g$  refers to the gravitational acceleration that the ferrofluid is subjected to, and  $\mu_0$  delineates the permeability of free space, which has a value of  $4\pi * 10^{-7}Vs/Am$ .

Before the critical field is reached, no surface perturbations occur. Thus, the magnetic field can be varied over a range of magnetic fields up to the critical field value, and the surface of the ferrofluid shall remain flat[Rosensweig, 1985]. The ferrofluid deforms abruptly once the magnetic field reaches this value.

**Ferrofluids in varying magnetic fields.** As the magnetic field increases, the wavelength of the ferrofluid, which corresponds to the distance between peaks, decreases. At the critical magnetic field the ferrofluid has a critical wavelength, which corresponds to the critical wavenumber, calculated as shown below in Equation 2.

$$k_{crit} = \frac{2\pi}{\lambda_c} = \sqrt{\frac{\rho g}{\sigma}} \quad (2)$$

At the critical magnetic field, the surface of an infinite, thin layer of ferrofluid will deform, forming a single wave along the surface. As the magnetic field increases, more peaks will form, and under a uniform magnetic field will be uniformly spaced. An increasing field will also cause the peak height of the ferrofluid to increase. This behavior is pictured in Figure 2.

**Ferrofluids in varying gravitational fields.** The ferrofluid's behavior is determined by the minimization of gravitational, surface, and magnetic energy. The gravitational and surface forces act as stabilizing forces against surface perturbations [Abou, Bérengère Wesfreid, José-Eduardo Rouz, 2000]. Surface deformation and the onset of NFI only occurs past the critical field at which the magnetic force exceeds the stabilizing forces. Gravitational forces play a key role in stabilizing the surface of the ferrofluid against surface deformation, and determining the value of the critical field. As the gravitational term in the critical magnetic field equation varies, so too does the critical magnetic field.

As the gravitational field decreases, the value of the critical magnetic field will also decrease. As the gravitational field increases, the critical magnetic field shall increase proportionally. Theoretically, the critical magnetic field should go to zero as the gravitational field approaches zero, and thus no critical magnetic field should exist in microgravity environments.

The study of the onset of NFI in ferrofluids in microgravity environments has been limited. Though studies of the behavior of a ferrofluid under the influence of a permanent magnet in microgravity and hypergravity have been carried out [Chong et al., 2012], they do not allow for observation of a ferrofluid's behavior under arbitrarily small increases of magnetic fields, under which conditions one may examine the onset of NFI. Additionally, literature is inconclusive on the existence of this critical field in microgravity. The existence of the critical magnetic field in microgravity is crucial in understanding the behavior of ferrofluids in microgravity environments and developing space-based ferrofluid applications.

**Ferrofluid applications.** Ferrofluids can be caused to form a variety of complex shapes due to their magnetic response [Rosensweig, 1985]. NFI causes the formation of peaks, but labyrinth patterns may also be imposed in thin layers of fluid [Chong et al., 2012]. On earth, their complexity allows ferrofluids to be used in a variety of commercial, scientific, and medical applications [Rosensweig, 1985], which could be applied to microgravity technology. In microgravity conditions, applications dealing with propulsion of small-scale satellites are under development. The peaks that ferrofluids are capable of assuming allow the substance to emit jets, which are capable of propelling small objects. They may also be used in the development of magnetic field based micro/nanoelectromechanical systems, including nanopumps, nanogenerators, and nanoactuators [Zahn, 2001].

## Methods

**The RockSat program.** In order to observe the behavior of a ferrofluid and test the existence of a critical magnetic field in microgravity conditions, an experiment must be developed to subject the ferrofluid to microgravity conditions. This requirement is fulfilled by development of a sounding rocket payload as part of the 2014 and 2015 RockSat program. The program allows student led teams to develop a sounding rocket payload for launch aboard a Terrior-Orion rocket, subjecting the payloads to approximately 5 minutes of microgravity time.

**Payload design.** Our payload had three main tasks: subject a ferrofluid sample to a time-varying uniform magnetic field, record video of the ferrofluid, and measure the magnetic field produced. To accomplish this, we placed a capsule containing the

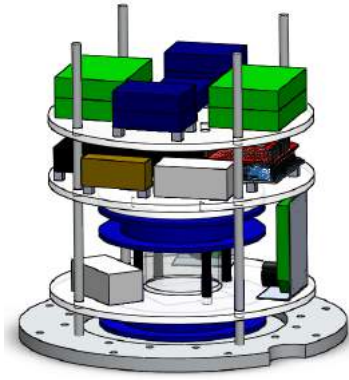


Figure 3: The internal structure of the sounding rocket payload. The Helmholtz coils are in blue, and bracket the clear ferrofluid capsule. A pair of cameras mounted to steel brackets record video of the ferrofluid's activity.

ferrofluid between a pair of Helmholtz coils, which produce a fairly uniform magnetic field between them which is proportional to the current driven through them.

The payload must comply with the Users Guide Compliance mandates as set by the RockSat program. The inner structure, which is that contained within a secondary containment structure, is composed of the electronics, Helmholtz coils, and ferrofluid capsule. All elements are mounted to polycarbonate base plates, which are light yet able to withstand the forces they are subjected to. These base plates are mounted to a system of threaded steel rods, which screw into the secondary base plate and protrude through the top of secondary containment, allowing them to be secured at both ends. The Helmholtz coils and ferrfluid capsule arrangement are mounted at the base of secondary, with two electronics plates mounted immediately above. An image of this design is found in Figure 3.

In order for accurate data on peak height to be obtained, a graph is affixed to the outer surface of the ferrofluid capsule. The graph is printed on transparent plastic so that it does not interfere with visibility of the peaks. The graph is marked in 1-millimeter intervals, with markers also clearly delineating every 5 millimeters and every centimeter. The graph over the container allows accurate measurements to be determined- correcting for fish-eye lens and curvature of the capsule.

**Electronics Design.** The payload electronics are controlled by an Arduino Uno, which both signals the various processes and records information from the various sensors. An accelerometer is used to record the spin and acceleration of the rocket during flight so that the behavior of the ferrofluid can be understood. A pair of magnetometers are used to record the magnetic field in the region of the ferrofluid capsule.

The Arduino Uno also controls the applied magnetic field of the payload, which is supplied by a switched-mode power supply. The switched-mode power supply outputs a signal at varying frequencies, which creates a current of varying strength. This allows the magnetic field to be continuously varied over a range, spanning 0 to 50 Gauss.

In order to have a second method of tracking the magnetic field, we added a simple

voltage divider between the Helmholtz coil battery pack and ground, allowing the Arduino to read the battery voltage (or rather, a fixed fraction of the battery voltage) through one of its analog in pins. We also placed a thermistor in contact with one of the Helmholtz coils and set up another voltage divider so that the Arduino could read its resistance through another analog in pin. The thermistor allows us to determine estimate any change in the resistance of the Helmholtz coils due to temperature variations.

**Software Subsystem.** Upon activation, the Arduino waits until the second-stage burns out, then begins activating the other components; it initializes the magnetometer and turns on the cameras (by flipping the relay that connects the camera button pins to ground). After waiting a few seconds for the cameras to begin recording, the Arduino turns the MOSFET on for five seconds, applying the full voltage of the battery pack to the Helmholtz coils to produce the strongest possible magnetic field (around 70 gauss). This is done in an attempt to condense the ferrofluid in case it has been dispersed by the vibration during launch. After the five seconds, the field is turned off, and then gradually ramped up by incrementing the PWM signal from 0 to 255 over the course of five seconds. During the ramp, the Arduino periodically reads from the magnetometer, as well as the battery voltage and thermistor analog pins. Once the ramp is completed, the field is turned off, and all of the readings taken during the ramp are written to the SD card. The coil voltage is then ramped up similarly over 10 seconds, then a third time over 30 seconds. At this point the cameras are signaled to stop recording and are powered off. This entire procedure (turn cameras on, ramp up over 5, 10, and 30 seconds, and turn cameras off) is repeated two more times, for a total of three cycles.

**Ferrofluid.** For the purposes of this experiment, approximately 1/4 of an ounce of light hydrocarbon ferrofluid was used. The remaining space in the two-ounce ferrofluid capsule is occupied by a suspension fluid, composed mainly of water. The suspension fluid prevents the ferrofluid from staining the glass capsule. Both the suspension fluid and ferrofluid were provided by ConceptZero. The ferrofluid used is Ferrotec's EFH1, developed for educational markets with well-documented physical properties.

**Testing results.** Throughout the initial design and construction process last year, we tested all of our components to verify their correct functioning and to determine optimal placement within the payload. For instance, we ran a large current through our Helmholtz coils for an extended period of time to verify that they wouldn't dissipate enough heat to cause any issues. We tested various placements of the cameras and adjusted their focus to get the best view of the ferrofluid sample and the grid lines on the outside of the container. We also tested various placements of the LEDs to find the optimal position for lighting the ferrofluid while avoiding glare on the glass container. The magnetometer placement had to be investigated as well, since its range of +/- 8 gauss meant that it would saturate if placed too close to the center of the coils. The magnetometer was also tested by attaching it to one of the electronics plates above the Helmholtz coils, and calibrations were done against the magnetic field at the center of the coils at the location of the ferrofluid capsule.

Finally, we ran numerous full mission simulations to verify that all components were properly integrated and that the payload performed as expected. The first full mission simulations were conducted on March 26th, and more were run on several occasions



Figure 4: A comparison of the ferrofluid bubble in microgravity with no applied magnetic field (left) and with an applied field of 50 Gauss (right).

between then and launch. Most full mission simulations were run without secondary containment, so that the g-switch could be manually triggered and the payload could be observed as it ran. In addition to verifying proper integration of all parts, we also used the full mission simulations to test possible failure scenarios, such as removal of the SD card or reset of the Arduino. These tests demonstrated that the payload was able to recover in both of those cases. We also ran a few full mission simulations with the payload spinning at approximately 2 Hz in order to see what effect the spin would have on the payload, and on the ferrofluid in particular. While this was significantly less than the spin of the rocket during flight, we saw no difference in the ferrofluid's behavior spinning at 2 Hz.

**Observing the onset of normal field instability.** In order to compare the onset of NFI in microgravity to that in earth-gravity conditions, ground data must be obtained. To do this, video of the ferrofluid subjected to a range of magnetic fields is obtained on Earth. Video was recorded, allowing the surface of the ferrofluid to be observed for deformation.

The onset of NFI is determined to occur when deformation is first seen. To do this, the surface of the ferrofluid was visually analyzed at each magnetic field level. At the point when a peak first begins to form, the applied magnetic field is obtained from the magnetometer data, and the height of the ferrofluid surface was recorded.

## Results

Our payload operated as expected during flight. Both cameras recorded the expected three videos, and the observed deformations of the ferrofluid indicate that the Helmholtz coils were supplied with the intended currents. The Arduino recorded reasonable values for the battery voltage, thermistor resistance, and magnetometer, suggesting that those components operated correctly, and the timestamps logged to the SD card show that the Arduino did not reset during the portion of the flight when the experiment was active.

The images in Figure 4 are taken from the second video recorded by one of the cameras during flight. In the first image no magnetic field is present, and in the second a field of about 50 gauss is applied to the ferrofluid. At the bottom left one of the signal LEDs is visible, which allows frames in the videos to be correlated with timestamps recorded by the Arduino. The air bubble in the container is visible at the center (due to the spin of the rocket).

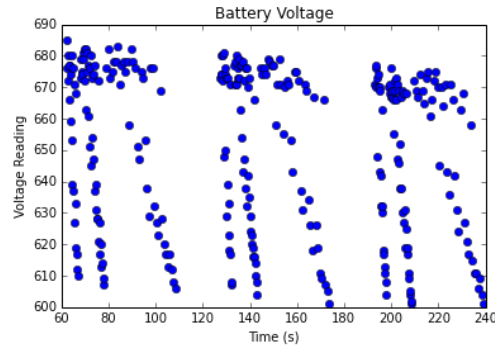


Figure 5: A plot of the battery pack voltage during flight. This was the primary source of data for calculating the magnetic field experienced by the ferrofluid.

Figure 5 shows the voltage of the battery pack supplying current to the Helmholtz coils throughout the duration of the experiment. The voltage data are analog readings from the Arduino, which we calibrated against the actual battery voltage prior to flight. During each of the three cycles, the battery voltage drops three times, over 5, 10, and 30 seconds. This occurs because the current to the coils is being ramped up; consequently the battery voltage drops due to the battery's internal resistance. The average battery voltage also decreases slightly over time as it is gradually discharged by powering the coils. Overall, this plot gives us confidence that the Helmholtz coils were supplied with the correct currents and that there were no power failures.

We also recorded readings from the thermistor placed in contact with one of the coils; the data shows a steady decrease in the thermistor's resistance throughout the experiment, corresponding to an increase in temperature resulting from the heat dissipated by the coils as a current is driven through them. The calibration we performed before flight indicates that the observed change in the thermistor readings does not correspond to a large enough temperature change to significantly affect the coils' resistance. Therefore we can conclude that any changes in the coils' resistance due to temperature variations can be ignored when determining the magnetic field present throughout the flight.

The magnetometer data, unfortunately, is not as useful. In Figure 6, the red, blue, and green points show the measurements of the magnetic field in the x, y, and z directions (which are determined by the orientation of the magnetometer). Two of these channels were vertically offset in the plot so they would not overlap. The solid line is proportional to the PWM signal to the MOSFET, which in turn is approximately proportional to the magnetic field. The green and blue channels appear to decrease linearly with increasing magnetic field at low fields, but the blue channel quickly saturates and the green channel starts trending upwards. The red channel also does not have any strong correlation with the magnetic field.

Since the ferrofluid did not form a flat layer during the flight, we were not able to test the theoretical predictions of the critical field and wave number of the Rosensweig instability. However, some of the videos showed small, nearly spherical droplets of ferrofluid which were elongated as the field increased. The images in Figure 7 show one of these droplets at different applied fields.

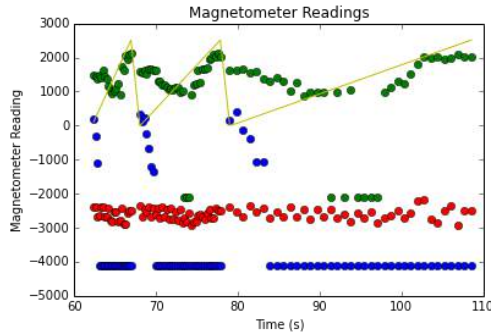


Figure 6: The data recorded by the magnetometer during flight.



Figure 7: A ferrofluid droplet experiencing various magnetic fields in microgravity.

We modeled these droplets theoretically in order to compare our predictions to their observed deformations under the applied field. We did so by considering the magnetic energy and surface energy of a prolate ellipsoid of a uniformly magnetized material with a given volume, surface tension, and magnetic susceptibility. We were able to show that for small deviations from a sphere, as the eccentricity of the ellipsoid increases (at constant volume), the magnetic energy decreases as the square of the eccentricity while the surface energy increases as the fourth power of the eccentricity. Thus the sphere is unstable under any nonzero applied field; while an ellipsoid may not be the true shape of the deformed droplet, since it is energetically preferable to the sphere, the droplet must deform into some other shape. Furthermore, by finding the eccentricity that minimizes the total energy, we can predict the approximate shape that a small droplet would adopt under a given applied field.

For the droplet shown in the images above, we estimated the ratio of the axes of the ellipsoid every five frames while the field was increasing, and plotted the axis ratios against the applied field. On this plot, Figure 8 we then superimposed the theoretical prediction of the axis ratio as a function of applied field, using values of the susceptibility and surface tension specific to our ferrofluid.

The discrepancy between the theoretical predictions and the observed behavior of the ferrofluid droplet in the video could result from distortion of the droplet by the camera, the centrifugal force pressing the droplet against the glass, a non-ellipsoidal true shape of the droplet, or a slight inaccuracy in our estimation of the magnetic field. Considering the number of possible sources of error, the plot shows fairly good agreement between data and theory.

## Conclusions

Our payload performed as intended during flight and collected the expected amount

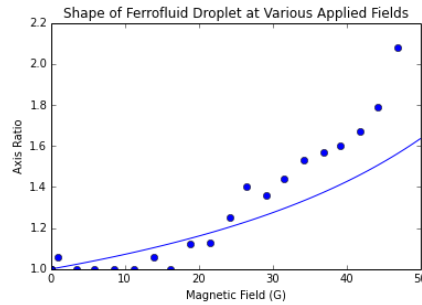


Figure 8: The theoretical prediction of the axis ratio of a drop of ferrofluid at various applied magnetic fields, superimposed with the measurements of an experimental droplet.

of data, so the operation of our payload was a success. Since the ferrofluid did not form a flat layer perpendicular to the magnetic field during flight, we did not observe the Rosensweig instability in the videos and were therefore unable to characterize the role of gravity in stabilizing the surface of the fluid against magnetically driven deformations. However, due to the presence of several small, isolated, nearly spherical droplets of ferrofluid, we were able to validate our theoretical modeling of the effects of magnetic and surface energy in determining the shape of a small droplet of ferrofluid in the absence of gravity.

**Potential Follow-up Work** Several improvements could be made if this experiment were to fly again. Other magnetometers and different placements of the magnetometer could be explored to obtain more reliable measurements of the magnetic field. As another method of tracking the magnetic field, a simple ammeter could be implemented; measurements of the current in the coils would likely correlate better with the field than battery voltage multiplied by the PWM duty cycle.

## References

- [Abou, Bérengère Wesfreid, José-Eduardo Rouz, 2000] Abou, Bérengère Wesfreid, José-Eduardo Rouz, S. (2000). The normal field instability in ferrofluids: hexagon-square transition mechanism and wavenumber selection. *Journal of Fluid Mechanics*, 416:217–237.
- [Chong et al., 2012] Chong, T. Y., Ho, K. L., and Ong, B. H. (2012). Investigations of field instability of ferrofluid in hypergravity and microgravity. *AIP Advances*, 2(1):012138.
- [Rosensweig, 1982] Rosensweig, R. (1982). Magnetic Fluids. *Scientific American*, 247(4):136–145.
- [Rosensweig, 1985] Rosensweig, R. E. (1985). *Ferrohydrodynamics*. Cambridge University Press.
- [Zahn, 2001] Zahn, M. (2001). Magnetic fluid and nanoparticle applications to nanotechnology. pages 73–78.

# Microwave Power Beaming using Ka-band Radar Tethered Aerostat Program

Travis Haugstad<sup>1</sup>, Joel Nielsen

Western Technical College

## Abstract

Power is transferred wirelessly from a ground based microwave transmitter to a receiver flown on a platform attached to a tethered aerostat. The signal is analyzed using consumer radar detection hardware and developed circuitry. This signal is analyzed by a programmable microcontroller, or Arduino, and data is then transmitted to a logging computer on the ground via flight computer and base station. Eventually, a rectenna and receiver will be developed to convert the microwaves to a useable voltage to power on-board instruments. This technology could be employed as a means to reduce the need for on-board power supplies for CubeSats deployed by the International Space Station, on orbit solar power generation, solar power satellites, etc.

## Introduction and Statement of Problem

The term microwave refers to the range of electromagnetic radiation with frequencies between 100 MHz to 1000 GHz. (Pozar, 2012) Wireless power transfer, based on the technology of microwave transmission and reception by rectifying antenna, rectenna, which converts the microwaves to a useable voltage. This concept has been tested and proven on a large scale where 10 kW of power was transferred between a transmitter and receiver. (Lan Sun Luk, Celeste, Romanacce, Chane Kuang Sang, & Gatina, 1997) However, there is also a need for small size applications which could, for example, reduce the design requirements for on-board power supplies of CubeSats, The purpose of this experiment is to receive a microwave signal from a ground transmitter to our airborne receive, amplify the signal, and generate a useable voltage to power onboard electronics.

## Equipment



---

<sup>1</sup> Special thanks to WSGC for funding, education, equipment, and technical support; County of La Crosse, WI Sherriff's Department for donation of equipment; Michael LeDocq for mentoring us throughout this entire project; the McCarty family for the use of their land to conduct our flight(s); and affiliate student interns: James Beier, Brian LaPlante, Landon Rudy, Josh Wagner, Nicholas Watson, and Lor Xiong for their hard work and dedication throughout the project.

**Aerostat and Winch Powered Spool (WPS).** This project used a tethered aerostat (Fig. 1) to suspend a payload equipped with instruments and circuitry required to carry out a specific experiment. When filled with 260 ft<sup>3</sup> of welding grade helium, the aerostat measured approximately 10 ft. in diameter and 7 ft. tall, and provided 10 lbs. of lift. The WPS used electromechanical equipment to deploy/retrieve the aerostat. A wooden wire spool is driven by an electric winch powered by a 12V car battery (Fig. 2).

*Figure 1: Aerostat and payload package in flight*

**Payload platform.** Flight instruments were attached to the platform which was suspended below the aerostat (Fig. 3). The instruments and subsystems included on the platform were the Aim Xtra flight computer, an Arduino microcontroller, and electronic circuitry that comprises the Electrical Power and Microwave Beam subsystems, all described next.

**Aim XTRA (AX) and base station.** The AX was responsible for real time data viewing during flights and controlled a safety feature that could deflate the aerostat in the event of failure. The AX arrived pre-programmed with its own native software used to view and manipulate data collected. The native AX sensors that were used are discussed later.

**Electrical Power System (EPS).** This subsystem powers the Arduino, radar detector, and AX.

**Arduino.** There are multiple inputs and outputs on this microcontroller used to monitor battery power, radar signal strength, and data acquisition from atmospheric sensors. This data was stored to an SD card which could be downloaded at a later time for analysis.

**Digital-to-analog converter (DAC).** Two voltage divider circuits were combined to one prototype board and allow a conversion from a digital value to an analog voltage that could be easily analyzed.

**Microwave beam subsystem (MWB).** The microwave transmitter, made by Kustom Electronics Inc., is a FALCON radar gun, a law enforcement tool to detect vehicle speed. It is used to generate 24.15GHz microwaves, 12-40mW output power at 12° beam width (Kustom Signals, Inc., 2011). The receiver is a consumer radar detector with additional circuitry to enable data collection regarding the strength of the signal received.

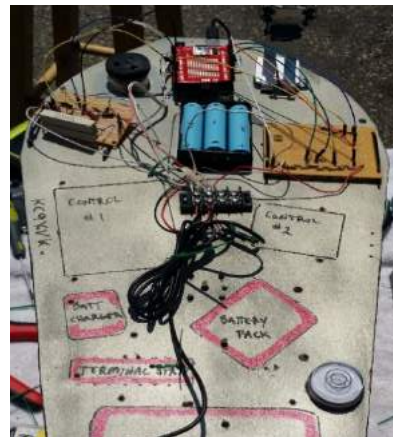


Figure 2: WPS without battery power or tether spooled.

Figure 3: Platform in development prior to launch.

### Subsystem Development, Theory of Operation, and Integration

**Microwave detection development.** The accurate detection of microwave signal strength is crucial when power transfer efficiency calculations are done after a rectenna is developed. It will serve as our baseline measurement. During the first flight, the signal received by the MWB detector was unreliable, which led to the development of the data collection system described here. To accomplish this, a consumer radar detector was used and supporting circuitry was developed. The radar detector had a 7-segment LED display which showed the radar signal strength detected on a scale from 0-5. In order to convert the visual output of the LED display to a useable digital value, the voltage was measured at each of the pins to determine which LED segment was lit. The LED display is a dual inline pin package with 10 pins, 3 of which were not used to generate the display. Five volts is applied to each LED segment. When the segment of the corresponding pin is lit, there is a 2V drop across the LED segment, leaving 3V at the pin. Table 1 shows which LED segments are illuminated for a given signal strength. As shown in Figure 4, when the LED display shows a “5”, LED segments a, c, d, f, and g are lit, causing pins 3, 6, 7, 8, and 10 to have a low voltage.

Signal Strength on LED Display	5	4	3	2	1
Pin 1, Segment B	High	Low	Low	Low	Low
Pin 2	n/a	n/a	n/a	n/a	n/a
Pin 3, Segment C	Low	Low	Low	High	Low
Pin 4	n/a	n/a	n/a	n/a	n/a
Pin 5	n/a	n/a	n/a	n/a	n/a
Pin 6, Segment A	Low	High	Low	Low	High
Pin 7, Segment F	Low	Low	High	High	High
Pin 8, Segment G	Low	Low	Low	Low	High
Pin 9, Segment E	High	High	High	Low	High
Pin 10, Segment D	Low	High	Low	Low	High

Table 1: LED status for specific signal strength  
Green=LED on; Red=LED off

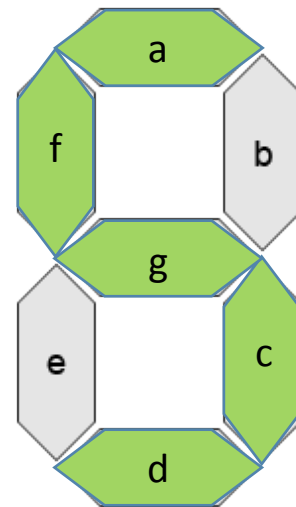


Figure 4: Example of “5” output on LED Display

The 7 voltage values from the LED pins are then sent to analog inputs on the Arduino. The Arduino's code was written to analyze these 7 inputs and provide a 5V output to multiple inputs on a voltage divider, based on which pins are high or low. This worked as a multiplexer/demultiplexer; based on the status of multiple inputs the Arduino will select which output to use. If the LED displays a "1", the 5V output is sent to the top of the voltage divider at D1 and most of the 5V is dropped across resistors 1-9 leaving only a small voltage at the output which is measured at point A (Fig 5). If the LED displays a "5", the output from the Arduino is sent to D5, only a small voltage is dropped, and we read a higher voltage at point A. The output from the voltage divider is sent to the AX, which sends that data in real time to a logging computer on the ground, determining the signal strength that is reaching the aerostat. This information will be critical for future efficiency testing.

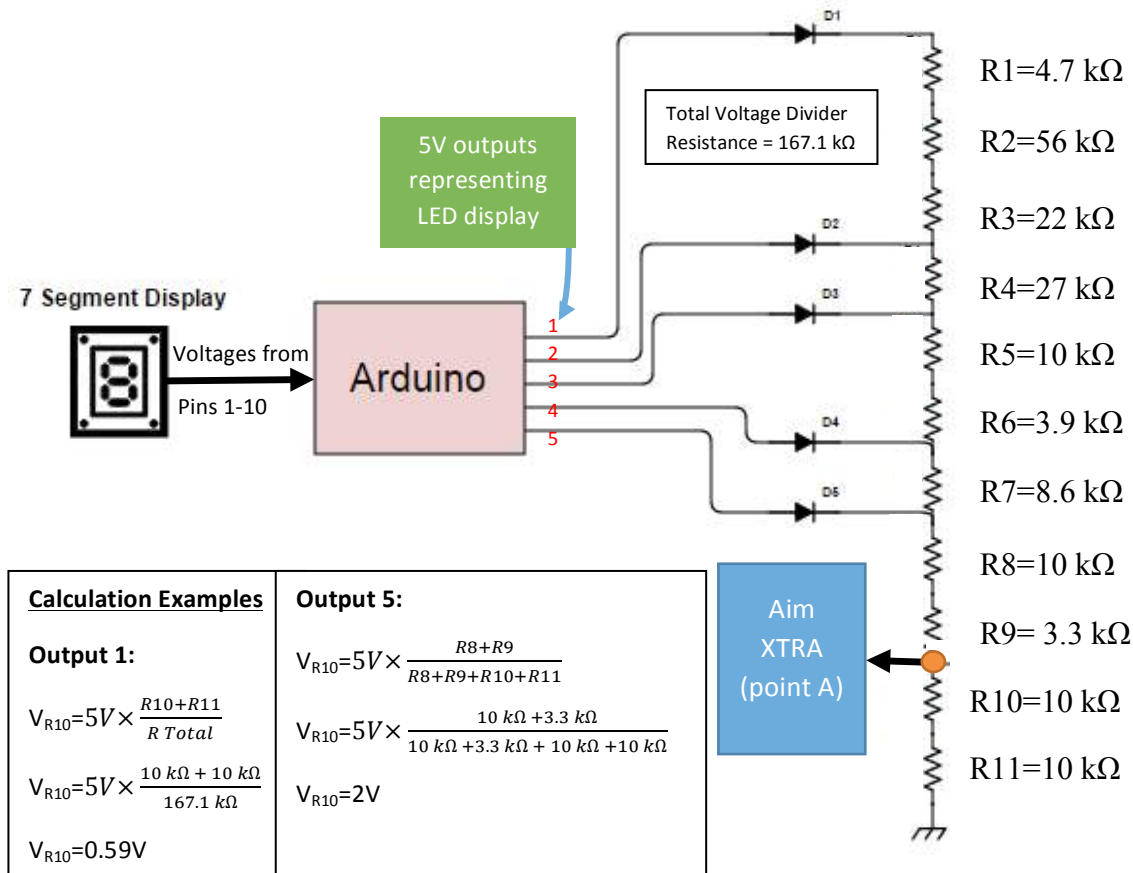


Figure 5: Simplified schematic of LED/Arduino/voltage divider/AX integration circuit

**Electrical power system development.** During operation, the Arduino required 7-20 volts, the radar detector required 10-12 volts, and the AX required 3.6-7.4 volts. One battery pack was used to reduce weight and consisted of three lithium ion batteries in series to supply the payload with 12.6 volts peak. Zener regulator circuitry was also developed to supply the AX with 6.8 V (Fig. 6).

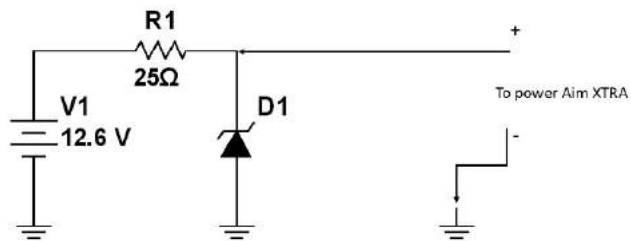


Figure 6: Zener Regulator Circuit

Battery life also needed to be monitored to prevent depleting the battery pack to dangerous levels. This was accomplished using the Arduino to control an NPN transistor circuit (Fig. 7) and voltage divider. To conserve energy the transistor was only forward biased every 5 seconds for one second. The voltage divider was used to step the battery voltage from 0 to 12.6 nominal volts down to 0 to 5 volts to be compatible with the Arduino. After the voltage was stepped down an analog input on the Arduino was then used to measure battery voltage. The measured voltage was used to make calculations, derived from the batteries' power curve that would decide which of four digital pins to turn high (5V). The four pins were designated 25%, 50%, 75%, and 100% battery life (Fig. 8). The pins were fixed to a DAC which depending on the pin that is high will supply the AX a signal voltage from 3.1V (100%) to .8V (25%). This was relayed in real time to the base unit via the AX.

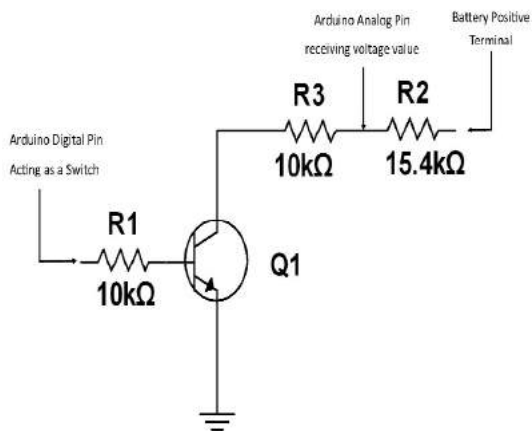


Figure 7: Transistor circuit used to monitor battery voltage. Transistor completes circuit when biased, and produces voltage at point A, which is then sent back to Arduino for analysis.

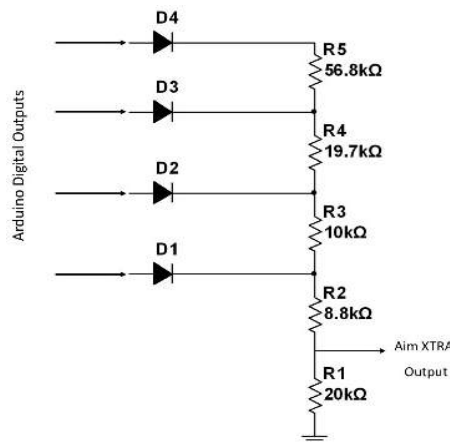


Figure 8: Arduino digital outputs provide 5V to one of 4 inputs to voltage divider depending on battery voltage. AX output received voltage from 0.8-3.1V which indicates battery condition.

**Radar efficiency testing.** With little background knowledge on the propagation of microwaves, it was important to understand the relationship of signal strength and alignment of the radar gun and detector. To test this relationship, a ground experiment measuring received signal strength versus distance at several offset angles,  $\theta$ , was performed (Fig. 9). It was found that the maximum signal strength was achieved when the radar horn was pointed directly at the radar gun. The signal strength degraded rapidly when the horn was oriented more than  $15^\circ$  from the axis to the radar gun, which was not surprising due to the  $12^\circ$  beam width of the radar gun (Fig. 10).

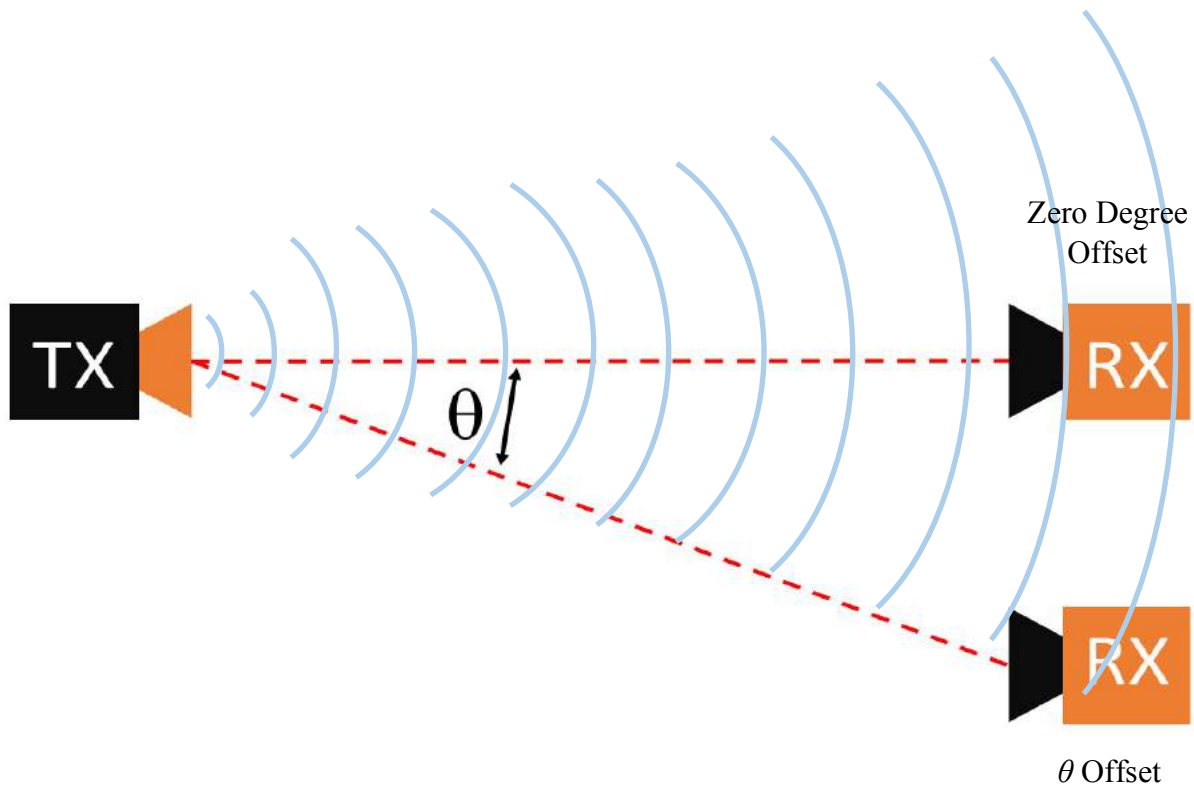


Figure 9: Illustrates the concept of offsetting the receiver (RX) from the transmitter (TX). The horn of the RX remains parallel to the horn of the TX, however, the RX is moved in one direction to create a change in the angle between the center of the TX and RX horns. Microwaves, shown in blue, have greater intensity when the RX is at zero degree offset. Simulated microwaves are shown in blue for visual purposes.

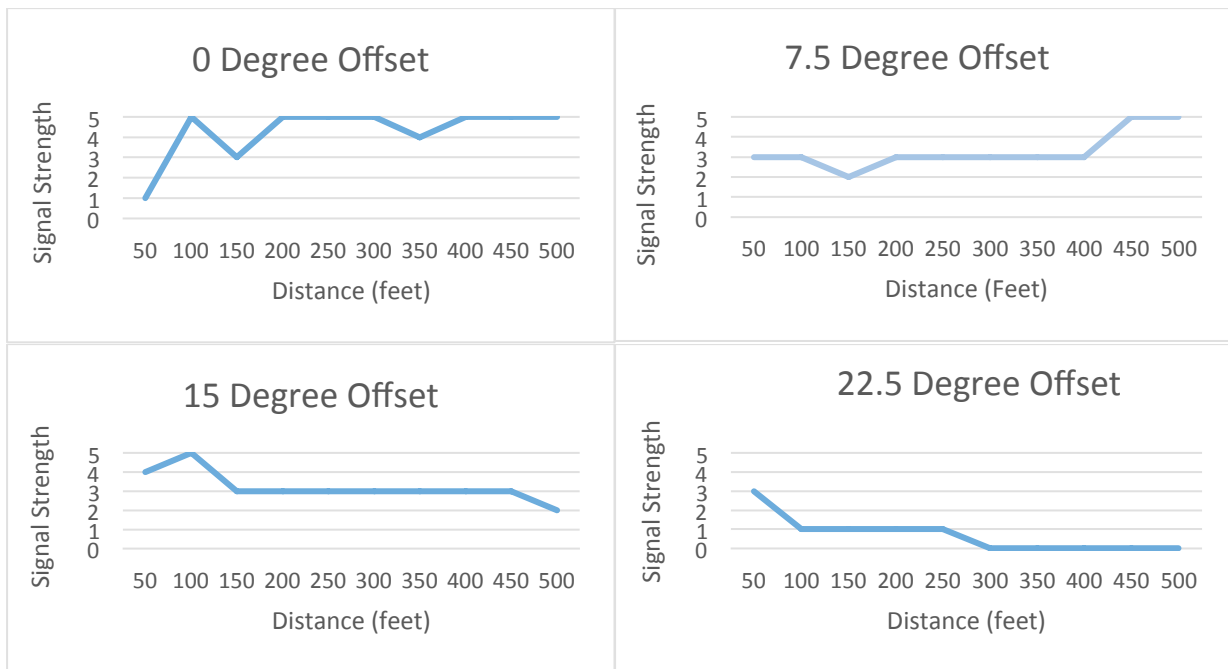


Figure 10: Changes in signal strength, as displayed by radar detector, for varying degrees of offset from transmitter.

Multiple trials were conducted with the radar detector horn facing directly towards the gun and directly away from the gun, or a 180° rotation (Fig. 11). The graph in Figure 12 shows the average signal strength is higher with the horn facing directly towards the gun. It is interesting to note there is still signal detection with the horn facing away from the gun. Perhaps scattered or reflected microwaves could still provide power transfer, but with decreased efficiency. It was also found that there was a direct relationship to signal strength and separation distance. The signal strength dropped, as expected, as the separation distance increase between the gun and detector.

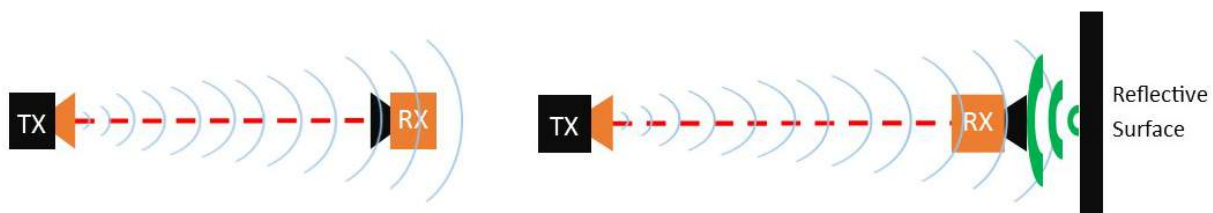


Figure 11: RX and TX orientation during testing. Reflective surface represents microwave scatter from surrounding vehicles, buildings, persons, etc. Reflected microwaves shown in green.

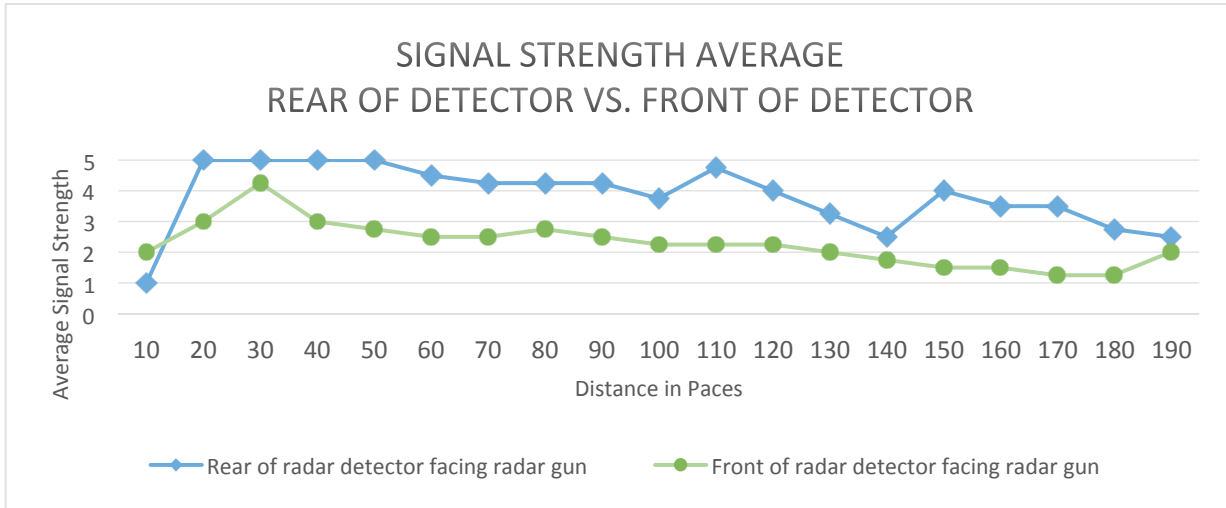


Figure 12: Average signal strength under 2 conditions over multiple trials.

**Arduino programmable microcontroller.** Weather monitoring was achieved with a Spark Fun HIH6130 chip to record humidity and temperature. These transducers would create a known voltage for a specific condition. Any changes in these voltages would indicate a change in conditions. These values were sent to an analog input on the Arduino for data logging. A Kestrel weather station ground unit was used to monitor weather conditions on the ground to enable comparison to the weather conditions on the aerostat. Any changes in conditions would indicate the conditions the microwaves will be propagating through. This data has not yet been analyzed.

For the data acquisition we used a Spark Fun SD shield. This shield was designed to be used with the Arduino Uno. Due to the need for a larger controller with more I/O pins, an Arduino Mega was implemented. This change required modification to the SD shield by clipping pins 11, 12, and 13, and using jumpers to make new connections to pins 51, 52, and 53. Signal strength, distance from the radar gun, battery power, weather conditions, and time stamps were saved to an onboard SD card in a .txt format. This data was later converted from a .txt file to a .csv file. The .csv file made enabled data viewing in an Excel format.

**AX flight computer.** The objectives of the AX were to act as the onboard flight computer, log voltage measurements of the EPS and MWB, provide GPS data including location and altitude, as well as provide a means to monitor this data in real time during flight. Some of the data, including atmospheric conditions, GPS, and altitude, were natively programmed sensors and were plug and play. To obtain data regarding the EPS and MWB, the data had to be converted to voltages in the range of 0-3.1V, which is explained under the respective subsystems. Once these voltages were produced, they were sent to the inputs of the AX and then transmitted wirelessly to the base station. These voltages then appeared as a function of time and could be easily analyzed during flight to provide an indication of performance.

## Flight 1 Analysis

**Pre-flight.** While preparing to launch the aerostat, each sub-team was able to efficiently set up the equipment necessary to perform the experiment and collect data. Extension cords were used to power laptop chargers and a DC power supply used for the radar gun. Ground testing of the platform was performed to ensure data transmission, and the aerostat was laid out for inflation. Once the payload had been armed and the aerostat was unpackaged, inflation began. We filled the aerostat to approximately neutral buoyancy to allow us to connect the payload platform and tether.

**Flight.** During the flight, irregular signals from the MWB and EPS subsystems to the AX base unit required the aerostat to be brought down for troubleshooting. Signals should have been smooth DC values but instead were noisy. 60 Hz noise was present everywhere on payload circuitry as seen on our oscilloscope. This could have been a result of noisy power supplied to the oscilloscope due to the long extension cords, or multiple instruments plugged into the power strip. In the future, a generator positioned near the microwave transmitter would be desirable to reduce line loss in the extension cords and eliminate noisy power. After several attempts to obtain data transmission from the AX to its base station, it was realized that the data was invalid due to wiring connection failure. No useable data from MWB was obtained.

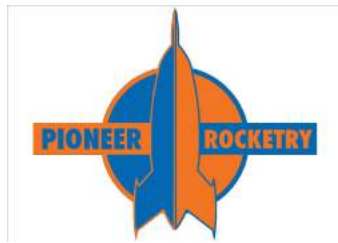
**Post flight discussion.** The original supplied helium tank was empty, requiring an emergency replacement. Wiring connection failures were present between the AX and Arduino producing unreliable data. MWB circuit produced a noisy, unusable signal. A uniform method to match time between AX, Arduino, and note taking will be required to reduce error in data analysis. The soldering of all connections between subsystems will help eliminate wiring connection failures on a launch day—although significant testing of subsystems prior to soldering will be required. Our team also hoped to compare results from the radar efficiency ground testing to the results from the flight. However, due to the wiring connection failures, we were unable to obtain any useable data, and therefore, unable to compare efficiency results. The WPS worked effectively but mounting WPS to trailer would simplify transportation and eliminate the need for ballast weighting.

## Conclusion and Next Steps

One luxury of this project is that it spans 2 years. We have nearly completed year 1, and now have year 2 to refine our processes and techniques. A new platform is in development which will allow for better organization of our instruments and reduction in weight, a gimbal system to aim the radar detector is also in development, and the beginning stages of research are being completed for development of a rectenna for microwave conversion to DC power. All of the developed systems bring the goal of wireless power transmission closer. For example, in developing the radar signal strength circuit, we can compare this data to the voltages produced by the rectenna to determine the efficiency of power transfer. Also, because this technology has been proven on a large scale, our team knows the concept is valid. However, the power of the transmitters used in this experiment was 10 kW, compared to our microwave transmitter which is 10 W. We feel this could present a challenge in reading the small signals we expect to receive at the rectenna.

## References

- Kustom Signals, Inc. (2011). *Falcon Hand-Held Traffic Radar Operator's Manual*. Lenexa, KS: Kustom Signals, Inc.
- Lan Sun Luk, J., Celeste, A., Romanacce, P., Chane Kuang Sang, L., & Gatina, J. (1997). Point-to-Point Wireless Power Transportation in Reunion Island. *48th International Astronautical Congress*. Turin, Italy: International Astronautical Federation.
- Pozar, D. M. (2012). *Microwave Engineer, Fourth Edition*. Amherst, MA: John Wiley & Sons, Inc.



## **Pioneer Rocketry 2015 WSGC Collegiate Rocket Competition**

Jake Ellenberger, Adrian Guither, Trent Cybela (et alt.)

Society of Physics Students: University of Wisconsin-Platteville

### **Abstract**

The objective of the 2015 Wisconsin Space Grant Consortium (WSGC) Collegiate Rocket Competition was to design and build a two stage "Boosted Dart" - style rocket to achieve maximum altitude. The rocket was propelled by a single grain 54mm rocket motor (I445 Vmax). Extensive design and modeling was done to optimize the design to achieve maximum altitude. An electronic device designed to measure the rotation of the rocket that would then be correlated to rotation observed with video captured by a camera system. The rocket performed as expected in most aspects, completing most objectives per competition parameters. The flight of the boosted dart however ended in failure, as a delayed ejection of the parachute resulted in compounding failures leading to the loss of the rocket. The camera, having fallen separate from the rocket body, had survived the flight. The video was analyzed and the flights apogee was estimated to be 6000ft. The following report details the design and construction of Pioneer Rocketry's 2015 competition rocket, along with information regarding Pioneer Rocketry's growth as both an educational and professional organization.

### **Year in Review**

Pioneer rocketry is now entering its third year of competition, and is now busier than ever before. Due to our success in last year's competition, Pioneer Rocketry has had the privilege presenting before the Dean of Engineering, Math, and Science (EMS) at the University of Wisconsin-Platteville's EMS Industrial Advisory Board Meeting. We were able to not only show Pioneer Rocketry's strength of presence on campus, but also the importance of aerospace and related fields to those who lead the university. We have made our presence known through several appearances on campus promoting Pioneer Rocketry and displaying our competition rockets in display cabinets.

This year Pioneer Rocketry made a greater emphasis on spreading our passion and excitement for both engineering and rocketry, as our team led two outreach events. The first was our instruction of the space exploration merit badge at the Merit Badge Midway hosted here on campus. Through three consecutive weekends our team taught boy scouts about space exploration as well as the design and construction of rockets. The second Pioneer Rocketry led

outreach event was through Sky's The Limit, an outreach program that introduces young women to careers in STEM fields. We led a group of girls through a rocketry related science experiment that allowed them to think through the scientific process and analyze how the setup for an experiment can affect the results. Pioneer Rocketry has taught about the exciting hobby of High Powered Rocketry and STEM in general to high schools in both Verona and Manawa, Wisconsin.

Beyond expanding Pioneer Rocketry's outreach; this year marks additional changes in how we design, build, and test rockets. This year we are focusing on reducing our reliance on per-manufactured parts and creating the ideal rocket for our organization. To achieve this goal we have spent the past year testing the application of 3D printed parts for rocketry. We have explored and validated their use for nosecones and fin construction.

One of the most influential changes since last year would be our ability to launch at Pioneer Farms, the university owned farm. Last spring we were able to obtain a waiver from the FAA to allow us to launch at the farms. Through a great deal of communication with both the university and farm's neighboring Pioneer Farms we were able to set up a launch site here in Platteville. This launch site removed our reliance on the Richard Bong Recreation Area as the only launch site in Wisconsin. We were able to make use of this launch site for the test launch of two boosted dart prototypes. Through these launches we were able to learn invaluable information about the boosted dart concept and the challenges this year's competition brings. In the future the accessibility of the farms as a launch site will allow the rapid testing of rocketry design and construction concepts.

Jake Ellenberger  
President, Pioneer Rocketry

## **Rocket Design**

**General Design:** The competition parameters for this year called for the development of an unpowered kinetic dart (also referred to as boosted dart), lifted by a separable booster stage. The objective will be to reach the highest altitude possible with the dart, which has no capability of producing thrust. The two stage configuration inspired the name "Thunder & Lightning" (actual designation PR-3) for the competition rocket - Thunder being the booster, and Lightning being the dart. A graphical cross section of PR-3 is shown in Figure 1. The dart carries a suite of electronics gathering data on both its orientation and altitude. Video is captured from the dart as well from an aft-mounted camera. The following section will break down the main design features of both the booster and dart sections of the rocket.

### **Dart**

#### **Nosecone**

The nosecone selected for the dart is a PLA 3D printed Nosecone. The shape is a 4.25 in LV Haack and was selected to maximize volume while reducing drag. This volume was

needed as the nosecone features a compartment to hold a 9 volt battery as well as a 3/8 in bolt counterweight. This nosecone's fineness ratio of 4.65 (length/diameter) was selected after extensive CFD Simulation in the program Star CCM+ to find the optimal ratio between length and diameter. It was determined that increasing the nosecone length will cause the viscous forces of the air to start increasing due to increased surface area. If the nosecone length decreased then the pressure forces will increase due to the increased bluntness of the nosecone.

### **Airframe**

The body tube selected for the dart is 1.5 in carbon fiber tube. Carbon fiber was selected for two main reasons. The first is the increased strength and reduced weight of the material. The second reason is the resistance to water. Given the wet conditions at the Richard Bong Recreation Area launch site, moisture resistance is an important factor. To minimize the drag on the dart the length of the body tube was minimized. The final length of 18 in was selected as a middle ground between internal volume, for things such as avionics and parachutes, and length reduction for things such as drag.

### **Weights**

The Dart has the capacity for housing up to 500g of counter weight. This modularity will allow the proper selection of weight to maximize altitude. To determine the difference between not enough momentum to overcome drag and too much mass a Simulink model was created. This model takes into account the booster mass and drag as well as the darts mass and drag.

The Simulink model indicates we should have a mass around 765g. An optimization was also run in open rocket to find an optimal mass of 753g.

### **Avionics Bay**

The avionics bay consists of a sled between two bulkheads. Two 6-32 threaded rods span the length of the AV bay and tie the nosecone, counterweights, AV sled, and parachute mounting point together. The rods will carry the load of parachute ejection and descent. Refer to the section on electronics titled "Avionics Bay" for further information on the data logging, video, recovery, and deployment systems.

### **Recovery**

The dart will fly on a 24 in hemispherical parachute made of ripstop nylon features a spill hole. The hemispherical shape and spill hole increase the stability of the parachute during descent. Attaching the parachutes to the rocket is Kevlar shock cord. The Kevlar was selected due to its incredible strength and heat resistance, both of these characteristics are valuable in rocketry. Unlike traditional rockets the parachute is deployed from the bottom of the rocket so there is a reduced chance of breaking fins on impact.

### **Camera Pod**

Like the nosecone on the dart the tailcone is also 3D printed with PLA plastic. 3D printing the tailcone allowed for a simple construction of an otherwise complex geometry which was needed to house the camera. The camera pod is roughly elliptical shape and is shaped around fitting the camera. The camera is sealed inside by a bulkhead attaching to the shock cord. Due to the camera being mounted to the bottom of the rocket and having the camera pod separate, the camera will always be pointed downward and have a view of the ground.

### **Fins**

The fins on the dart are composed of .06in thick carbon fiber plate. Their shape is trapezoidal, with dimensions that were selected to maximize stability and reduce drag. The fins are swept back at the mid chord 30 degrees to move the center of pressure backwards. The fins also have a higher than normal aspect ratio (span/average chord) with a span of 1.64in. This increased span of the lift generated by the fins. The root chord of the fins is 1.75 in tapering down to a tip chord of .875 in.

### **Booster**

#### **Transition**

The transition between the dart and booster is the third 3D printed part on this rocket. The Transition serves two purposes on the rocket. The first is to smoothly increase the rocket diameter from the 1.5 in tube of the dart to the 3 in tube of the booster. The second purpose of the transition is to hold the base of the dart during the boost portion of flight. The entire tailcone of the dart as well as 0.25 in of body tube are contained in the transition. Inside the transition there are two plates of wood with the exact profile of the tailcone cut into them allowing for secure retention against rotation and lateral movements but no restriction axially.

#### **Airframe**

Like the dart, the booster tube is also carbon fiber and is 3 in in diameter. To maximize momentum imparted to the dart the booster needs to be as light as possible. To achieve this, the booster was made to be as short as possible. The final length of 14 in was determined to produce an ideal combination between stability and weight.

#### **Recovery**

Due to the similar masses the booster also flies on a 24 in hemispherical parachute. This parachute size and design was determined using the same methods discussed previously with the dart. The shock cord is also Kevlar.

### **Fins**

For the booster the fins are also made from .06 in carbon fiber. For both aesthetic and aerodynamic purposes they are the same shape as the dart fins but scaled to be much bigger. The root chord is 4.125 in tapering to a tip chord of 2.063 in with a span of 3.867 in.

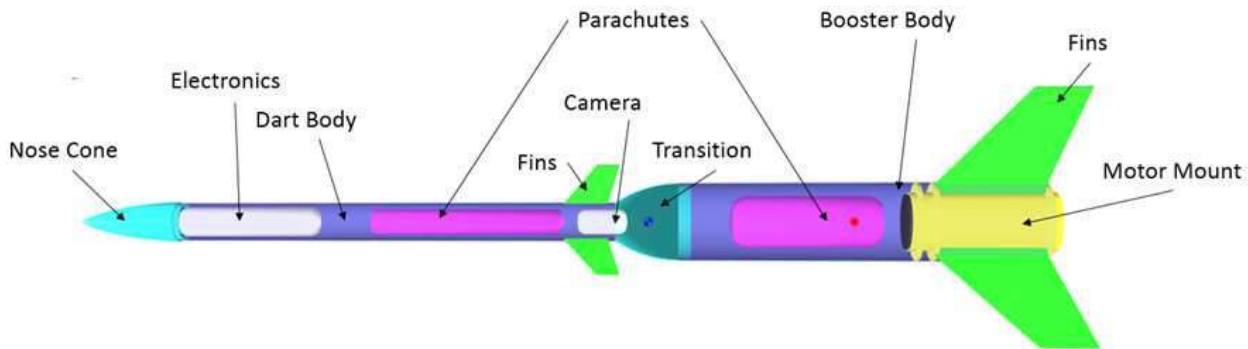


Figure 1: Cross section diagram of PR-3 “Thunder and Lightning”

### Stability Analysis

Based on the open rocket model the stability margin for the combined booster and dart with an unburnt motor is 2.5. At the moment before ideal separation, which occurs at motor burnout, the combined rocket’s stability margin will grow to 3.2. The center of gravity will move forward 2.2 in to 21.6 in from the tip of the rocket. As a combined entity the rocket is incredibly stable. After Separation the dart has a stability margin of 3.4. The separated booster has a stability margin of 0.5. While normally a rocket with a stability margin of 0.5 would raise concerns the fact that the rocket is already moving and stable at the point of separation mitigates these concerns. These claims can be supported through analysis of test flight video taken from the previous prototype dart. In that video you can see the booster trailing behind the dart perfectly stable.

### Propulsion System Specifications

In accordance to the competition parameters, Thunder and Lightning will be flown on a CTI I445-Vmax. This motor provides a more than adequate thrust to weight ratio of 28.8:1. The Vmax propellant is a good propellant choice for a boosted dart style of rocket because the burn time is very short, allowing most of the energy to be transferred to the dart. Flying on this motor, Thunder and Lightning will have a more than adequate velocity of 66 miles per hour upon leaving a six foot rail, ensuring a stable flight.

### Anticipated Performance

To anticipate the performance of the competition rocket, two main tools were used in its both design and simulation. The first of these tools is OpenRocket which throughout the past two years has been extensively used to simulate the team’s rocket flights and accuracy its continuity has been validated. OpenRocket serves as Pioneer Rocketry’s primary design tool.

The second simulation tool used is a custom made model in Simulink. Simulink is a MathWorks developed graphical programming language tool used for modeling and simulating dynamic systems. The custom model is a simplified 1 dimensional simulation that was created to explore the relationship between rocket characteristics such as dart mass, dart

drag coefficient, booster mass, and booster drag coefficient on flight performance like apogee, max velocity, and peak acceleration. This tool's purpose in design was to find the optimal mass for the dart to maximize apogee.

For the estimation of apogee an OpenRocket simulation was run under the assumption that separation occurs at motor burnout. This simulation predicts that the rocket has an apogee of 5,140 ft. OpenRocket simulations under predicted a previous boosted dart test flight by around 500 ft. It is believed that due to the unique nature of the boosted dart in terms of modeling the drag on a tailcone and sensitivity to separation timing led to the inaccurate simulation results. If OpenRocket is overestimating the drag then the predicted apogee of the dart should be higher, somewhere around 5,500 ft.

This same OpenRocket simulation was used to estimate the altitude of dart separation. This simulation predicts a separation at an altitude of 500 ft. In test flight there was unfortunately had excessive friction between the stages which delayed the separation until several seconds after motor burnout, there was no data that could be compared to predicted altitude.

The Peak Acceleration estimated by the simulation is 28.26G's. To compare that to the test flight rocket which had a predicted acceleration of 22.8G's and the two raven altimeters measured 24.8G's from the dart and 29.3G's from the booster. While it is not completely understood 5G difference between two accelerometers on the same rocket it shows that OpenRocket somewhat underestimates the acceleration. Since the results of the simulation are very reliant on the mass of the model being accurate it is predicted that OpenRocket is reliable with its estimation of 28.26G's.

### **Payload System**

This year's competition requirements were to measure and record the pitch, roll, and yaw, of the dart, namely the rotation around the dart's three major axes, during the duration of the dart's flight. Additionally, downward facing video captured from the dart during the airborne period following the launch. To achieve the latter goal, a striped down action camera which mounts inside the secondary electronics bay located in the tail cone of the dart was selected. This configuration allows us to get downward facing video without adding obstructions to airflow to the dart that would increase the air resistance. It also allows the camera to passively reorient to continue taking downward facing video after deployment of the parachute.

The primary challenge was to develop a system that records the rotation of the boosted dart during its flight for later comparison with our flight video. To do this a sensor kit around an Arduino Micro was built. This system utilizes a 9 Degree of Freedom sensor capable of recording the angular acceleration of the rocket as well as the magnetic field found at the rocket. The angular acceleration can be integrated to find the rocket's rotation. The earth's magnetic field will have a very nearly constant strength and direction, and this will be utilized to determine the rockets orientation.

## **Construction**

This year's competition posed many unique challenges to construction, due to the unique boosted dart design. This is the first 54mm motor, the smallest diameter, and the shortest rocket that Pioneer Rocketry has ever built.

A new construction technique, namely surface mounted fins, was used because of the unique design of this year's competition rocket and the inability to extend the fins through the darts body tube. This type of fin only appears on the dart; the booster section has traditional through the wall fins with precision milled fin slots. Laser cut fin guides were also used to ensure proper alignment of the fins.

Also, new from previous years is the addition of multiple new materials, including carbon fiber airframe, carbon fiber fins, and various 3D printed components. Because of the added strength of the carbon fiber airframe and fins, we chose not to fiberglass over the fins.

When dealing with potentially harmful materials, all proper safety measures were observed. Material safety data sheets were available for all volatile materials and proper safety equipment such as glasses and respirators were utilized.

The laser cutter was extensively used during the construction of the rocket. Components made on the laser cutter include bulkheads, centering rings, electronics sleds, and a cradle to hold the dart in place during boost.

## **Empirical Testing**

In order to prepare for the new concepts introduced by this year's competition, the booster section of a previously built Super DX3 that was previously used in a level 1 certification. The resulting rocket was dubbed the Super DartX3. Although the Super DartX3 was not a success due to several staging failures, a great deal was learned about the boosted dart concept and the challenges it brings. The Super DartX3 was our first rocket to utilize surface mounted fins, as well as 3D printed fins.

Building on what was learned from the Super DartX3, a prototype competition rocket was constructed, named "Dazed and Confused" for its ultra-visible paint scheme. In building this rocket, the goal was to be as close as possible to the final competition rocket. Dazed and Confused fixed the staging problems that had plagued the Super DartX3's test flight but unfortunately non fire resistant shock cord was used, resulting in a ballistic trajectory ending in a high velocity impact. In-flight video showing the stage separation can be seen in Figure 2. In the future, Kevlar shock cord will be used because it is sufficiently fire retardant.



Figure 2: Image taken from the Dazed and Confused, dart section video camera during ascent-

**Conclusion:** Pioneer Rocketry has been blessed with a lot of success this past year. Moving forward, we have worked with the University of Wisconsin-Platteville to obtain a launch location near campus. We have worked hard to fully utilize these opportunities, and we are grateful for all the guidance, assistance, and funding provided by the Wisconsin Space Grant Consortium and Tripoli Rocketry.

Our member base is not small, and for this reason Pioneer Rocketry is modeled differently than most contenders in this competition. Our intent is to become more than just an isolated group of rocketeers, but rather to become an integral part of our University's selection of student organizations. It is our hope that over the coming years we will expand our membership, build more rockets, conduct more launches, receive more High Powered Rocketry certifications, and lend credit to the use of aerospace applications as part of an undergraduate college curriculum.

## Red Hawk Rocketry Boosted Dart

Akash Sen, Paul Ninneman, Katie VanderGalien, Jadee Kellogg, Robert Enright, Jimmy Izewski

Ripon College

### Abstract

As part of the Wisconsin Space Grant Consortium competition, Red Hawk Rocketry built a rocket for the Collegiate Rocket Launch Competition's non-engineering contest. The launch went well, albeit a little unstable, veering in the direction of the wind. This was unexpected because our RockSim model was considerably overstable, so it should have turned into the wind. Its apogee was around 1000 feet because our rocket was rather massive compared to other teams. However, because of its low apogee, we were able to easily locate and retrieve the rocket upon landing, as intended. Finally, all three aspects of the challenge were completed successfully; the dart separated, we were able to access mid-flight rotation data from our gyroscope, and we obtained on board, down looking video during the flight.

SCHOOL	Ripon College		Team	Red Hawk Rocketry	
<b>1</b>	Operation (determined by RSO or designee)				✓
	Launch				✓
	Separation of Dart from Booster Before Apogee	Considered Unstable		✓	
	Recovery deployment - Booster				✓
	- Dart				✓
	Recovered				✓
	Determined to be in flyable condition				✓
			<b>Predicted</b>	<b>Actual</b>	
<b>2</b>	Maximum Altitude	(ft)	2331.21	1086	
<b>3</b>	Peak Acceleration	(ft/s <sup>2</sup> )	418.34	??	

**Figure 1:** Flight performance comparison sheet showing information about the flight operations as well as the maximum altitude and separation.

### Performance Characteristics

Operation characteristics were determined by a WSGC allflite on the day of the launch. Maximum altitude and peak acceleration prediction was made by the rocket flight simulation program RockSim. The actual maximum altitude was taken by the competition altimeter, the Raven. Unfortunately, our team was unable to retrieve the peak acceleration from our altimeter due to electronic complications involving the wires required to connect to a computer. As seen below in Figure 1, our dart did separate from the booster, but the separation was considered unstable because the entire rocket tipped around 45 to about a second into the launch. The recovery devices for the dart and the booster both deployed as expected, and we were able to recover both parts of our boosted dart.

Critical financial support was received by WSGC.

Although our rocket was in flyable condition after retrieval, small tears in two of the couplers were noticed, but were mild enough that our rocket could still be flown. The damages sustained on these couplers were due to the selection of low quality components. We believe the damage may have been caused by a lashing of the shock cord when the parachutes deployed. Unfortunately, since we were not able to retrieve the acceleration data from our gyroscope, we could not form a comparison graph with the predicted data. However, Figure 2 has our predicted acceleration graph.

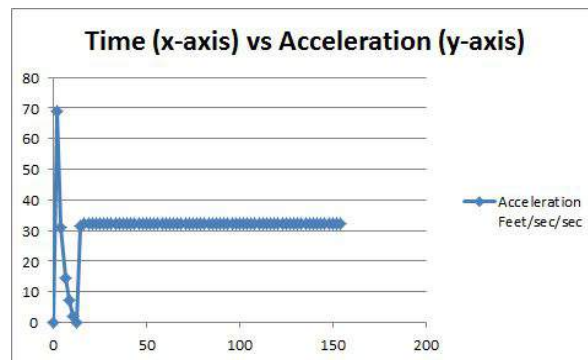


Figure 2: Predicted Acceleration Vs Time graph from RockSim

### Discussion and Results

Our apogee was less than half of what we originally thought it would reach, based on the RockSim file. This could be due to factors like adding mass to the booster last minute to balance out the flight of the rocket, not taking into account a large increase in mass for both electronic bays compared to our theoretical RockSim launch, as well as weather conditions on the day of the launch. We found that the direction that the rocket flew upon launch to be unexpected. Even with the unaccounted added mass, the rocket should have been noticeably overstable, thus weathercocking into the wind. However, upon launch the rocket veered away from the wind instead of into it. One possible explanation could be one or more of the fins vibrating, causing instability. The fact that the rocket turned early, suggesting that it was not flying perpendicular to the ground and probably a leading cause of our lower than expected apogee. The dart did not sit in the booster at a slight angle from vertical. The dart was not set exactly perpendicular to the ground. This slight construction error may have caused some of the instability and curve in the launch. Due to the pressure of the situation and the speed required, it is possible that the wires were not set correctly, thus causing the rocket's engine to not burn evenly pushing it away from the wind.

Critical financial support was received by WSGC.

An important note about the launch day is that our time on the pad had to be limited due to memory constrictions for the gyroscope data. We constructed switches out of wire that had to be twisted together and taped on the outside of the rocket to turn on all of our electronics. There was a total of four switches, which greatly increased the stress on the launch pad, especially with our time constraint. When we were ready to launch, there was no continuity for our rocket, and a launch assistant had to run back to the pad and reconnect the wires for the launch to take place. Although we had this small setback, we still had plenty of data from the gyroscope. For the future, we plan to buy physical switches to place in the rocket, so we don't have the added worry and time of twisting wires shortly before the launch.

The video captured by our internal camera was over 30 minutes long due to the fact it waited so long on the launch pad before connecting the switch to turn on the gyroscope. The camera had to be turned on remotely and placed inside the boat tail to record video. The camera was then secured into place using a bulkhead and screws and a piece of cloth was wrapped around it to limit movement. It was not until near the end of the video that the footage of the launch was recorded. Since our camera was placed inside the boat tail and looking down into the booster, the footage was completely black until separation. However, we were able to hear the countdown and the launch while the camera was filming the inside of the booster. After the dart separation occurred, the film became completely white until the camera adjusted for the light difference. Figure 3 shows a still image of the initial separation, which is still directed towards the inside of the booster.



**Figure 3:** A picture of the dart at the first point of separation from the booster.

More screenshots of the footage can be seen below in Figures 5-7. Figure 5 appears to be the dart's apogee, Figure 6 is showing the moment when the parachute comes out, and Figure 7 is a photo of the ground when the dart is descending.

Critical financial support was received by WSGC.



**Figure 5:** The ground as depicted from apogee



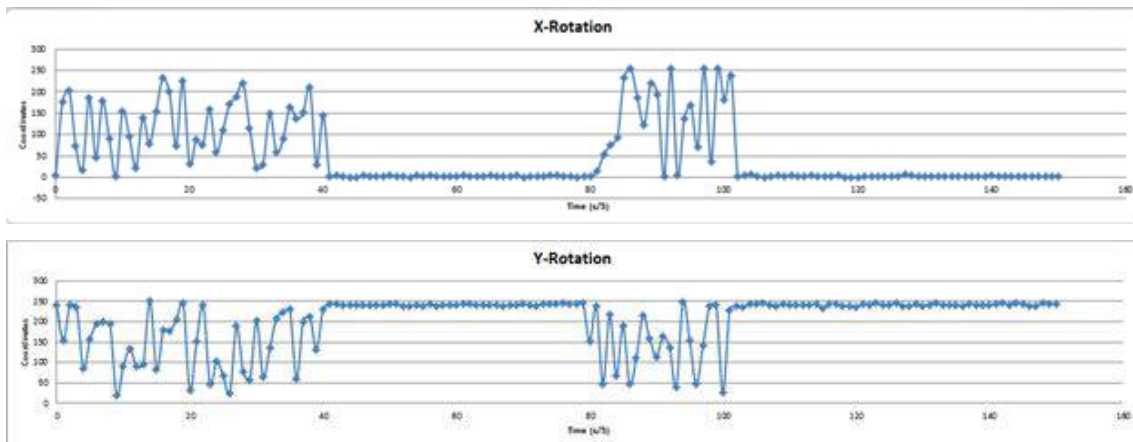
**Figure 6:** Picture of the dart jostling around due to the parachute ejection, the red spot being the parachute



**Figure 7:** View from the bottom of the boattail when descending down to the ground.

The white ring around our video is the boat tail, as we could not fit the camera down further to get a wider range of view without taking off too much of the boat tail. The ground looks more curved due to the camera having a fisheye lens. We were very happy with the success of our on board camera, as it allowed us to compare the rotation measured by the gyroscope.

Our method of measuring the rotation of the dart using the l3g4200d triple axis gyroscope breakout was successful. In order to properly visualize the x, y, and z data points that the gyroscope recorded, we needed to modify a few points. This is due to the fact that once the dart rotated around, the degrees looped from 0 to 360, which meant that the low numbers corresponded to the high numbers. It was clear from random spikes where this occurred and we simply bumped those numbers back down. Once this was done we were able to use Excel to create a scatter plot of each coordinate versus time. The graphs for the x, y, and z versus time are shown below in Figures 9-11. It is important to note that our Arduino was set to record approximately 5 data points per second.



Critical financial support was received by WSGC.

Figure 10: Degrees of rotation of our dart vs time in the y-direction

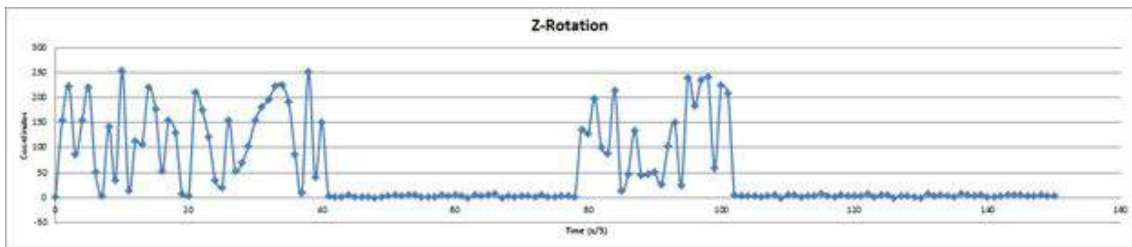


Figure 11: Degrees of rotation of our dart vs time in the z-direction

Here we can see that the z orientation is orientated vertically. If you look at the graph, we are able to interpret sections of the launch based off this knowledge. From the time of 0 to 5.4 seconds (which corresponds to the points 0 to 27 on the z-rotation graph), we are able to see our rocket weathercocking. Then from 5.4 seconds to 7 seconds (which corresponds to the points 27 to 35 on the graph), we are able to see that our dart clearly turns in one direction. This is confirmed from video footage, as we notice our dart veered mainly in the opposite direction that we had expected. From there we can see from 7.4 seconds to 8 seconds (corresponding to points 37 to 40), the parachute must deploy because of the sporadic movement of the dart. Once the parachute was fully deployed we can see that there is a clear period of time from 8.2 seconds to 15.4 seconds (points 41 to 77) in which there is a stable calm point for our dart. This area is clearly when our dart was descending to the ground. At 15.8 seconds to 20.2 seconds (corresponding to points 79 to 101) there is another section of sporadic movement. This is when the dart first hits the ground, and the parachute continues to pull it till both eventually settle down. The rest of our data points then settle down to a constant number for the remainder of the time. If we look at the x and the y rotation, we are able to conclude that the dart rotated approximately 12 times over 7.4 seconds before the parachute deployed. This means that it had a rotation rate of 1.6 rotations per second during that time frame.

## Conclusion

Our rocket had a much lower apogee than expected, but because of this we were able to recover our rocket and have it deemed flyable. We believe the low apogee was caused by the rocket's weight which was more than 130 oz and because the flight was not perfectly vertical. Our on board camera successfully filmed the separation of the dart and the booster, as well as the rest of the flight. We were also able to obtain data for the rotation of our dart in the x,y, and z directions over the course of its flight. Our rotation analysis from the gyroscope matched up with the footage from the camera. Overall, Red Hawk

Critical financial support was received by WSGC.

Rocketry had a largely successful flight, completing all of the challenges for this year's competition. Red Hawk Rocketry would like to thank WSGC once again for this wonderful opportunity, and we look forward to competing again next year!

Critical financial support was received by WSGC.

# 2015 WSGC Elijah High-Altitude Balloon Payload Project Final Report

September 14, 2015

Ben Jensen<sup>1</sup>, Nate Klassen<sup>2</sup>, Woodrow Walker<sup>1</sup>, Scott Frazier<sup>3</sup>, Kai Swanson<sup>1</sup>, Taylor Davitz<sup>1</sup>

<sup>1</sup>Milwaukee School of Engineering, <sup>2</sup>University of Wisconsin-Whitewater, <sup>3</sup>University of Wisconsin-Milwaukee

## Abstract

The purpose of this report is to discuss the research, development, and findings of several experiments performed on a high-altitude balloon payload platform. The team decided of the following five experiments to be performed during the flight: Oxygen Generation, Internal Heating, Speed of Sound Properties, Ozone Levels, and a new payload structure concept. The entire team was required to research and develop new skills to effectively design our experiments, including: Arduino programming, 3-D modeling/printing, soldering, launch equipment handling, and construction techniques. While the launch was successful, we did fall short of our overall goal in terms of data acquisition. The internship proved to be a rewarding introductory experience to real-world engineering. The project help us learn how to implement the entirety of the engineering process, using each person's strengths to achieve an objective.

## Introduction

The goal for the internship team was to research, design, and execute experiments aboard a high-altitude balloon platform. The team would collect and analyze data from each experiment. There were several constraints for the project, including budget, weight, and size. The team was given full control over what we wanted to research, and decided five upon concepts: Oxygen Generation, Internal Heating, Speed of Sound Properties, Ozone Levels, and a new payload structure concept.

## Oxygen Generation

As the altitude increases, we see a corresponding decrease in air pressure. This creates an increasingly hostile environment for human life, since as the air pressure decreases, there is less breathable air. With this idea in mind, we set out to research methods of producing breathable air in the near-space environment.

**Purpose:** There are several methods for producing oxygen that we could have used in this experiment. We narrowed it down to three options, from which one would be chosen for the experiment. These options were: electrolysis, ozone-UV manipulation, and perchlorate candles. The ozone-UV manipulation required the use of a heavy and expensive power source and the perchlorate candles required an open ignition source, which was not allowed aboard the payload. That left us with the electrolysis method, which we decided could be feasible after preliminary research.

We would like to thank WSGC and Dr. William Farrow for making this project possible

**Method:** The method for producing oxygen from an electrolytic solution is demonstrated in a device called a Hoffman Voltmeter. The idea is to use the solution to conduct a current, which separates the oxygen and hydrogen of the water at each electrode. This allows us to produce both gaseous oxygen and hydrogen from the electrolytic solution

However the Hoffman Voltmeter is not appropriately constructed to be used on a high-altitude balloon platform, so we would have to redesign it. We decided on a 5% Sulfuric acid solution as an electrolyte, as this would be much more conductive than water or saltwater. We determined that the weak concentration would not be a problem when interacting with other components, though we would eventually be proven wrong in this regard.

We used PVC tubing and polyurethane tanks to house the liquid, with a small PVC tube connecting the two tanks to form the bridge for the electric current. Early tests with the acid showed that the rate of gas production would be much more than we had previously thought. We resolved this by using a cylindrical electrode in place of copper plates.

Another issue that would have to be addressed is the buildup of gas pressure as the gas is produced in a fixed-volume container. To combat this, the team had to design an adjustable-volume system for the displaced solution to flow into, thus keeping the internal gas pressure at about fifteen psi. The displaced fluid would flow into a large syringe connected by tubing. A small LMP pressure sensor was connected to the fluid system, which would monitor internal fluid pressure, which would increase with gas pressure. This pressure sensor would control a Firgelli linear actuator. The actuator moved the plunger on the syringe, thus adjusting the volume of the entire electrolytic system to keep it at fifteen psi. In order to maintain a straight alignment while the syringe was being moved, a chassis for the syringe was 3-D printed. An image for the volume-control system can be seen in Figure 2. In the event that the syringe became full, the current through the solution would be cut off using an integrated relay, ceasing all gas production.

**Results:** We knew that this experiment had a decent chance of failure, which we were willing to accept. As such, the experiment was not in any condition to fly. The volume manipulation was successful, though all of the extra hardware needed to ensure success created a weight problem, which, when combined with the large weight of the solution already present, proved to be insurmountable. Another problem arose with the solution itself, as the 2-part resin/hardener that we used in the final sealing process ended up reacting negatively with the acid solution, causing the hardener to fail. These setbacks occurring so late in the design process did not leave us with enough time to redesign the system to rectify the problems with weight and leakage.

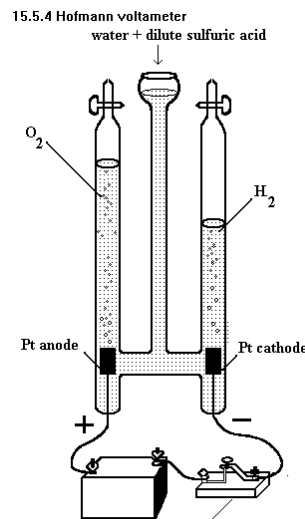


Figure 1: Diagram of a standard Hofmann Voltmeter



Figure 2: Image of the actuator-syringe system

**Conclusion:** This component of the balloon design was the most complicated experiment we wished to perform aboard the payload. We set out knowing that there was a chance that the experiment would not fly. There are several changes that I would make to the design for future attempts. Even though the conductivity is low, using a less volatile electrolyte would have been much easier, especially in the testing stage. The flexible tubes should be replaced with rigid, solid pipe connections, which are easier to seal and maintain. The tanks should have been smaller to reduce weight, which would have let us create a smaller volume-control system, saving more weight. Finally, a heavier duty sealant should have been used. We tried using JB Weld in early design stages, but the tubing proved to be incompatible with JB Weld's long drying time. With rigid pipe connectors, this problem could have been addressed more effectively. Overall, I believe that we laid important groundwork for what could be an interesting experiment for future payload teams.

### Internal Heating

The team began with experimental brainstorming. In this process the temperature of the payload affected several the experiments that were possible. For example, the CO<sub>2</sub>, Ozone, and sound sensors were constrained because they were rated to work at a certain temperature. (In most cases the limit was -40 degrees Celsius.) It was found that the temperatures on the inside of the payload would reach minus 20 degrees Celsius and the temperatures reached at around 100,000 feet were about minus 60 degrees Celsius.

(<http://www.aerospaceweb.org/question/atmosphere/q0112.shtml>)

Even though the payload would have insulation, there would be a change in temperature of eighty degrees Celsius at least.

**Purpose:** Our goal with this experiment was to maintain an internal temperature of 0 degrees Celsius. In order to accomplish this goal we brainstormed and researched several ideas. However, the one that seemed the most practical was to utilize the large change in temperature via a Peltier Junction. If one was used, power would be able to be generated and hopefully turned into heat to maintain the temperature of our payload.

**Method:** First the cell would have to gather heat from the inside, where it is pumped to a heat exchanger on the outside of the box. The collected heat is then released to the ambient air to warm the payload. This would all be accomplished using two heat sinks and fans in conjunction with a Peltier device.

The smaller heat sink was coded to temperature below that of the air in the box. The sink would then pick up the heat as the air circulates between the fins. The Peltier device is mounted between the low-heat sink and the larger high-heat sink. A fan located on the hot side would circulate ambient air between the sink's fins to absorb the collected heat. This would include the heat from the box and the heat produced by the cell itself. The outline of this process is demonstrated in Figure 3.

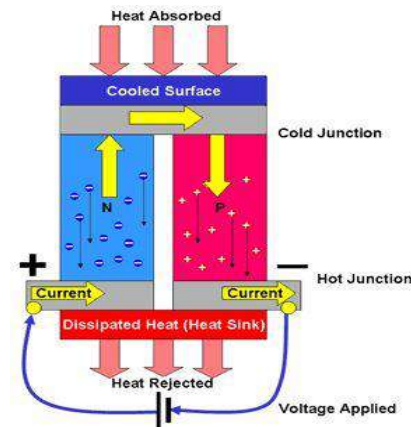


Figure 3: Diagram of the Peltier system

By using the device in Figure 3 with a reversed polarity, we could create a heater. After researching Peltier Cells for the purpose of creating thermal energy, it was found that power generation was not feasible. The change in temperature between the cold and hot nodes must be greater than 100 degrees Celsius for any significant energy to be harnessed especially since our power supply was restricted to any battery 9V and less due to the six pound weight restriction. In addition, the Peltier Cell requires 12 V or higher for an effective heating device. As a result, we decided to investigate a resistive heater as a means for heating the inside of the payload.

Even though the Peltier Cell was not feasible we could still use a simpler method of heating with energy generated through resistivity. Similar to the Peltier system, power can be generated through equation (1) below. The rate of heat transfer,  $q$ , is proportional to the power generated multiplied by time. Therefore if we have more current then the payload should get hotter over a shorter period of time [see equation (2)]. However, the current is restricted greatly by the voltage source and, in this case, we are limited to a 9V battery due to weight.

$$P=i^2*R \quad (1)$$

$$q\propto i^2*R*t \quad (2)$$

In researching the heater, we found a 10x5 cm metal-polymer fiber composite conductive yarn sold through Adafruit Industries. To find the power that it drains we took a multimeter to find its resistance. Using equation (1) and a 9V battery as its energy source the power was found to be 1.05 Watts. With the feasibility of the heater and our power source we decided to go with this configuration because it was the best that we could do in the given flight conditions and constraints.

The following was used in the fabrication of the heater:

- Arduino Mega
- MCP9809 digital temperature sensor
- N Channel MOSFET
- Lithium Ion 9 V Battery

The Mega was chosen so that multiple devices could be used along with the SD shield on the controller. The temperature sensor has a typical accuracy of  $\pm 0.25^\circ\text{C}$  over the sensor's  $-40^\circ\text{C}$  to  $+125^\circ\text{C}$  range and a precision of  $+0.0625^\circ\text{C}$  according to the Adafruit Ind. datasheet. The MOSFET was chosen so that code could be written to make the device act like a thermostat. . If the temperature is below 25 degrees then it sends a signal to the MOSFET to turn on the heater. If temperature is at the designated temperature of 25 then the code will emit "OFF" and the heater will turn off. One advantage of using the polymer fabric we have is that once the current is shut off from the heater, it cools very quickly. This allowed us to qualitatively feel if the MOSFET was working during testing. Lastly, a lithium ion battery was chosen because the device needed to last about three hours. The battery allows us to do so because of the higher rated current.

**Results:** We were not able to have the initial design that was wanted however the heater did increase the temperature on the inside of the payload, and the MOSFET allowed us to control the temperature to the highest extent we could with our design. The temperature in Figure 4 does indeed drop to minus 20 degrees Celsius as expected with the high altitude, but the temperature begins to increase shortly after. The heater was limited to a certain wattage level therefore it can only increase temperature slowly. In future studies, we would like to look into pulse width modulation for a more accurate temperature control along with a larger power source.

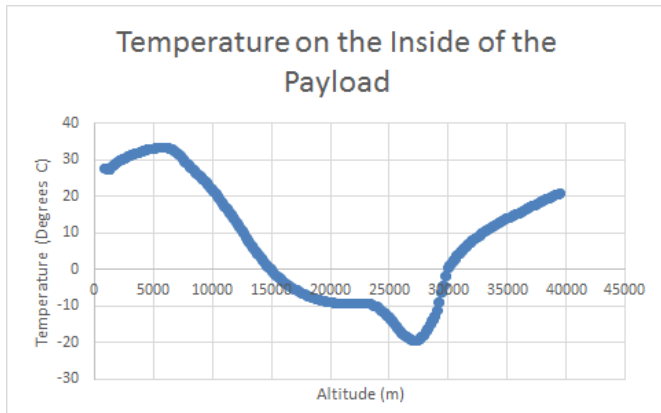


Figure 4: Graph of internal temperature over altitude during the flight

**Conclusion:** The internal heating system worked better than expected during the flight, though the results show it to be relatively inconsistent, where we had large drops in temperature at one point in the flight, however the temperature eventually rose in the higher stages of the flight, with a 20° C internal temperature at 40,000 meters. We believe that the experiment was a success.

### Speed of Sound Properties

One of the interesting results of being in a low pressure environment is the change to how we hear the world. Without a substantial medium to travel through, the properties of sound start to change, primarily the speed of sound, which is around 340 m/s at sea level.

**Purpose:** This experiment was designed to test how the speed of sound changes as the balloon goes higher in the atmosphere. The speed of sound is dependent on two main variables; temperature, and the composition of the medium it is traveling through Figure 4. As the payload rises the speed of sound should change due to the change in the medium, temperature will be negligible because the whole test will be in a heated chamber. We hope to see a linear relationship such as the one in Figure 4.

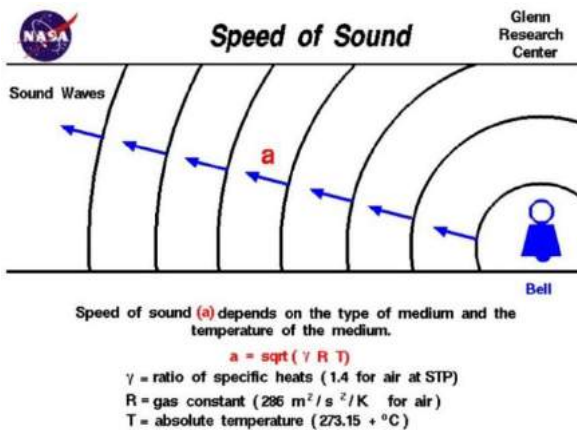


Figure 5: Diagram of how speed of sound changes with heat

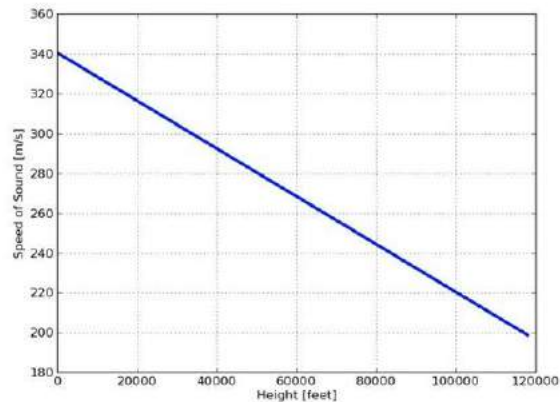


Figure 6: Graph of speed of sound as it changes with height

**Method:** As an initial idea the team came up with the simple idea of having a speaker and a microphone set a certain distance apart. A 77Hz tone would be played by the speaker, and it would then be timed to see how long it took to get to the microphone using a timer programmed on the Arduino. The initial problem with this idea was that there was too much background noise, even in a container that was designed to keep out ambient sound. The next step to fix this problem was to implement a band-pass filter between the microphone output and the Arduino. This filter would help filter out frequencies that are not in the same range as the 77Hz signal. A simple high pass and low pass filter was created using a 2.1  $\mu\text{F}$  and a 2  $\mu\text{F}$  capacitor and two 100 ohm resistors.

With the addition of the band-pass filter the readings were better, but there was still too much background noise to get an accurate reading. When the program was run for ten seconds with the tone playing continuously and data points being taken every eighth of a second, the Arduino was only able to recognize the tone about 15% of the time. With some research it was decided that a 741 op amp band-pass filter would be more accurate. When the filter was tested the same way as the original filter the results were better than before, with a percentage of 21%, but still not accurate enough.

At this point some extra testing was done and the problem was discovered. With a constant input of analog values into the Arduino, the analog ports themselves were adding feedback. There are methods to help with the Arduino feedback, but we decided to go a different route. We decided to test an ultrasonic module that uses the pulse width modulating (PWM) digital ports on the Arduino. The ultrasonic works by sending out a ping from the trig pin which then bounces off whatever is in front of it. It then comes back and triggers the echo pin sending a pulse to the Arduino board. Then using the PWM, which measures the length of the pulse, the length of the pulse in microseconds is the time it took for the ping to traverse the distance and bounce back. The speed of sound could then be calculated by taking the distance between the sensor and the object the ping bounced off of multiplied by two, as the ping went that distance twice so we had to account for that, and the time in microseconds. A test was done to determine how accurate the sensor was, and we found that the sensor gave us a reading that was accurate with a 2-3% in error.

Next was the housing for the experiment. We decided on a two inch diameter rocket tube body. The sensor is mounted on one end with the other end being closed off with painter's tape. The whole tube was 3.25 inches long. This housing would give the experiment a safe environment to test in, without being moved during flight. See Figure 7 for a visual of the housing.

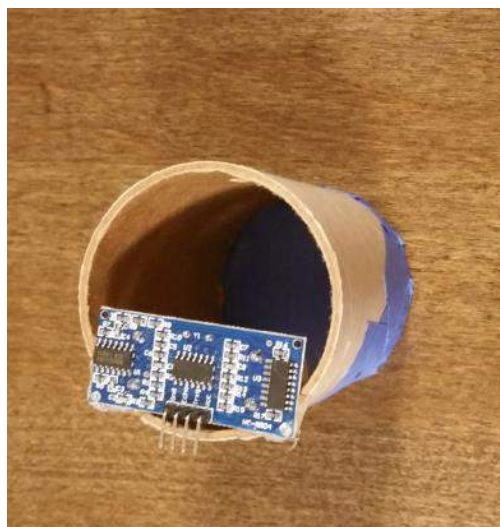


Figure 7: Image of the rocket tube housing with speaker attached

**Results:** The expected results from this experiment was that the speed of sound would slow as the balloon rises in the atmosphere. The Arduino took a data point every two minutes, and the goal was to get a set of data with the speed of sounding trending towards zero. Unfortunately we were unable to get a data set from this experiment because during launch a wire was disconnected which caused the sensor to send incorrect readings during the entirety of the flight.

**Conclusion:** The unfortunate equipment malfunction prevented us from retrieving our results. While the experimental systems worked well during the ground tests, and we believe that they would have worked during the flight, we obviously should have devoted more time to ensuring that the hardware could survive the flight. We could have built in redundancy systems to the circuits that could have bypassed the broken solder and allowed the system to function.

### Ozone Detection

Climate Change and pollution are urgent issues that face us today, and keeping tabs on the Carbon Dioxide and Ozone in the atmosphere is one way to monitor our environmental impact. A cheap and effective way of doing this is to send a simple set of sensors connected to an Arduino with the payload. The parts included the MQ131 Ozone sensor, the MG811 Carbon Dioxide Sensor, and an Arduino Uno. Both of the sensors are built physically identical, but they use different chemical reactants to detect different gasses. See Figure 8 for more technical details on the two sensors. Unfortunately, due to technical limitations, we had to cut the CO2 experiment entirely.

**Purpose:** The overarching goal was to take sensor data from the flight, model it against predictions made by previous similar surveys, and report the difference. First, in order to achieve this goal, the sensors must be calibrated. Secondly, they must have a way to log their data in real time. Third, they must be capable of taking accurate readings at high altitude.

**Method:** The first experiment was to ensure that the sensors were both operable. Unfortunately, the CO<sub>2</sub> sensor failed this first test. Using the CO<sub>2</sub> sensor manufacturer’s program code, it produced results that were completely illegible. The ozone sensor, on the other hand, produced quantifiable results. In order to ensure the efficacy of the results, two experiments are required: 1) exposing the ozone circuit to extreme low pressure and checking the response, and 2) calibrating it against an existing and functioning ozone sensor. Unfortunately, we were never able to find a sensor to use for calibration, so it flew un-calibrated. In order to log the data in real time, we needed an SD card Arduino shield, which we provided for the group. The ozone sensor was temperature dependent, as well as other aspects of the payload, so to combat this issue, we provided the heating aspect to this project.

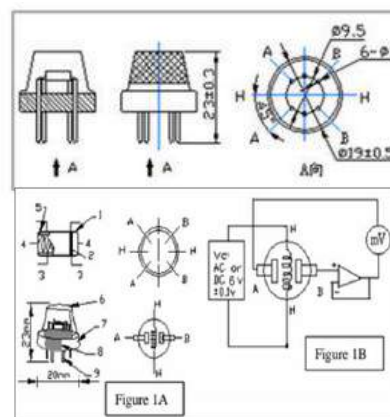


Figure 8: Diagram of sensors used within the ozone experiment

The physical dimensions of the sensors are inconsequential to the overall space constraints of the payload, so that was not a concern. The parts were mounted and added to the other breadboard already in use by other aspects of the payload experiments, so mounting was of little concern.

**Results:** We decided to keep the ozone sensor as a part of our final payload, but we cut the CO<sub>2</sub> sensor due to difficulties and the limitations of the sensor itself. The idea was that the ozone sensor would give acceptable data given the temperature kept relatively constant, and the sensor performed on launch day. However, the temperature did not remain constant, and due to the sensor being un-calibrated, the data received remains indecipherable without calibration.

**Conclusion:** We believe that improved functioning with the internal heating system would have allowed us better results with the ozone detection system. As it stands, we were not able to interpret the results of the experiment.

## Payload Structure

**Purpose:** Previous year's payload structures all seemed to revolve around the use of a capsule to protect the onboard experiments from the environment. Our team wanted to go a bit further than that with our payload structure. We wanted to create a shape that could use the windy nature high altitudes to remain stable.

**Method:** When creating the payload structure, the concept of using a design that created the least amount of spin was used as the key factor, besides the actual structural properties. Looking at past designs, it was easy to see that most of them were spherical in shape and that is what caused them to spin radically. In order to prevent the spinning, the basis of a flag or sail idea was used to conceptualize the shape. To properly store experiments, this sail had to be widened to create the space needed. This then led to the idea of using a triangular prism design. See Figure 9 for a visualization of our structure.

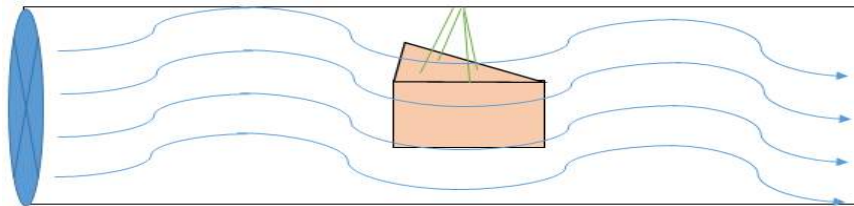


Figure 9: Image of the new structure design. Here it is shown conceptualized during wind tunnel testing

Once the overall shape was determined, the actual characteristics of this prism had to be determined. Using a wind tunnel, a series of tests in which individual factors of the prism were changed, face width, tail length, face shape, and mounting point shape, it was determined that the best shape to use was a triangular prism with a width to length ratio of 3:1, a flat face, and a trapezoidal mounting system to hold it to the balloon. See Figure 10 for details.

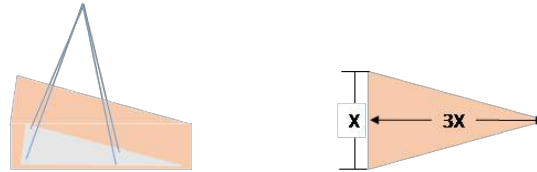


Figure 6: Layout of size proportions and string support locations of the structure

**Results:** With the addition of the final size specifications of each experiment, the interior support system for the payload could finally be designed and built. Due to the restrictions brought up by the oxygen renewal system, the payload had to be tall, thin, and long. The oxygen system would only take up the exteriors of the payload and leave the top  $\frac{2}{3}$ 's open. To make the best use of this space and still keep everything in the payload securely attached to the balloon, a base-plate was created on the top and then all the corresponding experiments would hang from it; this was done using an upside down shelves. The drop shelving system worked by using washers and bolts to connect each shelf to four threaded rods that extended the entire length of the payload. These four rods were also used then to connect the top of the payload to the rest of the insulation board sheathing that made up the exterior of the payload.



Figure 11: Payload electronics board before the flight

**Conclusion:** The different payload capsule worked well for our design, allowing us easy attachment to the balloon, while simultaneously giving us enough room for the moving actuator systems included with the oxygen generation system. While the oxygen generation system was not included in the flight, the structure did a nice job for compensating for the large amount of space required by it. The system also worked nicely for allowing us to run wires from power sources to their respective experimental systems. Overall, the structure was successful in its design.

## **Project Conclusion**

Our team had a set of ambitious objectives in mind for this experiment. We knew full well that several of them might lead to failure. Some of the experiments turned out well, while others laid important groundwork for future teams to work with, if they choose to do so. We all learned much about experimental design and the engineering process. Overall, our experience with this project was invaluable in teaching us skills in design, teamwork, communication, and problem-solving.

**Team Whoosh Generator**  
**2015 WSGC Collegiate Rocket Competition**

James Ihrcke, Eric Johnson, Leeta Russell, Stephan Skibinski, Braden Thiel

Milwaukee School of Engineering

**Abstract**

The objectives of the 2015 Wisconsin Space Grant Consortium (WSGC) Collegiate Rocket Competition were to design and build a “boosted dart” high-powered rocket to allow the dart stage to reach the highest possible apogee and to conform to design restrictions and added design objectives. The rocket was required to use a Cesaroni I-445 motor as specified by WSGC, use a flight data recorder provided by WSGC, and be safely recovered in a flyable condition by use of a parachute system. The dart was required to be an unpowered upper stage that drag separates from the booster without imparting momentum onto the dart. In addition to the altimeters already on board, a noncommercial data acquisition system was required to record data on the rotation of the rocket in the X, Y, and Z axes over time. Finally, the rocket was required to record downward facing video of the flight starting at the time of launch.

Included in this report are design details considered, anticipated performance, photos of constructed components, and flight results.

Team Whoosh Generator thanks the Wisconsin Space Grant Consortium (WSGC) for the funding to make this project possible. Also thanks to this year’s rocket shadows: Lucas Ferrandoquielz, Henry Moroder, Jordan Petrie, and Cameron Wilson for their help in the design and construction of this year’s rocket.

## 1.0 Rocket Design and Construction

The following subsections will detail the airframe design, nosecone and fin design, rocket stability, electronics bay design, the data acquisition system, camera system, pressure relief considerations, and recovery method.

**1.1 Airframe design.** The body tubes could be selected from several different kinds of materials, including cardboard, fiberglass, and PVC. Cardboard was selected as the body tube material for the rocket because of its simplicity, strength, price, and ease of cutting and drilling. Cardboard LOC body tubes have also proven to work well in the construction of previous years' rockets.

The rocket's diameter was determined after several brainstorming sessions. The final two designs were a dart diameter of 38 millimeters with a booster diameter of 54 millimeters or a dart diameter of 54 millimeters with a booster diameter of 3 inches. After weighing the pros and cons, the 54 millimeter dart, 3 inch booster combination was chosen because it was the minimum size required for the electronics to fit in the dart and still provide a large enough drag difference from dart to booster to cause drag separation upon motor burnout.

The body tube lengths were heavily dependent on the size of the components being placed inside of them. OpenRocket, a free open source rocket design software program, was the primary software used to design much of the rocket. OpenRocket was used to calculate the optimum body tube lengths. It was found that the booster section (that houses the motor mount and a parachute) would have a body tube length of 21.5 inches and a total length of 29 inches including transition and tail cone. The dart section (that houses a smaller parachute, the electronics bay, and the downward facing camera) would have a total body tube length of length of 23.75 inches and a total length of 38.25 inches including nose cone and tail cone. The total length of the rocket including the nose cone and the tail cone motor retainer was 64.61 inches.

**1.2 Nose cones.** With the body tube size of the dart chosen as a 54 millimeter LOC body tube, an ogive 54 millimeter PNC nose cone was selected to be used. The ogive shape was chosen because it has a low coefficient of drag which allows for an increased apogee. In order to provide a strong base for the dart and reduce drag, another nose cone was purchased to act as a tail cone. The tail cone was cut to a length of 5 inches to allow for the downward facing camera to be recessed in approximately 0.25 inches. The tail cone also provided a sturdy base for the attachment point of the dart to the booster and it reduced the pressure drag on the dart, increasing its apogee. For the transition on the booster, a 3 inch PNC ogive nose cone was used. The transition was cut to a length of 6 inches to allow the dart's tail cone to slide into it for alignment purposes. The dart needs to be aligned and held plumb with the rest of the rocket during the thrust phase. In order to do this, a custom bulkhead was created and epoxied inside of the booster transition cone which allowed the dart's tail cone to firmly fit inside of it yet still allow for easy separation.

**1.3 Fins.** The fins are the main component that determines the location for the center of pressure on a rocket and therefore the stability of the rocket. The fin design was determined by placing different shapes and sizes of fins in OpenRocket until a stable ratio between the center of gravity and center of pressure was obtained. The complete rocket was modeled and the dart and booster separately to ensure the rocket would stable throughout its entire flight. It was determined to use 3 fins spaced evenly around the rocket on both the booster and the dart. The fins chosen for the

dart were A-08 G-10 prism fiberglass fins and for the booster were B-08 G-10 prism fiberglass fins from Public Missiles. The fins were attached to the booster by placing them through fin slots in the lower body tube and using epoxy to attach them to the motor mount tube on the outer and inner surfaces of the body tube. The fins were attached to the dart by epoxying them directly to the outside of the rocket. A photo of the booster and dart fins is shown in Figure 1.

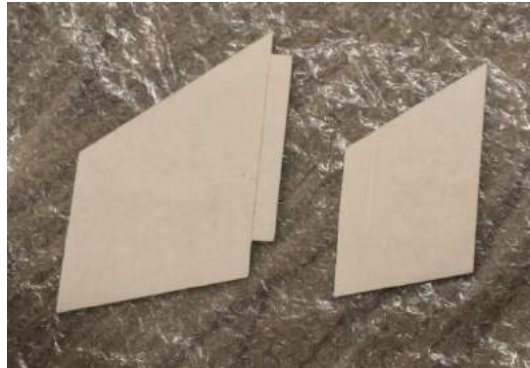


Figure 1: Booster and Dart Fins

**1.4 Rocket stability.** The relationship between the center of pressure (CP) and center of gravity (CG) is one of the most important relationships in high-powered rocketry. The center of pressure is defined as the point at which aerodynamic forces on the rocket are centered. The center of gravity is the location at which the full weight of the rocket can be considered to act as a single force. The ratio between the locations relative to the rocket diameter can be used to predict the stability of the rocket during flight. Generally, the center of gravity must be at least one (but not more than two) body tube diameters in front of the center of pressure. The locations of the center of pressure and center of gravity were determined for this design using the OpenRocket software.

Table 1 shows the locations of the CP and CG and the caliber of stability for the full rocket at ignition and for the dart after separation according to the OpenRocket simulation.

**Table 1: Locations of CP and CG (In Inches from Nose Cone Tip)**

	CP	CG	Stability (Caliber)
<b>Full Rocket at Ignition</b>	46.58	41.23	1.73
<b>Dart after Separation</b>	25.31	21.62	1.63

From this analysis, it can be concluded that both the dart and the booster will be stable during the entire ascent portion of the flight.

**1.5 Electronics bay.** To save on space in the dart, the dart’s nose cone was cut open and a bulkhead was epoxied inside 3.5 inches aft of the tip of the cone with a threaded rod extending out. This allowed a fiberglass sled to be fed onto the rod and make use of the space in the nose cone that would otherwise be wasted. The nose cone was coupled with a 6.75 inch long 54 millimeter diameter body tube and a 4.75 inch long 2.14 inch diameter coupler tube. The coupler fit perfectly into the 54 millimeter airframe, joining the electronics bay with the rest of the dart. One barometric pressure altimeter was placed in the electronics bay, an ALTS25 which had been used in previous years. The altimeter was used to deploy the parachute in the dart as well as record

the altitude of the rocket. The electronics bay also held an Arduino Uno with a 3 axis accelerometer that recorded roll data during the flight. Finally the electronics bay held the Raven 3 (WSGC flight data recorder) along with a 9 volt battery that powered the previously mentioned electronics. Two screw switches were placed in the electronics bay to allow easy arming of devices on the launch pad. One screw switch was for turning on the WSGC flight data recorder and Arduino and the other was for arming the altimeter. A terminal block was placed at the end of the bay to allow easier attachment of the black powder charge on launch day. The assembled electronics bay is shown in Figure 2.

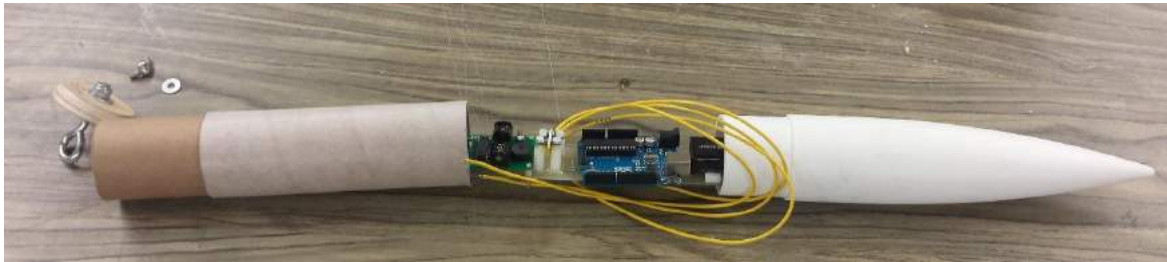


Figure 2: Electronics Bay Assembly

**1.6 Data acquisition system (DAS).** A requirement of this year’s competition was to record flight data that could be used to determine the rotation of the dart during flight using a device other than an off-the-shelf pitch or roll data logger.

It was determined that a 3-axis accelerometer would be the most cost-effective and compact device that could be used to acquire both pitch and roll data. In an effort to utilize existing resources, the search for the right accelerometer was limited to those compatible with an Arduino Uno. After searching through a variety of accelerometer options, it was determined that the Analog Devices ADXL-335 three-axis accelerometer was best suited for our needs, shown in Figure 3.

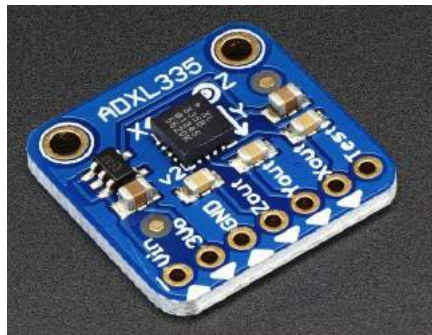


Figure 3: Three-axis Accelerometer

This three-axis accelerometer was available in two different breakout boards with either a digital interface or an analog interface. The analog interface was favored over the digital interface simply due to familiarity and the bypass of potential bit error when using i2c protocol. The output of the ADXL-335 consists of an analog voltage output with respect to each Cartesian linear acceleration, the output voltage ranging from 0 to 3.3 volts. The acceleration sensing capabilities of this accelerometer was listed as  $\pm 3g$  in the data sheet. Equation 1 was determined using the voltage and acceleration range of each axis.

$$g_n = 1.818V_n - 3 \quad (1)$$

After choosing the accelerometer, the logging of the three-axis data was addressed. Arduino Uno shields were evaluated to determine the best way to record data and extract it after flight. Several breakout boards were considered, each using some form of SD storage and digital interface to record data. It was determined that the Adafruit 1141 SD shield for the Arduino Uno was the best option, providing compact design and direct compatibility shown in Figure 4.

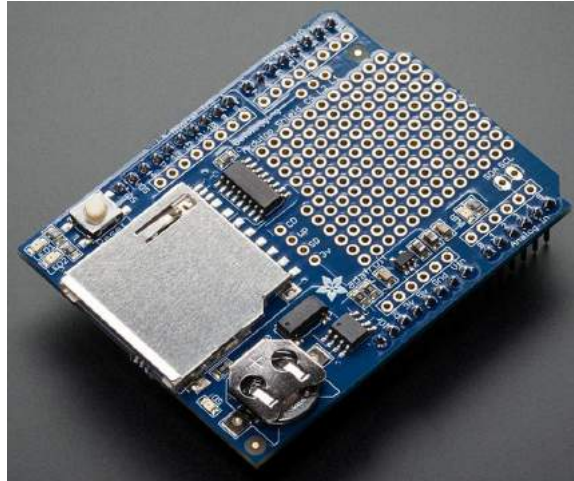


Figure 4: Adafruit 1141 SD shield for the Arduino Uno

To record data with the SD shield on the Uno, a data logging file was written in the Arduino code interface. This data logging file used three analog channels on the Uno to read each of the analog outputs of the accelerometer. These analog voltages were sampled at a rate of 100 Hz and saved into individual data files on the SD card for each of the three axes. The code was designed to start recording data after a short delay, allowing excess data to be left unrecorded while preparing the rocket on the launch pad.

The data stored on the SD card could be accessed using Microsoft Excel, opening a single column dataset for each accelerometer axis. The recorded values were analog voltages ranging from 0 to 3.3 volts. These data points were turned into points of linear acceleration using Equation 1. After converting each set of voltage data to acceleration, Equations 2 and 3 are used to calculate the desired pitch and roll characteristics needed to meet the flight requirements.

$$pitch = \arctan\left(\frac{G_y}{\sqrt{G_x^2 + G_z^2}}\right) \quad (2)$$

$$roll = \arctan\left(-\frac{G_x}{G_z}\right) \quad (3)$$

By using the combination of the Arduino Uno, SD shield, and three-axis accelerometer, a data logging setup was constructed. The Arduino Uno collected analog voltage data from the three-axis accelerometer representing the linear acceleration on each Cartesian axis. The firmware on the Arduino logs the analog signals at a sampling frequency of 100Hz onto the SD card on the Arduino shield. The data extracted from the SD card was then used to model the roll in the rocket's flight in Microsoft Excel.

**1.8 Camera system.** The competition required a downward facing camera to record the entirety of rocket’s flight. Different action cameras were researched and compared against one another to determine which would work best. A decision matrix was created to make the comparison easy shown in Table 2.

**Table 2: Decision Matrix of Possible Camera Choices.**

	<i>Polaroid Cube</i>		<i>Contour ROAM 2</i>		<i>Mini Cylinder Shaped Sport</i>		<i>Go Pro Hero</i>		Weight
	Rank*	Score	Rank*	Score	Rank*	Score	Rank*	Score	
Dimensions	4	16	2	8	3	12	1	4	x4
Price	3	6	2	4	4	8	1	2	x2
Weight	2	4	1	2	4	8	3	6	x2
Trusted Brand	4	4	4	4	1	1	4	4	x1
Video Quality	1	1	1	1	1	1	1	1	x1
View Angle	2	2	4	4	1	1	3	3	x1
<b>Weighted Total</b>		<b>33</b>		<b>23</b>		<b>31</b>		<b>20</b>	

*\*Rank: 1 = least beneficial, 4 = most beneficial*

From the decision matrix it was shown that the Polaroid Cube would work the best. Its small cubed shape provided flexibility in the different directions that it could be mounted inside the body tube. Its price was also a plus because it was the second cheapest option and had a trusted brand name. The Polaroid Cube was also easy to operate. It is controlled by only one large button, making it easily accessible when it was in the rocket. The camera was held at the bottom of the dart’s tail cone where a small hole allowed a dowel to be inserted to turn the camera on while on the launch pad. A photo of the Polaroid Cube is shown in Figure 5.



Figure 5: Polaroid Cube

In order to have video footage for the first stage of flight, the camera located in the tail cone of the dart had to film outside and downward on the booster section. To accomplish this, two designs were theorized. Using mirrors or fiber-optic cable, the camera would take in light from a hole in the transition on the booster and reflect it back to the camera in the tail cone of the dart. In theory, the fiber optic cable would be a simpler design however, imaging fiber is very expensive and the low cost end glow fiber purchased for testing did not have the cladding necessary for the total internal reflection making the image transmitted through the cable indistinguishable. For this

reason the design using mirrors was chosen. One mirror was placed directly under the camera at a 45° angle, and another mirror was placed outside of the rocket at a 45° angle facing downward next to a hole in the transition. The mirrors were attached to the bulkhead used to support the dart during launch to provide a strong base during the rocket's flight.

**1.7 Pressure relief.** In order to deploy the parachutes, barometric pressure altimeters were implemented which require static pressure port holes to allow for the equalization of air pressure between the interior and exterior of the rocket. Without this equalization, the parachutes would not deploy at the right time and could deploy early or late depending whether the ports have the correct sizing. A general rule for the sizing of ports is to use a ¼ inch diameter hole (or hole area equivalent if several smaller holes are used) for each 100 cubic inches of volume in the electronics bay. Another general rule is the use of at least three holes that are spaced evenly around the circumference of the body of the rocket to negate the effect of crosswinds.

The diameter of the electronics bay is 2.14 inches and the inner length of the bay is 13.75 inches, yielding a volume of 49.5 cubic inches. A single port hole diameter was calculated to be 0.176 inches with an area of 0.024 square inches. Three holes were drilled into the electronics bay each with a diameter of 0.1015 inches, which is a #38 drill bit. These holes were then spaced 120 degrees apart.

During the rocket's ascent the atmospheric pressure surrounding the rocket decreases. In order to relieve the pressure in other areas of the rocket, a quarter inch hole was drilled into each of the body sections of the rocket. Without these holes, the higher pressure inside the body sections of the rocket could cause early separation as well as early deployment of the parachutes.

**1.9 Recovery.** The dart and booster sections of the rocket used their own parachutes. The parachute's sizes were determined using online decent rate calculators and OpenRocket simulations to achieve a descent rate slow enough for the rocket to be recovered in a safe and flyable condition. The booster used a 44 inch SkyAngle parachute deployed with a time delay on the motor's ejection charge and the dart used a 36 inch parachute deployed at apogee using an altimeter. The dart had a descent rate of 13 feet per second and the booster had a descent rate of 11 feet per second once their respective parachutes opened. The parachutes are shown in Figure 6.



Figure 6: Dart and Booster Parachutes

## 2.0 Anticipated Performance

The anticipated performance of the rocket was simulated using OpenRocket to estimate the performance of the rocket on launch day. The following sections detail these simulations.

**2.1 OpenRocket.** OpenRocket is a free, open source, software similar to RockSim. It is capable of calculating acceleration, velocity, and position data. This is done while accounting for variables including: elevation, wind speed, and the effects of individual components on performance. Also included in the program is the ability to construct full to-scale schematics of the rocket design. From this schematic the CP and CG can also be approximated.

OpenRocket was the main source used in designing the rocket. The rocket was modeled entirely in the program, providing a way to design and calculate proper lengths of body tubes, optimal fin and nosecone designs, rocket weights, acceptable locations of the CP and CG, and drag coefficients. The weather parameters were monitored on launch day and entered into the simulations for better accuracy.

**2.2 Flight predictions.** The peak altitude, velocity and acceleration for the OpenRocket simulation on the day of the launch are shown in Table 3.

**Table 3: Maximum Flight Predictions**

	<b>OpenRocket</b>
<b>Altitude (ft)</b>	2914
<b>Velocity (ft/s)</b>	590
<b>Acceleration(ft/s<sup>2</sup>)</b>	679

## 3.0 Results

An OpenRocket simulation was run to estimate flight performance of the rocket. Actual flight data was recorded using a Raven 3 flight data recorder provided by WSGC. In comparison, the flight of the rocket matched well with the estimates of the simulation. A comparison between predicted and measured results is shown in Table 4.

**Table 4: Flight Performance Comparisons**

	<b>Apogee (ft)</b>	<b>Maximum Velocity (ft/s)</b>	<b>Maximum Acceleration (ft/s<sup>2</sup>)</b>
<b>OpenRocket</b>	2914	590	679
<b>Actual</b>	3185	509	584
	<b>Percent Error From Actual (%)</b>		
<b>OpenRocket</b>	9	14	14

The predicted and actual acceleration data was compared graphically as well shown in Figure 7.

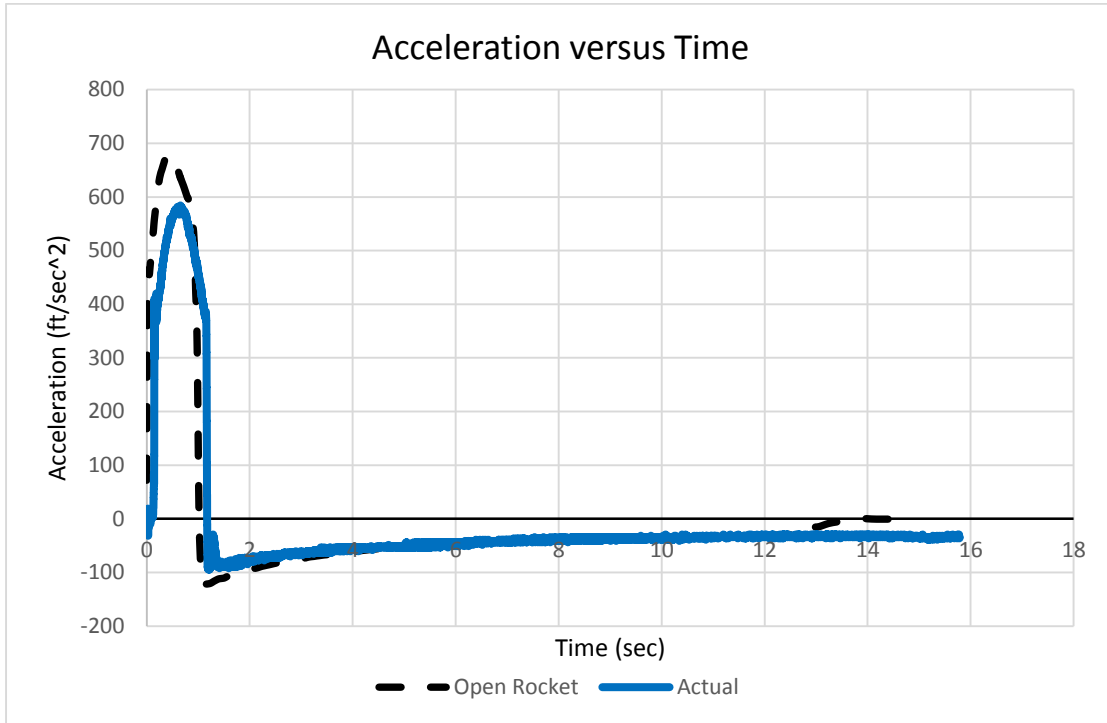


Figure 7: Comparison between Predicted and Actual Acceleration

The pitch and roll data recorded by the DAS is shown in Figure 8.

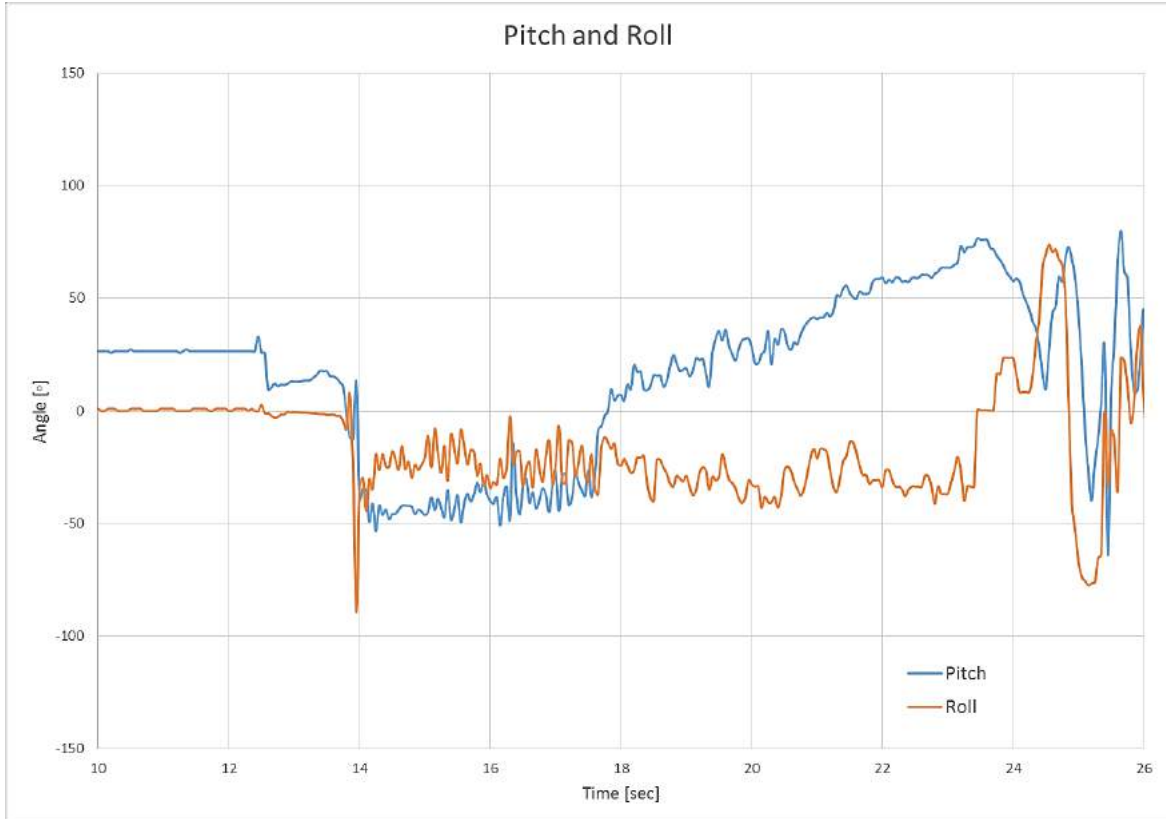


Figure 8: Pitch and Roll Data

The plot shown in Figure 8 shows the pitch and roll of the dart during flight to apogee, calculated using the linear acceleration values from each axis on the dart. The pitch and roll data corresponds to the angle of the dart during launch, separation, apogee, and finally the black-powder charge ignition. The initial pitch offset is due to the angle of the launchpad, which was not perfectly vertical. The pitch plot shows the dart turning over as it approaches apogee while the roll plot shows that the dart experienced very little roll until the black-powder charge ignited. This is very close to what the rocket experienced during its flight.

The time to apogee was about 14 seconds. The rocket experienced a different acceleration curve than predicted shown in Figure 7. This could have been from the rocket's motor not producing the same thrust as the thrust curve data used in the OpenRocket simulation. The rocket overshot the predicted altitude of 2914 feet by 271 feet. The under prediction of the simulation was expected since the tail cone on the dart was not able to be modeled in the OpenRocket simulation. The tail cone reduces the base drag on the dart and thus gives the dart a higher apogee. With the expected under prediction of the simulation, a 14% error in the maximum acceleration and maximum velocity and a 9% error in apogee shows the simulation was still accurate and thus was a good representation of the actual flight. The rocket performed mostly as planned. One system that was not properly implemented was the camera recording system. The camera was improperly turned on causing photos to be taken instead of video. This caused no flight video to be recorded.

#### 4.0 Conclusion

The rocket was successfully recovered in a flyable condition in compliance with the competition rules. The software utilized for this design predicted the altitude of the rocket to a good margin given the uncertainties present in the launch and design. The camera system was improperly used showing that every system implemented on the rocket needs to be tested and re-tested in advance to ensure it will work as planned on launch day. The DAS recorded pitch and roll data that closely matched what occurred during the rocket's flight. Lessons learned through this design will be incorporated into future competitions by returning team members. A photo of the team is shown in Figure 9.



Figure 9: Team Whoosh Generator 2015 (not pictured, Lucas Ferrandoquiely)

## 2015 Elijah High Altitude Balloon Launch Team Summer Proceedings Report

Jadee Kellogg, Daniel Ochoa, Jordan Petrie, Alana Tirimacco

Milwaukee School of Engineering, attended by Ochoa, Petrie, Tirimacco; Ripon College, attended by Kellogg

### Abstract

The 2015 Wisconsin Space Grant Consortium Elijah High Altitude Balloon Launch Team was comprised of three students from Milwaukee School of Engineering and one student from Ripon College. This year, all members of the team had experience with high altitude balloon launches due to previous participation on either the Elijah Payload or Launch Team, or both. A training session was hosted by the 2014 Elijah Launch Team to familiarize the new team with the physical set up of a launch train as well as how to run track predictions and how to read the jet stream charts. Launches were planned for both Carthage College and the Elijah High Altitude Balloon Payload Team, but only the launch for the Payload Team came to fruition. This launch was successful, reaching a peak altitude of 31,021m.

### Introduction

The purpose of the 2015 Wisconsin Space Grant Consortium (WSGC) Elijah Balloon Launch program was to provide four students from WSGC affiliate universities with the opportunity to organize and launch high altitude weather balloons in order to fly science experiments in near-space environments. The team was responsible for coordinating with the WSGC Elijah Balloon Payload design team in order to create and execute a flight plan in order to carry the payload constructed by the design team to an altitude of approximately 31,000m in elevation.

The balloon launch program provided the team members with experience in planning and organizing experiments and scientific events. The team needed to coordinate with multiple third parties which provided the opportunity to improve on their communication and problem solving techniques.

### Launch Planning

**Team meetings.** The team held meetings throughout the summer to discuss and plan the launch of the scientific payload built by the Elijah High Altitude Payload Team. Due to the geographical locations of the members, these meetings occurred online using Skype. On 22 July 2015, the Launch and Payload teams met to discuss the prospective launch for the Payload team, scheduling it for 5 August 2015. The launch team continued to run predictions and check weather at their various locations leading up to the scheduled launch. On 4 August 2015, the day before the launch, Launch Team member Jordan Petrie met with the Payload Team to train them on how to use the launch equipment.

**Flight predictions.** A key part of choosing a launch location was the predicted flight path. In preparation for a launch, the team conducted daily flight predictions using an online software created by Cambridge University Spaceflight to find an appropriate launch location (Greig, March 2010). The team began running these predictions beginning seven days before launch up until the morning of the launch itself. Both the launch and landing locations were required to be over five miles away from any airports and free of trees, power lines, and wind turbines. The landing location also needed to be at least five miles away from a large body of water, such as Lake

Acknowledgments: Wisconsin Space Grant Consortium and Advisor Dr. William Farrow

Michigan. Over the years, a list of launch locations had been compiled by the launch teams (Farrow, et. al., 8 July 2014). The location was chosen from this list, as long as it met all of the requirements laid out for a launch location. Based on the predicted flight paths, Mount Horeb, WI was chosen as the launch location for the Payload Team's flight. Figure 1 is a screen capture of the final path prediction run before the launch for the Payload Team occurred.

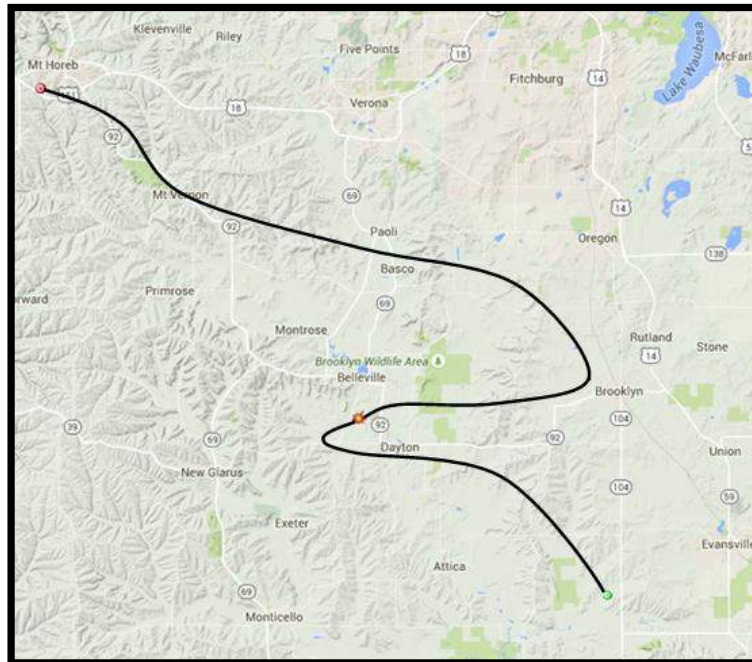


Figure 1: The last path prediction run before the launch for the Payload Team on 5 August 2015 in Mount Horeb, WI.

**Weather forecasting.** The weather forecast and jet stream were also analyzed beginning five days before launch. The team looked at wind speeds and ground weather using weather reports and analyzed the jet stream using an online program created by affiliates of San Francisco State University (Dempsey, 19 June 2012). Figure 2 shows the jet stream map for the 5 August 2015 launch. The speed of the jet stream on launch day was less than 60 mph, which meant the team was able to launch the balloon without fear of the jet stream winds interfering with the flight.

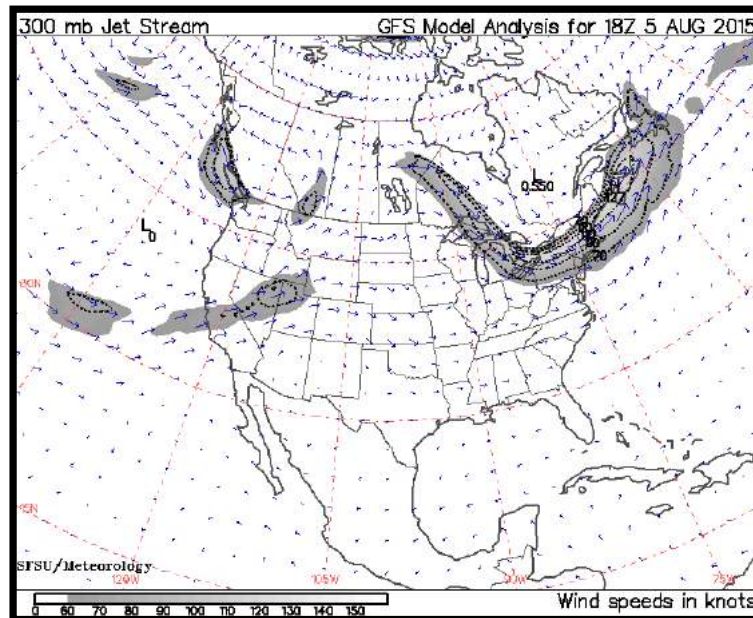


Figure 2: Jet Stream for 5 August 2015 - Launch Successful

**Balloon and payload set-up.** The balloon was set up with the goal to successfully recover the payload in an undamaged condition. To increase the chances of this, the balloon had two tracking payloads attached to it. The primary tracking payload used GPS to transmit its location to Microsoft Mappoint, a tracking software downloaded on the laptops in the Chase Vehicles. The secondary payload sent out a radio signal that could be tracked inputting the frequency of the tracker to a website, enabling the team to collect the data. The purpose of having two tracking payloads was to have a fail-safe in case one of them stopped working. Both tracking payloads were battery powered and were insulated to avoid damage from the low temperatures of the upper atmosphere. The balloon also had a parachute attached that opened when the balloon burst at its apogee. The purpose of the parachute was to slow the descent of the payloads in order to prevent damage to them upon landing. The scientific payload launched was designed by the Elijah High Altitude Payload Team. The payload contained experiments researching oxygen generation, internal heating, ozone detection, and the speed of sound.

The balloon set up from top to bottom goes as follows:

1. Balloon
2. Parachute
3. Primary Tracking Payload
4. Secondary Tracking Payload
5. Elijah Payload Team Scientific Experimental Payload

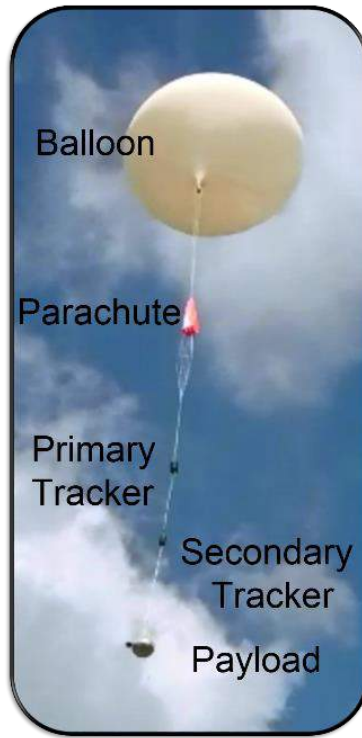


Figure 2: Image of Balloon Set-Up

### **Launch**

The launch team successfully completed one launch that took place on August 5<sup>th</sup>. This launch was for the payload team where they were able to test their payload. Figure 5 shows the actual path the balloon took during flight. It was extremely similar to the predicted track, shown in Figure 1, supporting the reliability of the prediction software.

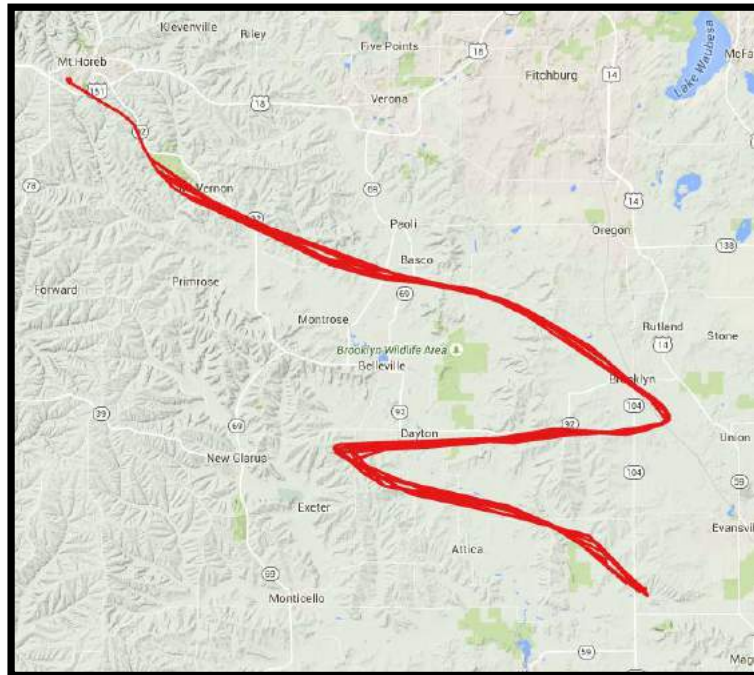


Figure 3: Actual Balloon Track

The launch took place in Mt. Horeb, WI, which had a latitude and longitude of  $43.00^{\circ}$  and  $-89.75^{\circ}$  respectively. The elevation of the launch location was 1160 meters and the jet stream speed for that day was under 69 mph.

Overall for this launch, and the launch team, there were many successes. For example, the team was able to select a satisfactory launch location from a list of possibilities all throughout Wisconsin. The payload was successfully launched, despite troublesome ground wind, reached peak altitude of 31,021 meters before bursting, and safely recovered from a tree. Finally, the team met weekly via Skype to encourage positive communication even when regular face-to-face meetings were impractical.

**Cancelled launches.** This past spring, Dr. Matthew Zorn from Carthage College contacted the 2014-2015 Launch team, expressing interest in conducting a launch with the group. Dr. Zorn wished to bring his classes, specifically meteorology courses, to launches so that they could analyze the balloon's flight and subsequent data. For the launch to be as beneficial as possible for all involved parties, last year's Launch Team decided to use the Launch as a training experience for this year's team. The launch date was set for 18 April 2015 with 19 April 2015 as the "rain date." A small training session was held on the ground on 8 April 2015. Unfortunately, jet stream and ground wind conditions led to both 18, 19 April 2015 launches being cancelled. The launch was then rescheduled for 26 April 2015, but once again, it was cancelled due to wind and weather conditions. With the end of the school year approaching, Dr. Zorn's students were unable to attend another launch. Since the new launch team had already had a ground training session, the teams felt it unnecessary to launch a balloon only for the new team since helium is in short supply and

launches are expensive. The team plans to be in contact with Dr. Zorn again during the 2015-2016 academic year to attempt to fly a meteorological payload for his classes.

### **Conclusion**

Overall the team had great communication throughout the summer and was well prepared for the launch on 5 August 2015. The team was able to develop teamwork, problem solving, and organizational skills while learning how to plan and conduct high altitude balloon launches. The team hopes to complete at least one more successful launch in fall 2015 for Carthage College and then another launch in spring 2015 to train next year's Launch Team.

## References

- Dempsey, Dave, PhD. "Animation of Jet Stream Forecasts for North America." *Jet Stream Analyses and Forecasts at 300mb*. Department of Earth & Climate Sciences, 19 June 2012. Web. July-Aug. 2015.
- Farrow, William, PhD, Alana D. Tirimacco, and Amber L. Korn. *Potential Launch Locations*. N.p.: Google Drive, 8 July 2014. DOCX. <<https://drive.google.com/file/d/0ByGu7nLB3XJKa0d5SGtuTXhHUXc/view?usp=sharing>>.
- Greig, Adam. "CUSF Landing Predictor 2.5." *Cambridge University Space Flight*. Cambridge University, Mar. 2010. Web. July-Aug. 2015.

**Badger Ballistics**  
**WSGC Collegiate Rocket Team 2015**

Adrien Bossogo-Egoume, Lucas Jewell, Audrey Packer, Michael Warren

Engineering Mechanics, University of Wisconsin - Madison

**Abstract**

This report provides an overview of the design features, construction and analysis of a high-powered rocket and payload. The rocket was designed and constructed to be a boosted dart that could be recovered in a flyable condition in accordance with the WSGC Collegiate Rocket Competition objectives. The boosted dart was comprised of an unpowered dart and a rocket booster. The two stages of the rocket were designed to separate as a result of drag after the boosted dart stopped providing thrust. After the drag separation, the unpowered dart was to continue coasting on a parabolic trajectory until an electronic deployment system released its parachute. The rocket booster also contained a parachute recovery system that was to release after separation. The payload of the unpowered dart was designed and constructed to collect on-board, nadir video and characterize the rotation of the rocket in the X, Y, and Z axes over time. Badger Ballistics achieved a successful flight with a successful launch, dart separation from booster, successful deployment of the booster recovery system, successful deployment of the dart recovery system, and the recovery of both stages in flyable condition. The predicted maximum apogee was 3248 ft. but the apogee recorded on flight day was 2059 ft. The approximately 57% error in this calculation is due to over simplification of the OpenRocket flight simulation software, launch alignment, and loss of energy due to pitching during flight. Additionally, overuse of construction materials, such as epoxy putty and paint, likely lowered the expected apogee because of their unaccounted weight.

---

<sup>1</sup>Badger Ballistics would like to thank WSGC for their generous financial and educational support throughout this competition.

## 1.0 Rocket Design and Construction

**1.1 Airframe design** Three primary design specifications were considered in the conceptualization of the team's rocket. These were: spatial accommodation of the required avionics, stability of at least 1 cal, and achieving maximum apogee. In accordance with these requirements, the overall rocket body dimensions were determined using a bottom-up design approach. The avionics system to be used was specified first. Then, using the dimensions of these components, it was found that a minimum dart diameter of 6.5 cm was required for spatial optimization. A booster tube with a diameter of 9.8 cm was then selected based on the sufficient drag it provided for stage separation.

The rocket design specifications also encompass the stability of the rocket before separation. Stability was accounted for in the design through ensuring that the center of pressure was a sufficient distance behind the center of gravity. This enabled the rocket to counteract any turbulence experienced during flight with restorative forces occurring behind the center of gravity.<sup>2</sup>

Achievement of the rocket's maximum possible apogee was also considered in the design. To accomplish this without adversely affecting the stability, the center of pressure was held constant with respect to the proportions of the rocket. The overall height of the rocket was scaled down significantly to a final value of 146 cm. This decrease in height greatly increased the maximum apogee from the original design by significantly decreasing the skin drag of the rocket. The final dimensions of the rocket ensured stability without sacrificing a great amount of apogee height.

**1.2 Dart system** The dart system consisted of the second stage of the rocket. This was the unpowered dart that was intended to reach maximum apogee. LOC tube was chosen as the material for this system because of its adequate structural stability and minimal weight. The length of the dart was 40 cm. It had an inner diameter of 6.5 cm and an outer diameter of 6.68 cm. The wall thickness of .18 cm provided sufficient strength to accommodate the dart's payload system.

**1.3 Booster system** The booster system consisted of the first stage of the rocket. This system was comprised of the engine mount and the booster recovery system. This system was integral in propelling the unpowered dart so that it could achieve maximum apogee. LOC tube was again chosen as the material for this system. The length of the booster tube was 50 cm. It had an inner diameter of 9.8 cm and an outer diameter of 10.16 cm. The wall thickness .36 cm provided sufficient strength to accommodate for the thrust of the engine that would be mounted in the engine mount. The 5.4 cm engine mount was attached to the rest of the booster system with 5.4 cm to 9.8 cm centering rings and glue. This apparatus ensured that the engine mount and

---

<sup>2</sup> "Rocket Stability." NASA. N.p., 12 June 2014. Web.

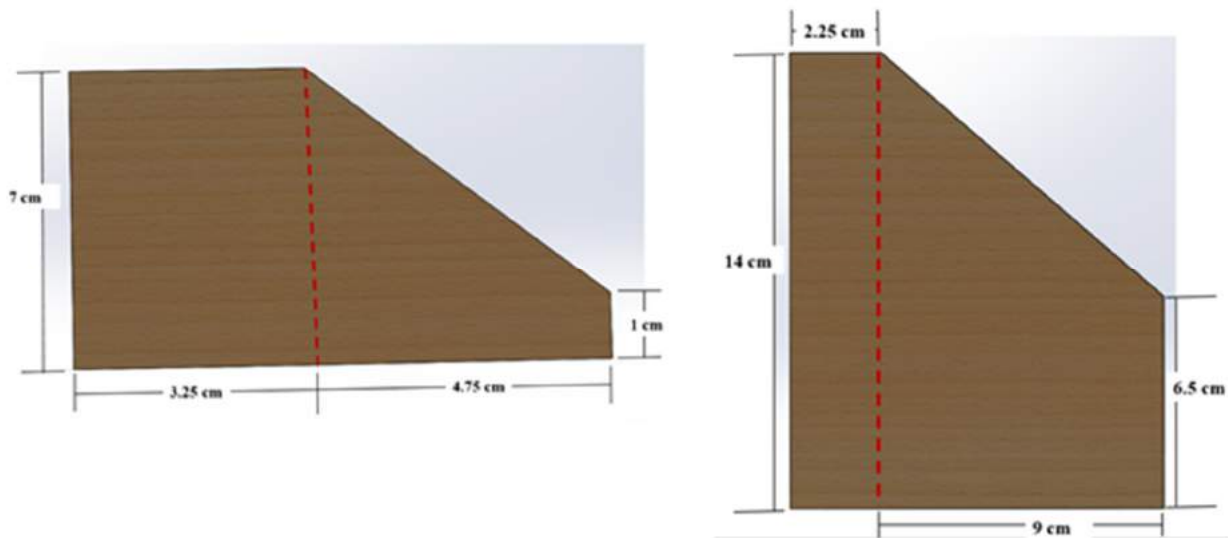
<<https://spaceflight systems.grc.nasa.gov/education/rocket/rktstab.html>>. (This excerpt from NASA describes the restoring and destabilizing forces present during rocket flight as well as how to align the CG and CP to achieve the desired forces.)

engine would remain straight during the flight. The aft end of the booster also included an aluminum boat tail retainer that both reduced drag at the end of the booster and acted to hold the engine and casing in place during flight.

**1.4 Transition system** The transition system was in place to allow for a smooth drag separation event. In order to achieve this, a 6.5 cm plastic nosecone was attached to the back of the dart. Next, a larger 9.8 cm nosecone was truncated on the fore end and attached to the booster at the aft end. This allowed the rear nosecone of the dart to nest in the larger, truncated nosecone of the booster. A 9.8 cm bulkhead was used to seal the aft end of the larger nosecone. This apparatus enabled a smooth drag separation while still ensuring the dart remained vertical during the rocket's ascent.

**1.5 Fins** The fins for both the booster and the dart were custom manufactured in-house using 1/8<sup>th</sup> in. 5-ply birch plywood. Plywood was chosen because of its maximum strength during launch as well as ease of fabrication. 5-ply was selected to ensure that the fins had sufficient stiffness to prevent deformation under turbulent conditions (i.e. high winds). A table saw, miter saw, and band saw were used for fabrication.

The fins for both the dart and booster were dimensioned with consideration to their effect on the overall stability and structural integrity of the rocket. Numerous simulations using different fin dimensions were run on OpenRocket. The final dimensions enabled a balance between the stability and maximum apogee of the rocket. The fins were also dimensioned to ensure that they remained fixed to the rocket during flight. The booster fins were attached to both the engine mount and the outside of the rocket to ensure structural integrity. The dart fins were attached both at the point where all the fins converged at the center of the rocket as well as the outside of the rocket. The final dimensions are shown below.



**1.6 Recovery system** The recovery system allowed both the dart and the booster to be recovered after the rocket's flight. For the booster, the ejection event was supplied by the motor

used during flight. Because the aft end of the transition system was sealed, the transition would separate from the rest of the booster during the ejection event. This enabled the release of the 36 in parachute that was attached via shock cord to the transition and the motor mount centering ring. The dart recovery was supplied by black powder ejection canisters. The ejection canisters were connected to the StratoLoggerCF altimeter, which was to signal for detonation shortly after the dart's apogee. These caps were attached to the aft end of the electronics payload bay that separated the dart tube near the middle. This allowed a 24 in parachute to deploy.

**1.7 Engine** The engine used in this launch was a Cessaroni I455-VMAX engine. The engine was mounted within the booster via the 5.4 cm engine mount and then retained using the aluminum boat tail retainer.

## 2.0 Payload System Design Features

**2.1 Rotation sensor system** The intent of the rotation sensor system was to capture rotational data in the X, Y, and Z axes as a function of time for use in post flight analysis. To accomplish this, Badger Ballistics considered the need for a user-friendly software platform with a large support community, compatibility of the sensor and microcontroller, and component size and weight. Ultimately an Arduino Uno microcontroller and a three-axis Grove gyro sensor were selected.

The Arduino Uno (ATmega328) was 2.7 in. by 2.1 in and weighed 25g. The Arduino possessed flash memory to store input data until it could be accessed by a computer via a USB cable. A 9V battery was required to power the microcontroller and included in the system.

Implementation of the gyro sensor took place in a two-phase process. In the first phase the gyro sensor and microcontroller were physically connected and open source code was used to write software for the implementation of the sensor. It is important to note that the sensor was intended to be manually actuated by the flight operator and record continuously for the estimated 65 second flight until manually shut down by the operator. This significantly simplified the software implementation by removing the need for the sensor to self-activate. In hindsight, the software could be written to self-activate in order to begin as soon as the rocket began to move.

After software implementation was complete, the hardware was tested to ensure correct functionality. To simulate flight conditions a simple jig of the nose cone was mocked up. The sensor was attached to the jig and rotated about its longitudinal axis. Data from the mock up was then compared to simple calculations performed by Badger Ballistics to ensure system operation. The functionality of the hardware was confirmed.

**2.2 Video recording system** The primary goal of the video recording system was to capture images of the drag separation of the rocket from the booster for post flight analysis. Cost

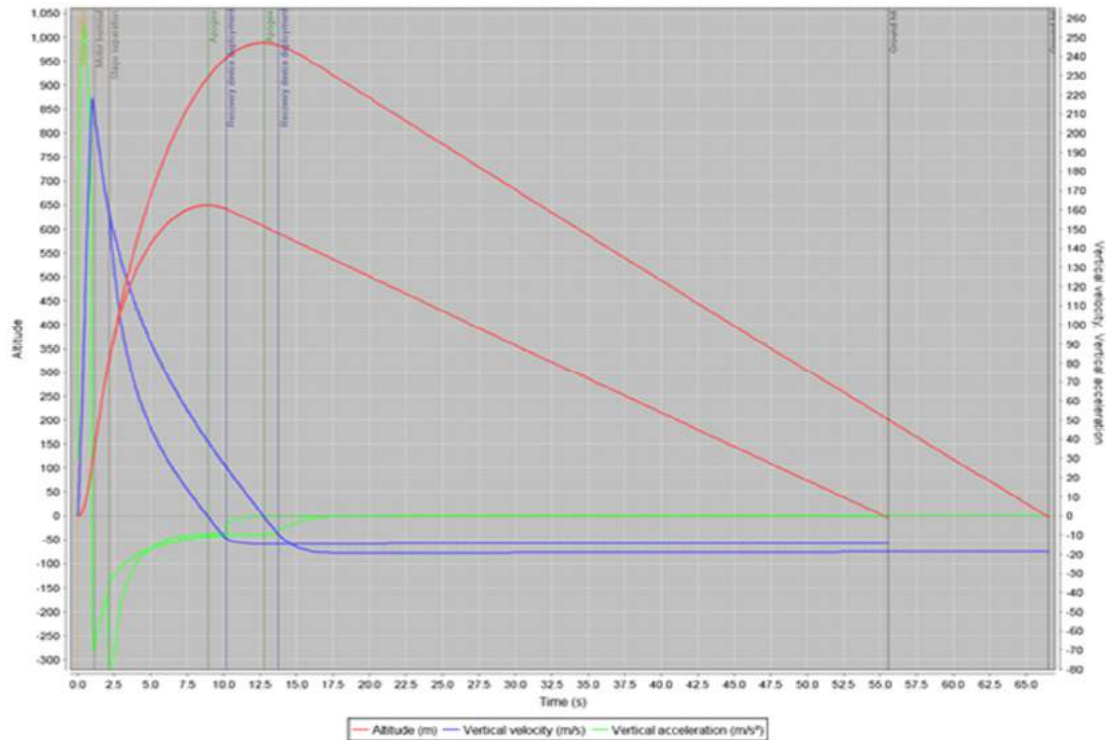
effectiveness, low weight, small size, and electronic compatibility were the primary considerations in the selection of this system.

To accomplish this, a key chain camera was repurposed. The fully encased camera weighed 3.2 ounces, but the plastic housing was removed before installation to reduce overall system weight. This construction required that the rocket be recovered to acquire stored data, as it was saved on board the rocket.

To capture the drag separation, high attention to detail was placed on the positioning of the camera lens. It was mounted to the nosecone of the dart in the downward-facing (nadir) position. This created a counter-balance of weight in the nosecone. To counteract this imbalance, and ensure that the rocket dart flew straight, the opposite side of the nose was counterweighted with steel.

### 3.0 Analysis of Anticipated Performance

The anticipated flight of the rocket was predicted using OpenRocket, an open source model rocket simulator. Using this simulation, the altitude of the booster separation was predicted to be 1394.36 ft. (425 m), the apogee of the dart was predicted as approximately 3248 ft. (990 m), and the rocket peak acceleration was predicted as approximately 840 ft/s<sup>2</sup> (256 m/s<sup>2</sup>). These results can be seen below. Note that some error is expected in this simulation as it is unable to account for the prevailing atmospheric conditions present during the true flight.



**3.1 Flight and stability analysis** Based on OpenRocket, the rocket had a center of pressure (CP) of approximately 39 in. (99.3cm) from the top of the rocket and a center of gravity (CG) of approximately 34 in. (87.2cm) from the top. This gave a stability of 1.19 cal which was above the benchmark of 1cal, and therefore inherently stable.

After separation, the booster and dart each had different centers of gravity and pressure. The dart had a CG located approximately 18 in. (46.2 cm) from the top and a CP approximately 21 in. (53.2 cm) from the top yielding an overall stability of 1.05 cal for the post-separation portion of the flight. This kept the pitching of the overall rocket and the dart to a minimum during the flight.

In contrast, the booster had a negative stability after separation that caused pitching. This was due to a CP of 17.5 in (44.6 cm) and a CG of 18 in (45.9 cm) from the top of the rocket. Because the separation occurred after motor burnout, and the incurred pitching is not considered to be a safety hazard, this was deemed allowable.

**3.2 Recovery analysis** To ensure recovery and reusability of the rocket, dual recovery systems were deployed to carry both the dart and booster safely to the ground. A fail safe recovery system was critical not only to retrieve data from the on board avionics but also to prevent property damage and injury.

The booster and dart were equipped with 36 in. and 24 in. chutes respectively. These were mounted via industrial hooks and kevlar cord. For their descents, the booster was expected to fall at a constant velocity of around 39 ft/s (12 m/s) and the dart was expected to fall at approximately 55ft/s (17 m/s).

**3.3 Environmental conditions analysis** Because the stability factor on the full rocket was above 1 cal, restorative forces on the aft end of the rocket should have mitigated any effect that the wind had on its flight. This would hold for light to moderate wind speeds (~10 m/s). If the wind speed was higher than that, it was possible for the rocket to tumble while the engine was burning, so launch was not recommended. The booster tumbled after separation, but this occurred without hazard as it was unpowered at this point of the flight. The dart had similar flight characteristics as the full rocket, although it most likely faced higher wind speeds at higher altitudes. These speeds were of little concern as the dart was unpowered, and therefore posed little safety risk.

#### **4.0 Competition Flight**

The flight took place on May 2, 2015 at the Richard Bong State Recreation Area just outside of Milwaukee, WI. During the competition day the only adjustment made to the rocket was rerouting the arming wires for the altimeter to allow greater control of the firing of the rocket. The rocket was launched with a stable trajectory, and dart separation occurred before apogee. Upon recovery deployment at dart apogee, the dart tailcone came out of the dart, and the

electronics package fell out with it. Both items were easily recovered. Booster recovery also deployed and the booster was recovered.

## **5.0 Post Flight Analysis**

The predicted apogee for the flight was 3248 ft, however the rocket actually only reached an apogee of 2059 ft. This means our results had an error of 57%, which is quite high. It is likely that multiple factors contributed to the lower than theoretical apogee. Among possible causes are: overuse of construction materials and adhesives, energy loss due to unexpected pitching, and inadequate or oversimplified modeling. The flight performance was predicted using OpenRocket's open source simulation software. The software, while very helpful to the design of the rocket, was not sufficient to account for all aspects and variables of the actual rocket launch. For example, the simulation software assumed a perfectly vertical launch, but on the launch day the rocket was not launched entirely perpendicular to the ground. The software was also unable to account for pitching in the rocket's flight path. The pitching of the rocket during its flight, while minimal, almost certainly decreased its maximum apogee.

Upon dart recovery deployment, it appeared from the ground that the dart tailcone fell out of the dart body, and our electronics with it. After further inspection, we believe that the tailcone was actually ejected from the rocket due to the recovery event. Because we had to modify the rocket on launch day, the electronics bay had a hole running through its length. This hole should have been filled, acting as a bulkhead. Since it wasn't, when the black powder charge detonated, the exhaust gasses were forced through the electronics bay. This caused both ends of the rocket to separate, and allowed some of the electronics to fall out.

The electronics were recovered in operating condition, but unfortunately with no relevant data. Despite our previous successful testing of the electronics system, we had unforeseen issues on launch day that adversely affected our data. There were last second problems with lining the dart up with the booster at the launch pad which caused a time delay from when we activated the electronics to when the rocket was actually launched. By the time the rocket was launched, we had run ten minutes of sampling on the launch pad, and did not receive data from the actual flight.

## **6.0 Conclusion**

We approached the competition with the desire to gain experience in rocketry while honing our skills developed at UW-Madison. Our design was meant to be a simple one. We sacrificed performance for safety, and took a traditional design approach to our rocket in terms of materials and structure.

The flight did not go exactly as expected, but it was considered successful. The rocket flew lower than we thought by a 57% margin, and we did not collect the data we had hoped to collect. However, our flight was stable, our dart separated before apogee, our parachute deployed for

both the booster and the dart, and all of the pieces were recovered in flyable condition. Thus, the flight itself was successful by meeting these parameters.

This competition was an incredible learning tool. Not only did it allow our team to put engineering principles into practice, but we also received a wealth of experience in designing a system from the ground up. We also gained experience in meeting and presenting, writing technical papers, and dealing with firm deadlines. These are experiences that are difficult to recreate in a classroom setting, but are vital for a career in engineering. If future competitions were to be attempted, we would take what we've learned from this rocket build and try to implement unique design elements. Specifically, we learned of the pitfalls of using only an open source simulation software to simulate the flight of the rocket. In future competitions, more simulation sources would be used and checked against one another. We also learned of the problems and unintended consequences of modifying the rocket on launch day. In future competitions, more testing would be done prior to launch to ensure that the rocket would not need to be modified on launch day.

In conclusion, the design was considered successful. The flight on launch day was safe and successful and the simple design of the rocket enabled its construction to come in about 20% under budget. Much was learned through this opportunity and Badger Ballistics is grateful for the knowledge and experience gained.

# Exploring the Capabilities of Drones for Undergraduate Research<sup>1</sup>

Erlan Wheeler

Mathematics Department  
Carthage College  
Kenosha, Wisconsin

Abstract: Carthage College initiated a program to explore the use of drones in undergraduate research at a small, liberal-arts college. We provided an environment of “toys” for the students to explore and encouraged them to choose their own projects. Our experience was that projects involving mapping, 3D modeling, and programming were more successful than engineering-oriented projects, but this could be due to the expertise of the faculty facilitator. Overall, the experience was highly rewarding and educational to all involved.

## Background

Carthage College is a small, liberal-arts college with a strong tradition of undergraduate research. Since 1993, Carthage College has run a ten-week Summer Undergraduate Research Experience (SURE) program, which in recent years has involved roughly 40 students. The majority of these students majored in physics, mathematics, chemistry, and biology. The physics department in particular has been a leader in the college’s undergraduate research program, annually supporting 10-15 students performing externally funded research and has been identified by the American Institute of Physics as an exemplar in its Carnegie Class for career placements in physics. In addition, every Carthage student must complete a senior thesis.

Carthage does not have an engineering major or any institutional experience with unmanned aerial systems, colloquially known as drones. Despite being a joint appointment in the mathematics and computer science departments, I developed a personal interest in drones and decided to explore their potential to motivate and facilitate undergraduate research. I felt that this effort would directly align with the workforce development mission of the Wisconsin Space Grant Consortium (WSGC) through its emphasis on providing exposure and training to STEM students in an emerging and rapidly growing field in which job demand is very strong [1] and use “the excitement and vision of space and aerospace science to equip the citizens of Wisconsin with the math, science, and technology tools they need to thrive in the 21st century.” [2]

## Procedure

I decided to form a *drone team* of students working within the context of Carthage’s SURE program. The positions were advertised as summer research grants, and twenty-one students applied. This was an unusually large number of applicants, which I attribute to the public’s current fascination with drones. The same selection committee that reviews our traditional SURE grants selected the four students – two of whom had just finished their third year of college work, one had finished two years, and the final student had finished a single year. Not only were the

---

<sup>1</sup> The research was made possible by a 2014-2015 Wisconsin Space Grant Consortium Higher Education Incentives (HEI) Award, made available through the National Space Grant College and Fellowship Program NASA Training Grant #NNX14AP22H.

student varied in terms of college experience, but they were diverse in terms of majors, gender, racial background, and life-experience as well. I believe that diversity contributed to them working so well as a team.

Many undergraduate research projects begin with a known objective or goal. By contrast, I provided laboratory space with drones, a 3D printer, electronic and computer equipment, a flight simulator, hardware, and tools, and encouraged them to “play around” to get familiar with the equipment and develop their own project. As an additional resource, we were fortunate to have established connections with Adam Andrews, the director of operations for Aeroworks Productions, a local company involved in all aspects of UAV technology. Adam agreed to be our consultant and provide training and support.

One student with a background in photography became very interested in using drones for mapping and 3D-modeling. Another who has aspirations of being an engineer decided to design and build his own custom drones using polystyrene foam and 3D-printed parts. A third student in the group figured out how to hack the drone’s mission-planning software to extend its capabilities. And finally, the last student began working with Arduino micro-controllers, Raspberry Pi’s, and sensors to develop a collision-avoidance system.

Not having an engineering or photography background myself, my role was to facilitate their efforts by following their progress, recommending experts that they could talk to, making suggestions, and using our budget to buy the parts and equipment that they needed. After just a few weeks in the lab, the team settled into a comfortable flow of working independently and with each other toward their individual goals. I believe that by letting them choose their own projects according to their interests and strengths, the team members each took ownership of their work and were internally motivated to put in long hours (and even a voluntary extra week) all summer.

## **Results**

The efforts in mapping and 3D-modeling were very successful. The required software is extremely expensive, and so we spent the summer using the limited trial periods provided by the vendors to evaluate their products. By the end of the summer, we could make impressive 3D digital models of buildings and regions at very high resolution. One thing we learned was that our current computing facilities are inadequate for serious 3D work.

The various programming efforts were also highly successful. We had purchased systems that had mostly open-source interfaces, and the students were able to learn what was needed during the summer because none of them came in with particularly strong programming backgrounds. In particular, one student developed a library of parametric equations that could be used to program drones to fly complex paths autonomously.

The engineering projects proved to be less successful. The students learned a lot in their attempts, but much of what they learned is just how complicated the engineering aspect of drone hardware and flight-controllers is.

## **Conclusions**

Looking forward, we discovered that drones are an excellent vehicle for undergraduate learning and projects, but none of the results would be characterized as basic science research in the traditional sense. The trendiness of drones attracts students who might not otherwise become involved in traditional research programs and motivates them to work hard on their projects. The model of providing a laboratory of “toys” to play with and then choose their own projects also worked well, though in the future our collective experience from this summer would put us in a better position to provide more guidance to minimize the time until the students could start working on individual projects.

As for specific areas, working seriously with 3D-modeling requires substantial investment in computer hardware and software, but provides learning opportunities accessible to many students and training that has great value in the job market. Working the programming side of drones is a great way for students to develop their computer skills. As for engineering, without a facilitator with more experience than I had, the recommendation would be to stick with the out-of-the-box equipment.

## **References**

[1] Concerning the demand for those with UAV skills:

- <http://www.aviationschoolsonline.com/faqs/uav-pilot-jobs.php>
- <http://jobs.aol.com/articles/2013/12/12/wheres-the-future-aviation-boom-drone-jobs/>
- <http://www.washingtonpost.com/blogs/innovations/wp/2014/05/13/graduates-with-drone-skills-are-going-to-be-in-demand-soon-heres-why/>

[2] <https://spacegrant.carthage.edu/about/mission/>

# 24<sup>th</sup> Annual Wisconsin Space Conference

## PART FIVE

### Conference Program

# INNOVATIONS IN FLIGHT



2015

Wisconsin Space Grant Consortium and  
Experimental Aircraft Association Present:

## The Twenty-Fifth Annual WISCONSIN SPACE CONFERENCE

EAA AirVenture Museum  
Oshkosh, Wisconsin

Friday, August 14, 2015

# WSGC Presentation Schedule

August 14, 2015

7:30-8:15am      **Registration & Continental Breakfast**      **(Lobby & Founders Wing)**

8:15-8:30am      **Welcome & Introductions**      **(Founders Wing)**

**Christine Thompson:** Program Manager, WSGC; Carthage College

**Kevin Crosby:** Director, WSGC; Dean, Division of Natural and Social Sciences, Carthage College

**Mike LeDocq:** Chair, WSGC Advisory Council; Natural Science Department Head and Physics Instructor, Western Technical College

## **Session 1: Plenary Speaker**      **(Founders Wing)**

8:30-9:15am      **Moderator: Bret Steffen,** Director of Education, EAA

**John Monnet:** President and Founder, Sonex Aircraft LLC

## **Session 2: NASA Partnerships**      **(Founders Wing)**

**Moderator: William Dirienzo,** WSGC Advisory Council; Department of Computer Science, Engineering, Physics, and Astronomy, UW-Sheboygan

9:15-9:30am      **HUNCH: Matt Heer,** *NAVi3: Stabilizing and Controlling a GoPro Camera with Gyroscopes in Microgravity*; Physics & Engineering; Teacher, Platteville High School

9:30-9:45am      **USIP: Tessa Rundle, Kevin LeCaptain, Benjamin Tillema,** *Microgravity Propellant Gauging Using Experimental Modal Analysis*; Physics; Undergraduates, Carthage College

9:45-10:00am      **X-HAB: Nicole Przybyla,** *Design of Carbon-fiber/FDM Spacecraft Structural Fabrication System (SSFS)*; Engineering & Applied Sciences; Undergraduate, UW-Milwaukee

10:00-10:15am      **Senior Design: Justin Collins, Stephen Skibinski,** *Thermal Energy Management on Enceladus*; Mechanical Engineering; Undergraduates, Milwaukee School of Engineering

10:15-10:20am      **FNL Video: Chris Thompson,** Carthage College

## Session 3A: Student Research

(Vetti)

**Moderator: Lindsay McHenry**, WSGC Associate Director, Undergraduate Scholarships and Graduate Fellowships; Associate Professor of Geosciences, UW-Milwaukee

- 10:30-10:45am **Stephanie Bradshaw**, *Thunderstorm Electrification*; Physics & Astronomy; Undergraduate, Carthage College
- 10:45-11:00am **Christopher Christopherson**, *Observing Nebulosities*; Physics & Astronomy; Undergraduate, UW-Oshkosh
- 11:00-11:15am **Jordan Zimmerman**, *Riveting Hammer Vibration and Nerve Damage*; Biomedical Engineering & Cell Biology; Undergraduate, Marquette University/Medical College of Wisconsin
- 11:15-11:30am **Sarah Martens** – *Star Forming Rates and HI Gas Content in Galaxy Groups*; Astronomy & Physics; Undergraduate, UW-Madison
- 11:30-11:45am **Trent Cybela**, *Developments in Fire Suppression on Orbit*, Mechanical Engineering; Undergraduate, UW-Platteville
- 11:45-12:00am **Aaron Olson**, *Recent Progress in Lunar Helium-3 Extraction Research*; Engineering Physics; Graduate, UW-Madison

## Session 3B: K-12 General Outreach

(Batten)

**Moderator: Karen Broitzman**, WSGC Associate Director, Aerospace Outreach; Aviation Education Program Manager, Wisconsin Department of Transportation

- 10:30-10:45am **Barbara Bielec**, *Wild Weather! & Biotechnology: Basics* – BTC Institute Outreach; K-12; Program Director, BTC Institute
- 10:45-11:00am **Susan Kelly**, *NASA Astronaut at Middle School 2016 Summer Science Camps at UW-La Crosse*; Mathematics; Professor, UW-La Crosse
- 11:00-11:15am **John Heasley**, *Driftless Dark Skies: STEM Careers for Rural Students*; Environmental Education; Space Science Educator, Kickapoo Valley Reserve
- 11:15-11:30am **Chris Janssen**, *Space Simulator Engaging Youth for Leadership and Engineering Skills*; Planetarium; Director, Wausau School Planetarium

11:30-11:45am **Thomas Consi**, Learning Spacecraft Engineering with Underwater Vehicles; Freshwater Sciences; Assistant Professor, UW-Milwaukee

## Lunch

(Founders Wing)

11:45-12:45pm **Lunch**

11:45-12:45pm **Individual Awardee Photos**

## Session 4: Academic and Industry Research

(Founders Wing)

**Moderator: Gubbi Sudhakaran**, WSGC Associate Director, Research Infrastructure; Chair of Physics Department, UW-La Crosse

12:45-1:00pm **Seth King**, *Effects of Gamma Irradiation on ZnO*; Physics; Associate Professor, UW-La Crosse

1:00-1:15pm **Robert Benjamin**, *Variable Stars of the Galactic Disk*; Physics; Professor, UW-Milwaukee

1:15-1:30pm **Brian Kragh, Rachel Post, Nathaniel Lee, Stephen Janke**, *Exploring Drone Capabilities for Academic Research*; Natural Science Division; Undergraduates, Carthage College

1:30-1:45pm **Taviare Hawkins**, *Microtubule Mechanics in the Presence of Lattice Defects*; Physics; Assistant Professor, UW-La Crosse

1:45-2:00pm **Todd Treichel**, *Astronaut Crew LED Lighting & Human Factor Effects*; Senior Systems Engineer, Orbital Technologies Corporation

2:00-2:15pm **Eric Compas**, *Investigating the Use of Low-Cost UAVs for Low-Altitude, High-Temporal Resolution Aerial Photography for Natural Resource Research and Teaching*; Geography, Geology, and Environmental Science; Assistant Professor, UW-Whitewater

2:15-2:30pm **Lindsay McHenry**, *Developing Impact Cratering Labs for an Online Introductory Planetary Geology Course*; Geosciences; Associate Professor, UW-Milwaukee

2:30-2:45pm **Robert Ragan**, *Predicting Equilibria in 1-d Collisionless Gravitational Systems*; Physics; Professor, UW-La Crosse

## Session 5: Networking & Poster Session

(Fergus Plaza)

2:45-3:45pm

**Poster Session; Refreshments in Hallway**

**3:30pm - Group Photo in Eagle**

**Moderator: Michael LeDocq**

**Ryan Manske**, *Using Radio Frequencies to Spatially Track ID Tags*; Natural Sciences; Science Teacher, East Troy High School

**Evan Dowling**, *Can Dark Matter Halos Change Shape?*; Physics; Undergraduate, UW-La Crosse

**Zachary Dercks, Matthew Arnoldussen**, *Asteroid Attachment*; Mechanical Engineering; Undergraduates, Milwaukee School of Engineering

**Andrew Eagon**, *The Circulation of Ionized Gas on the Milky Way*; Astronomy; Undergraduate, UW-Whitewater

**RockSat-C Team: Amelia Gear, Tessa Rundle, Jordan Rice, Justin Barhite:** *Normal Field Instability of Ferrofluid in Microgravity*; Physics; Undergraduates, Carthage College

**Collegiate Rocket Launch: Second Place – Engineering Division – Team Badger Ballistic;** Undergraduate Student, University of Wisconsin-Madison  
Represented by Lucas Jewell

**2015 Elijah High Altitude Balloon Program Launch Team:**

Alana Tirimacco; Mechanical Engineering, MSOE

Jordan Petrie; Mechanical Engineering, MSOE

Danny Ochoa; Mechanical Engineering, MSOE

Jadee Kellogg; Physics, Ripon College

**Henri LeMieux** – *Massive Stellar Content of the Cygnus Superbubble*; Physics and Astronomy; Undergraduate, UW-Oshkosh

**Stephen Dornbos** – *Early Life on Land: Evaluating the Biogenicity of Mesoproterozoic Fluvial-Lacustrine Stromatolites*; Geosciences; Associate Professor, UW-Milwaukee

**Geoffrey Ament** – NASA Internship; Engineering Physics; Undergraduate, UW-Platteville

## Session 6: WSGC Team Projects

(Founders Wing)

**Moderator: Bill Farrow**, WSGC Associate Director, Student Satellite Initiatives;  
Assistant Professor, Milwaukee School of Engineering

3:45-4:00pm

**Collegiate Rocket Launch: First Place – Non-Engineering Division – Team Red Hawk Rocketry**; Undergraduate Students, Ripon College

Jadee Kellogg

Akash Sen

Paul Ninneman

James Ihrcke

4:00-4:15pm

**Collegiate Rocket Launch: First Place – Engineering Division – Team Whoosh Generator**; Undergraduate Student, Milwaukee School of Engineering

Represented by Eric Johnson

4:15-4:30pm

**Midwest High-Powered Rocket Launch: Third Place – Engineering Division – Team Pioneer Rocketry**; Undergraduate Student, UW-Platteville

Represented by Jake Ellenberger

4:30-4:45pm

**Elijah Balloon Payload Team**; Mechanical Engineering

Benjamin Jensen, Milwaukee School of Engineering

Kai Swanson, Milwaukee School of Engineering

Taylor Davitz, Milwaukee School of Engineering

Woodrow Walker, Milwaukee School of Engineering

Nate Klassen, UW-Whitewater

Scott Frazier, UW-Milwaukee

4:45-5:00pm

**Tethered Aerostat Program**; NASA STEM Persistence Grant

Amy Jozwiak, College of Menominee Nation

Marilyn Madosh, College of Menominee Nation

Larry Madden, College of Menominee Nation

Jesse Banick, UW-Fox Valley

Kathryn Lentz, UW-Fox Valley

Jeshanah Zolkowski, UW-Fox Valley

Travis Haugstad, Western Technical College

Joel Nielsen, Western Technical College

## Awards Ceremony

(Founders Wing)

5:00-5:25pm

### **Award Presentation**

Chris Thompson – EmCee  
Kevin Crosby – Award Presenter  
Mike LeDocq – Award Presenter

### **Student Programs – Presenters**

Lindsay McHenry – Undergraduate Scholarship  
Gubbi Sudhakran – Undergraduate Research  
William Farrow – Student Satellite Programs  
Dan Hawk – Tethered Aerostat Program  
Robert Morrow – Aerospace Internships  
Lindsay McHenry – Graduate & Professional Programs

### **Non-Student Programs – Presenters**

Karen Broitzman – Aerospace Outreach Program  
Nicole Wiessinger/Michael LeDocq – Special Initiatives Program  
Gubbi Sudhakran – Research Infrastructure Program  
Michael LeDocq – Higher Education Incentives  
Robert Morrow – Aerospace Industry Program

5:25pm

### **Closing Remarks – Kevin Crosby**

# WSGC Evening Schedule

August 14 2015

5:30pm	<b>Reception</b>	<b>(The Voyager)</b>
6:30pm	<b>Welcome – Chris Thompson</b>	<b>(Founders Wing)</b>
7:30pm	<b>Plenary Speaker:</b>  <b>Introductions: Kevin Crosby</b>  <b>Dr. R. Aileen Yingst; <i>Innovations in Spaceflight: Three Years with Curiosity on Mars</i>, Senior Scientist, Planetary Science Institute; Participating Scientist, Mars Exploration Rover Mission; Deputy Principal Investigator, Mars Handlens Imager instrument on Mars rover Curiosity</b>	
8:20pm	<b>Closing Remarks – Kevin Crosby</b>	

# WSGC Workshop Schedule

August 15, 2015

9:00-9:10am	<b>Welcome and Introductions</b>	<b>(Vetti)</b>
	<b>Dan Choffnes</b> , Carthage College, Workshop Leader <b>William Farrow</b> , Milwaukee School of Engineering <b>Aaron Olson</b> , UW-Madison <b>Madeline Klothe</b> , UW-Madison	
9:10-9:20am	<b>Dan Choffnes: <i>Overview of Workshop Themes</i></b>	
9:20-9:30am	<b>Dan Choffnes: <i>Intentionality and Serendipity in the Careers of Scientists and Engineers</i></b>	
9:30-9:45am	<b>Bill Farrow: <i>Developing and Articulating Career Goals</i></b>	
9:45-9:55am	<b>Aaron Olson: <i>Career Path and Advice</i></b>	
9:55-10:05am	<b>Morning Break</b>	
10:05-10:15am	<b>Making Connections</b> <ul style="list-style-type: none"><li>- Networking with Academic Faculty &amp; Staff</li><li>- Reaching out to WSGC Institutional Representatives</li><li>- Courting Potential Internship Sponsors &amp; Graduate Supervisors</li></ul>	
10:15-10:45am	<b>The Statement of Purpose</b> <ul style="list-style-type: none"><li>- Role of Personal Statement/Declaration of Goals in Career (Scholarships, Graduate School)</li><li>- Common Myths about the Personal Statement</li><li>- Mock Review of Sample Personal Statements</li></ul>	
10:45-10:55am	<b>Maddie Kothe: <i>Career Path &amp; Advice</i></b>	
10:55-11:00am	<b>Wrap Up and Conclude</b>	

## MORNING KEYNOTE SPEAKER | JOHN MONNETT

President and Founder, Sonex Aircraft LLC

We are honored to have John Monnett, Founder and President of Sonex Aircraft LLC, as our Event Keynote Speaker. John, a multi-thousand hour private pilot with both glider and float plane ratings and an A&P Mechanic, has many de-signs to his credit including the Sonerai sport aircraft series, Monerai sailplane, Moni motorglider, Monex racer, along

with numerous other homebuilt aircraft. John has over 40 years of homebuilt aircraft and restoration experience along with extensive engine development and testing experience. John was inducted into the EAA Homebuilder's Hall of Fame in 2001 and his designs are on display in the Udvar-Hazy National Air & Space Museum and the EAA AirVenture Museum.



## EVENING KEYNOTE SPEAKER | Dr. R. Aileen Yingst

Dr. R. Aileen Yingst is a Senior Scientist at the Planetary Science Institute, a research institution headquartered in Tucson, AZ. She is a Participating Scientist on the Mars Exploration Rover Mission and Deputy Principal Investigator for the Mars Handlens Imager instrument on the Mars Science Laboratory rover Curiosity. Other missions that Dr. Yingst has worked on include Dawn at Vesta, Mars Pathfinder, Mars Polar Lander, and Galileo. Dr. Yingst also served as Director of the Wisconsin Space Grant Consortium for 14 years.



Dr. Yingst received her AB from Dartmouth College in Physics and Astronomy, and her M.Sc. and Ph.D. in Geological Sciences from Brown University.

## STUDENT PROGRAMS

**Undergraduate Research (UGR)**  
**Dr. Laurel Salton Clark Memorial Graduate & Professional Fellowship (LSC)**  
**WSGC Graduate & Professional Research Fellowship (GPP)**  
Application Deadline: February 1, 2016  
Award Announcement: April 1, 2016

**Undergraduate Scholarship**  
*Two-year Academic Institutions*  
Application Deadline: September 30, 2015  
Award Announcement: December 1, 2015  
**Industry Internship Program (IIP)**  
Application Opportunity: February 1 – 26, 2016  
Award Announcements: Determined by Industry Partners

## TEAM PROGRAMS

**Collegiate Rocket Launch (CRL)**  
*Notice of Intent (NOI) to compete due:*  
Application Deadline: September 30, 2015  
Selection Announcement: October 9, 2015  
Launch Competition: April 23, 2016 (TBC)

**High-Altitude Balloon Program - Elijah**  
*Launch Internship (EBL)*  
Work period April 1, 2016 – May 15, 2017  
*Payload Internship (EBP)*  
Work period May 15, 2016 – August 15, 2016  
Application Deadline: February 26, 2016  
Award Announcements: April 15, 2016

### **Tethered Aerostat Program**

Western Technical College, UW-Fox Valley, College of Menominee Nation  
*Lead Student Internship, Affiliate Student Internship*  
Work Period September 19, 2015 – September 18, 2016  
Application Deadline: September 30, 2015  
Award Announcements: October 30, 2015

## ACADEMIC & INDUSTRY PROGRAMS

**Aerospace Outreach Program (AOP)**  
**Special Initiatives Program (SIP)**  
Application Deadline: October 16, 2015  
Award Announcements: December 7, 2015

**Higher Education Incentives (HEI)**  
**Research Infrastructure Program (RIP)**  
Application Deadline: December 10, 2015  
Award Announcements: March 1, 2016

**Industry Internship Program (IIP)**  
Application Deadline: November 16, 2015  
Award Announcements: February 1, 2016

For more information on upcoming events, please visit our website: [spacegrant.carthage.edu](http://spacegrant.carthage.edu)